The chemistry of high reactive species and their role on the oxidative capacity at polar regions

Albane Barbero

Université Grenoble Alpes

THÈSE

Pour obtenir le grade de

DOCTEUR DE L'UNIVERSITE GRENOBLE ALPES

Spécialité : **Sciences de la Terre, de l'Univers et de l'Environnement**

Arrêté ministériel : 25 mai 2016

Présentée par

Albane BARBERO

Thèse dirigée par **Joël SAVARINO**, Directeur de recherche, Université Grenoble Alpes, et
codirigée par **Roberto GRILLI**, Chargé de recherche, Université Grenoble Alpes

préparée au sein de **l'Institut des Géosciences de l'Environnement**
dans **l'École Doctorale Sciences de la Terre de l'Environnement et des Planètes**

Chimie des espèces réactives et leur rôle sur la capacité oxydante en régions polaires

The chemistry of high reactive species and their role on the oxidative capacity of the atmosphere at polar regions

Thèse soutenue publiquement le **11 juin 2021**,
devant le jury composé de :

Monsieur Aurélien DOMMERGUE
Professeur des Universités, Université Grenoble Alpes, Président
Madame Kathy LAW
Directeur de recherche, CNRS, Rapporteure
Monsieur Valéry CATOIRE
Professeur des Universités, Université d'Orléans, Rapporteur
Madame Anne MONOD
Professeur des Universités, Université Aix-Marseille, Examinatrice
Monsieur Markus FREY,
Docteur en sciences, British Antarctic Survey, Examinateur
Madame Irène VENTRILLARD,
Maître de conférence, Université Grenoble Alpes, Examinatrice
Monsieur Joël SAVARINO,
Directeur de recherche, CNRS, Directeur de thèse
Monsieur Roberto Grilli
Chargé de recherche, CNRS, Co-Directeur de thèse

"S'il est vrai, ajoute-t-il, que, comme certains le prétendent, les glaces ne se forment en mer que de l'eau douce qui coule des terres, il faut conclure qu'il y en a [des terres] vers le pôle austral..." Amédée Frézier 1682-1773

Abstract

The Antarctic snowpack has long been considered to be a chemically and biologically inert material where chemical species that had been transported over long distances were indefinitely archived without undergoing significant new changes. This assumption is partly true, as evidenced by the 800,000-year records of atmospheric temperature and CO_2 content successfully retrieved through the chemical analysis of ice cores from the Antarctic Plateau. However, over the last two decades, the paradigm of snow as an inert material has been challenged by the discovery of substantial chemical activity within the snowpack and, in particular, its elevated nitrogen oxides content. When sunlight resumes at the end of the polar night, it triggers photochemistry (chemistry involving the absorption of a photon by chemical species, such as the photolysis reaction) within the porous snowpack. The highly reactive products of this photochemistry can be exchanged between snow and atmosphere, and these exchanges will redistribute the species governing the oxidizing capacity of the atmosphere.

Many studies that sought to better understand these polar processes have shown that: i) highly reactive species (such as NO_x, OH, HO_2, RO_2, and XO) play a key role in such a remote environment, controlling the oxidative capacity and the atmospheric chemistry and ii) snow emissions also locally control the oxidative capacity. Indeed, gaseous nitrogen species, especially nitrogen oxides NO_x ($NO_x \equiv NO + NO_2$), emitted from the photolysis of nitrate contained in the snowpack, lead to a strong production of O_3 and OH radicals in the atmosphere. Unfortunately, these mechanisms are still poorly understood due to the lack of information on the behavior of nitrate in snow and the absence of direct measurements of NO_2 at the snow-atmosphere interface. A better understanding of the mechanisms generating these snow-sourced emissions is therefore fundamental for a deeper learning of the atmospheric chemistry occuring at snow covered regions. Thus it is important to obtain accurate observations of nitrogen species despite the technical challenge related to their very low concentration levels of the order of 10^{-9} to 10^{-12} mol mol^{-1}. Therefore, the objectives of this research work are: i) to validate and deploy accurate instruments dedicated to the direct measurement of NO_2; ii) to better characterize nitrate photolysis through the study of different snows from the Antarctic Plateau (different ages and locations); and iii) to measure NO_x concentrations in the Antarctic atmosphere with a better accuracy.

First, we applied a NO_x measurement technique based on incoherent broadband cavity enhanced absorption spectroscopy (IBBCEAS) that is different from those previously used in Antarctica. This technique allows direct measurement of NO_2 and NO_x, and thus it reduces concentration level uncertainties. We developed, tested, and validated two robust instruments, for NO_2 and NO_x detection, respectively, that reached detection limits around 30×10^{-12} mol mol^{-1} (3σ) and we deployed these instruments in the Antarctic field at Dome C.

Two hypotheses explain the behavior of nitrate in the snowpack facing the absorption of a photon. The first one, commonly accepted, assumes the existence of two nitrate fractions: one subject to photolysis and the other not easily accessible to photons. However, recent studies have proposed a single mechanism for the localization of nitrate into the snow during its deposition. In order to better understand the nitrate behavior, we performed flux chamber experiments using different types of snow of various ages and locations. These innovative experiments showed that the photolysis rate constant of nitrate is similar for all snow samples. This result suggests that the localization of nitrate in snow is identical regardless of snow type and age, which supports the single nitrate fraction model of recent theoretical studies.

Finally, using the developed IBBCEAS instruments, we studied the summer diurnal variability of

NO and NO_2 levels above the snowpack. The NO_2:NO ratio observed at the beginning of the photolytic season (December) appears to be too high with respect to the expected photochemical equilibrium, while in January, the photochemical equilibirum seems reached. This excess of NO_2 could be explained by summer variability of the main NO_2 source, where the photo denitrification of the snowpack is stronger in December than in January.

These three years of research have validated the use of optical cavity instruments in remote and challenging field sites such as Antarctica. Their stability, specificity, and ease of use open the way to new measurement and scientific opportunities in polar regions. The use of flux chambers for the first time in Antarctica has confirmed the existence of a single mechanism of nitrate photolysis. This research thus provides a firm foundation for future research work where integrated observations and modeling bring the scientific community closer to a fully coherent interpretation of the reactive chemistry above the snowpack.

Résumé

Le manteau neigeux de l'Antarctique a longtemps été considéré comme un matériau chimiquement et biologiquement inerte où les espèces chimiques transportées sur de longues distances étaient archivées sans subir de nouvelles transformations significatives. Cette hypothèse est en partie vraie, comme en témoignent les enregistrements de 800 000 ans de température atmosphérique et de teneur en CO_2 obtenus avec succès grâce à l'analyse chimique des carottes de glace du plateau antarctique. Cependant, au cours des deux dernières décennies, le paradigme de la neige en tant que matériau inerte a été remis en question par la découverte d'une activité chimique substantielle au sein du manteau neigeux et, en particulier, de sa teneur élevée en oxydes d'azote. Lorsque la lumière du soleil reprend à la fin de la nuit polaire, elle déclenche la photochimie (chimie impliquant l'absorption d'un photon par une espèce chimique, comme la réaction de photolyse) au sein du manteau neigeux poreux. Ainsi, de nombreux échanges air-neige redistribuent les espèces régissant la capacité oxydante de l'atmosphère.

De nombreuses études cherchant à mieux comprendre ces processus polaires ont montré que : i) les espèces hautement réactives (telles que NO_x, OH, HO_2, RO_2 et XO) jouent un rôle clé dans un environnement aussi éloigné, contrôlant la capacité oxydante et la chimie de l'atmosphère et ii) les émissions de la neige exercent également un contrôle local sur la capacité oxydante. En effet, les espèces azotées gazeuses, notamment les oxydes d'azote NO_x ($NO_x \equiv NO + NO_2$), émises par la photolyse du nitrate contenu dans le manteau neigeux, conduisent à une forte production d'oxydants O_3 et OH dans l'atmosphere. Malheureusement, ces mécanismes sont encore mal compris du fait du manque d'informations sur le comportement du nitrate contenu dans la neige mais aussi de l'absence de mesures directes du NO_2 à l'interface neige-atmosphère. Une meilleure compréhension des mécanismes générant ces émissions d'origine neigeuse est donc fondamentale pour une meilleure connaissance de la chimie atmosphérique qui se produit dans les régions couvertes de neige. Il est donc important d'obtenir des observations précises des espèces azotées malgré le défi technique lié à leurs très faibles niveaux de concentration, de l'ordre de 10^{-9} à 10^{-12} mol mol^{-1}. Ainsi, les objectifs de ce travail de recherche sont : i) valider et déployer des instruments précis dédiés à la mesure directe du NO_2 ; ii) mieux caractériser la photolyse des nitrates par l'étude de différentes neiges du plateau Antarctique (âges et provenances variés) et iii) mesurer les concentrations de NO_x dans l'atmosphère Antarctique avec une meilleure précision.

Dans un premier temps, nous proposons d'appliquer une technique de mesure des NO_x basée sur la spectroscopie d'absorption large bande associée à une cavité à haute réflectivité (IBBCEAS), différente de celles utilisées précédemment en Antarctique. Cette technique permet de mesurer directement le NO_2 et les NO_x, et réduit ainsi les incertitudes liées à leurs niveaux de concentration. Nous avons développé, testé et validé deux instruments robustes, l'un pour la détection du NO_2 et le second pour celle des NO_x, atteignant des limites de détection de 30×10^{-12} mol mol^{-1} (3σ) et nous avons déployé ces instruments sur le terrain antarctique à Dôme C.

Deux hypothèses expliquent le comportement du nitrate dans le manteau neigeux suite à l'absorption d'un photon. La première, communément admise, suppose l'existence de deux fractions de nitrate : l'une sujette à la photolyse et l'autre difficilement accessible aux photons. Mais, des études récentes proposent un mécanisme unique de localisation du nitrate dans la neige lors de son dépôt. Cherchant à comprendre le comportement du nitrate, nous avons réalisé des expériences en chambre à flux en utilisant différents types de neige, d'âges et de localisations variés. Ces expériences inédites ont montré que la constante de vitesse de photolyse du nitrate est similaire pour tous les échantillons de neige étudiés. Ce résultat suggère que la localisation du nitrate dans la neige est identique

quels que soient le type et l'âge de la neige, ce qui corrobore le modèle de fraction unique de nitrate des études théoriques récentes.

Enfin, en utilisant les instruments IBBCEAS développés, nous avons étudié la variabilité diurne estivale des niveaux de NO et de NO_2 au-dessus du manteau neigeux. Le rapport NO_2:NO observé au début de la saison photolytique (décembre) apparaît trop élevé pour respecter l'équilibre photochimique attendu, équilibre qui semble être atteint en janvier. Cet excédent de NO_2 pourrait s'expliquer par la variabilité estivale de la principale source de NO_2, où la photo dénitrification du manteau neigeux est plus forte en décembre qu'en janvier.

Ces trois années de recherche ont permis de valider l'utilisation d'instruments à cavités optiques sur des terrains aussi éloignés que l'Antarctique. Leur stabilité, leur spécificité et leur facile mise en œuvre ouvre la voie à de nouvelles mesures en milieux polaires. L'utilisation, pour la première fois en Antarctique, de chambres à flux, a permis de confirmer l'existence d'un seul mécanisme de localisation du nitrate. Ces travaux de recherche fournissent une base solide pour les futurs travaux de recherches, mêlant observations et modélisations, ce qui pourrait nous rapprocher un peu plus d'une interprétation cohérente de la chimie réactive au-dessus du manteau neigeux.

"L'important, ce n'est pas la destination, mais le voyage en lui-même"
Robert Louis Stevenson

Remerciements

Ces quelques lignes, me permettent de prendre le temps de remercier toutes les personnes sans lesquelles la thèse que vous êtes en train de lire, véritable aventure scientifique et humaine, n'aurait été possible.

En premier lieu, je tiens à remercier Kathy Law et Valéry Catoire, pour avoir accepté d'évaluer ce tapuscript. Merci également à Anne Monod, Markus Frey, Irène Ventrillard et Aurélien Dommergue pour leur participation au Jury. Les échanges scientifiques qui ont eu lieu lors des questions sont la preuve de l'attention qu'ils ont apportée à mon travail.

Je souhaite remercier mes directeurs de thèse : Joël Savarino, pour m'avoir fait confiance: d'abord comme hivernante à Concordia il y a déjà 9 ans, puis comme ingénieure d'études (mes narines ont encore en mémoire l'extraction du fumier avant son analyse isotopique!). Puis enfin comme doctorante. Tes qualités scientifiques et ta franchise m'ont poussée à creuser toujours plus mes réflexions scientifiques. Je te suis reconnaissante pour le temps conséquent accordé à la relecture de mon tapuscrit. Je remercie également mon co-directeur de thèse, Roberto Grilli: alors même que nous ne nous connaissions pas, tu as accepté de m'encadrer. Ces travaux ne sont peut-être pas ceux que tu avais imaginés initialement, mais la détection des radicaux halogénés à Dumont D'Urville avec un LP-MOCAMAR sera sans doute l'occasion pour toi d'écrire cette satanée HDR! Les deux semaines intensives à Cork m'ont fait découvrir ton énergie et ta capacité de rebondissements aux aléas instrumentaux, qualités motrices pour moi et qui ont été prépondérantes à la bonne réussite de cette thèse. Grâce à la confiance que tu m'as accordée, j'ai pu apprivoiser les IBBs et participer pleinement à leur perfectionnement.

Merci à mon comité de thèse, pour leurs conseils qui m'ont apporté une ouverture et une expertise scientifique complétant celle de mes directeurs: Jennie Thomas, Markus Frey et Karine Sellegri.

Je tiens également à remercier les chimistes de l'IGE, pour leur disponibilité à échanger sur mes données et leurs interprétations: Jennie T., Shaddy. A, Didier V., Olivier M., Patricia M., Suzanne P., Michel L. Un grand merci à Guillaume M., Daniele R. et Irène V. du LiPhy et Camille B. de l'IGE pour leur patience dans les explications de la physique des lasers et du développement instrumental. Un remerciement particulier à Camille B., pour m'avoir laissé prendre le contrôle des IBBs. Merci également à Franck D. du LECA pour m'avoir autorisée à tester mes équipements à la station du Lautaret. Merci à Ghislain P. et Laurent A., pour l'initiation à la physique de la neige et au flux actinique. Merci aussi à Charles A. pour les simulations MAR.

Un grand merci aux équipes d'administration et de direction de l'IGE (Amélie V., Carole B. , Mélissa D., Shaïnez K., David L., Eric C. et Bérénice B.; Pierre B., Sandrine A., et Gael D.) et de l'ED TUE (Guy D., Emmanuel C., Florence T.) sans lesquels mes recherches auraient eu des difficultés à voir le jour. Mention spéciale à Amélie, notre gestionnaire d'équipe, pour sa disponibilité et son éternelle bonne humeur, mais aussi pour nos discussions autour des vans aménagés qui m'ont accordé des instants d'évasion durant les moments intenses de la fin de thèse.

Un grand merci à mes partenaires du bureau 122.2 pour nos discussions et confessions dans un mélange de français, d'espagnol et d'anglais, que du bonheur! Merci à la team isotope dans laquelle règne un esprit d'équipe fort: llann et Joseph, plus à l'IGE, mais jamais très loin; Elsa d'une disponibilité et d'un soutien moral non négligeables; Sarah et Alexis, pour avoir patiemment écouté mes problèmes de déraillements de nombreux matins mais surtout pour avoir résolu le problème (ça y est, j'ai un nouveau vélo!); Pete pour la relecture INTEGRALE du tapuscrit de thèse et pour

cette mission terrain 2019-2020! Enfin, une mention très spéciale à Nico, alias Dj Pompon, pour ton humanité, ton soutien, ton aide dans mes recherches de projet professionnel et plus que tout, pour ton amitié.

Merci à tous les amis, rencontrés avant et pendant l'aventure de la thèse, (liste non exhaustive et dans le désordre avec probablement quelques oublis, non intentionnels) :

- Aux copains de Grenoble, de Lyon et d'ailleurs, il serait beaucoup trop long de tous vous nommer!
- Aux anciens du labo, ces collègues et amis qui m'ont donné envie d'y revenir: Eric L., Delphine S., Nicolas C., Nicolas J., Laurent A., Vincent F., Vincent P., Manu L., Bruno J., Elsa G., Laure T., Ilann B., Hélène A., Marion R., Julien B., Pedro C., Greg T., Benoît L., Olivier M., Oliver A., Catherine R., Philippe P., Luc P., Romain D.; et aux nouveaux qui rendent le départ encore plus difficile: Ugo N., Alvaro R., Hans S., Anil K., Camille B., Sarah A., Pete A., Alexis L., Maria S., Jinwha S., John W., Jordi B., Etienne L., Laura G., Cruz G., Fanny B., ...
- Merci au Conseil de Laboratoire, qui m'a permis de découvrir le fonctionnement de la "maison IGE". Merci à la team Friday Beer, pour ces rencontres de fin de semaine toujours appréciées. Merci aussi à la team footing, sans qui vous auriez probablement dû me rouler jusqu'à ma soutenance: Delphine S., Carole B., Elsa G., Gaëlle U., Sarah A., Fanny B., sans oublier la team "Prest'IGE" et notre superbe performance lors de l'EKIDEN 2019. Un merci spécial à Delphinounette, pour ton soutien, ta motivation communicative et ton amitié!
- Aux copains de l'Antarctique, cette étrange famille de tous horizons: Marie-Anne, Guillaume, Vivien, Nicoco, Bruno, Tinou, Rémi Elec, Rémi Chef, Benoît, Kiki, Damien, Quentin, Massimo, Doris, Arnaud, Yann & Simon, Clémeeent, Elisa, Celas, Fanny, Pete, Anna, Véro, Dadou, Fanfoué... avec une mention spéciale aux hivernants glacios que j'ai eu le plaisir de côtoyer et de suivre: Julien (Jujuuuu) et Inès (Titchat, ma petite sœur de cœur!). Sans vous, les missions n'auraient pas eu ce goût de "reviens-y".

Je rajoute un merci très particulier à Bruno Jourdain, alias "Chef", sans qui toute cette aventure n'aurait jamais existé, un "P'tiot" qui, il y a de cela 9 ans, a parié sur une "P'tite" pour hiverner à la station Concordia de Dome C, lui ouvrant ainsi la porte de ce monde incroyable de l'Antarctique; ainsi qu'à Éric Lefebvre, ce confident d'hivernage, grâce à qui mes premiers pas dans cet univers magique ont été une réussite. Merci Éric pour ta présence, ton humeur bougonne, ta capacité d'écoute incroyable, ton soutien sans faille et par dessus tout, ton amitié. Il n'y a qu'un seul ours blanc en Antarctique, et j'ai la chance de le compter parmi mes amis.

Enfin je remercie ma famille, que j'ai quelque peu délaissée ces derniers mois pour achever cette thèse. Leur attention et leurs encouragements m'ont accompagnée tout au long de ces années. Merci à mes parents, pour leur soutien moral et leur confiance, et particulièrement à ma maman, pour avoir si souvent corrigé mes fautes d'orthographe et de syntaxe, jusqu'à ces dernières lignes que j'écris. Merci à mon frère et mes sœurs, à mes neveux et nièces, auxquels je vais enfin pouvoir consacrer plus de temps!

Il m'est impossible d'achever ces remerciements sans une pensée particulière à mon pilier: Sammy. Merci pour ton soutien quotidien indéfectible, pour ton aide précieuse en Python et Latex mais pas uniquement, pour ton regard critique sur mes questionnements scientifiques, pour ta patience extrême de tous les jours, et surtout à la fin! Notre couple a grandi en même temps que cette thèse: la réalisation simple et naturelle de nos projets de maison et de van qui nous faisaient rêver n'a fait que renforcer cette complicité si forte que nous partageons! Je t'aime.

Contents

Chapter 1

Introduction

Contents

1.1 The study of the Earth's atmosphere

« We live at the bottom of an invisible ocean called the atmosphere, a layer of gases surrounding our planet. » National Geographic Encyclopedia, 2011

The Earth's atmosphere is the layer of gases and particles surrounding our planet. The air is composed mainly of nitrogen (N_2) and oxygen (O_2) as well as other gases, such as argon (Ar), carbon dioxide (CO_2), and trace gases such as tropospheric ozone (O_3), volatile organic compounds (VOCs), reactive nitrogen gases (NO_y), and reactive sulfur gases (SO_y) at low concentrations of the order of 10^{-6} to 10^{-12} mol mol^{-1}.

In the upper atmosphere, the interactions between molecular oxygen and solar light radiation result in the formation of an ozone layer insulating the Earth's surface from part of the ultraviolet radiation harmful to biological development (Fig. 1.1). In the lower layers of the atmosphere, greenhouse gases, such as atmospheric water vapour (H_2O), CO_2, methane (CH_4), nitrous oxide (N_2O), and O_3, exert a considerable influence on the Earth's climate: without them, the average surface temperature would be about -18 °C (Ma and Tipping, 1998).

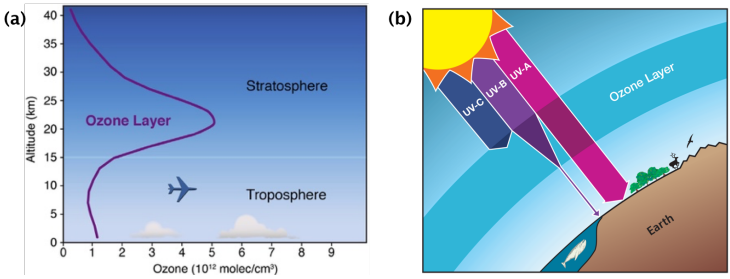

Figure 1.1 – **(a)** Vertical profile of ozone in the atmosphere. Approximately 90 % of Earth's protective ozone layer is located in the stratosphere, the region of the atmosphere that extends from ≈ 10 to 16 km above the surface up to ≈ 60 km, (Wilmouth et al., 2018). **(b)** Much like sunscreen for the Earth, the ozone layer shields the Earth from the sun's damaging UV-C and UV-B radiation, which can adversely affect living species and ecosystems, (© NOAA Chemical Sciences Laboratory)

Suspended particles, called aerosols, also influence the climate according to their physical and chemical characteristics: for example, sulfuric acid aerosols cool the atmosphere by reflecting some of the solar radiation back to the upper layers of the atmosphere, while black carbon areosols warm the atmosphere by absorbing radiation.

Finally, the so-called "reactive species" have lifetimes that are extremely short (i.e., a few seconds to a few minutes) and are present in small quantities in the atmosphere. These reactive species have a fundamental role in the transformation of compounds emitted to the atmosphere, naturally or as a result of human activities. For the most part, these reactive species progressively oxidize elements entering the atmosphere and indirectly influence the climate. For example, carbon and hydrogen species are transformed into the two major greenhouse gases of CO_2 and H_2O, while nitrogen and sulfur species form nitric acid (HNO_3) and sulfuric acid (H_2SO_4), resulting in acid rains. Figure 1.2 shows the complexity of the chemical and transport processes related to the atmospheric composition.

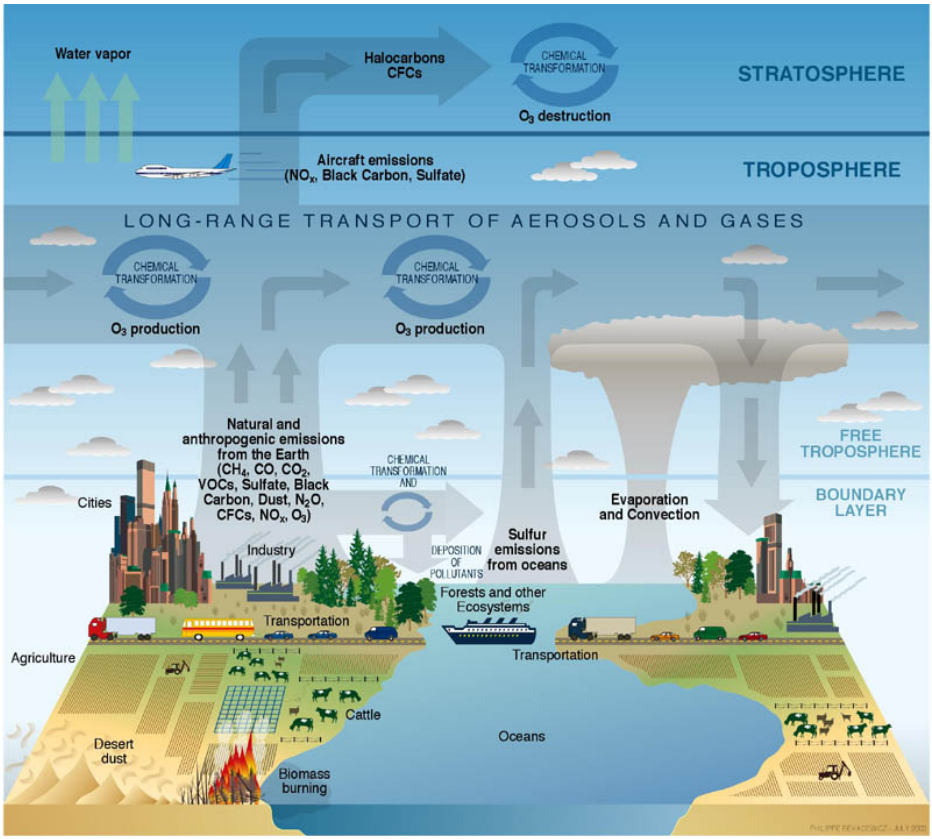

Figure 1.2 – Diagram of chemical and transport processes related to atmospheric composition: these processes link the atmosphere with other components of the Earth's system, including the oceans, land, terrestrial and marine plants and animals, (© Phillipe Rekacewicz - Strategic Plan for the U. . Climate Change Science Program).

The "oxidizing capacity" of the atmosphere reflects its ability to destroy or oxidize the compounds that enter it through the rate of those oxidation mechanisms, and this power depends mainly on its content of hydroxyl radicals (OH) (Prinn, 2003).

1.1.1 A brief history of the Atmospheric Chemistry

The following discussion of atmospheric chemistry will highlight important historical discoveries and the evolution of the field, starting with the discovery of the hole in the stratospheric ozone layer. This summary heavily draws upon two excellent reviews of atmospheric chemistry, Briday (2014) and Monks et al. (2021) and further details on this subject can be found therein.

1.1.1.1 The stratospheric ozone layer

The first steps in global atmospheric chemistry concern chemical reactions in the upper atmosphere, and in particular the chemistry of stratospheric ozone. Ozone occurs naturally at low concentrations throughout the Earth's atmosphere. But ozone is particularly "good" in the stratosphere, 10 to 50 km above Earth's surface, as it protects life on Earth from the sun's ultraviolet radiation (Fig. 1.2). In 1929, Sydney Chapman proposed the first stratospheric ozone production (R1.1 to R1.4) and destruction (R1.5 and R1.6) mechanism:

Production

$$O_2 + h\nu \rightarrow 2O \qquad (120 \leq \lambda \leq 210 \text{ nm}) \qquad \text{(R1.1)}$$

$$O + O_2 \rightarrow O_3 \qquad \text{(R1.2)}$$

$$O_3 + h\nu \rightarrow O_2 + O \qquad (200 \leq \lambda \leq 300 \text{ nm}) \qquad \text{(R1.3)}$$

$$O + O_2 \rightarrow O_3 \qquad \text{(R1.4)}$$

Destruction

$$O + O_3 \rightarrow 2O_2 \qquad \text{(R1.5)}$$

$$O + O \rightarrow O_2 \qquad \text{(R1.6)}$$

This cycle takes place in the ozone layer (Fig. 1.1.a) in a stable equilibrium, while protecting the lower layers of the atmosphere from UV radiation, which is harmful to most living species (Fig. 1.1.b). The overall level of ozone in the stratosphere is determined by a balance between production through solar radiation and destruction through oxidation (Chapman, 1930).

1.1.1.2 The ozone hole

This ozone-oxygen cycle, named the Chapman-cycle, was later scrutinzed because O_3 observations did not match theoretical equilibrium values, with O_3 levels overestimated by a factor of two. Crutzen (1970) identified nitrogen oxides as catalysts of ozone destruction matching theory and observation. This led to Crutzen and Johnston investigating how anthropogenic nitrogen oxides, such as nitrous oxides from the ground, and nitrogen oxides released from supersonic aircraft, (Johnston, 1971), affected O_3 levels. These investigations resulted in the discovery and intensive study of stratospheric O_3 depletion, popularly known as the "ozone hole".

In 1974, Molina and Rowland formulated the theory of the O_3 depletion under the impact of Chlorofluorocarbons' (CFCs), anthropogenic chemical compounds that were first industrialized in the 1930s and were widely used in refrigeration, air conditioning and aerosol spray cans (Molina and Rowland, 1974). In 1985, Joseph Farman and collaborators measurements at the British station at Halley Bay, in Antarctica, revealed the extent of the problem: more than half of the stratospheric ozone over Antarctica disappeared during the southern spring season (Farman et al., 1985). Following the work of a 1986 scientific expedition to Antarctica, Susan Solomon and then James Anderson demonstrated that chlorine levels were significantly higher than normally observed in the regions most affected by the disappearance of ozone (Anderson et al., 1991; Solomon, 1999), confirming Rowland-Molina hypothesis that halogens destroy ozone. This suggested that CFCs were not broken down by solar radiation present in the troposphere but instead accumulated here and were eventually transported into the stratosphere, where they begin to be photolysed leading to the release of Cl atoms, e.g., $CFCl_3 + h\nu \rightarrow CFCl_2 + Cl$. This causes an increase in chlorine reservoir compounds such as HCl and $ClONO_2$, two very stable compounds, whose chemistry, in the absence

of light, with ice crystals present in high altitude clouds (polar stratospheric clouds or PSC) produces chlorine (Cl_2), readily photolysed when the sun returns in spring, producing active chlorine, the main cause in ozone depletion.

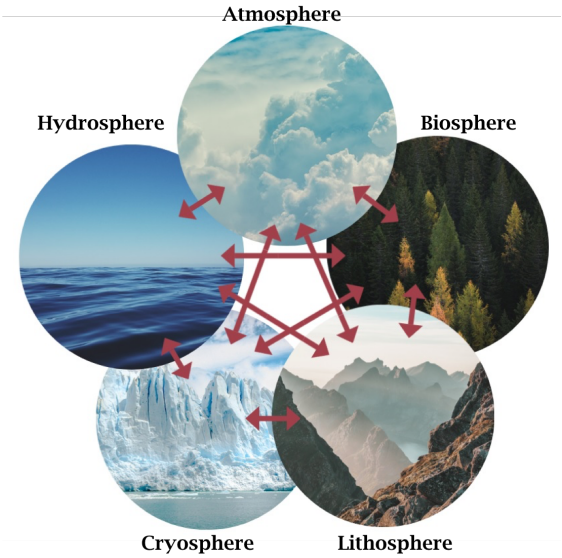

Figure 1.3 – Earth's climate arises from the interaction of five major climate system components: the atmosphere, the hydrosphere, the cryosphere, the lithosphere and the biosphere, (© BY-SA 4.0).

However, CFCs are not the only species responsible for the O_3 hole observed over Antarctica in spring. Four families of chemicals are actually responsible for catalyzing O_3 depletion: nitrogen oxides ($NO_x \equiv NO + NO_2$), hydrogen oxides ($HO_x \equiv OH + HO_2$), chlorines ($ClO_x \equiv Cl + ClO$), and bromines ($BrO_x \equiv Br + BrO$). The sources of the last two families are entirely anthropogenic, whereas much of NO_x and HO_x sources are natural from tropospheric N_2O, CH_4, H_2, and H_2O. However, their concentrations are increasing in recent decades due to industrial and agricultural activities.

The development of atmospheric chemistry as a scientific domain on its own over the last century was the result of a crucial need in atmospheric observations to decipher the impact of human activities on our climate (Fig. 1.3). Indeed, it is the interaction of five major components of the planet, namely the hydrosphere (water), cryosphere (snow, ice and permafrost), lithosphere (the Earth's upper rocky layer), biosphere (living species), and atmosphere (air), that defines the nature of the Earth's climate.

1.1.2 Oxidative capacity of the atmosphere

The oxidative capacity of the atmosphere, or oxidative power, refers to the ability of the atmosphere to "clean" itself by oxidizing the chemical species that enter it. The oxidative degradation of most organic compounds is an oxidation process initiated by the hydroxyl radical OH attack. Thus, the

ability of the atmosphere to remove a particular level of pollutants is usually associated with the abundance of OH radicals, even though many other oxidants are present in the atmosphere. These oxidants of lesser importance include O and O_3 along with free radicals (other than OH) such as nitrate radicals (NO_3), nitrogen oxides, peroxy radicals and reactive halogen species (halogen oxides radicals and halogen atoms). Therefore, estimating the oxidative capacity of the atmosphere remains quite difficult as an oxidizing agent may have different effects on the overall OH concentration. Additionally, the discovery of new mechanisms involving these or other species is still possible and expected.

1.1.2.1 Tropospheric ozone

There are two types of atmospheric O_3: a "good" O_3 located in the stratosphere, that protects the Earth's surface from harmful radiation (Section 1.1.1.1) and harmful or "bad" O_3, located in the troposphere. Tropospheric or ground level O_3 is created by chemical reactions between NO_x and volatile organic compounds (VOCs) in the presence of sunlight. This O_3 is created in the troposphere, i.e., in the air we breathe, at concentrations from 10 part per billions (ppb or 10^{-9} mol mol^{-1}) over tropical oceans to more than 100 ppb in the upper layers of the troposphere (Cooper et al., 2002). When inhaled, O_3 can trigger a variety of health problems, such as chest pain, coughing, throat irritation, and airway inflammation, and it also harms lung tissue and worsens bronchitis, emphysema, and asthma (European Environment Agency). Along with human health effects, O_3 also affects sensitive vegetation and ecosystems, including forests, parks, and wilderness areas, particularly during the growing season. Most of the radicals participating in the oxidizing capacity of the atmosphere are initially produced via processes involving O_3. For example, the production of OH radicals is linked to the photolysis of O_3 under the effect of ultraviolet radiation:

$$O_3 + h\nu \rightarrow O_2 + O(^1D) \tag{R1.7}$$

where $O(^1D)$ corresponds to an excited state of the oxygen atom. The product of reaction R1.7 allows the production of OH radical via R1.8 (Sheppard and Walker, 1983):

$$O(^1D) + H_2O \rightarrow 2OH \tag{R1.8}$$

OH radicals are considered to be the atmospheric detergents because of their role in the degradation of volatile organic compounds (VOCs) injected into the atmosphere (Crutzen, 1996). Indeed, OH radicals have a high reactivity towards any volatile organic compound, which can be represented by RH, where R represents a carbon chain (e.g., CH_3 or C_2H_5):

$$RH + OH \rightarrow R + H_2O \tag{R1.9}$$

$$R + O_2 \rightarrow RO_2 \tag{R1.10}$$

RO_2 here represents a peroxyl radical and includes the special case of the hydro-peroxyl radical (HO_2).

1.1.2.2 Nitrogen chemistry

Nitrogen oxides play an important role in tropospheric processes and have a direct impact on air quality and climate change. In most case, in the presence of volatile organic compounds (VOCs) and under solar radiation, nitrogen oxides stimulate ozone formation in the troposphere. NO_x also plays an important role in rain acidification and ecosystem eutrophication by its transformation in nitric acid (Jaworski et al., 1997; Vitousek et al., 1997).

Finally, NO_x contributes to the production of particulate matter in ambient air and to aerosol formation leading to cloud development (Atkinson, 1998). The NO_2 mixing ratio in the troposphere ranges from a few tens of part per trillions (ppt or 10^{-12} mol mol^{-1}) in remote areas to hundreds of ppb in urban atmospheres (Finlayson-Pitts and Pitts, 2000b).

The tropospheric chemistry of O_3 follows a photochemical cycle initially described by Leighton (1961) and refined by Crutzen (1970) and other works, involving mainly ozone, nitrogen oxides and peroxyls radicals:

$$NO_2 + h\nu \rightarrow NO + O(^3P) \quad \text{(R1.11)}$$

$$O(^3P) + O_2 + M \rightarrow O_3 \quad \text{(R1.12)}$$

$$NO + O_3 \rightarrow NO_2 + O_2 \quad \text{(R1.13)}$$

$$NO + RO_2 \rightarrow NO_2 + RO \quad \text{(R1.14)}$$

where M represents constituent molecules of air (essentially N_2 or O_2) acting as stabilizer for the O_3 produced by reaction R1.12. Regardless of the presence of peroxy radicals, the ozone content at the photostationary steady-state is given by Equation 1.1:

$$[O_3] = \frac{J_{NO_2}}{k_{NO+O_3}} \frac{[NO_2]}{[NO]} \quad (1.1)$$

where J_{NO_2} is the NO_2 photolysis rate constant of R1.11 expressed in s^{-1} and k_{NO+O_3} the kinetic rate constant of R1.13 expressed in cm^3 $molecules^{-1}$ s^{-1}. This equilibrium implies that tropospheric ozone is produced only by the photolysis of NO_2, (R1.11), providing the oxygen atoms used for ozone formation (R1.12). However, in R1.13, NO tends to destroy ozone. But, in the presence of RO_2 radicals, NO molecules will also be mobilized by reaction R1.14, producing NO_2, whose photolysis can in turn produce O_3. This series of four reactions outlines the principle of O_3 air pollution: it can only develop in the presence of nitrogen oxides and volatile organic compounds, whose oxidation produces peroxyl radicals (Haagen-Smit, 1952). Because NO_x has a rather short chemical atmospheric lifetime, usually not exceeding a few days, (Browne et al., 2014; Kenagy et al., 2018; Valin et al., 2013), this chemistry is usually found in polluted areas. On the contrary, ground-level ozone generally has a longer atmospheric lifetime of the order of a month. Therefore, in the marine and polar boundary layer, ozone is mainly derived from long-range transport from areas of intense photochemical activity combining important sources of NO_x and VOCs. The polar troposphere is also sometimes affected by the transport of ozone-rich air masses from the lower stratosphere.

1.1.2.3 NO_x sources and sinks

With the important role of NO_x in ozone chemistry established, it is important to consider the production sources of NO_x and their eventual environmental sinks. It is clear today that NO_x has significant natural and anthropogenic sources. The main natural sources of NO_x are soils emissions (Skiba and Fowler, 1993), lightning (Penner et al., 1991), and transport from the stratosphere (Garcia, 1992). These sources produce NO_x through three predominant processes: atmospheric nitrogen fixation, organic nitrogen oxidation, and nitrification/denitrification (Schumann and Huntrieser, 2007; Van der A et al., 2008).

The fixation of atmospheric molecular nitrogen in the production of nitrogen monoxide NO exists at temperatures > 1500 K, (Young, 2002), and is usually associated with anthropogenic combustion

processes (e.g., automobile engines, industrial processes for energy production, etc.). NO_x produced following this pathway is usually called thermal NO_x. In nature, molecular nitrogen fixation also occurs during lightning strikes (Schumann and Huntrieser, 2007).

NO_x can also be produced by oxidation of the nitrogen present in the fuel itself. High nitrogen content in the fuel and low combustion temperature make this process very significant. In nature, these emissions, known as fuel NO_x, are mainly related to biomass fires, where the combustion temperature is lower than the threshold for the formation of thermal NO_x (Dennison et al., 2006). Anthropogenic fuel NO_x emissions are primarily associated with coal combustion (Arenillas et al., 2005).

Finally, soils are another important natural contributor to the atmospheric NO_x balance, as NO is a reactive intermediate in ammonium nitrification and nitrate denitrification reactions, which can be emitted to the atmosphere (Davidson and Kingerlee, 1997; Delon et al., 2008).

During daylight, NO_x is oxidized by RO_x producing peroxy nitrates (RO_2NO_2), alkyl nitrates ($RONO_2$) and nitric acid (HNO_3) through the following reactions, known as the primary daytime NO_x sinks:

$$NO_2 + RO_2 + M \rightarrow RO_2NO_2 \quad \text{(R1.15)}$$

$$NO + RO_2 + M \rightarrow RONO_2 \quad \text{(R1.16)}$$

$$NO_2 + OH + M \rightarrow HNO_3 \quad \text{(R1.17)}$$

These sinks can be temporary, leading to the possibility of a NO_x re-emission to the atmosphere, or permanent, whose products are eventually washed out of the atmosphere by deposition.

During nighttime, another chemical process involving dinitrogen pentoxide (N_2O_5) and nitrate takes place. NO_2 plus O_3 form NO_3 (R1.18) which can be an important NO_x intermediate at night when there is neither sunlight nor high concentrations of NO present to remove it. At night, NO_3 can react with another NO_2 molecule to form N_2O_5 (R1.19). Upon collision with aerosol, N_2O_5 can hydrolyze to form nitric acid (R1.20) or, in the presence of aerosol-phase chloride, will react to form nitryl chloride and nitric acid (R1.21). Alternatively, NO_3 reacts with alkenes at night to generate alkyl nitrates (R1.22) and with VOCs to form nitric acid (R1.23). NO_3 also reacts with RO_2 and HO_2 radicals (R1.24) and (R1.25) to recycle NO_x (Kenagy et al., 2018; Stone et al., 2014).

$$NO_2 + O_3 + M \rightarrow NO_3 + O_2 \quad \text{(R1.18)}$$

$$NO_3 + NO_2 + M \leftrightarrow N_2O_5 \quad \text{(R1.19)}$$

$$N_2O_5 + H_2O \rightarrow 2HNO_3 \quad \text{(R1.20)}$$

$$N_2O_5 + HCl + M \rightarrow HNO_3 + ClNO_2 \quad \text{(R1.21)}$$

$$NO_3 + \text{alkene} + M \rightarrow RONO_2 \quad \text{(R1.22)}$$

$$NO_3 + VOC \rightarrow HNO_3 + \text{products} \quad \text{(R1.23)}$$

$$NO_3 + RO_2 \rightarrow NO_2 + RO + O_2 \quad \text{(R1.24)}$$

$$NO_3 + HO_2 \rightarrow NO_2 + OH + O_2 \quad \text{(R1.25)}$$

The ground-level ozone balance is crucially dependent on the rate of local NO_x production and transport. As mentioned previously, the average lifetime of NO_x in the lower atmosphere is in the range of a few hours to a few days. However, the long-range transport of NO_x is possible in the form of "reservoir species". These species, grouped under the term NO_y, constitute all species that

can produce NO_x, either by thermal decomposition or by chemical reaction. A non-exhaustive list of species are grouped under this name: $NO_y = NO_x + NO_3 + HNO_3 + N_2O_5 + HNO_4 + HONO + PAN + \ldots$

1.2 Polar atmospheric chemistry

« It is in the polar regions that global warming due to greenhouse gas emissions has the greatest impact. The Arctic and parts of the Antarctic are warming twice as fast as the rest of the world. »
Thomas Jung of the German Alfred Wegener Institute, 2017

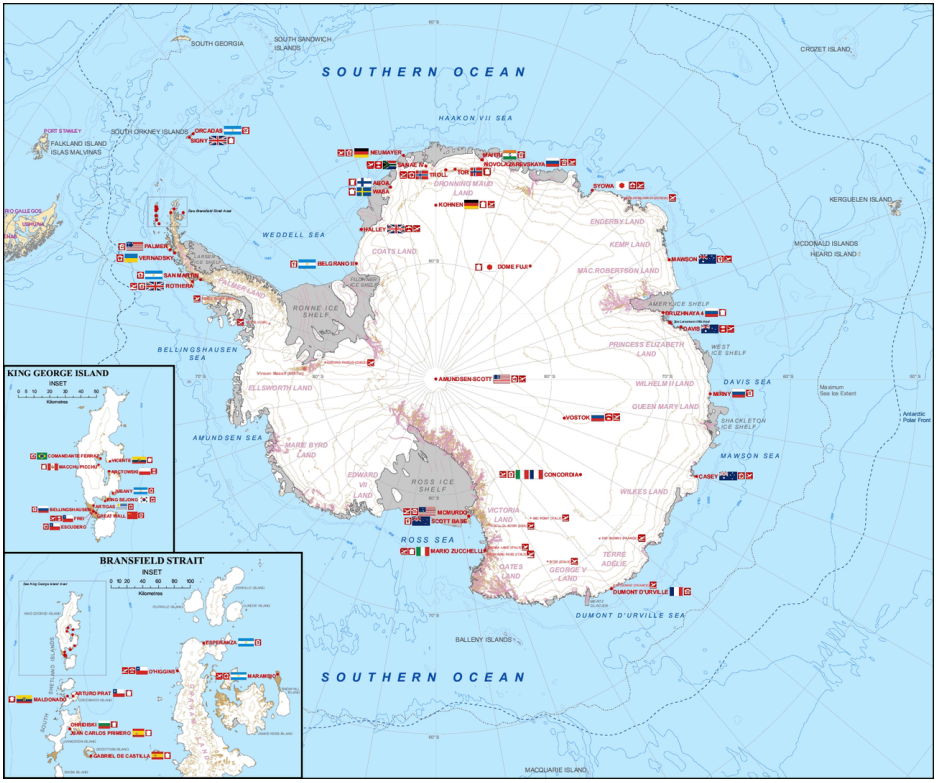

Figure 1.4 – Location of permanent Antarctic Research stations, (COMNAP)

1.2.1 General interest in polar regions

Undoubtedly, since the beginning of the industrial era (1750), mankind has emitted billions tons of CO_2 and other greenhouse gases into the atmosphere. The concentration of carbon dioxide (CO_2) in the atmosphere has expanded from 277 parts per million (ppm or 10^{-6} mol of CO_2 per mol of air) in 1750 (Joos and Spahni, 2008), to 417 ± 0.1 ppm in March 2021 (www.esrl.noaa.gov/gmd/ccgg/trends/).

Over time, the Earth's thermodynamic regulator, i.e., the balance of interactions between the atmosphere, lands, and oceans, has not been able to absorb this excess CO_2, and there has been a gradual rise in the average global temperature since the 1950s. Today, global warming has clearly evident consequences at the poles, placing them at the forefront of regions to be further investigated for the comprehension of the global system.

1.2.2 Specificities of polar regions

High latitude southern regions present specificities that are highly relevant for studying the climate in connection with atmospheric chemistry. These regions are very sensitive to the global changes through the previously mentioned appearance and growth of the Antarctic ozone hole (Thomason and Peter, 2006), the rapid change of the sea-ice conditions (Wolff et al., 2003), the rapid increases in air and sea temperature (Muto et al., 2011), and the changes in precipitation mass balance (DeConto and Pollard, 2016). Due to its proximity to heavily industrialized countries and interconnected atmospheric and oceanic transport pathways, the Arctic has suffered much more rapidly from the effects of anthropogenic activities, perhaps most notably in the decline of Arctic sea ice extent and concentration. On Greenland, snowfall is no longer sufficient to compensate for seasonal ice loss (King et al., 2020), based on the observations of more than 200 glaciers monitored by satellite since the 1980s. There is no longer serious doubt that major climate change is affecting all ecosystems and human activities in all seasons. This climate change is also, to a certain extent, affecting the antipode of the Arctic: Antarctica. Contrary to regions of the rest of the world, Antarctica is still considered as a relatively pristine environment not yet overly influenced by predominant anthropogenic emissions and thus represents the last continental-size laboratory for studying natural emissions and processes.

To understand the impact of the global change on the fragile equilibrium of these regions, a good knowledge of their specific characters is needed. The desire to unravel climate connections has motivated unprecedented technical and scientific endeavors for ice core retrieval and past-climate reconstruction from Antarctica's archives. The continent's ice sheet constitutes a true scientific treasure for studying the Earth's past climate as the deep ice on the high Antarctic Plateau has conserved ancient air further back in time than any other place on Earth (EPICA community members, 2004; Jouzel et al., 2007; Petit et al., 1999). The understanding of the air-snow exchange is key for the ice-core community to accurately reconstruct past environmental changes (Wolff, 1995). Thus, there exists great motivation to further understand polar processes and this interest has revealed that high reactive species, such as NO_x, OH, HO_2, RO_2, and XO, are playing a key role in such a remote environment, controlling the oxidative capacity and the atmospheric chemistry at this location. Therefore the study of the present atmosphere will help the understanding of the atmospheric signals recorded in the ice.

1.2.3 Polar atmospheric chemistry and snowpack reactivity

For many years, scientists considered the snowpack as chemically and biologically inert. Over the last twenty to thirty years, however, numerous studies carried out in the polar regions have shown that far from being a passive material, the snowpack hosts substantial chemical reactions, especially due to its nitrate content. Nitrate is the end product of the oxidation chain of nitrogen oxides, responsible for tropospheric ozone formation (Section 1.1.2.1). Under the effect of solar radiation, the nitrate trapped in the snow can be photolyzed to nitrogen oxides which, after released from the

snowpack, react to produce ozone at the surface. This ozone production is typically seen as a symptom of intense human activity, and its presence in "pristine" polar regions came as a shock.

Honrath et al. (1999) discovered that photochemical reactions were taking place in the Greenland snowpack. Here, NO_x and NO_y were measured in the interstitial air of surface snow as well as in ambient air. NO_x levels in firn air were found to be three to ten times greater than in ambient air. Additionally, those levels varied following a diurnal cycle, suggesting a photochemical generation within the snowpack.

In 2000, the hypothesis that nitrate was photolyzed in the snow to produce NO_x was confirmed by snow photochemistry chamber experiments (Honrath et al., 2000). Vertical fluxes of NO_x, HONO and HNO_3 measured above the snowpack at Summit in Greenland confirmed the emission of NO_x and HONO from the snowpack (Honrath et al., 2002). NO_x emissions were found to be more important than the nitrate deposition in the snow, suggesting a strong transport of NO_x in the atmosphere, with significant implications for the interpretation of nitrate variability recorded in the ice-cores. However, the amount of NO_x emissions from Greenland are not large enough to play a significant role in the global NO_x budget.

The role of nitrite in the photochemical formation of radicals in the snow has also been established by Jacobi et al. (2014) from measurements done in Barrow, Alaska. The results demonstrated that pollution events were at the origin of an increase in nitrite concentrations in the surface snow layer during night time. They also showed that, in addition to its photolysis, nitrite could be a significant source of reactive hydroxyl radicals and nitrogen oxides in the snow.

The true nature and origin of this Arctic nitrate-nitrite-NO_x flux was still poorly understood, and one could argue that the reactivity of the Arctic snowpack shown by Honrath et al. (1999, 2000) and confirmed by Jacobi et al. (2014), among others, could be linked to its geographical position, very close to the heavily industrialized regions of North America, Europe, and Asia. However, findings from the remote regions of Antarctica would lead to a re-evaluation of nitrogen dynamics in polar snowpack.

Originally, the study of the air-snow exchange in Antarctica was aimed at a better understanding of the sulfur record in Antarctic ice-cores with respect to past global climate change. Indeed, studies of Antarctic ice cores had revealed a strong inverse relationship between past atmospheric temperatures and concentrations of methane sulfonic acid (MSA) and non-sea-salt aerosol (NSS) in the ice (Legrand et al., 1992; Saigne and Legrand, 1987). This discovery lead to field campaigns, such as SCATE (Sulfur Chemistry in the Antarctic Troposphere Experiment) at Palmer station in 1998, and ISCAT (Investigation of Sulfur Chemistry of the Antarctic Troposphere) at South Pole station in 2000 (Berresheim and Eisele, 1998; Davis et al., 2004). Those studies revealed that at South Pole, the gas phase sulfur was a minor chemical player as its oxidation is controlled by intense HO_x/NO_x photochemistry prior reaching the pole. NO_y emissions were also observed at Neumayer station in Antarctica during the austral summer of 1997, with NO_y concentrations following a diurnal cycle (Weller et al., 1999). The diurnal variation of HNO_3 seemed to be controlled by the changing surface temperature and they hypothesized that a co-condensation mechanism of HNO_3 with water vapor and evaporation was triggering this variability. However, they also suggested that the emissions of photochemically produced NO_x within the snowpack should be an additional factor for explanations, as the diurnal variation of NO was consistent with a source other than the NO_2 photolysis. Jones et al. (2000) investigated the production of NO and NO_2 from snow at Neumayer's atmospheric observatory and concluded that the nitrate contained in the snowpack was the source reservoir of NO_x emissions in the Antarctic lower troposphere. Nevertheless, as for Arctic emis-

sions, NO_x emissions from Antarctica remain negligible with respect to the global budget (Jones et al., 2001).

Additionally, the photolysis of nitrate ions (NO_3^-), produces nitrogen oxides, nitrous acid and other reactive gaseous compounds, all of which then diffuse into the polar atmosphere, as numerous field campaigns at different locations of Antarctica highlighted. The following list of campaigns and publications is not-exhaustive but gives an idea of the intensive studies of the Antarctic atmospheric chemistry for evaluating the air-snow transfer-function for the chemical proxy species in ice-cores.

- **ANTCI** (The ANtarctic Tropospheric Chemistry Investigation) deployed two field studies between 2003 and 2005 with large ground-based winter-over sampling components at South Pole station, in the Antarctic Plateau, and aircraft chemistry and photochemistry measurements (Davis et al., 2008; Eisele et al., 2008; Helmig et al., 2008; Wang et al., 2007).
- **CHABLIS** (CHemistry of the Antarctic Boundary Layer and the Interface with Snow) measurement campaign was conducted at Halley station, in coastal Antarctica, from January 2004 through February 2005 (Anderson and Bauguitte, 2007; Bauguitte et al., 2012; Bloss et al., 2007, 2010; Jones et al., 2008, 2011; Mills et al., 2007; Read et al., 2008; Saiz-Lopez et al., 2008; Salmon et al., 2008; Wolff et al., 2008).
- **SUNITEDC** (SUlfate and NItraTe surface snow Evolution at Dome C) aimed to document and use isotopic anomalies of oxyanions (sulfate and nitrate) to constrain the sources, transformations, and transports of these compounds to the polar regions where they are archived over thousands of years (Bock et al., 2016; Erbland et al., 2013; Meusinger et al., 2014; Savarino et al., 2007; Vicars and Savarino, 2014; Frey et al., 2009).
- **OPALE** (Oxidative Production over Antarctic Land and its Export) campaign took place at both coastal Antarctica (Terre Adélie, Dumont D'Urville station) and the plateau (Dome C, Concordia station), with the aim to quantify, understand, and model the level of oxidants present in the lower atmosphere of East Antarctica (Berhanu et al., 2015; Erbland et al., 2015; Frey et al., 2013, 2015; Gallée et al., 2015a,b; Kukui et al., 2014; Legrand et al., 2014, 2016; Preunkert et al., 2015, 2012; Savarino et al., 2016).

The reactivity of the snowpack considerably modifies the chemistry on which it is based to the point, for example, that during the summer, the content of oxidizing molecules (especially the OH radical) in Antarctica is of the same order as at the equator (Bloss et al., 2005; Grilli et al., 2013; Jefferson et al., 1998; Kukui et al., 2014; Mauldin et al., 2001; Preunkert et al., 2012).

1.2.4 Implications

1.2.4.1 Polar chemical context

Despite the previous intensive studies to understand the oxidative capacity observed in Antarctica, several unknown remain. Notably, Frey et al. (2015) concluded that the large NO_2:NO ratios observed at Dome C during the OPALE project are the result either of: i) an unknown measurement bias as they acknowledged instrumental interferences of HO_2NO_2 and HONO with the NO_2 measurements or ii) a yet unidentified mechanism in the boundary layer oxidation chemistry. Additionally, difficulties to represent the snowpack photochemistry in models led to large discrepancies between models output and observations.

For example, previous works have proposed different mechanisms to explain the nitrate photolysis behavior in ice and snow (e.g., Blaszczak-Boxe and Saiz-Lopez (2018) and reference therein). Chu and Anastasio (2003) studied the nitrate photolysis on ice and their results suggested that the ice nitrate photolysis is occurring in a "quasi-liquid layer" rather than in the bulk ice. Davis et al. (2008) developed a theory driven by two photo-chemical domains affecting the nitrate photo-dissociation, namely the photo-labile and buried domains. The nitrate contained in the photo-labile domain is consumed first, being more available than the buried nitrate, hindered by a cage effect. Bock et al. (2016) developed a nitrate air-snow exchange model and tested it against the observations at Dome C, which demonstrated that co-condensation, the simultaneous condensation of water vapour and trace gases at the air–ice interface, was the most important process to explain nitrate incorporation in snow and to reproduce summer observations.

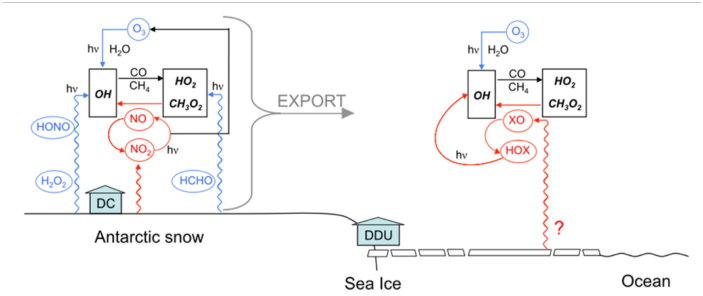

Figure 1.5 – A schematic of the different chemistry that may occur in Antarctica. In blue are primary sources leading to the production of OH radical, while in red are possible recycling reactions. In the plateau, over the Antarctic snow, the main possible sources are related to the chemistry of NO_x, while at the coast OH may be recycled either by the presence of XO or by the export of NO_x from the inland, (OPALE Campaign)

However, the model does not reproduce the summer observations at the coast, where the temperature, relative humidity and concentration of atmospheric aerosol are much larger than on the plateau, and where snow surface melt is possible. Chan et al. (2018) developed a new model and were able for the first time to reproduce the observations on the Antarctic Plateau and at the coast, concluding that, during summer, the major interface between snow grain and surrounding air is still air-ice, but it is the equilibrium solvation into liquid micro pockets, based on Henry's solubility law, that dominates the exchange of nitrate between air and snow. To date, no consensus can be found in literature about the different forms of nitrate that would allow us to reduce the ranges of the modeled snowpack NO_x fluxes (F_{NO_x}).

Presently, the unsolved characterization of nitrogen oxide species on the Antarctic Plateau limits our capacity to model the oxidative capacity and its consequences on short- and long-term records of paleo-climate tracers. Furthermore, as re-noxification of the atmosphere is a global phenomenon not limited to polar regions, understanding the specificity of the NO_x chemistry in the polar regions may well have implications far beyond snow-covered regions (Baergen and Donaldson, 2013; McCalley and Sparks, 2009; Michoud et al., 2015; Su et al., 2011; Ye et al., 2016; Zhou et al., 2011). Therefore, more studies with reduced uncertainties in NO_2 measurements are needed to understand the behaviour of reactive nitrogen in the polar boundary layer.

This context inspired the CAPOXI (CAPacité OXIdante) 35-75 °S Project in which the research de-

scribed in this thesis is embedded. The project aims to document the oxidizing capacity of the Southern Hemisphere along a North-South gradient, extending from the island of Amsterdam (37 °S) to Concordia station (75 °S) via the coastal station Dumont D'Urville (67 °S). The possibility to study the oxidizing capacity of the atmosphere in very contrasting environments allows an easier highlighting of the interactions between the reactive species in the atmosphere. The project focuses on the chemistry of reactive nitrogen and halogenated species in relation to the chemical balance of ozone.

1.2.4.2 Overall questions

As we have established, highly reactive species, such as NO_x, OH, HO_2, RO_2, and halogen oxide radicals, XO (X ≡ I, Br, Cl), play a key role in such a remote environment, controlling the oxidative capacity and the atmospheric chemistry at this location. Reliable in-situ measurements of these reactive species represent a main challenge for atmospheric chemists. In polar regions, halogen oxide radicals may be responsible for the depletion of ozone and alteration of HO_x and NO_x ratios, consequently changing the oxidizing capacity of the atmosphere (Saiz-Lopez et al., 2007b). In Antarctica, the high levels of OH observed may be explained through recycling reactions either in presence of NO_x or XO (Fig. 1.5).

Halogen oxide radicals in Antarctica have mainly been measured by remote technique such as satellite measurements (Schönhardt et al., 2012; Theys et al., 2011), Zenith-sky DOAS (Carroll et al., 1989; Frieß et al., 2001, 2004; Kreher et al., 1997) and MAX-DOAS (Frieß et al., 2010). Only few local measurements are available, such as an aircraft deployment of a resonance fluorescence instrument for BrO measurements, at Palmer station (Brune et al., 1989), measurements by LP-DOAS at Halley station in West Antarctica (Saiz-Lopez et al., 2007a) and by the Mocamar optical instrument at Dumont D'Urville Station on the East Antarctic coast (Grilli et al., 2013).

Satellite measurements, integrated over the entire vertical column (Fig. 1.6), have revealed that IO and BrO share similar spatial and temporal characteristics, with a circular distribution at coastal regions (mainly on sea ice and ice shelves) and most emissions are occuring during springtime (particularly for BrO). However, differences are also visible, such as: i) IO distribution is largely spread over the continent; ii) IO is observed over the sea ice at slightly later time than BrO and for a shorter time; iii) BrO gradually decreases during summer and does not appear again over the year, while IO stays more constant and its concentration increases again in Autumn.

Those differences suggest the possibility of distinct emission sources of the two radicals. The circular shape of the distribution of IO over the sea ice only appears during the summer (Oct/Nov), when the sea ice cover starts to decrease and becomes more porous and permeable (Fig. 1.6). This can support the hypothesis that iodine precursors (I_2 and volatile iodocarbons) may be emitted from the marine biosphere, and notably from algae living underneath the sea ice. Carpenter et al. (2007) measured iodine species in the water and gas phase above the water during spring and summer. They found substantial amounts of halocarbons, correlated with areas of high sea ice melting and therefore supporting the possibility that halogens may be emitted by ice algae. Therefore, the melting and breaking of sea ice, its increase in temperature, porosity and permeability may play an important role.

If the sources of the halogen oxide radicals are still unknown, also their role in particle formation requires deeper investigation. IO may nucleate via the self-reaction to form atmospheric particles and eventually growing into cloud condensation nuclei (Burkholder et al., 2004). Frey et al. (2020)

observed for the first time sea salt aerosol production from blowing snow above sea ice. Additionally, these observations suggest that atmospheric reactive bromine is produced by blowing snow. To better constrain the role of halogen oxide radicals at polar regions, and particularly at the coast and over the sea ice, it is therefore crucial to produce more local measurements which would allow, together with backward trajectories, the identification of their sources.

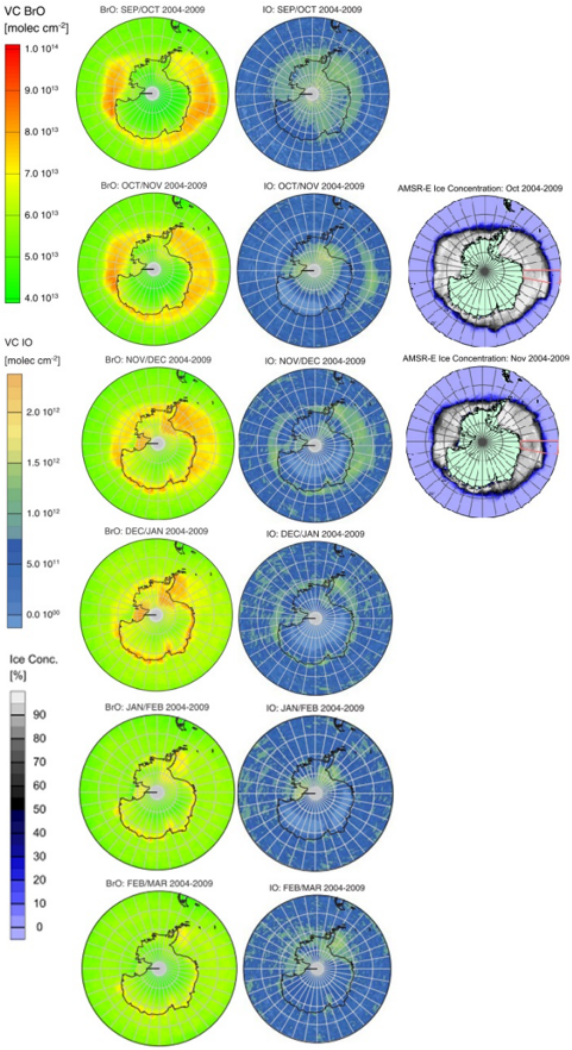

Figure 1.6 – Satellite measurements of vertical columns, VC in molecules cm^{-2}, of IO and BrO showing some similarities as well as differences in the spatial distribution and temporal evolution, and highlighting the possibility of different radical sources, (Schönhardt et al., 2012).

Today, important scientific questions are still open to discussion, and further investigations need to be carried out:

- **What is the role of halogen chemistry?**

Though a comparison between the different devices that are able to measure BrO is certainly welcome, all previous studies tend to show that the presence of sea-ice strengthens the bromine chemistry. For iodine chemistry, large levels differences are observed from sites to sites. However, this question could not be answered in the framework of this thesis and a follow up PhD project proposes to use the LP-DOAS technique for atmospheric BrO and IO observations.

- **What is the chemical reactivity of the snowpack and how does it connect to the overlying oxidative atmosphere? How does it influence the snow chemical composition?**

As mentioned, at the base of the high oxidative capacity of the Antarctic atmosphere, there is the snow emission of oxidized nitrogen gases (NO, NO_2, HONO) from photodenitrification of nitrate in the snow. It is thus fundamental to understand the physical conditions that drive the NO_x emissions (wind, solar radiation, temperature, etc.).

- **Does the high NO_2:NO ratio measured at Dome C represent a lack of our understanding of the NO_x chemistry?**

This question is likely the most puzzling and fundamental question to answer. This ratio is a metric in photochemistry as it influences the ozone and OH production, and answering this question first require an evaluation of any artifacts that can be introduced by species like HONO, PAN, or other nitrogen input. This analytical need leads to another important question:

- **Can NO_2 be measured without or at least with controlled interferences?**

If the high ratio NO_2:NO is confirmed, and the hypothesis of the presence of instrumental bias is excluded, the next question will be to find the chemistry that can justify a high conversion rate of NO to NO_2.

1.3 NO_x detection techniques

« Measurements have always been a critical driver in tropospheric chemistry. »
Monks et al. (2021)

The NO_x measurement in natural or anthropized environments is difficult because NO_x typically exists at very low concentrations and exhibits high spatial and temporal variability in concentration.

Being able to measure such species in situ, at low levels, and at a time scale compatible with its reactivity (i.e., in minutes) is challenging and puts stringent constraints on the instrument sensitivity, time response, energy consumption, and compactness. The various techniques that have so far been developed, and that we will describe in this sub-chapter, are all based on the analysis of electromagnetic radiation emitted, absorbed or scattered by atoms or molecules, called spectroscopy. It provides information on the identity, structure and energy levels due to their interaction with the electromagnetic radiation. Additionally, spectroscopy allows the study of reactions kinetics. The

set of radiations constitutes the electromagnetic spectrum, covering many orders of magnitude in terms of frequency or wavelength as shown in Figure 1.7.

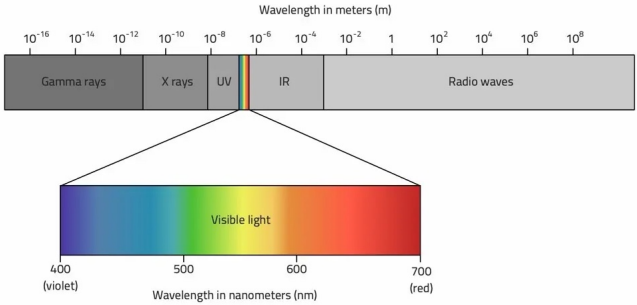

Figure 1.7 – Electromagnetic Spectrum, (https://www.radio2space.com).

The energy, E expressed in J, associated with the electromagnetic radiation is defined as the product of Planck's constant h ($h = 6.62 \times 10^{-34}$ J s) and the frequency ν (s^{-1}). The later is the ratio between the speed of light c ($c = 3 \times 10^8$ m s^{-1}) and the wavelength λ expressed in m. The interactions of electromagnetic radiation with matter can be classified into three main categories:

- **Absorption processes:** radiation from a source is absorbed by the sample
- **Emission processes:** the sample is emitting radiation
- **Scattering processes:** scattering is a physical process by which a particle in the path of an electromagnetic wave continuously abstracts energy from the incident wave and re-radiates that energy in all directions

Absorption and emission processes involve transitions between different energy levels or states. These transitions correspond to absorption bands at wavelengths that characterize the different energy levels of the absorbent species. Each energy of absorption/emission of an atom corresponds to a specific wavelength. The objective of this sub-chapter is to present the advantages and drawbacks of the various techniques that have so far been developed for the NO_x detection.

1.3.1 Emission spectroscopy: ChemiLuminescence for NO_x measurement

Chemiluminescence is a form of spectrofluorometry where fluorescence is defined as the emission of light by molecules without the release of heat. Depending on the source of energy input, a distinction is made between chemiluminescence, where energy is provided by a chemical reaction; bioluminescence, where energy is provided by an enzymatic reaction; and fluorescence, where energy is provided directly by photon absorption. Chemiluminescence (CLD) is therefore observed as a result of a chemical reaction that produces a molecule in an excited energy level (C^*). This molecule then emits radiation, in the form of light emission ($h\nu$), when returning to its fundamental state.

$$A + B \rightarrow C^*$$

$$C^* \rightarrow C + h\nu$$

The efficiency of this phenomenon is called the quantum yield, $\phi(T,pH)$, defined by the ratio of the number of photons emitted to the number of photons absorbed. It ranges between 0, no emission, and 1, where each absorbed photon leads to an emission. The quantum yield depends on the molecule, the medium, the pH, and the temperature: for example, $\phi(T,pH)$ decreases when the temperature increases. It does not depend, however, on the intensity of the light source nor on the excitation wavelength, λ, because only the absorbed photons are taken into account. The chemiluminescence detection technique is based on the principle that nitric oxide (NO) reacts with ozone (O_3) to produce nitrogen dioxide (NO_2), electronically excited nitrogen dioxide (NO_2^*) and oxygen. Following the NO-O_3 reaction, the NO_2 molecules immediately revert to NO_2. This process creates a light emission directly proportional to the NO concentration in the sample. The intensity of the resulting light emission is then measured by a photomultiplier tube and associated electronics. An NO_2 to NO converter is used for NO_x (NO + NO_2) analysis, and the NO_2 concentration is determined by subtracting the signal obtained in NO mode from the signal obtained in NO_x mode. Different types of converters are used for the NO_2 to NO reduction: heated metal converters, mostly molybdenum (Mo), or photolytic converters.

The light source for the photolytic conversion is usually a gas discharge lamp, (Xe-vapour Lamp, metal halide lamp..) or a UV light-emitting diode (LED).

The CLD technique is today the most widely used method for nitrogen oxides measurements with sensitivities better than 100 ppt (or 10^{-12} mol mol^{-1}) (Ryerson et al., 2000). However, despite the impressive efforts to reduce the response time and detection limits of these instruments in the past half-century, the technique suffers from interferences from other chemical species. Indeed, the use of a Mo-converter may be reliable and efficient, but it is not specific and instead of measuring NO_x, the instrument rather measures NO_y.

Villena et al. (2012) demonstrate that the interferences on an urban atmosphere for the CLD technique implied positive interferences when NO_y species photolysis occurred, leading to an overestimation of daytime NO_2 levels, while negative interferences were attributed to the VOCs photolysis followed by peroxy radical reactions with NO. The use of a photolytic converter specific to NO_2 might resolve those uncertainties, however, the converter efficiency remains low and needs to be calibrated at regular intervals (Grosjean and Harrison, 1985; Williams et al., 1998). Still, this technique is widely used for urban air quality measurements where high NO_x concentrations are expected. The uncertainties on the absolute mixing ratio of NO_x, caused by the non-direct measurement of NO_2 is an issue for resolving mechanisms and processes that remain unsolved in remote regions where sub-ppb levels of NO_x are expected, such as polar regions.

The CLD technique was also widely used in the previous field campaigns mentioned in Section 1.2.3. However, due to the lower concentrations of NO_x in polar regions, uncertainties of the measurements were quite significant, pushing the scientific community to tackle the reliability of the data and trying to identify possible artifacts using different detection methods.

1.3.2 Absorption spectroscopy

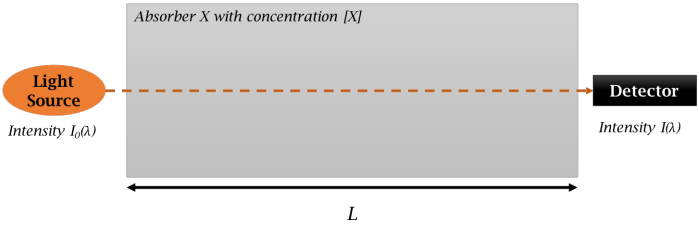

Figure 1.8 – The basic principle of absorption spectroscopy trace gas detection. A beam of light passes through a volume of length L containing the absorber at concentration [X]. At the end of the light path, the intensity is measured by a suitable detector, (Platt and Stutz, 2008).

When the light arrives on a measurement cell of length L, defined as the optical pathway, containing an homogeneous medium, part of this incident light, $I_0(\lambda)$, may be absorbed by the medium, with the rest, $I(\lambda)$, being transmitted. The fraction of the incident light absorbed by a substance X of concentration [X] (mol m^{-3}) contained in a cell of length L (m) is given by Beer-Lambert's empirical law, Equation 1.2:

$$A(\lambda) = \epsilon(\lambda, T)L[X] = ln\left(\frac{I_0(\lambda)}{I(\lambda)}\right) \tag{1.2}$$

were A is the absorbance, $\epsilon(\lambda,T)$ the extinction coefficient, wavelength and temperature dependent, and expressed in m^2 mol^{-1}.

In other words, considering a cylinder of length L (Fig. 1.8) with a number, N, of absorbent molecules, i, if a beam of intensity I_0 passes through the cylinder, the absorbance is equal to the total of each molecules absorption intercepting the initial radiations leading to Equation 1.3. Therefore, effective cross-section, $\sigma_{x_i}(\lambda)$, reflects the probability of interaction between a photon and a molecule of the gas X. And the Beer-Lambert's Law can be written as follows in Equation 1.4:

$$A(\lambda) = L\sum_{i}^{N} \epsilon_i(\lambda, T)[X]_i \tag{1.3}$$

$$I(\lambda) = I_0(\lambda)e^{-L\sum_i^N \sigma_{x_i}(\lambda)[X]_i} \tag{1.4}$$

The weaker is the product between the extinction coefficient and the concentration, the closer the $\frac{I(\lambda)}{I_0(\lambda)}$ ratio will be to 1. Thus, in order to be able to determine very low concentrations, the effective cross-section, $\sigma_{x_i}(\lambda)$, must be maximized by selecting strong transitions between energetic states of the molecule, or a long absorption pathlength should be considered. Long optical pathways are naturally obtained by long-path differential optical absorption spectroscopy (LP-DOAS) (Platt and Perner, 1980; Platt and Stutz, 2008) and multi-axis differential optical absorption spectroscopy (MAX-DOAS) techniques (Hönninger and Platt, 2002).

Additionally, compact, highly sensitive and point-source measurements may be achieved using cavity enhanced techniques such as cavity ring-down spectroscopy (CRDS) (O'Keefe and Deacon, 1988; O'Keefe et al., 2002) and cavity-enhanced absorption spectroscopy (CEAS) (Fiedler et al., 2003). All those techniques are described further in this chapter.

1.3.2.1 Infrared absorption spectroscopy

As mentioned, acting on the effective cross-section, $\sigma_{x_i}(\lambda)$, is possible when using strong transitions. The spectral regions where NO_x shows strong fundamental absorption transitions are 5.26 µm for NO and 6.2 µm for NO_2, in the infrared region. Therefore, working in infrared absorption spectroscopy in order to lower the detection limit to observe NO_x in remote regions could be an interesting solution (Tuzson et al., 2013).

Several groups have worked on developing robust instrumentation that would allow the multi-species detection of NO and NO_2 in the IR spectral region. For example, Jágerská et al. (2015) developed a dual-wavelength setup, based on a quantum cascade laser emitting single-mode at wavenumbers σ ($\sigma = \frac{1}{\lambda}$) 1600 cm^{-1} and 1900 cm^{-1}. These emissions correspond to strong absorption bands of NO_2 and NO, and their spectrometer reaches detection limits of 0.5 and 1.5 ppb for NO_2 and NO, respectively, which is well-suited for monitoring pollution at a suburban site but not for our application in Antarctica. Additionally, the laser source needs to be cooled at a stable temperature of 0 °C to detect targeted NO and NO_2 transmission peaks. More recently, Ventrillard et al. (2017) developed an instrument able to measure NO in the mid-infrared region with a detection limit of 8.3 ppt in 10 seconds measurement. Richard et al. (2018) were able to take advantage of the recent developments on Interband Cascade Laser (ICL) to upgrade Ventrillard et al. (2017) method and reach 0.9 ppt in 12 minutes measurement.

However, with the development of instruments operating in MIR (mid-Infrared), a new effect inducing bias on concentration measurements has been observed: the optical saturation (Demtröder, 2014). This phenomenon reflects a certain transparency of the gas induced by the presence of a significant number of molecules in the excited state. The absorption signal is proportional to the difference in population in the low and high states involved in the transition: if a significant fraction of molecules are excited, a decrease in absorption results. In other words, at those wavelengths the transitions are optically saturated, i.e., the transition is too strong and most of the molecules are at the excited state. Therefore, the light will be less absorbed by the molecules of interest and this phenomenon induces an artifact on the measurement. Indeed, if most of the molecules are in the excited state, the photons will have less molecules to excite and thus the transmitted signal will no longer be proportional to the number of molecules present in the measurement cell. Although calibrations are possible, as developed by Ventrillard (2018), this technique requires more development to free itself from these interferences.

Above all, as mentioned in Section 1.2.4.2, one of the main questions that still remains is also the role of the halogen. Therefore, having a multi-species detection instrument, able to measure simultaneously NO_x and halogens may be an advantage. And for this, the detection in the visible region is favorable.

1.3.2.2 Differential Optical Absorption Spectroscopy

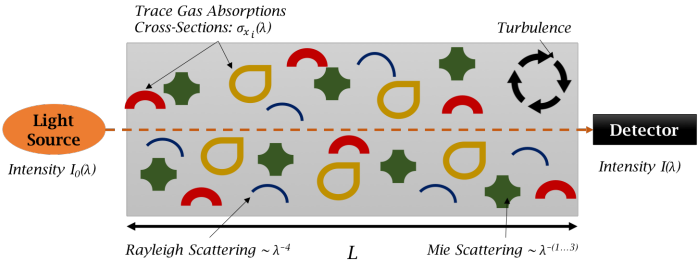

Figure 1.9 – Schematic of an experiment to measure trace gas absorption in the open atmosphere, (Platt and Stutz, 2008).

In their book "Differential Optical Absorption Spectroscopy: Principles and Applications" Platt and Stutz (2008) provide a complete text explaining more than forty years of the DOAS technique's development. The objective of such technique is to subtract from the atmospheric signal the extinction features due to aerosol particles (and instrumental effects) to determine the absorption of target trace gases in the atmosphere and therefore their concentrations (Clemitshaw, 2004; Finlayson-Pitts and Pitts, 2000a; Platt and Perner, 1980).

Figure 1.9 represents a sketch of an experiment to measure trace gas absorption in the open atmosphere. In this case, the atmosphere is the absorber. The intensity of the light traveling through the atmosphere is reduced by the absorption of the trace gas components, and scattering by either molecules and aerosol particles. The analytical instrument itself, through its components, will also decrease the light intensity between the light sent (intensity = I_0) and the one experiencing the long path through the atmospheric medium (intensity = I). Finally, the light beam is widening because of the natural divergency of the beam and its intensity is reduced by the presence of turbulence.

Therefore, it is necessary to consider all the factors influencing the light intensity; i.e., Rayleigh and Mie extinctions, $\epsilon_R(\lambda) + \epsilon_M(\lambda)$; instrumental effects and turbulence, $T(\lambda)$; and absorption of various trace gases, $\sum_i^N(\sigma_{x_i}(\lambda)[X]_i)$ leading to an extended Beer-Lambert's Law described in Equation 1.5:

$$I(\lambda) = I_0(\lambda)e^{-L(\sum_i^N(\sigma_{x_i}(\lambda)[X]_i+\epsilon_R(\lambda)+\epsilon_M(\lambda))T(\lambda))} \tag{1.5}$$

Quantifying all factors influencing the intensity of light to determine the concentration of a particular trace gas is impossible in an open atmosphere. However, it is possible to overcome this challenge in differential optical absorption spectroscopy by using the fact that aerosol extinction processes, the effect of turbulence, and many trace gas absorptions show very broad and smooth spectral characteristics (Platt and Stutz, 2008), while the target trace gases have narrow band absorption structures. The objective of DOAS is thus to separate broad- and narrowband spectral structures in an absorption spectrum and isolate the narrow trace gas absorptions.

As each trace gases possesses a unique absorption structure, the separation of the different absorptions is then possible. To do so, this method requires the measurement of the light intensity at multiple wavelengths in order to determine precisely the concentrations of the different absorbing

trace gases, making the DOAS technique advantageous for different reasons: i) no calibration on the optical properties of the analytical instrument is necessary; ii) the instrumentation can be relatively simple and low-cost; iii) it can be adapted to high reactive species as the measurement does not require sample collection; iv) it offers multispecies simultaneous detection; and v) the ability to use very long light paths in the atmosphere which increases the sensitivity of the technique. Additionally, the DOAS technique can be used in several light path arrangements and observation modes as illustrated in Figure 1.10 taken from Platt and Stutz (2008).

Techniques such as multi-axis and long-path differential optical absorption spectroscopy (MAX-DOAS and LP-DOAS) has been widely used to measure halogens, NO_x, and other interesting species for our study, both in urban environment, (e.g., Dooly et al. (2008); Hönninger et al. (2004); Jin et al. (2016); Lee et al. (2005, 2008b); Sinreich et al. (2007); Thalman and Volkamer (2010); Wagner et al. (2010)), as well as in remote regions, (e.g., Baccarini et al. (2020); Hönninger and Platt (2002); Leser et al. (2003); Ma et al. (2020a); Nasse et al. (2019); Pikelnaya et al. (2007); Pöhler et al. (2010); Prados-Roman et al. (2018); Saiz-Lopez et al. (2007a,b, 2008); Stutz et al. (2000, 2011); Theys et al. (2007, 2011); Wittrock et al. (2004)).

Although MAX-DOAS is relatively simple to deploy, the data analysis makes it a complex approach for in-situ field measurements due to the influence of clouds on the radiative transfer which alters the path length of light (Rozanov and Rozanov, 2010; Wittrock et al., 2004).

While in LP-DOAS the optical path length is known, the signal degradation due to the environment (clouds, rain and wind) remains of importance for the data retrieval, and results are integrated over the long path leading to a limited spatial resolution (Chan et al., 2012; Pöhler et al., 2010). Other disadvantages of the LP-DOAS are the complexity of the installation, which makes it unsuitable for use in all locations. Moreover, the alignment and holding the alignment over several kilometers during the measurement time is a major drawback.

Compact, highly sensitive, and point-source measurements may be achieved using cavity based absorption spectroscopy, such as cavity ring-down spectroscopy (CRDS) and cavity-enhanced absorption spectroscopy (CEAS) (Gagliardi and Loock, 2014). The potential of the cavity based techniques for accurate, sensitive and rapid measurements of NO_x in a compact and transportable instrument has already been demonstrated (Brown et al., 2002; Fuchs et al., 2009). For example, Fuchs et al. (2009) reached a sensitivity of 22 ppt for NO_2 within 1 s of integration time using the CRDS technique and Grilli et al. (2012b) presented an instrument based on mode-locked cavity-enhanced absorption spectroscopy (ML-CEAS) reaching NO_2 detection limit of 5 ppt, among others. Also, incoherent broadband cavity-enhanced absorption spectroscopy (IBBCEAS) (Fiedler et al., 2003) is a simple and robust technique for in situ field observations.

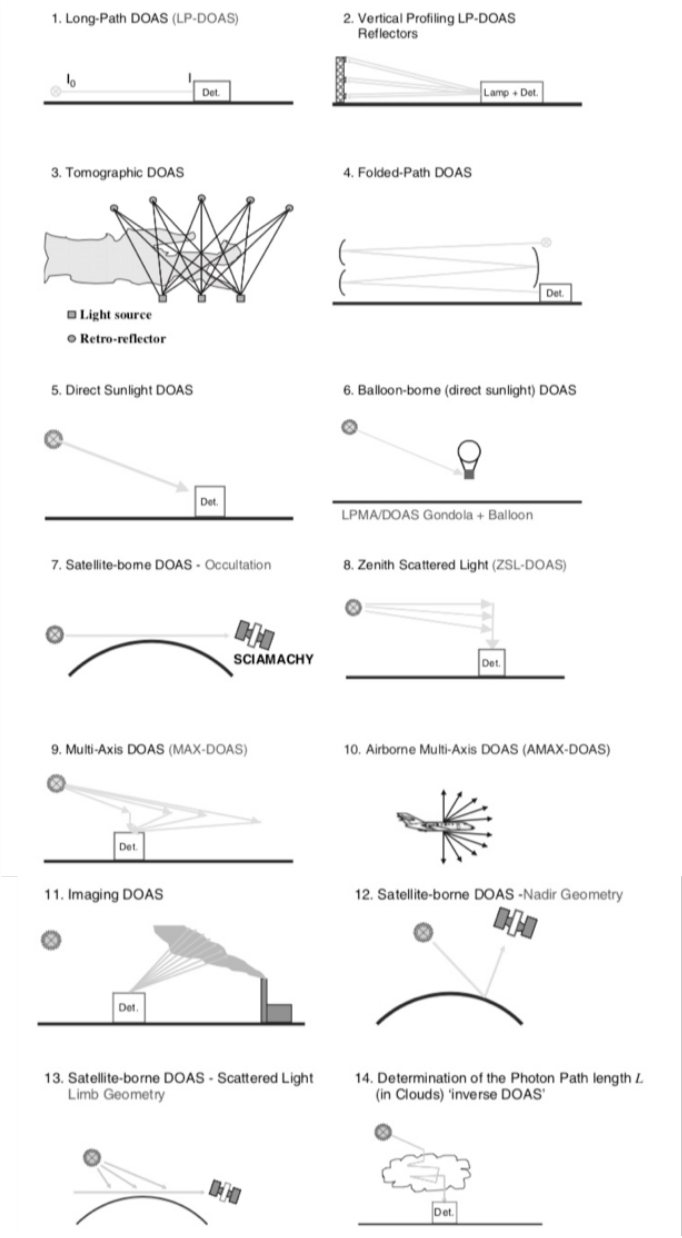

Figure 1.10 – The DOAS principle can be applied in a wide variety of light arrangements and observations modes, using artificial **(1-4)** as well as natural direct **(5-7)** or scattered **(8-14)** light sources. Measurements can be done from the ground, balloons, aircrafts and from space, (Platt and Stutz, 2008).

1.3.2.3 Cavity based absorption spectroscopy

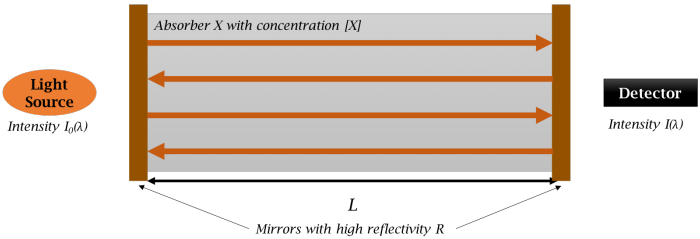

Figure 1.11 – Principle of an optical cavity

In cavity based absorption spectroscopy, the light passes through an optical cavity, i.e., an arrangement of highly reflective mirrors called resonator, and is reflected multiple times by the mirrors to reach long absorption path lengths on the order of several kilometers with a compact cell. Interferences, or encounters of waves, result in different effects: creation of a new wave with greater, lower or same amplitude, but also suppression of a wave by destructive interferences. In other words, the resonator has a characteristic frequency called free spectral range (FSR) given by its length L (FSR $= \frac{c}{2L}$). When this length corresponds to a multiple of half the radiation wavelength, constructive interferences will form in the resonator leading to a stationary wave: the condition for resonance. If destructive interferences dominate, no coupling between the radiation and the cavity is possible. This phenomenon is creating radiation patterns, known as the modes of the resonator that are reproduced every round-trip of the light (Hodgson and Weber, 1997). The fundamental transverse mode of a resonator is a Gaussian beam.

Cavity ring-down spectroscopy (CRDS) and cavity enhanced absorption spectroscopy (CEAS) are types of cavity based absorption spectroscopy where the sample is placed inside a highly reflective optical cavity.

Cavity Ring-Down Spectroscopy

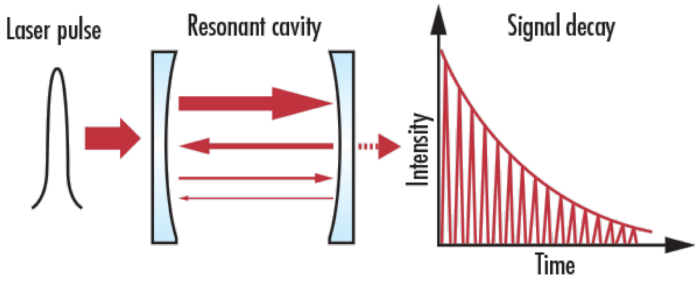

Figure 1.12 – Principle of CRDS

In CRDS, a laser pulse is introduced to a resonant cavity bounded by two (or more) highly reflective mirrors (Fig. 1.12). The reflected laser light oscillates in the resonant cavity and a small amount of

light is lost at each reflection. A detector placed behind one mirror monitors over time the decreasing in intensity of the intra-cavity radiation. This leads to an exponential decay signal called "ring down" with a characteristic exponential decay constant (ring down time).

The rate of decrease depends on the losses of light at the cavity mirrors but also due to absorption and scattering inside the cell. Therefore this technique is suitable for trace gases detection. The measurement of absorbance loss is performed on the refracted laser beams. The incident beam, on the other hand, continues its cyclic path inside the optical cavity leading to the concept of cavity finesse, F. The finesse is the ability of the mirrors to reflect light, defined by Equation 1.6 and represented in Figure 1.13.

$$F = \frac{\pi\sqrt{R}}{(1-R)} \tag{1.6}$$

Thus the greater the reflectivity of the mirrors, R, i.e., close to one, the greater the path of the light beam will be. In CRDS, effective light path lengths on the order of many kilometers can be reached under favorable conditions with resonator lengths below 1 m (Romanini et al., 2014). The sensitivity of a CRDS instrument is directly related to the light path length. The higher the cavity finesse, the longer the optical path length and therefore the better the sensitivity. However, injecting in a very high finesse cavity is challenging, because as shown in Figure 1.13, the width of the cavity modes can be very thin.

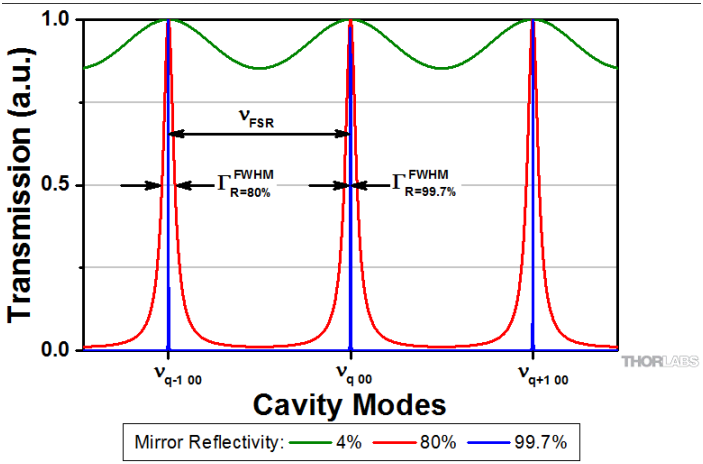

Figure 1.13 – Mode spectrum for mirror reflectances R of 99.7 % (blue), 80 % (red) and 4 % (green). The more reflective the mirrors are, the narrower are the transmission peaks, (© Thorlabs).

The "ring-down", or, in other words, the photons lifetime in the cavity, τ, is dependent on the absorbing medium encountered. The absorption coefficient, α, is determined by Equation 1.7:

$$\alpha = \frac{L}{cd}\left(\frac{1}{\tau} - \frac{1}{\tau_0}\right) \tag{1.7}$$

with c, the speed of light; τ_0 and τ, the photons lifetime without and with the absorbing medium; L, the distance between the mirrors; and d, the optical path length (O'Keefe and Deacon, 1988).

As with all methods used in analytical chemistry, there are also advantages and disadvantages in CRDS. One of the main advantages of using CRDS is that it is insensitive to fluctuations of the laser intensity. With the ring-down measurement, the length of the optical absorption path is precisely known. Therefore, in theory, the uncertainty on the absorption measurement depends only on the uncertainty on the effective cross sections making the instrument calibration-free.

Additionally, CRDS is known for its high sensitivity. This high sensitivity is explained by the fact that in CRDS, the mirrors may have reflectivity up to 99.9999 % and therefore allow a light beam to be easily retained, and as said earlier, the increase in the length of the light path positively influences the sensitivity. It is therefore possible to obtain concentrations on the order of 10^{-12} mol mol^{-1}. Finally, it is a technique that is simple to understand and in practice to use.

The major drawbacks associated with this method are due to the width of the laser pulse spectrum as mentioned above. Additionally, the broadening of the laser beam on the longitudinal and transverse planes causes a loss of selectivity for the molecules to be analyzed (Romanini et al., 2014).

Incoherent Broadband Cavity Enhanced Absorption Spectroscopy

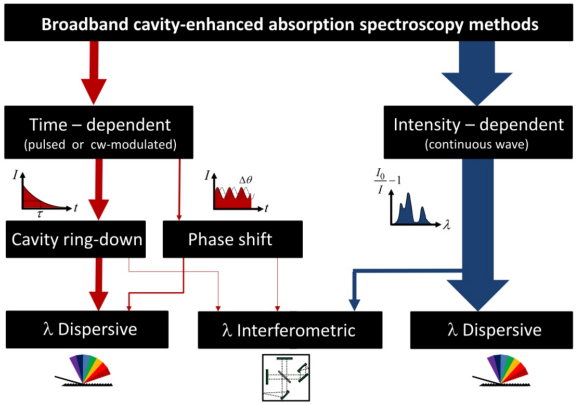

Figure 1.14 – Classification of broadband cavity-enhanced absorption approaches and detection schemes, (Ruth et al., 2014).

Fiedler et al. (2003) demonstrate the potential of incoherent broadband cavity-enhanced absorption spectroscopy (IBBCEAS) as a simple and robust technique for in-situ field applications. The use of incoherent light sources in high finesse optical cavities was not considered for a long time because of their poor coupling efficiency and their generally significantly lower brightness, compared to lasers (Gherman and Romanini, 2002; Ruth et al., 2014). The resolution of the spectrometer is not sufficient to resolve the structure of the large number of transverse modes. However, the use of incoherent light sources allows a broadband spectrum, which, coupled with a dispersive detection after the cavity, allows to obtain the spectrum transmitted through the cavity. Figure 1.14, taken from Ruth et al. (2014), shows the classification of broadband cavity-enhanced absorption approached and detection schemes.

Contrary to CRDS technique, that are calibration-free, in IBBCEAS, the mirror reflectivity needs to

be calibrated as the attenuation of the light intensity, or absorption coefficient, α, is related to the mirror reflectivity following Equation 1.8:

$$\alpha = \frac{1-R}{L}\left(\frac{I}{I_0}-1\right) \tag{1.8}$$

with R, the mirror reflectivity; L the distance between the mirrors; I and I_0 the intensity with and without absorbent.

The technique holds numerous advantages that are widely defined in Ruth et al. (2014) and Zheng et al. (2018) among other IBBCEAS reviews. Here, a summary is given:

- Sensitivity: low photon flux and coupling efficiency of the incoherent light source make it impossible to achieve ultimate sensitivities as good as what can be achieved using narrow band laser. However, low detection limits have been demonstrated recently, e.g., NO_2 detection limits ranging from 15-200 ppt min^{-1} (Barbero et al., 2020; Jordan et al., 2019; Liang et al., 2019; Liu et al., 2019; Min et al., 2016).
- Selectivity and multi-component detection: broadband methods allow a significant spectral range to be covered simultaneously. This multiplex advantage enables several species to be monitored at once, while gathering information over the entire spectral region from $\approx$ 190 nm (UV) to $\approx$ 10 µm (IR).
- Time resolution: a natural restriction of the time resolution for cavity-enhanced methods is the ring-down time. Indeed, the transmission integration time is assumed to be substantially larger than the ring-down time in the method, leading to Equation 1.8.
- Versatility/Adaptability: depending on the light source and the high reflectivity range of the mirrors, broadband CEAS methods offer a high degree of adaptability. Even though developed first for gas phase absorption measurements, the method is also applicable for liquid phase systems, transparent solids, films and surface layers.
- Practical parameters: compact and portable, simple to implement and "user-friendly", robust and stable, inexpensive with low maintenance requirements making the experimental setup cost-effective and suitable for field measurements.

The drawbacks of the method are coming essentially from the light source. For example, short-arc Xe lamp intensity fluctuates and requires high energy consumption (Fiedler et al., 2003) and light emitting diode (LED) are sensitive to temperature and current fluctuations (Wang et al., 2017). However, this technique seems to be well suited for our study, allowing multi species detection. Indeed, in the visible region, around 445 nm, NO_2, IO and CHOCHO can be detected directly and simultaneously, providing key information for understanding the mechanisms taking place in remote areas.

1.4 Overview of the manuscript

As mentioned previously, new direct and in-situ observations of NO_2 at the air-snow interface are needed. The reader will find in Chapter 2 a description of an IBBCEAS instrument for direct detection of NO_2, O_3, IO, and CHOCHO and indirect detection of NO at sub-ppb levels developed and upgraded during the first two years of my research work. Chapter 2 is based on Barbero et al. (2020), a study published in *Atmospheric Measurement Techniques*. It describes an instrument allowing the direct detection of four species by a broadband blue-light-emitting diode centered at

445nm. The wavelength region was selected in order to optimize the NO_2 detection. Unfortunately, at this wavelength, the direct detection of NO was not possible. To overcome this matter, an indirect measurement was also developed, relying on the quantitative oxidation of NO to NO_2 under a controlled excess of O_3, leading to the sum of NO + NO_2.

The difficulty in explaining the observed oxidative capacity of the atmosphere in Antarctica also lies in the fact that the deposition processes of reactive species in the snowpack are not yet fully understood. In fact, with today's knowledge, it is not possible to model this oxidizing capacity without wide ranges of uncertainty. New experiments were also designed during my first two years of research to enable the study of snow nitrate photolysis. The reader will find in Chapter 3 the results of seven dynamic flux chamber experiments deployed for the first time at Dome C, on the Antarctic Plateau, during the 2019-2020 summer campaign. Such experiments allow a better characterization of the nitrate photolysis and its relation to NO_x emissions. Chapter 3 is based on a scientific paper, submitted early April 2021 to *Journal of Geophysical Research: Atmospheres*.

Also, the NO_2:NO ratio observed in the atmosphere in the past does not explain such a high summer oxidative capacity. Atmospheric observations were also performed during the same summer campaign, with direct detection of NO_2 and indirect measurements of NO. The summer variability of the NO_2:NO ratio was studied throughout the photolytic season at Dome C in order to decipher the chemical mechanisms at stakes during the summer Antarctic Plateau troposphere. The reader will find Chapter 4 in the form of a scientific paper to be submitted to *Atmospheric Chemistry and Physics*.

Finally, a summary of the scientific conclusions and discussions on future works is provided.

Chapter 2

NO_x measurement using a compact incoherent broadband cavity enhanced absorption spectrometer

After: *Barbero, A., Blouzon, C., Savarino, J., Caillon, N., Dommergue, A. and Grilli, R.: A compact incoherent broadband cavity-enhanced absorption spectrometer for trace detection of nitrogen oxides, iodine oxide and glyoxal at levels below parts per billion for field applications, Atmospheric Measurement Techniques, 13(8), 4317–4331, doi:10.5194/amt-13-4317-2020, 2020*

Contents

Abstract

In this chapter, a compact, affordable and robust instrument based on Incoherent Broadband Cavity Enhanced Absorption Spectroscopy (IBBCEAS) for simultaneous detection of NO_x, IO, CHOCHO, and O_3 in the 400–475 nm wavelength region is presented. The instrument relies on the injection of a high-power LED source in a high-finesse cavity ($F \approx 33{,}100$), with the transmission signal be detected by a compact spectrometer based on a high-order diffraction grating and a CCD camera. A minimum detectable absorption of 2.0×10^{-10} cm^{-1} was achieved within $\approx$ 22 minutes of total acquisition, corresponding to a figure of merit of 1.8×10^{-10} cm^{-1} $Hz^{-1/2}$ per spectral element. Due to the multiplexing broadband feature of the setup, multi-species detection can be performed with simultaneous detection of NO_2, IO, CHOCHO, and O_3 achieving detection limits of 11, 0.3, 10 ppt, and 47 ppb (1σ) within 22 min of measurement, respectively (half of the time spent on the acquisition of the reference spectrum in absence of absorber, and the other half on the absorption spectrum).

The implementation on the inlet gas line of a compact ozone generator based on electrolysis of water allows the measurement of NO_x ($NO + NO_2$) and therefore an indirect detection of NO with detection limits for NO_x and NO of 10 and 21 ppt (1σ), respectively. The device has been designed to fit in a 19", 3U rack-mount case, weights 15 kg, and has a total electrical power consumption < 300 W. The instrument can be employed to address different scientific objectives such as better constrain the oxidative capacity of the atmosphere, study the chemistry of highly reactive species in atmospheric chambers as well as in the field, and looking at the sources of glyoxal in the marine boundary layer to study possible implications on the formation of secondary aerosol particles.

2.1 Introduction

Free radicals are controlling the oxidative capacity of the atmosphere and therefore contribute to the upholding of its chemical balance. With their unpaired valence electron, they are highly chemically reactive, and are, therefore, considered the "detergents" of the atmosphere (Monks, 2005; Monks et al., 2009).

Even if present at extremely low concentrations, radicals are constantly formed by photochemical and combustion processes. They may be removed from the atmosphere by biological uptakes, dry and wet deposition, and chemical reactions (Finlayson-Pitts and Pitts, 2000b). Free radicals in the troposphere such as nitrogen oxides (NO_x), hydroxyl radical (OH), peroxy radicals (HO_2, RO_2), and halogen oxides (BrO and IO), can be found at mixing ratios (i.e. mole fractions) ranging from less than one part per trillion (10^{-12} mol mol^{-1} or ppt) up to a few parts per million (10^{-6} mol mol^{-1} or ppm) in the atmosphere (Wine and Nicovich, 2012).

Measuring their concentration and dynamic variability in different atmospheric environments is key for addressing specific questions regarding air quality, the oxidative state of the atmosphere, the ozone budget, aerosol nucleation, as well as carbon, nitrogen, and sulfur cycles. The understanding of the complex interactions involving those species has led to numerous investigations during the past decades. Especially, nitrogen oxides ($NO_x \equiv$ NO and NO_2), have a direct impact on air quality and climate change. In presence of volatile organic compounds (VOCs) and under solar radiation, nitrogen oxides stimulate ozone (O_3) formation in the troposphere. NO_x also plays an important role in rain acidification and ecosystems eutrophication by its transformation in nitric acid (HNO_3) (Jaworski et al., 1997; Vitousek et al., 1997). Finally, NO_x contribute to the formation of particulate matter in ambient air and to the aerosol formation leading to clouds formation (Atkinson, 1998).

The NO_2 mixing ratio in the troposphere ranges from a few tens of ppt in remote areas to hundreds of ppb (10^{-9} mol mol^{-1}) in urban atmospheres (Finlayson-Pitts and Pitts, 2000b).

Being able to measure such species in situ, at low levels of concentrations, and at a time scale compatible with its reactivity (i.e. in min), is challenging and puts stringent constraints on the instrument sensitivity, time response, energy consumption, and compactness. Among the various techniques that have so far been developed, ChemiLuminescence Detection (CLD) (Maeda et al., 1980; Ryerson et al., 2000), Long-Path Differential Optical Absorption Spectroscopy (LP-DOAS) (Lee et al., 2008a, 2005; Pikelnaya et al., 2007), and Multi-AXis Differential Optical Absorption Spectroscopy (MAX-DOAS) (Platt and Perner, 1980; Sinreich et al., 2007; Wagner et al., 2010), have been used to detect nitrogen species and halogen oxides. The CLD technique, using the chemiluminescence reaction occurring between O_3 and NO after the reduction of NO_2 into NO, is widely used for air quality measurements with sensitivities better than 100 ppt (Ryerson et al., 2000). Nevertheless, the interferences in the reduction of NO_2 to NO with other species (i.e. HONO, HNO_3) and the sensitivity to environmental conditions (temperature and humidity) leave uncertainties on absolute mixing ratio measurements (Grosjean and Harrison, 1985; Williams et al., 1998). The MAX-DOAS technique has been used to measure BrO and NO_2 by making use of the characteristic absorption features of gas molecules along a path in the open atmosphere (Leser et al., 2003). Although MAX-DOAS is relatively simple to deploy, the data analysis makes it a complex approach for in situ field measurements due to the influence of clouds on the radiative transfer which alters the path length of light (Wittrock et al., 2004; Rozanov and Rozanov, 2010). While in LP-DOAS the optical path length is known, the signal degradation due to the environment (clouds, rain, wind) remains of importance for the data retrieval and results are integrated over the long path leading to a limited spatial resolution (Chan et al., 2012; Pöhler et al., 2010).

Compact, high sensitive, and point-source measurements may be achieved using cavity enhanced techniques such as Cavity Ring Down Spectroscopy (CRDS) and Cavity Enhanced Absorption Spectroscopy (CEAS) (Atkinson, 2003). The potential of the CRDS for accurate, sensitive, and rapid measurements in a compact and transportable instrument has already been demonstrated, e.g., Fuchs et al. (2009) reached a sensitivity of 22 ppt for NO_2 within 1 s of integration time using the CRDS technique. Incoherent Broadband Cavity Enhanced Absorption Spectroscopy (IBBCEAS) is a simple and robust technique for in situ field observations. Different sources and wavelength regions have been used for the detection of NO_2 leading to different performances: Venables et al. (2006) were able to detect simultaneously NO_3, NO_2, O_3, and H_2O in an atmospheric simulation chamber with a sensitivity of tens of ppb for NO_2; Gherman et al. (2008) reached $\approx$ 0.13 ppb and $\approx$ 0.38 ppb for HONO and NO_2 in a 4 m^3 atmospheric simulation chamber between 360 and 380 nm; Triki et al. (2008) used a red LED source centered at 643 nm reaching a sensitivity of 5 ppb; Langridge et al. (2006) developed an instrument with a blue light emitting diode (LED) centered at 445 nm allowing detection limits ranging from 0.1 to 0.4 ppb; Ventrillard-Courtillot et al. (2010) reached 600 ppt detection limit for NO_2 with a LED centered at 625 nm; while Thalman and Volkamer (2010) reported a detection limit of 30 ppt within 1 min of integration time.

More recently, Min et al. (2016) proved a precision of 80 ppt in 5 s of integration at 455 nm using a spectrometer with a thermoelectric cooled CCD camera and very high reflective mirrors. This non-exhaustive list of works underlines the need of robust, compact, and transportable instruments also allowing direct multi-species detection and low detection limits for applications in remote areas such as Antarctica, where the expected mixing ratio of NO_2 could be as low as a few tens of ppt. Fuchs et al. (2010), during the NO_3Comp campaign at the SAPHIR atmospheric simulation chamber, demonstrated the potential of theses optical techniques to compete with the CLD instruments

as routine measurements of NO_2 concentrations in the future.

The present chapter describes a compact and affordable instrument based on the IBBCEAS technique, allowing the simultaneous detection of nitrogen dioxide, iodine oxide, glyoxal, and ozone (NO_2, IO, CHOCHO and O_3), with detection limits of 11, 0.3, 10 ppt, and 47 ppb (1σ), respectively, for a measurement time of 22 min (half of the time spent on the acquisition of the reference spectrum in absence of absorber, and the other half on the absorption spectrum).

The four species are directly detected by a broadband blue light emitting diode centered at 445 nm. The wavelength region was selected in order to optimize the detection of NO_2. Direct detection of NO is only possible in UV region for wavelengths around 226 nm (Dooly et al., 2008) or in the mid-infrared region at 5.3 μm (Richard et al., 2018), wavelengths difficult to achieve with LED technology. Here, an indirect measurement is proposed which relies on the oxidation of NO to NO_2 under a controlled excess of O_3. The sum of NO and NO_2 is therefore measured, leading to a supplemental indirect measurement of NO if concentration of NO_2 is also monitored.

The field deployment for the measurements of NO_2 and NO_x consists of two twin instruments, IBBCEAS-NO_2 and IBBCEAS-NO_x, the later equipped with an ozone generator system.

2.2 Method

In IBBCEAS a broadband incoherent light source is coupled to a high-finesse optical cavity for trace gas detection. A picture of the spectrometer and a schematic diagram of the setup are shown in Figure 2.1.

In the present study, the broadband light source consisted of a high-power LED Luminus SBT70 allowing $\approx$ 1 W of optical power to be injected into the resonator. A thermoelectric (TEC) Peltier cooler (ET-161-12-08-E) and a fan/heatsink assembly were used to directly evacuate outside of the instrument up to $\approx$ 75 W of thermal heat from the LED. A temperature regulator (RKC RF100) with a PT100 thermistor was used to stabilize the LED temperature at $\pm$ 0.1 °C. The LED spectrum was centered at 445 nm with 19 nm FWHM (Full Width at Half Maximum) which covers the main absorption features of NO_2, IO, CHOCHO, and O_3. For better collimation of the LED spatially divergent emission (7 mm^2 surface), a dedicated optic (Ledil HEIDI RS) was used and coupled with a 25 mm focal lens (L1, Thorlabs, LA1951-A).

The high-finesse optical cavity was formed by two half-inch diameter high reflectivity mirrors (maximum reflectivity at 450 nm $\geqslant$ 99.990 $\pm$ 0.005 %, Layertec, 109281) separated by a 41.7 cm-long PFA tube (14 mm internal diameter, 1 mm thick) hold by an external stainless-steel tube. Both mirrors were pre-aligned and glued with Torr Seal epoxy glue on removable stainless-steel supports which were then screwed on the cavity holders. This enables the easy cleaning of the mirrors when required and also the removal of the cavity tube to perform open-cavity measurements, which is of interest for the detection of the highly reactive IO radical.

Behind the cavity, a Thorlabs FB450-40 filter was used in order to remove the broadband component of the radiation sitting outside the highly reflective curve of the cavity mirrors. The radiation is focused on an optical fiber (FCRL-7UV100-2-SMA-FC) using a 40 mm focal lens (L2, Thorlabs, LA1422-A). The optical fiber input was composed of 7 cores in a round shape pattern on the collecting side, whereas, at the fiber end, on the spectrometer side, the cores were assembled in a line for better matching the 100 μm slit at the spectrometer. The spectrometer (Avantes,

AvaSpec ULS2048L) was composed of a diffraction grating (2,400 lines mm^{-1}) and 2,048 pixels charge-coupled device (CCD). The resolution of the spectrometer was 0.54 ± 0.10 nm.

All the optics including the cavity were mounted on a Z-shaped 8-mm thick aluminum board fixed on the rack using cylindrical dampers (Paulstra). On the board, four 5 W heating bands and one PT100 sensor were glued, and a second RKC module used to regulate its temperature. The board therefore acts as a large radiator inside the instrument, allowing to minimize internal thermal gradients and thermalize the instrument. Air circulation from outside is ensured by an aperture at the front and a fan placed at the back wall of the instrument (Fig. 2.1).

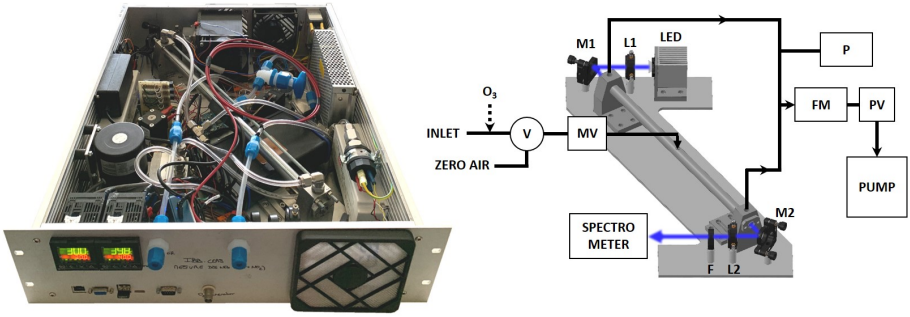

Figure 2.1 – **(left)** A picture of the instrument mounted on a 19", 3U rack-mount case. **(right)** Schematic of the instrument. The LED is protected by a cap in which a photodiode (PD) is monitoring its power. The light from the LED is collimated by lens L1 and injected into the cavity. The exiting light is then collimated with lens L2, and injected into the spectrometer. M1 and M2 are steering mirrors and F is an optical filter. The gas line is composed of a pump, a pressure sensor (P), a flow meter (FM), and a proportional valve (PV). At the inlet, a 3-way 2-position valve in PTFE (V), is used to switch between the sample and zero-air. A manual PFA needle valve (MV), is used to fix the flow rate. An ozonizer can be inserted in the inlet line for NO_x measurements.

The gas line system was composed of a manual PFA needle valve, MV, and a 3-way 2-position PTFE valve, V (NResearch, 360T032) at the entrance ; while a proportional valve, PV (Burkert, 239083), a flowmeter, F (Honeywell, HAFUHT0010L4AXT), a pressure sensor, P (STS ATM.ECO - accuracy ± 0.2 %), and a diaphragm pump (KNF, N 816 AV.12DC-B) were placed after the cavity. The entire line was made of ¼" PFA tubing which was found to be least lossy for the transport of highly reactive species (Grilli et al., 2012a). The pump provided a constant flow that can reach 11 L min^{-1} at the end of the gas line while a constant pressure in the cavity was obtained by a PID regulator on the proportional valve. A data acquisition card (National Instruments, USB 6000) was interfaced to read the analogue signal from the pressure sensor, while a microcontroller (Arduino Due) drived the proportional valve.

The manual valve at the entrance allowed to tune the flow rate. At the inlet, a 3-way 2-position PTFE valve allowed to switch between the gas sample and zero-air mixture for acquiring a reference spectra in the absence of absorption. Zero-air was produced by flowing outdoor air through a filtering system (TEKRAN, 90-25360-00 Analyzer Zero Air Filter). Particle filters (Whatman® PTFE membrane filters – TE 38, 5 μm, 47 mm) were also placed in the inlet lines (reference and sample) for preventing optical signal degradation due to Mie scattering as well as a degradation of the

mirror reflectivity for long term deployment.

The air flow was introduced at the center of the cavity and extracted at both ends of the cavity. The optimal cavity design was selected by running SolidWorks flow simulations at flow rates between 0.5 and 1 L min^{-1}. Solid works simulations were made with two different mirrors positions without purge flow (Fig. 2.2). With the cavity mirrors placed one or two centimeters away from the exit of the air flow, presence of turbulences in front of the mirrors can be observed, which may compromise the long term cleanliness of the high reflectivity mirrors, Figure 2.2(top). By placing the mirrors close to the gas flow exit, the absence of dead-volume minimizes the residence time of particles by avoiding localized turbulences to take place as shown in Figure 2.2(bottom) and prevents the mirrors surface from deposition of dust and organic matter.

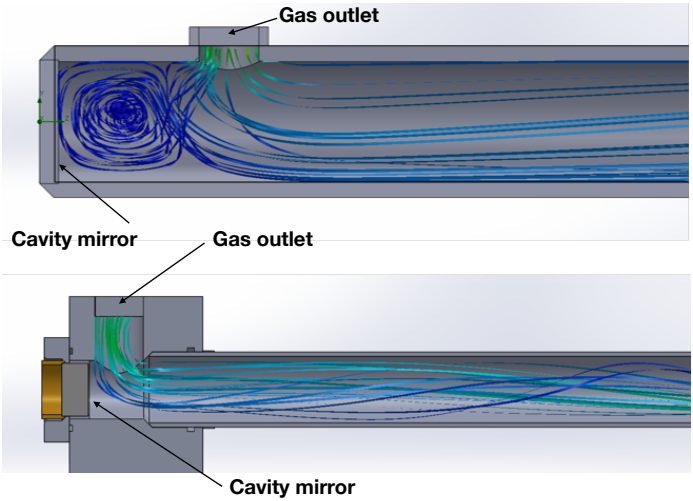

Figure 2.2 – SolidWorks simulations of the air flow entering the cavity at 1 L min^{-1}. **(top)** Turbulences created by the presence of a dead-volume between the cavity mirror and the gas exhaust. **(bottom)** Configuration with an optimum distance between the high reflective mirror and the gas outlet which maximize the effective optical pathlength, avoiding the use of purging gas at the mirrors while preserving the mirrors cleanliness during the measurement. The gas inlet is placed at the center of the cavity.

The LED's power is monitored over time using a photodiode, PD, (Hamamatsu, S1223-01), allowing to discriminate if a decreasing of intensity at the CCD (during the acquisition of the spectra in absence of asborber) is due to a decreasing of the LED intensity or to the mirrors cleanliness degradation (Fig. 2.3). A photodiode was mounted on a cap placed in front of the LED assemble. This allows to continuously monitor the LED intensity as PD_{meas}. After a calibration with a standard gas, the value at the photodiode and the mean light intensity at the CCD, while flushing with zero air and averaged over all the pixels, are stored as PD_{calibr} and $I_{0-calibr}$, respectively. At any time, the expected intensity, $I_{0-expected}$, at the CCD can be calculated following Equation 2.1:

$$I_{0-expected} = I_{0-calibr}\left(\frac{PD_{meas}}{PD_{calibr}}\right) \tag{2.1}$$

and compared to the intensity at the CCD during measurements, I_{0-meas}. The ratio $\frac{I_{0-meas}}{I_{0-expected}}$ is therefore a direct indicator of the mirrors cleanliness as the variability of the LED intensity is accounted for in real time.

Figure 2.3 shows a timeseries of 10 days measurements during which no calibrations were made. The variability of the LED intensity, Figure 2.3.a, is less than 0.05 % over 10 continuous days, implying that the variability of the signal intensity, Figure 2.3.b, only represents the mirror cleanliness over time. The variability of the latter, being less than 2 % (3 σ), validates the stability of the mirror reflectivity over time with the described set-up of our instruments and without purge flow.

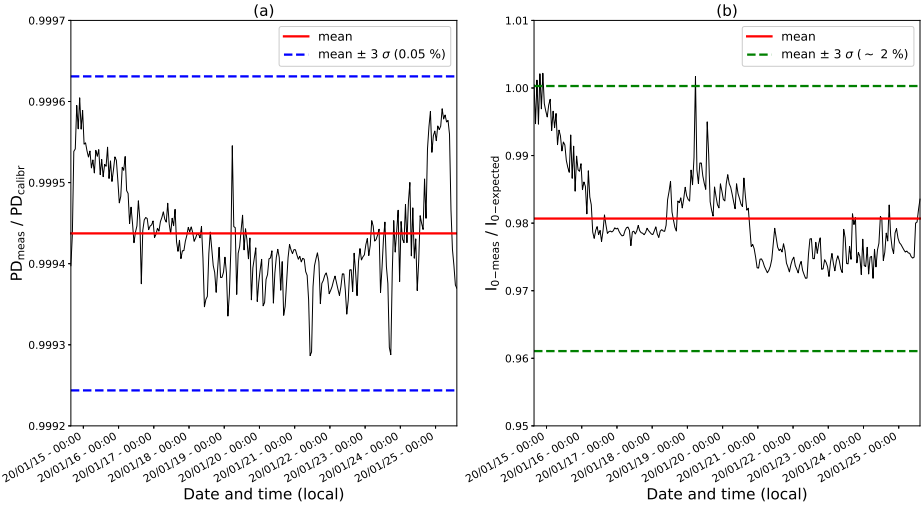

Figure 2.3 – Monitored signals over 10 continuous days of measurement without any adjustment or calibration of the instrument. **(a)** $\frac{PD_{meas}}{PD_{calibr}}$ and **(b)** $\frac{I_{0-meas}}{I_{0-expected}}$.

All the components fit in a 19", 3U aluminum rack-mount case, have a total weight of 15 kg, and a total electrical power consumption < 300 W. Instrument interface, measurements, and data analysis are performed automatically, without the intervention of an operator, by dedicated LabView software. Instrument calibrations, however, must be performed by an operator on a regular basis.

2.3 Spectral fit

The absorption spectrum is calculated as the ratio between the spectrum of the light transmitted through the cavity without a sample, $I_0(\lambda)$, and with a sample in the cavity, $I(\lambda)$. It is expressed as the absorption coefficient (in units of cm^{-1}) and follows Equation 2.2 (Fiedler et al., 2003) herafter:

$$\alpha(\lambda) = \left(\frac{I_0(\lambda)}{I(\lambda)} - 1\right)\left(\frac{1 - R(\lambda)}{d}\right) \tag{2.2}$$

where $R(\lambda)$ is the wavelength dependent mirror reflectivity and d the length of the sample inside the cavity. Equation 2.2 is derived from the Beer-Lambert's law and applied to light in an optical resonator, (Ruth et al., 2014). The light transmitted through the optical cavity is attenuated by different processes such as absorption, reflection, and scattering of the mirror substrates and coating, as well as losses due to the medium inside the cavity. The losses of the cavity mirrors are assumed to be constant between the acquisition of the reference and the sample spectrum.

Mie scattering is minimized with a 5 μm particle filter in the gas inlet, while Rayleigh scattering losses were calculated to be 2.55×10^{-7} cm^{-1} at 445 nm at 25 °C and 1 atm (Kovalev and Eichinger, 2004) and thus negligible with respect to the cavity losses normalized by the cavity lengh ($\frac{1-R}{d} = 2.28 \times 10^{-6}$ cm^{-1}). Therefore, the light transmitted through the cavity is mainly affected by the absorption of the gas species, which leads to well-defined absorption spectral features, $\alpha_i(\lambda)$, that are analyzed in real time by a linear multicomponent fit routine.

Experimental absorption spectra of the species i (i = NO_2, IO, CHOCHO and O_3) have been compared with literature cross-section data accounted for the gas concentration, experimental conditions of temperature and pressure, and convoluted with the spectrometer instrumental function. Those experimental spectra are then used as reference spectra for the fit.

$$\alpha(\lambda) = \sum_i \sigma_i(\lambda) c_i + p(\lambda) \tag{2.3}$$

A fourth order polynomial function, $p(\lambda) = a_0 + a_1\lambda + a_2\lambda^2 + a_3\lambda^3 + a_4\lambda^4$, is added to the absorption coefficient Equation 2.3 to adjust the spectral baseline and account for small changes between the reference and the sample spectra.

The transmitted light intensity, as well as the optical absorption path, will be modulated by the shape of the mirror reflectivity curve. Therefore, the later should be defined in order to retrieve the correct absorption spectrum recorded at the cavity output.

2.4 Calibration, performance and multi-species detection

2.4.1 Calibration

Washenfelder et al. (2008) described a procedure for retrieving the mirror reflectivity curve by taking advantage of a different Rayleigh scattering contribution to the cavity losses while the measuring cell was filled with different bulk gases (e.g., helium versus air or nitrogen).

The Rayleigh's empirical cross-sections used by Min et al. (2016) and the theoretical ones used by Thalman and Volkamer (2010) were found to disagree, leading this work to propose an easier approach consisting of using trace gases at known concentrations; in this case NO_2 produced by a calibrator "Gas Standard Generator FlexStream™" from Kin-Tek Analytical, Inc. and CHOCHO produced by evaporating a glyoxal solution 40 % in water from Sigma-Aldrich, since O_3 spectrum is less structured and IO is highly reactive; and their literature cross-sections Vandaele et al. (1998) for NO_2 and Volkamer et al. (2005) for CHOCHO, for retrieving the wavelength dependent reflectivity curve.

Literature spectrum from Vandaele et al. (1998) was convoluted by the known instrumental function of the spectrometer (18 cm^{-1} Lorentzian broadening). The convoluted literature spectrum is then transformed into absorption coefficient for given NO_2 and CHOCHO concentrations, in this

case 49.6 and 32.7 ppb, respectively, by using the combination of Equations 2.2 and 2.3 reported in Section 2.3. It should be noticed that the trace gas concentration only plays on the mirror reflectivity curve offset and is not critical for determining its shape.

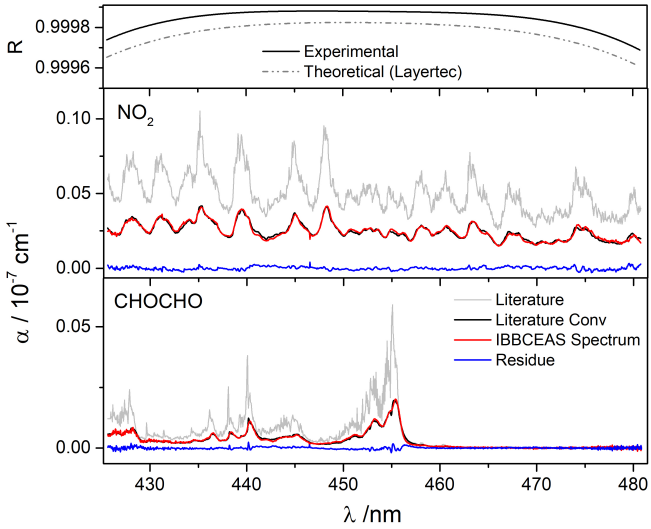

Figure 2.4 – **(top)** The optimal mirror reflectivity curve (well matching in shape the one provided by the manufacturer) which provides the best match between the literature and experimental spectra. **(middle)** and **(bottom)** The convoluted and unconvoluted literature spectra (Vandaele et al. (1998) for NO_2 and Volkamer et al. (2005) for CHOCHO) and the experimental IBBCEAS spectrum. The blue lines are the residues, i.e. the difference between the experimental and the literature spectra.

As a first guess for the reflectivity curve, the theoretical values provided by the mirror manufacturer were used. The polynomial coefficients used to describe the mirror reflectivity curve were then slightly adjusted to achieve the best match between the convoluted literature spectrum and the measured spectrum (i.e. lower root-mean-square on the difference between the two data sets). This was done for NO_2, for which the concentration was known since delivered by the Kin-Tek calibrator.

The shape of the curve was then confirmed by comparing another experimental spectrum of CHOCHO with its litterature cross-sections (convoluted with the same convolution function). In Figure 2.4(top) the optimal mirror reflectivity curve is reported, together with the theoretical curve provided by the manufacturer. Figure 2.4(middle) and (bottom) show the convoluted (black) and unconvoluted (grey) literature spectra from Vandaele et al. (1998) for NO_2 and Volkamer et al. (2007) for CHOCHO, in unit of absorption coefficient, together with the acquired IBBCEAS spectra (red). The blue lines represent the difference between the experimental and the convoluted literature spectra.

Small discrepancies are visible which could be due to small anomalies in the mirror reflectivity curve or to some experimental bias, either on the literature or the IBBCEAS spectra (i.e., an inho-

mogeneous response of the pixels of the CCD camera or a bad baseline subtraction). Nevertheless, this does not represent an issue here since the references spectra used for the fit analysis are the ones experimentally acquired by the same IBBCEAS instrument and calibrated against literature cross-sections.

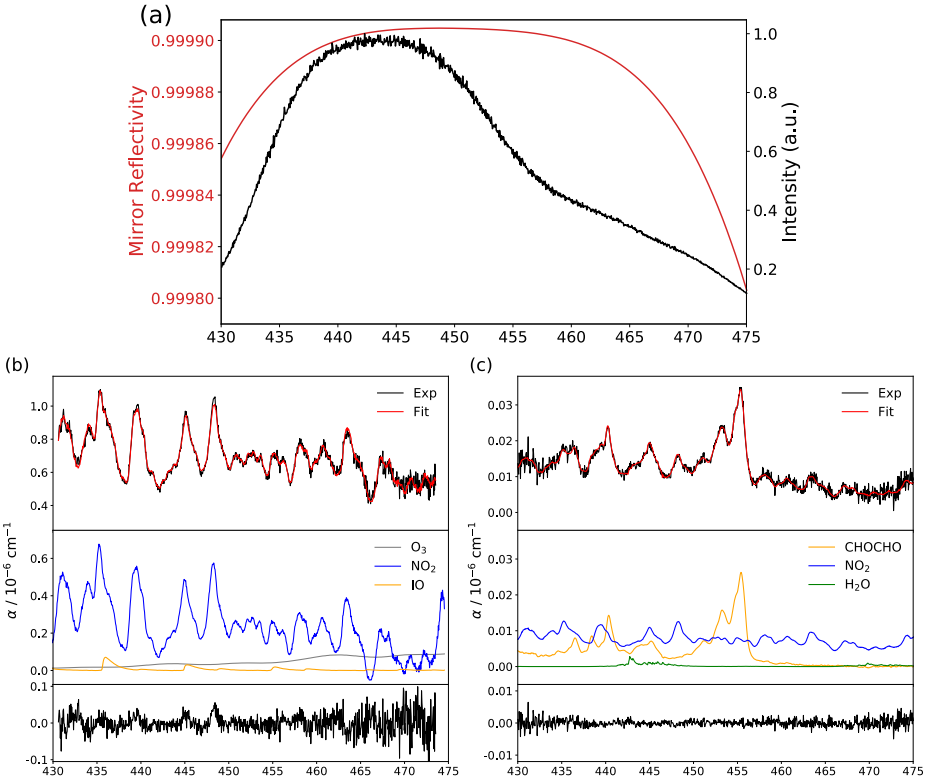

Figure 2.5 – **(a)** The mirror reflectivity curve (red) in comparison with the spectrum of the LED light transmitted by the cavity and the optical filter for a single acquisition of 250 ms. **(b)** In black, an example of an experimental spectrum of NO_2, IO, and O_3 at concentrations of 191.8 ppb, 425.6 ppt, and 28.9 ppm, respectively; in red, the multi-species spectral fit; and in blue, orange, and grey the absorptions of the different species. At the bottom (in black) the residual of the experimental fit with a 1σ standard deviation of 4×10^{-8} cm^{-1} after 1,000 averages. **(c)** In black, an example of an experimental spectrum of NO_2, CHOCHO and H_2O at concentrations of 1.40 ppb, 4.3 ppb, and 0.54 %, respectively; in red, the multi-species spectral fit; and in blue, orange, and green the absorptions of the different species. At the bottom (in black) the residual of the experimental fit with a 1σ standard deviation of 5×10^{-9} cm^{-1} after 1,000 averages.

Such an approach to calculate mirror reflectivity has been proposed before (Venables et al., 2006) and has been used by previous studies (Duan et al., 2018). Figure 2.5.a shows the resulting reflectivity curve and the transmitted light through the cavity and the optical filter. The maximum reflectivity achieved with both mirrors given by the calibration procedure is 99.9905 % leading to

an effective optical path length of ≈ 4.4 km and a cavity finesse ($F = \frac{\pi\sqrt{R}}{(1-R)}$) of ≈ 33,100. While the shape of the mirror reflectivity curve is determined once and for all, its offset is slightly adjusted after each mirrors cleaning, by flushing in the cavity a known concentration of NO_2. The spectral emission of the LED centered at 445 nm is well suited also for the detection of IO, CHOCHO, and O_3, which are other key species in atmospheric chemistry.

For the field measurements of NO_2 and NO_x, two twin instruments, named IBBCEAS-NO_2 and IBBCEAS-NO_x, are deployed, with the later equipped with an ozone generator on the gas inlet line (Section 2.5). At this wavelength region, water vapor also absorbs and is accounted for in the spectral fit analysis. However, the absorption of oxygen dimer is not required in the fit routine since the absorption feature will be present in the reference (I_0) as well as in the an absorption (I) spectra.

In Figure 2.5.b simultaneous detection of NO_2, IO and O_3 is reported. Ozone, at 28.9 ppm, is produced by water electrolysis as described in Section 2.5, 191.8 ppb of NO_2 are provided by a permeation tube, and 425.6 ppt of IO is generated by photochemical reaction of sublimated iodine crystals and ozone in the presence of radiation inside the cavity. For this spectrum, the light transmitted is integrated for 350 ms on the CCD and averaged over 1,000 spectra, yielding to a 1σ standard deviation of the residuals of 4×10^{-8} cm^{-1}, Figure 2.5.b (bottom). In Figure 2.5.c simultaneous detection of NO_2, CHOCHO, and H_2O is reported. CHOCHO at 4.3 ppb is produced by evaporating a glyoxal solution (40 % in water, Sigma-Aldrich) at the sample gas inlet of the instrument, NO_2 at 1.40 ppb, and H_2O at 0.54 % are ambient concentrations observed in the laboratory during the experiment. For this spectrum, the light transmitted is integrated for 250 ms on the CCD and averaged over 1,000 spectra, yielding to a 1σ standard deviation of the residuals of 5×10^{-9} cm^{-1}, Figure 2.5.c (bottom). The top Figure 2.5.b and 2.5.c show the experimental spectra (black traces), the fit result (red traces), and contributions from each species (middle pannels), which are included in the spectral fit. The concentrations of the species are retrieved with respect to the literature cross-sections using the calibrated reflectivity curve discussed above.

2.4.2 Instrumental calibration and inter-comparison

A calibrator (Gas Standard Generator FlexStream™, Kin-Tek Analytical, Inc.) was used to produce a stable NO_2 source. The sample was produced using a permeation tube of NO_2 (Kin-Tek ELSRT2W) calibrated at an emission rate of 115 ng min^{-1} at 40 °C loaded into the calibrator. This type of calibrator is ideally suited for creating trace concentration mixtures (from ppt to ppm).

The instruments were calibrated against the calibrator delivering NO_2 at 49.59 ± 0.51 ppb (3σ). To confirm the calibration process as well as the stability of the instrument within a greater range of concentrations, two inter-comparisons of the IBBCEAS with two different CLD instruments (42i NO_x analyser and 42iTL NO_x trace analyser from ThermoFisher™,) were performed in outdoor air over 39 and 12 hours, respectively. Results are reported in Figure 2.6.

The experiments took place at the Institute of Geosciences of the Environment (IGE) in Saint Martin d'Hères, France. The IGE is located in the university campus, ≈ 1 km from the city center of Grenoble and ≈ 300 m from a highway. Ambient air was pumped simultaneously from the same gas line by the instruments at flow rates of 1.0 and 0.5 L min^{-1} for the IBBCEAS and the CLD instrument (ThermoFisher™, 42i NO_x analyser), respectively. The measurements were conducted in September 2018. On Saturday 29^{th} of September evening, the NO_2 peak occured at slightly later time than normally expected (from 8 pm to midnight), Figure 2.6.a. This may be due to the fact that during

Saturday night, urban traffic can be significant until late, but also due to severe weather conditions prevailing at this time, with a storm and lightnings known to be a major natural source of NO_x (Atkinson, 1998). For the second experiment shown in Figure 2.6.b, ambient air was pumped at flow rates of 1.0 and 0.8 L min^{-1} for the IBBCEAS and the CLD trace instrument (ThermoFisher™, 42iTL NO_x trace analyser), respectively. The measurements were conducted in July 2019. Both instruments showed the expected variability of an urban environment with an increase of NO_2 in the evening and morning due to photochemical processes and anthropogenic activities (i.e mainly urban traffic).

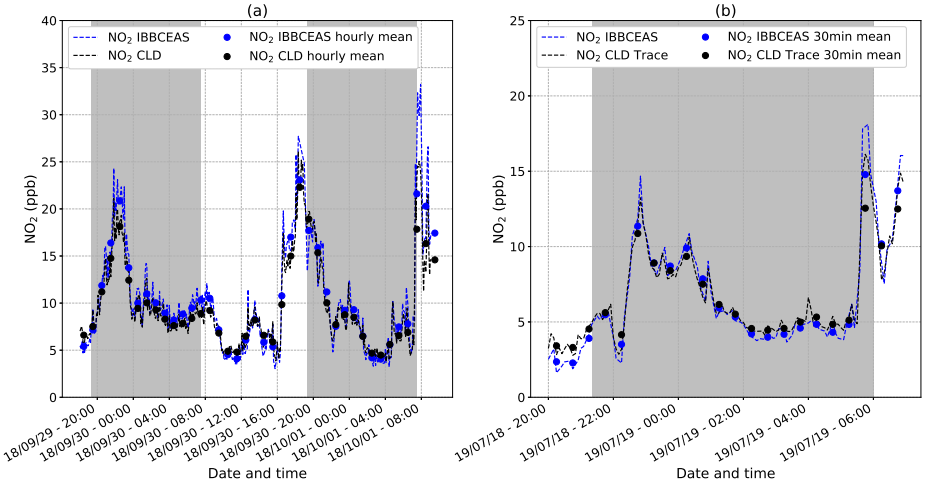

Figure 2.6 – **(a)** A 39h-long intercomparison of the IBBCEAS instrument and a commercial CLD instrument (ThermoFischer™, 42i analyzer) on the NO_2 detection in outdoor urban area performed in September 2018. The plot reports continuous (dashed lines) and hourly (dots) average data for both techniques. The grey area corresponds to night time period. **(b)** A 12h-long intercomparison of the IBBCEAS instrument and a commercial CLD trace instrument (ThermoFischer™, 42iTL trace analyzer) on the NO_2 detection in outdoor urban area performed in July 2019. The plot reports continuous (dashed lines) and 30 minutes (dots) average data for both techniques. The grey area corresponds to night time period.

The correlation plot, based on data of all instruments, Figure 2.7.a, shows good linearity with a slope of 1.088 ± 0.005 and a correlation coefficient R^2 = 0.989 with measurements averaged over 5 minutes. In order to perform linearity tests, the previous NO_2 FlexStream™ calibrator was used to produced various concentrations of NO_2 covering a large range of concentrations. Figure 2.7.b shows the good linearity, from ppt to ppb range, of the IBBCEAS instrument with a slope of 1.015 ± 0.006 and a correlation factor of R^2 = 0.9996, confirming the validity of the calibration approach.

The discrepancies observed between the IBBCEAS and the CLD techniques might be explained by positive and negative interferences on the CLD technique. While the system presented here measures NO_2 directly, the CLD technique applies an indirect measurement of NO_x from the oxidation of NO through a catalyzer, then in CLD, the NO_2 mixing ratio is obtained by the subtraction of the NO signal to the total NO_x signal. Villena et al. (2012), demonstrate that the interferences on a urban atmosphere for the CLD technique implied positive interferences when NO_y species photolysis

occurred, leading to an over-estimation of daytime NO_2 levels, while negative interferences were attributed to the VOCs photolysis followed by peroxyradical reactions with NO.

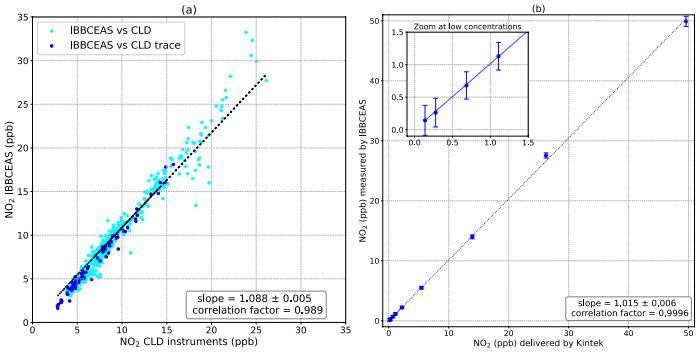

Figure 2.7 – **(a)** A linear correlation was obtained with a slope of 1.088 ± 0.005 and a correlation coefficient R^2 = 0.989 between the IBBCEAS system and the ThermoFisher instruments. **(b)** Results of the system's calibration using a NO_2 FlexStream™ calibrator. A linear correlation was obtained with a slope of 1.015 ± 0.005 and a correlation coefficient of R^2 = 0.9996

2.4.3 Performances: sensitivity and long-term stability

In remote area such as East Antarctica, NO_2 ranges from a few tens to a few hundreds of ppt (50 - 300 ppt) (Frey et al., 2013, 2015). Due to the low signal-to-noise ratio of the spectrometer, a single acquired spectrum (with an integration time ranging between 200 and 350 ms) does not provide the required detection limit. However, the sensitivity can be improved by averaging the measurements for longer times, over which the instrument is stable.

The stability of the IBBCEAS system is mainly affected by temperature fluctuations, mechanical instabilities and pressure drifts. In order to characterize the long-term stability of the instrument, two different studies were conducted on the IBBCEAS-NO_2 and the IBBCEAS-NO_x during the antarctic field campaign at Dome C in 2019– 2020. For both studies, the light transmitted through the cavity, I, was integrated at the CCD for 250 ms, providing a signal-to-noise ratio of 110 for a single spectrum. The reference spectrum, I_0, was taken by averaging 2,000 individual spectra (≈ 8 min) while flushing the cavity with zero air. Subsequently, a 9h long time series was recorded for each instrument maintaining the zero-air flow. The instruments were regulated at 12.0 ± 0.2 °C, with a cavity pressure of 630.0 ± 0.7 mbar and a gas flow of 1.02 ± 0.11 L min^{-1} for the IBBCEAS-NO_2 and 1.07 ± 0.10 L min^{-1} for the IBBCEAS-NO_x, respectively.

The minimum absorption coefficient, α_{min}, corresponding to the standard deviation of the residual of the spectrum, was deduced for different time averages. The results are shown in the log-log plot of Figure 2.8, were the dots are the data and the dashed line indicates the trend in case of pure white noise regime.

On Figure 2.8 one can see that both the instruments follow the white noise trend for about 22 min (5,200 averages), afterwards, the baseline noise start to deviate due to the arise of frequency dependent noise. The choosen α_{min} value corresponds to 2.0 × 10^{-10} cm^{-1} within ≈ 22 min (5,200 spectra) of measurement during wich a reference spectrum in absence of absorbers and the absorption

spectrum are acquired. The corresponding figure of merit (Noise Equivalent Absorption Sensitivity, NEAS or $\alpha_{min(BW)} = \alpha_{min} \times \sqrt{\frac{t_{int}}{M}}$) is therefore 1.8×10^{-10} cm^{-1} Hz$^{-1/2}$ per spectral element, with t_{int} the integration time, $\approx$ 11 min, and M the number of independent spectral elements, here 800 spectral elements are considered for the spectral fit.

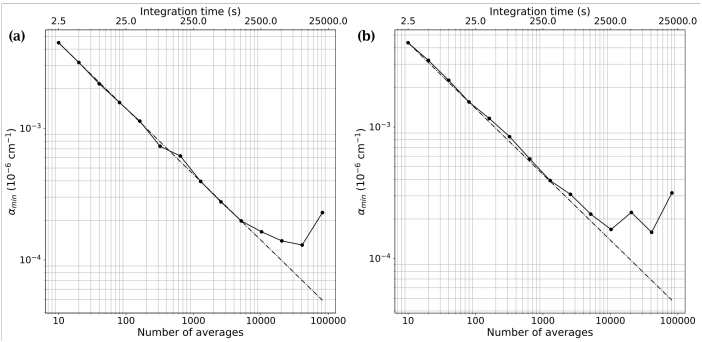

Figure 2.8 – The minimum absorption coefficient α_{min} versus the number of spectral average for **(a)** the IBBCEAS-NO_2 instrument and **(b)** the IBBCEAS-NO_x instrument. For these measurements the cell was continuously flushed with a zero-air flow of 1.02 L min^{-1} (IBBCEAS-NO_2) and 1.07 L min^{-1} (IBBCEAS-NO_x). The α_{min} was calculated from the standard deviation of the spectra residual at different time averages.

For the same time series, an Allan–Werle (AW) statistical method on the measured concentrations was employed (Werle et al., 1993). In this case, spectra were averaged in a block of 10 and analysed by the fit routine. The results of the fit are reported on Figure 2.9.a for the IBBCEAS-NO_2 and on Figure 2.9.c for the IBBCEAS-NO_x. For an acquisition time of 2.5 s, corresponding to 10 averaged spectra, the AW standard deviation σ_{AW-SD} was 175, 4.8, 125 ppt, and 725 ppb for NO_2, IO, CHOCHO, and O_3, respectively (IBBCEAS-NO_2). By increasing the integration time, the σ_{AW-SD} decreased following the white-noise trend, the colored dashed line of Figure 2.9.b, with a characteristic N slope (where N is the number of averaged spectra).

Because a reference spectrum in the absence of absorbers is required by this CEAS technique, depending on the shape of the AW plot, different strategies may be followed. In our case, the AW trends continue to decrease for all species for $\approx$ 22 min (5,200 averages); this means that one can spend 11 min acquiring the reference spectrum and a further 11 min for the absorption spectrum, leading to limits of detection (LODs) for the IBBCEAS-NO_2 instrument of 11, 0.3, 10 ppt and 47 ppb (1σ) for NO_2, IO, CHOCHO, and O_3, respectively.

In our case, we chose to divide the measurement times by 2 (i.e., $\approx$ 11 min and 2,600 averages for acquiring both the reference and the absorption spectra), offering equally interesting LODs for the IBBCEAS-NO_2 instrument: 16, 0.4, 12 ppt, and 72 ppb for NO_2 , IO, CHOCHO, and O_3 (1σ), respectively, and allowing us to stay within the white-noise regime.

The same analysis is done for the IBBCEAS-NO_x (Fig. 2.9.d), where the σ_{AW-SD} reaches 18, 0.42, 12 ppt, and 65 ppb for NO_2, IO, CHOCHO, and O_3 (1σ), respectively. If the optimum time of measurement is doubled, the system can achieve ultimate detection limits of 10, 0.32, 9 ppt, and 50 ppb for NO_2, IO, CHOCHO, and O_3 (1σ), respectively.

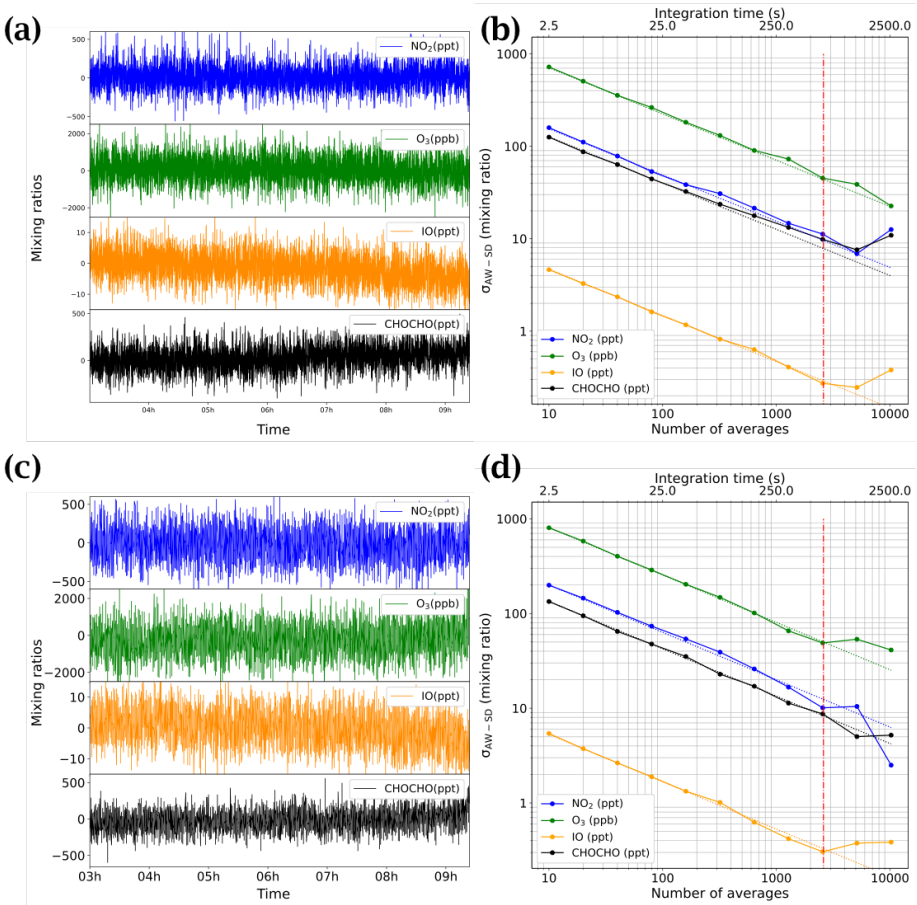

Figure 2.9 – **(a, c)** Mixing ratios of the target species NO_2, O_3, IO, and CHOCHO measured during a 9h Allan–Werle variance statistical experiment flowing zero air through the cavity on the IBBCEAS-NO_2 and IBBCEAS-NO_x instruments, respectively. **(b, d)** The log–log Allan–Werle standard deviation plot, illustrating that the instrument performance follows the white-noise regime up to a certain extent, identified by the dashed lines. This represents the optimum integration time, after which instrumental instabilities start to dominate.

Figure 2.10 shows FIT residuals retrieved using different number of averages (10 - 5,210 - 40,960 and 81,980). The more frequency noise is introduced, the more structures are observed on the residuals. It is therefore a question of finding the right number of averaging operations in order to use the instruments to the best of their respective abilities.

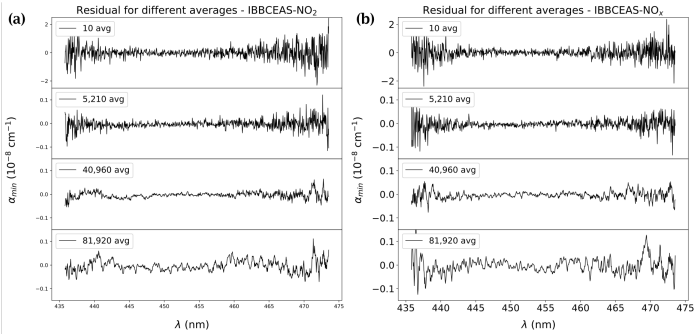

Figure 2.10 – Residuals of the spectral fit at different number of averages for the IBBCEAS-NO_2 **(a)** and IBBCEAS-NO_x instruments **(b)**, showing the arise of structured frequency-dependent noise on the residual of the fit at larger averages.

The long-term stability and repeatability of the instruments were further studied by taking regular reference spectra within the optimum integration time of the instruments while continuously flushing the instrument with the zero-air mixture. In this case ≈ 5 and ≈ 3 min intervals were chosen, corresponding to 1,024 and 580 averages (for 350 and 300 ms integration time, respectively) and a sensitivity on the NO_2 concentrations of 55 and 53 ppt (1σ), respectively. The results are reported in Figure 2.11. Test1 (1,024 averages) was run for 9 hours, and Test2 (580 averages) was run for 15 hours.

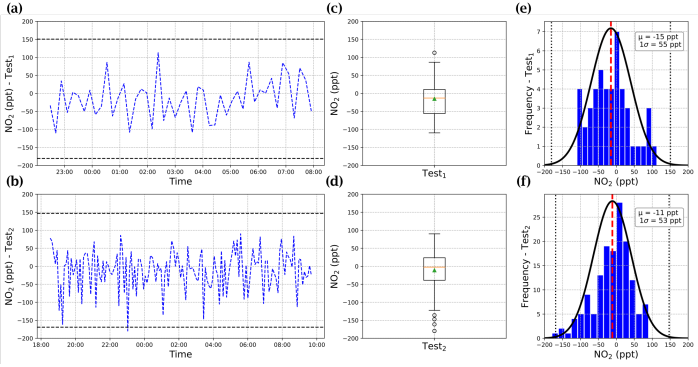

Figure 2.11 – **(a, b)** Time series of two long-term stability tests, with the black dashed lines representing the 3σ level; **(c, d)** boxplot of the stability test while continuously flushing zero air in the cavity, with means over 46 and 148 measurements (for Test1 and Test2, respectively) shown as green triangles and dots representing the outliers; **(e, f)** histogram analysis showing well distributed measurements within the 3σ level (black dashed lines).

These tests highlight the reliability of the measurement protocol, with the long-term measurement well distributed within the 3σ level of the measurements precision (165 and 159 ppt, respectively). A boxplot is also reported representing the average values (green triangles) and medians, quartiles, and minimum and maximum values. The histogram analysis of those tests shows a good distribution of the measurements within the 3σ level.

While the pressure is regulated with a pressure meter with ± 0.2 % accuracy, the cavity's temperature is regulated to be 3 °C above ambient room temperature using a PT100 temperature probe, a temperature controller, and heating bands, as described in Section 2.2. The heating bands were positioned on the aluminum board which holds all the optics and the cavity. AW analysis were made with and without those heat bands to quantify how sensitive the instruments were to temperature changes, the latter influencing the mechanical stability of the materials. Figure 2.12 shows the results obtained with the IBBCEAS-NO_2 instrument.

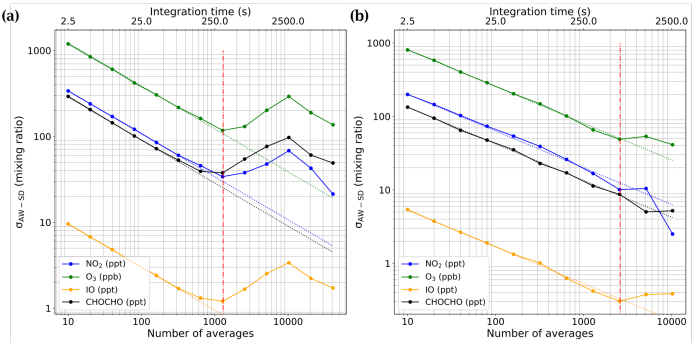

Figure 2.12 – The log-log Allan-Werle standard deviation analysis for the IBBNO$_2$, without **(a)**, and with **(b)**, the temperature regulation of the instrument.

Figure 2.12.a shows the results without the temperature regulation of the instrument and one can see a deviation from the white noise after 1,300 averages with a maximum at ≈ 10,000 averages or ≈ 42 minutes corresponding to the laboratory temperature regulation cycle. However, by regulating the instrument temperature with the heating bands, the instrument is stable for longer time, and is no longer affected by the external temperature variabilities as shown in Figure 2.12.b; similar results were observed for the IBBCEAS-NO_x instrument.

Table 2.1 – Comparisons of the performances with other recently developed IBBCEAS systems

References	Centered wavelengh (nm)	Source FWHM (nm)	NO_2 detection limit (ppt min^{-1})	Sample path lengh (cm)	Mirror reflectivity (%)	Optical lengh (km)	Mirrors purged	CCD cooled (°C)	Minimum σ_{AW-SD} deviation (s)
Min et al. (2016)	455	18	16	48	99.9973	17.8	no	-70	100
Jordan et al. (2019)	505	30	200	102	99.98	5.1	yes	-80	300
Liu et al. (2019)	455	18	33	84	99.993	10.3	yes	-70	100
Liang et al. (2019)	448	15	15	58.9	99.9942	11.7	yes	-10	3,500
Barbero et al. (2020)	**450**	**19**	**40**	**41.7**	**99.9905**	**4.4**	**no**	**no**	**1,300**

Table 2.1 shows a comparison between the instrument presented in this chapter and other recently developed IBBCEAS systems. The detection limits are given in ppt min^{-1} (1σ) with the normaliza-

tion time that accounts for the acquisition of the reference (without absorption) and sample spectra to allow for a better comparison.

It should be noticed that all the other developments took advantage of an optical spectrometer with a cooled CCD device to reduce dark noise. A more compact and affordable spectrometer was preferred in this work. The cooling at the CCD would allow for a gain of up to a factor of 10 on the signal-to-noise ratio, which would directly apply to the achievable detection limits. Furthermore, a CCD with a higher sensitivity would allow for selecting higher-reflectivity mirrors and increase the optical pathlength. Noteworthy, the optimum integration time, corresponding to a minimum of the σ_{AW-SD}, is at 1,300 s ($\approx$ 22 min), allowing for the achievement of low detection limits even without a cooled CCD.

2.5 Indirect measurement of NO

Measuring NO and NO_2 simultaneously is important to study the NO_x budget in the atmosphere. In the selected blue visible region, there are no NO absorption features for direct optical measurements, and optical absorption detection of NO is typically done in the infrared region (Richard et al., 2018).

However, its detection can be performed by indirectly measuring NO_2 after quantitative chemical conversion of NO to NO_2 in a controlled O_3 excess environment. This will lead to the measurement of NO_x, which, coupled by a simultaneous detection of NO_2 will provide the concentration of NO ([NO] = [NO_x] - [NO_2]) (Fuchs et al., 2009):

$$NO + O_3 \rightarrow NO_2 + O_2 \qquad k_1 = 1.80 \times 10^{-14}\ cm^3\ molec^{-1}\ s^{-1} \text{ at } 25\ °C \qquad \text{(R2.1)}$$

O_3 was produced by electrolysis of water using commercial ozone-micro-cells (INNOVATEC) allowing the generation of O_3 without nitrogen oxides impurities and without the need of an oxygen gas bottle. The cells were mounted in a home-made plastic container offering a 200 cm^3 water reservoir. With a miniaturized design (15 × 15 × 15 cm^3), ozone production can be controlled upon injection into the inlet line. The sample air flow to be analyzed works as carrier gas for flushing the ozone enriched surface water.

The design of the container, Figure 2.13, allows a maximization of the contact area between the air flow and the water and, therefore, a high ventilation at the surface. The cap was designed with a twisted channel for allowing a better mixing of the gas and preventing water droplet from entering the outlet line. This design also prevents the production of unwanted oxidizing agents such as peroxides, as well as sample dilution, causing a signal degradation and requiring precise flow measurements for quantitative analysis.

The production of O_3 is controllable by the amount of electrolytic cells used and the supplied current, offering a dynamic range of 0 – 50 ppm of O_3 for a 1 L min^{-1} total flow rate. For long-term use of the instrument, the overall water consumption should be considered. Losses due to evaporation were estimated to range from 7 to 30 cm^{-3} d^{-1} at 10 and 30 °C, respectively, for a flow rate of 1 L min^{-1}, while losses due to electrolysis are negligible, with only 0.024 cm^{-3} d^{-1} of consumption. The other parameter to consider is the mixing time between the ozone generator and the measurement cell with respect to the O_3 excess.

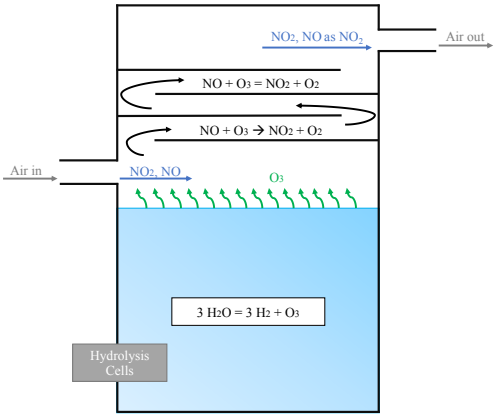

Figure 2.13 – Schematic design of the compact ozone generator. The system sizes is $15 \times 15 \times 15$ cm^3 with a water reservoir of 200 cm^3. A series of electrolytic cells is placed at the bottom, and the air is flushed at the surface before being send to the spectrometer. The cover is designed for enhancing the contact between the water surface and the air as well as preventing water droplets to enter the outlet line.

For instance, the calculated production rate of NO_2 from Reaction (R2.1) (i.e., reaction or conversion rate of NO) is $v = 4.20 \times 10^{11}$ molec cm^3 s^{-1} for 5 ppb of NO and 8 ppm of O_3. Under these conditions, a mixing time of 0.29 s is required for completing the conversion. With an air flow of 1 L min^{-1}, a 40 cm long 4 mm internal-diameter tube is therefore required between the ozone generator and the measurement cell.

The performance of the ozone generation system was tested on the IBBCEAS instrument with a nitrogen oxide standard gas bottle containing $\approx$ 195 ppb of NO in air (Air Liquide). Kinetic simulations using Tenua software (Wachsstock, 2007) were made in order to establish the O_3 excess concentrations needed to achieve the complete conversion of NO to NO_2, which, along with its detection, was tested with the IBBCEAS instrument by varying the excess concentration of O_3 until complete conversion of NO was achieved at different flows (i.e., different reaction times before reaching the measurement cell - Fig. 2.14.a). The experimental results are in good agreement with the simulations. In addition, the instrument was found to have a linear response regarding the detection of the produced O_3. The response of the IBBCEAS-NO_x instrument was tested by injecting different concentrations of NO (0, 1.1, 2.7, and 3.9 ppb). A NO cylinder from Air Liquide (NO in N_2 at 1 ppm $\pm$ 5 %) was used through a dilution line (Mass Flow Controllers from MKS instrument - ratio of 10,000 : 10) to perform the experiment. The cylinder was previously calibrated with a ThermoFisher™, model 42iTL trace analyzer. The results are shown in Figure 2.14.b where a linear response with a slope of (0.911 ± 0.029) and a correlation factor $R^2 = 0.996$ can be observed.

The $\approx$ 200 ppt offset read when no NO are expected is due to a leftover of NO_2 in the sampling line from a previous NO_2 calibration at high concentrations of NO_2 ($\approx$ 500 ppb), underlining the

importance of flushing the lines with zero air between calibration and measurement.

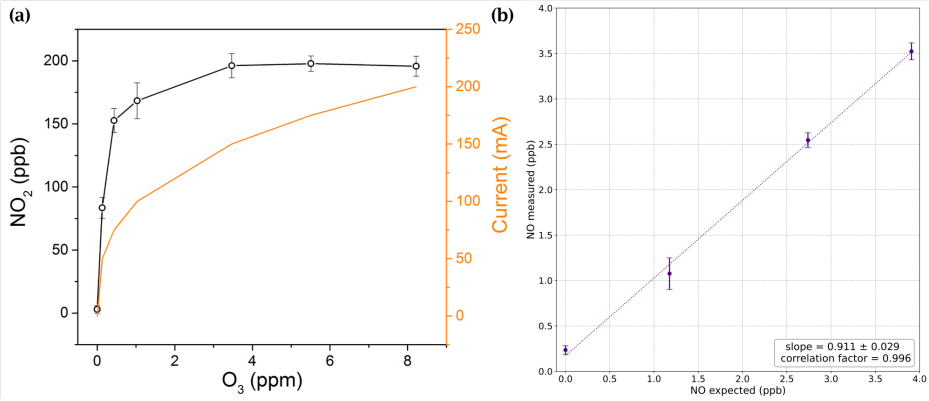

Figure 2.14 – (a) The results from the conversion of NO to NO_2 under ozone excess. The measured NO_2 produced is plotted against the level of O_3 produced by applying a certain current to the sequence of four electrolysis ozone-micro-cells. For the experiment a bottle of ≈ 195 ppb of NO in air was used. **(b)** IBBCEAS-NO_x response at different known concentrations of NO (0, 1.1, 2.7, and 3.9 ppb)

The detection limit for the NO_x measurement was found to be similar to the one of NO_2, 10 ppt (1σ) in 22 min of integration time, while for NO, retrieved as the difference between the NO_x and the NO_2 concentrations, the detection limit estimated from the error propagation corresponds to 21 ppt.

2.6 Possible chemical and spectral interferences

Further possible interferences on NO_2 detection in the presence of high levels of O_3 were also studied, since a large excess of O_3 could trigger the following reactions, with rate constants that are few orders of magnitude lower than k_1 (from the NIST Kinetics Database):

$$NO_2 + O_3 \rightarrow NO_3 + O_2 \qquad k_2 = 3.8 \times 10^{-17}\ cm^3\ molec^{-1}\ s^{-1} \text{ at } 25\ °C \qquad \text{(R2.2)}$$

$$NO_2 + O_3 \rightarrow 2O_2 + NO \qquad k_3 = 1.0 \times 10^{-18}\ cm^3\ molec^{-1}\ s^{-1} \text{ at } 25\ °C \qquad \text{(R2.3)}$$

$$NO_3 + O_3 \rightarrow 2O_2 + NO_2 \qquad k_4 = 1.0 \times 10^{-17}\ cm^3\ molec^{-1}\ s^{-1} \text{ at } 25\ °C \qquad \text{(R2.4)}$$

To study those possible interferences, 100 ppb of NO_2 produced by a permeation tube were pumped through the ozonizer and the spectrometer at a flow rate of 1 L min^{-1} while varying the concentration of O_3 from 0 to 10 ppm. NO_2 concentration was stable at low ozone concentrations, while a drop of 14 % was observed at high levels of O_3 ($\gtrsim$ 8 ppm). Kinetics simulations showed that the NO_2 consumption in favor of the NO_3 production ($NO_2 + O_3 \rightarrow NO_3 + O_2$) was kinetically possible under those conditions.

The consumption of NO_2 is strongly dependent on the reaction time and the concentration of O_3. The later should be selected according to the reaction time imposed by the volume of the inlet line and the flow rate, therefore making this interference negligible. Other chemicals reactions could

led to an overestimation of NO_2 mixing ratios:

$$HONO \rightarrow NO + OH \qquad k_5 = 3.9 \times 10^{-21}\ cm^3\ molec^{-1}\ s^{-1} \text{ at } 25\ °C \qquad \text{(R2.5)}$$

$$HO_2NO_2 \rightarrow NO_2 + HO_2 \qquad k_6 = 1.3 \times 10^{-20}\ cm^3\ molec^{-1}\ s^{-1} \text{ at } 25\ °C \qquad \text{(R2.6)}$$

Couach et al. (2002) estimated the background levels of HONO and HO_2NO_2 in Grenoble to be 4 and 2 ppq (or 10^{-15} mol mol^{-1}), respectively. With such low concentrations and kinetic constant rates, interferences due to reactions (R2.5) and (R2.6) can be neglected in an urban environment. However, in remote areas such as the East Antarctic Plateau, HO_2NO_2 levels were estimated by indirect measurements to be around 25 ppt (Legrand et al., 2014).

Because the lifetime of HO_2NO_2 decreases with temperature ($\tau_{HO_2NO_2}$ = 8.6 h at -30 °C and 645 mbar), its measurement using an instrument stabilized at higher temperature would lead to an overestimation of the NO_2 due to the thermal degradation of the HO_2NO_2. However, this interference can be minimized by working at low temperatures: at 10 °C and 1 L min^{-1} flow in our IBBCEAS instrument, the NO_2 signal would be overestimated by only 1 ppt, which is below the detection limit of the sensor. The instruments were therefore designed for working at low temperature (up to few degrees Celsius).

One more reaction, (R2.7), may also lead to possible interferences on the NO_2 detection:

$$HONO + OH \rightarrow NO_2 + H_2O \qquad k_7 = 4.89 \times 10^{-12}\ cm^3\ molec^{-1}\ s^{-1} \text{ at } 25\ °C \qquad \text{(R2.7)}$$

In urban environments OH radicals can be observed up to 4×10^6 OH radicals cm^{-3} (Heard et al., 2004). With background levels of HONO such as 4 ppq in the city of Grenoble and around 30 ppt in Dome C, Antarctica (Legrand et al., 2014), very low mixing ratios of NO_2 (< few ppq) would be produced by (R2.7) in less than 8 s (residence time of the molecules in the instrument at 1 L min^{-1}). Therefore, contribution from this interference can be neglected.

Previous works also highlighted possible artifacts through the heterogenous reaction of NO_2 and H_2O occurring in thin films on surfaces: the approximate rate production of HONO plus NO calculated in their study was reported to be between 4×10^{-2} and 8×10^{-2} ppb min^{-1} per ppm of NO_2 (Finlayson-Pitts et al., 2003). Assuming linearity between production rates and concentrations, this would represent a range of 8 to 16 ppq for 200 ppt of NO_2 in remote area such as the East Antarctic Plateau. The losses that may occur on the thin films on surfaces through the heterogeneous reaction of NO_2 and H_2O are therefore negligible.

Finally, detection of NO_2, CHOCHO and IO may be affected by spectral interferences. For instance, water vapour also shows an absorption signature at this wavelength region, which was included in the fit routine. Its spectral fit is important particularly for the measurement of NO_x, where the inlet sampling line gets saturated in water vapor while passing through the water reservoir of the ozone generator. In addition, artifacts on the signal and the spectral fit were studied by varying the O_3, NO_2, and NO mixing ratios in cavity. Small imperfections of the fit could lead to large effects on the NO_2 retrieved mixing ratio, particularly at sub-ppb concentrations and in presence of large amounts of ozone. However, no appreciable effects of possible artifacts were observed while O_3 concentrations up to 8 ppm were used. These performance studies and the simplicity of the ozone generator, compact and fully controllable, make it suitable for field applications.

2.7 Conclusions

A compact, robust, affordable and highly sensitive IBBCEAS instrument for direct detection of NO_2, IO, CHOCHO and O_3 and indirect detection of NO is reported in this chapter. The instrument relies on the injection of incoherent radiation from a compact, high power, and low cost LED source, into a high-finesse optical cavity.

The instrument provides a minimum detectable absorption of 2.0×10^{-10} cm^{-1} corresponding to a figure of merit (Noise Equivalent Absorption Sensitivity, NEAS) of 1.8×10^{-10} cm^{-1} $Hz^{-1/2}$ per spectral element. Due to the multiplexing broadband feature of the setup, multi-species detection can be performed with simultaneous detection of NO_2, IO, CHOCHO, and O_3 achieving detection limits of 11, 0.3, 10 ppt, and 47 ppb (1σ) within 22 min of measurement (which account for the reference and absorption spectra acquisition), respectively. Detection limits for the indirect measurement of NO_x and NO are 10 and 21 ppt (1σ), respectively.

The instrument has been designed to fit in a 19", 3U rack-mount case, weights 15 kg, and has a total electrical power consumption < 300 W. The detection limits could be further improved by replacing the ULS2048L Avantes spectrometer, which offers, at this working wavelength, a signal to noise ratio on a single acquisition of 110 and a sensitivity of 172,000 counts μW^{-1} ms^{-1}, with a spectrometer with an integrated cooled CCD. The cooling would allow to gain up to a factor of ten on the signal to noise ratio, which would directly apply to the detection limits. Better sensitivity of the CCD would also allows the use of higher reflectivity mirrors as done by Min et al. (2016), providing an effective optical path length of ≈ 18 km (with similar cavity length), ≈ 4 times higher than the one obtained here.

The dynamic ranges, detection limits, and multi-species detection character make this instrument well suitable for measurements in different environments, from highly polluted to very remote areas such as polar regions. The instruments can be used in the future to address different scientific questions, related to the oxidative capacity at particular regions (i.e., inland and coastal polar atmospheres), where variability of NO_x and IO would provide key information for understanding the mechanisms taking place in such remote areas. The detection of the α-dicarbonyl CHOCHO may have applications at the marine boundary layer, where its source remains unknown and its contribution to secondary aerosol particle formation may be relevant (Ervens et al., 2011; Volkamer et al., 2007; Fu et al., 2008).

This chapter is based on the published article Barbero et al. (2020). This work couldn't have been possible without the great help of the co-authors but also of others and institutions. Therefore, many thanks to the LabEx OSUG@2020 for funding the ThermoFisher™ 42i NO_x analyzer and IPEV for funding the ThermoFisher™ 42iTL NO_x trace analyzer that were used during the development of the IBBCEAS instruments presented here. Many thanks to Guillaume Méjean and Daniele Romanini from LiPhy, France, for the very useful exchange of information regarding IBBCEAS techniques as well as Andy Albert Ruth from the University of Cork, Ireland, for his very useful feedback on the paper. Thanks also to Andy and his team for welcoming us so well during our intercomparison campaign in Cork, where the IBBs were able to make their first steps before being sent to Antarctica. Thanks to Stephan Houdier for discussions about glyoxal measurement. And finally, a sincere gratitude is addressed to the technical staff of the IGE.

Chapter 3

New estimation of the NO_x snow-source on the Antarctic Plateau

After: *A. Barbero, J. Savarino, R. Grilli, C. Blouzon, G. Picard, M. M. Frey, Y. Huang, and N. Caillon: New estimation of the NO_x snow-source on the Antarctic Plateau, Journal of Geophysical Researh: Atmospheres., revised in August 2021*

Contents

"D'où vient l'étrange attirance de ces régions polaires, si tenace qu'après en être revenu on oublie les fatigues morales et physiques pour ne songer qu'à retourner vers elles ? "
Commandant Jean-Baptiste Charcot, 1905

Abstract

To fully decipher the role of nitrate photolysis on the atmospheric oxidative capacity in snow-covered regions, NO_x flux must be determined with more precision than existing estimates. Here, we introduce a method based on dynamic flux chamber measurements for evaluating the NO_x production by photolysis of snowpack nitrate in Antarctica. Flux chamber experiments were conducted for the first time in Antarctica, at the French-Italian station Concordia, Dome C (75°06'S, 123°20'E, 3233 m a.s.l) during the 2019-2020 summer campaign. Measurements were gathered with several snow samples of different ages ranging from newly formed drifted snow to 6-year-old firn.

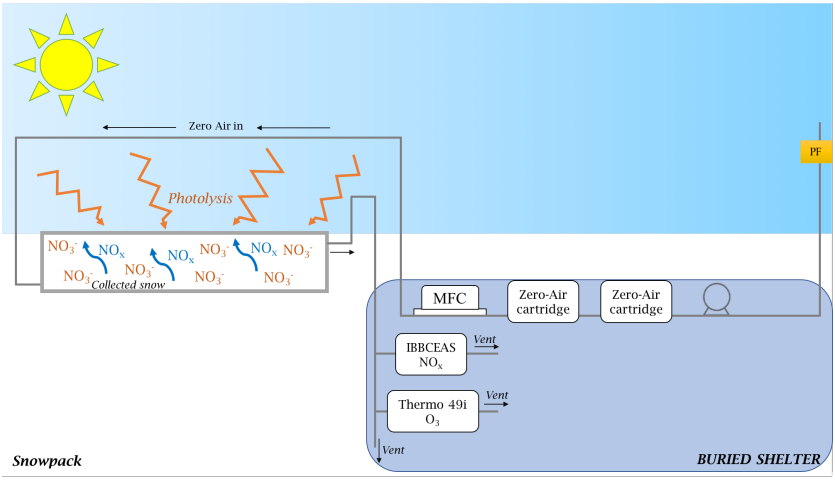

Figure 3.1 – Schematic of the entire experiment and instrumentation: the zero-air flow was produced by pumping external air through two zero-air cartridges mounted in series. A particle filter (PF) was installed at the inlet to prevent any particles entering the pump and the zero-air cartridges. The air flow is controlled using a Mass Flow Controller (MFC) and sent into the chamber. The supply of zero-air drives an equivalent amount of in-chamber air, containing any NO_x produced by photolysis, out through tubing toward the downstream analytical instruments: IBBCEAS and ThermoFisher™ 49i, for NO_x and O_3 monitoring, respectively.

Contrary to existing literature expectations, the daily average photolysis rate coefficient, $\overline{J_{NO_3}}$, did not significantly vary between differently aged snow samples, suggesting that the photolabile nitrate in snow behaves as a single-family source with common photochemical properties, where a $\overline{J_{NO_3}}$ = (2.37 ± 0.35) x 10^{-8} s^{-1} (1σ) has been calculated from December 10^{th} 2019 to January 7^{th} 2020. At Dome C summer daily average NO_x flux, F_{NO_x}, based on measured NO_x production rates, was estimated to be (4.3 ± 1.2) x 10^8 molecules cm^{-2} s^{-1}, which is 1.5 to 7 times less than the net NO_x flux observed previously above snow at Dome C using the gradient flux method. Using these results, we extrapolated an annual continental snow sourced NO_x budget of 0.017 ± 0.003 Tg·N y^{-1}, ~ 2 times the nitrogen budget, (N-budget), of the stratospheric denitrification previously estimated for Antarctica. These quantifications of nitrate photolysis using flux chamber experiments provide a road-map towards a new parameterization of the $\sigma_{NO_3^-}(\lambda, T)\phi(T, pH)$ product that can improve future global and regional models of atmospheric chemistry.

3.1 Introduction

The southern high-latitude regions of Antarctica are ideal for studying the connections between climate and atmospheric chemistry due to the continent's distinct geographic advantages. Antarctica's great distance from major sources of pollution, the outflow of low-level katabatic winds, and the insulating nature of the predominant atmospheric circulation combine to maintain a relative cleanliness of the Antarctic Plateau atmosphere (Savitskiy and Lessing, 1979). Therefore, Antarctica offers a continental sized natural laboratory with relatively limited direct human influences on biogeochemical cycles. Snow-air-radiation interactions and their link to the specific oxidizing character of the polar atmosphere is key to correctly deciphering the past environmental information preserved in the ice and to understanding the present chemical stability of the Antarctic atmosphere. Previous studies suggest that a highly reactive lower atmosphere exists above the snowpack (Domine and Shepson, 2002; Grannas et al., 2007), and this raises questions about how the basic air composition within the polar atmosphere is being altered.

Unexpectedly high levels of oxidants have been discovered in the continental interior as well as in the coastal regions, with atmospheric hydroxyl radical (OH) concentrations up to 4 x 10^6 cm^{-3} (Davis et al., 2008; Grilli et al., 2013; Kukui et al., 2014; Mauldin et al., 2010, 2001, 2004; Wang et al., 2007). These levels make the summer Antarctic boundary layer as oxidative as urban atmospheres, which was not expected for an atmosphere thought to have the most pristine boundary layer on Earth (Berresheim and Eisele, 1998; Davis et al., 2004). It is now well established that such high reactivity of the summer Antarctic boundary layer results, in part, from the emissions of nitrogen oxides ($NO_x \equiv NO + NO_2$) produced during photochemical release of nitrogen species from the snowpack (Honrath et al., 1999, 2000; Jones et al., 2000, 2001).

Despite the numerous observations collected at various sites during previous campaigns such as ISCAT 1998, ISCAT 2000, ANTCI and OPALE, (Davis et al., 2008; Mauldin et al., 2001, 2004; Preunkert et al., 2012; Wang et al., 2007), using the flux gradient method with very detailed NO_x and HONO flux measurements above the snow, questions remains about how to best parameterize the snowpack source in models. Indeed, the NO_x production rate, P_{NO_x} [molecules s^{-1}] and estimated NO_x fluxes, F_{NO_x} [molecules cm^{-2} s^{-1}] above the snow are difficult to constrain, largely because of the poorly constrained quantum yield of NO_3^- photolysis in snow (Chan et al., 2018). Therefore, a robust quantification of the NO_x sources on a continental scale over Antarctica is still lacking (Frey et al., 2013, 2015; Legrand et al., 2014; Savarino et al., 2016).

The chemical reactivity of the snowpack and its connection to the overlying atmosphere need further study to fully understand their linkage to snow chemical composition. Previous works have proposed different mechanisms to explain the nitrate photolysis behavior in ice and snow, (e.g., Blaszczak-Boxe and Saiz-Lopez (2018) and references therein). Chu and Anastasio (2003) suggested that the nitrate photolysis on ice is occurring in a "quasi-liquid layer" rather than in the bulk ice with a quantum yield ϕ = 0.003 molecules $photon^{-1}$. Zhu et al. (2010) found very high values of NO_3^- quantum yield from the photolysis of HNO_3 on ice films at 308 nm and 253 K: $\phi = 0.60 \pm 0.34$ molecules $photon^{-1}$ (2σ) with the error representing the experimental scatter.

Thomas et al. (2011, 2012) used this simplified representation of the liquid-like layer and its chemistry to represent the complex processes occurring in the Greenland snowpack. Davis et al. (2008), developed a theory driven by two photochemical domains affecting the nitrate photo-dissociation, namely the photo-labile (with nitrate adsorbed at the snow grain surface) and buried domains. Davis et al. (2008) also proposed that surface adsorption becomes more efficient with decreasing

temperatures. Zatko et al. (2013) followed Davis et al. (2008) by assuming that the NO_3^- incorporated in the snowpack by wet deposition is ingrained in the snow crystal compared to dry NO_3^- deposition, where it stays at the surface of the snow-grain, therefore more likely to dissociate into NO_x after encountering a photon, and diffuse to the surface. Meusinger et al. (2014) followed Davis et al. (2008) to decipher the quantum yield of nitrate photolysis and described the micro-physical properties of the region around the nitrate chromophore affecting its dissociation. The nitrate contained in the photo-labile domain is consumed first, being more available than the buried nitrate, hindered by a cage effect. The derived apparent quantum yields for both nitrate family were very different: $\phi^*_{buried} = 0.05$ molecules photon^{-1} and $\phi^*_{photo-labile} = 0.26$ molecules photon^{-1}.

Bock et al. (2016) developed a nitrate air-snow exchange model and tested it against the summer observations at Dome C, which demonstrated that co-condensation, i.e., the simultaneous condensation of water vapor and trace gases at the air–ice interface, was the most important process to explain nitrate incorporation in snow. Bock et al.'s (2016) model works well at cold sites on the Antarctic Plateau, where air temperatures are well below freezing and in fact below the eutectic point year-round, and where no snow melt occurs. However, the model does not reproduce the summer observations at the coast, where the temperature, relative humidity and concentration of aerosol in air and snow are much higher than that on the Plateau, and where snow surface melt is possible, strengthening previous theory of several photolytic domains aforementioned. Nonetheless, Chan et al. (2018) developed a new model and concluded that winter air-snow interactions of nitrate between the air and skin layer snow can be described as a combination of non-equilibrium surface adsorption and co-condensation on ice, coupled with solid-state diffusion inside the grain, similar to Bock et al. (2016). In addition, Chan et al. (2018) were able for the first time to reproduce the summer observations on the Antarctic Plateau and at the Coast, concluding that it is the equilibrium solvation into liquid micro-pockets, based on Henry's solubility law, that dominates the exchange of nitrate between air and snow at warmer sites, i.e., where the temperatures are above the eutectic temperature.

To date, no consensus can be found in the literature about the different forms of nitrate that would allow us to reduce the modeled F_{NO_x} uncertainties. Models usually use the quantum yield of 0.003 molecules photon^{-1} found by Chu and Anastasio (2003), therefore often under-predict the observations, e.g. at night time at Dome C (Frey et al., 2013). A better parameterization of nitrate photolysis quantum yield as a function of snow micro-physical properties and nitrate form (ion or HNO_3 molecule) is needed to improve the models.

A major difficulty encountered for estimating F_{NO_x} is that it depends upon two components: transport (both inward and outward to the snowpack) and photochemical production/loss. Previous field studies did not separate these two phenomena, and it was argued that transport could be neglected because the photochemical lifetime is only a few minutes while the time-scale needed for substantial transport above the snowpack is on the order of a few hours. The difficulty in measuring NO_x fluxes is due to the rather weak NO_x gradient in the atmosphere with respect to the relatively high measurement uncertainties, the measurement itself being disturbed by re-deposition of nitrate, convection and ventilation. Here, to circumvent this challenge, we present measurements of P_{NO_x} [molecules s^{-1}] under controlled flux, further converted into area flux F_{NO_x} [molecules cm^{-2} s^{-1}] to allow: i) comparison with above-snow measurements as first approximation; and ii) new leads or suggestions for atmospheric models. The net flux above the snow surface has been previously estimated using the flux-gradient method (Frey et al., 2013): Fick's law describes how concentration gradient, $\frac{\partial c}{\partial z}$, and diffusion coefficient, K_c, of a chemical tracer relate to the diffusive

flux, F : $F = -K_c \frac{\partial c}{\partial z}$ (Lenschow, 1995). However, potential impacts of photochemical transformation during transport in the open pore space of the snowpack and above may reflect on the flux estimate.

Photochemical production rates, P_{NO_x} [molecules s^{-1}], can also be measured directly using dynamic flux chambers (FC). Cotter et al. (2003) were the first to measure NO_x production rates using a laboratory FC experiment, varying temperature and UV irradiation, to determine the mechanism involved in NO_x release from snow. These experiments did not exactly represent the Antarctic snowpack behaviour because: i) the physical properties of the snow sample had most likely changed significantly during storage due to snow metamorphism and ii) the UV lamp used was much stronger than natural light conditions. This motivated us to conduct FC experiments on the Antarctic plateau, at Dome C, during the 2019–2020 campaign. Flux chambers are the most widely used equipment to quantify gaseous emissions from solid or liquid surface sources (Besnard and Pokryszka, 2005; Cotel et al., 2015; Pokryszka and Tauziède, 1999; Verginelli et al., 2018), and they are widely used nowadays to assess emissions of pollutants into the atmosphere from the surface (Scheutz et al., 2008; Sihota et al., 2010; Tillman et al., 2003). A dynamic FC method developed to measure production rates from hazardous waste sites employs an inert gas that is continuously introduced at a controlled rate while an equivalent amount of gas is allowed to leave the chamber (Eklund, 1992). In our Antarctic experiments, we adapted this method for NO_x monitoring, using an open circuit FC with clean air injected and $NO_{x-bearing}$ air at the outlet of the chamber analyzed, similar to Cotter et al. (2003) laboratory FC experiment.

Our study was novel in that it directly measured photochemical production rates as close as possible to the natural system. Such experiments allow us to measure an integrated parameter: $\overline{J_{NO_3^-}}$, the daily nitrate photolysis rate coefficient. In section 3.2 we provide details of the experimental studies undertaken. In section 3.3 we describe the data validation process applied. In section 3.4 we present the results and their analysis to evaluate the impact of this method on the NO_x production from the snowpack at Dome C and provide a rough continental extrapolation. Finally, in section 3.5, we provide conclusions.

3.2 Method

3.2.1 Site Description

The FC experiments were conducted from December 10^{th} to January 7^{th} at the French-Italian station Concordia, Dome C (75°06'S, 123°20'E, 3233 m a.s.l) during the 2019-2020 campaign. At this latitude, the station experiences polar night during the austral winter as the sun remains below the horizon from May to August. In summer (November to January) the solar zenith angle (SZA) does not go above 52° (i.e., lower than 38° above the horizon).

The annual climate at Dome C is mainly cold and dry (T_{mean} = -53 ± 14 °C and surface mass balance SMB = 26 kg m^{-2} yr^{-1}), typically with clear skies or elevated cirrus clouds (Palchetti et al., 2015), light winds ($W_{speed-mean}$ = 3.3 ± 2.1 m s^{-1}) and mean atmospheric pressure of P_{mean} = 641 ± 27 hPa, as shown in Figure 3.2.a. These conditions are due to a dry and cold boundary-layer flow predominantly originating from the south ($W_{dir-mean}$ = 172 ± 90 °), depicted in Figure 3.2.b, as well as being on a dome of high altitude with an albedo close to 1. Summer is warmer and more humid than the annual mean, and the conditions encountered during the 2019–2020 FC experiments were typical of the summer climatology observed at Dome C: T_{mean} = -29 ± 5 °C; P_{mean}

= 655 ± 3 hPa; $W_{speed-mean}$ = 3.1 ± 1.5 m s^{-1} and $W_{dir-mean}$ = 173 ± 80 °. More information about the meteorological conditions encountered during the experiments can be found in appendix A.1.

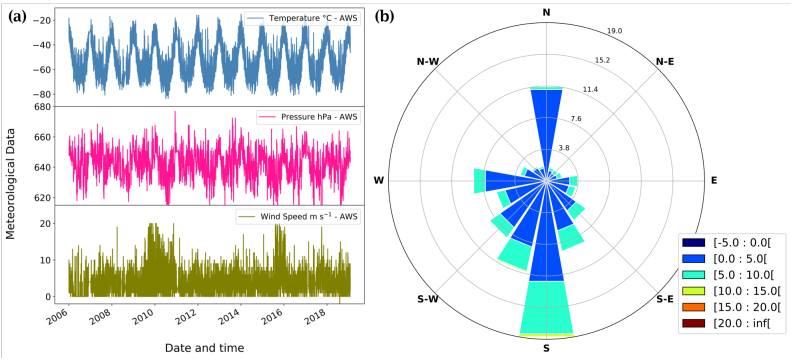

Figure 3.2 – **(a)** Multiyear meteorological observations 2-m records at Dome C, Concordia station, Antarctica measured by the local automatic weather station (AWS – Vaisala Milos 520) and **(b)** the corresponding wind rose in m s^{-1} during the period of 2006-2019.

3.2.2 Experiment location and setup

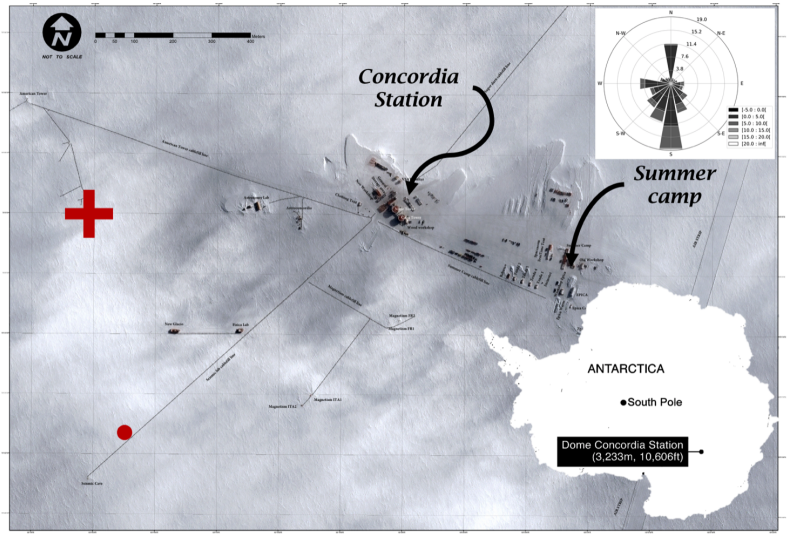

Figure 3.3 – Aerial view of the station: the red cross marks the position of the experiments and the red dot the location of the automatic weather station (AWS – Vaisala Milos 520). The dominant wind rose is shown in the upper right-hand corner. The location of Concordia station is shown in the lower right-hand corner. (*Pléiade Satellite Image – Concordia Station, Antarctica @ CNES 2016, Distribution Airbus DS*).

The experiment was located in the station's clean area sector, about 1 km south-west and upwind of the main station buildings (red cross in Fig. 3.3) in a zone less subjected to pollution linked to activities taking place at Concordia since 1997. A container buried under the snow and maintained at 8 °C was used to host the measuring instruments and all the equipment necessary for the experiments.

The FC experiments were designed in order to study different types of snow while working as close as possible to natural conditions (natural snow, radiation, temperature and actinic flux). By controlling the transport component of the NO_x, their production can be estimated through Equation 3.1:

$$P_{NO_x} = J_{NO_3^-} \times N_{NO_3^-} \tag{3.1}$$

where P_{NO_x} is the NO_x production in molecules s^{-1}; $J_{NO_3^-}$ is the photolysis rate constant of the snowpack nitrate in s^{-1} and $N_{NO_3^-}$ is the amount of nitrate contained in the snow expressed in molecules. Therefore, the objective was to study the NO_x production from different snows, i.e., varying $N_{NO_3^-}$, and the associated diurnal cycles, i.e., varying $J_{NO_3^-}$. $J_{NO_3^-}$ depends on several parameters following Equation 3.2:

$$J_{NO_3^-} = \int_{(\theta,\psi,\lambda)} \sigma_{NO_3^-}(\lambda,T)\phi(\lambda,T,pH)I_{act}(\theta,\psi,\lambda,z)d\theta d\psi d\lambda \tag{3.2}$$

where θ is the SZA; ψ marks the sun declination; λ [nm] is the wavelength; and z [m] is the snowpack's depth; $\sigma_{NO_3^-}(\lambda,T)$ is the absorption cross-section of nitrate; $\phi(\lambda,T,pH)$ and $I_{act}(\theta,\psi,\lambda,z)$ are nitrate photolysis quantum yield and actinic flux, respectively. Although the nitrate photolysis reactions (R3.1 to R3.5) produce both NO and NO_2 in the gas phase (Bartels-Rausch and Donaldson, 2006; Grannas et al., 2007), it is more relevant to directly referred to NO_x. To that end, this study focuses on the sum of $NO + NO_2 \equiv NO_x$.

$$NO_3^- \xrightarrow{h\nu} NO_2(g) + O^- \tag{R3.1}$$

$$NO_3^- \xrightarrow{h\nu} NO_2^- + O(^3P) \xrightarrow{H^+} HONO(g) \xrightarrow{h\nu} NO(g) + OH \tag{R3.2}$$

$$NO_2^- \xrightarrow{h\nu} NO(g) + O^- \tag{R3.3}$$

$$O^- + H_2O \rightarrow OH^- + OH \tag{R3.4}$$

$$NO_2^- + OH \rightarrow NO_2(g) + OH^- \tag{R3.5}$$

Because photolysis of nitrate in snow occurs under UV radiation ($\lambda > 300$ nm with 305 nm the optimal wavelentgh), UV-transparent chambers are essential for the experiment. The most UV-transparent material after glass is polymethyl methacrylate (PMMA). It is lighter than glass and therefore more practical to use in the field; however, it gets very brittle in cold environment. Several PMMA materials were tested to find the best compromise between thickness and UV transparency. We found that a thickness of 8 mm offered general robustness and cold resistance while keeping the weight of an empty chamber reasonable for handling in the field (~ 5 kg). Within the different PMMAs, the Plexiglas Clear GS2458 GT (EBLA-GmbH Kunststofftechnik) provided the best transparency in the UV: > 71 % of transmitted light for $\lambda > 305$ nm (transmission spectra provided in appendix A.2). The chamber dimensions (70 cm x 21 cm x 21 cm) give a volume of $V_{FC} \sim 0.03$ m^3 and a total surface area of $S_{FC} \sim 0.62$ m^2, providing enough NO_x production to be detected by the monitoring instruments.

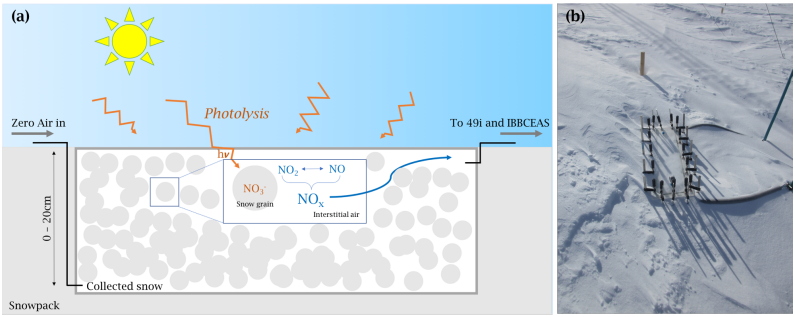

Figure 3.4 – **(a)** Schematic and **(b)** picture of one FC experiment in the field. Note that more detailed schematic of the experiment is given in Figure 3.1.

Because light attenuates quickly with depth in the snowpack following an exponential decrease, this makes the first few centimeters of the snow column dominate the availability of photons for photochemical reactions in the UV (Brandt and Warren, 1993; Domine et al., 2008; Simpson et al., 2002). At Dome C, the radiative transfer model developed by Libois et al. (2013, 2014) predicts a 95 % loss of light in the snowpack after 50 cm depth at $\lambda > 305$ nm (e.g., the actinic flux is effectively null below 50 cm). This defines the photic zone (Erbland et al., 2013) of 3 times the e-folding depths, and the model therefore assumes a mean e-folding depth of 17 cm, which is consistent with France et al. (2011) observations of ~ 10 cm for windpack layer and ~ 20 cm for hoar-like layer at 400 nm. We chose a chamber depth that covered one e-folding depth for all our snow samples, representing ~ 63 % of NO_x produced in the snow column.

The chamber was filled with the desired snow and closed with clamps, allowing the snow to be changed and weighed easily. It was then connected to a zero-air flow at the inlet and to the analysis instruments at the outlet using $\frac{1}{4}$" (~ 0.64 cm) diameter Teflon® tubing and connectors. The sample inlet and outlet tubes were protected from solar radiation and kept 2 to 3 °C above ambient temperature to avoid any condensation occurring inside the lines. The chamber was then buried in the snow, with the upper cover at the same height as the snowpack surface, to ensure the most natural experimental conditions (Fig. 3.4).

The zero-air flow was produced by pumping outdoor air through two serial zero-air cartridges connected in series (TEKRAN, 90-25360-00 Analyzer Zero Air Filter) and pushed into the FC at F_{air} = 58 ± 17 cm^3 s^{-1} (3.50 ± 1.05 slpm, standard liters per minute). Only the volume of air in the chamber should be considered when calculating the residence time, and thus the volume of the chamber need to be corrected from the snow porosity: $n = 1 - \frac{\rho_{snow}}{\rho_{ice}}$ with ρ_{snow} the snow density in g cm^{-3} calculated by gravimetry, and ρ_{ice} the ice density (0.917 g cm^{-3}). Snow density ranging from 0.32 to 0.45 g cm^{-3} were measured and consistent with previous observations (Gallet et al., 2011). Snow samples porosity ranging from 0.51 to 0.59, lead to residence times, $\tau = \frac{nV_{FC}}{F_{air}}$, from approximately 3 to 7 min. Previous estimates of NO_x chemical lifetime, τ_{chem}, range between 6.4 h (daily mean) at Halley (Bauguitte et al., 2012) and 8 h (median) at South Pole (Davis et al., 2004). Based on observed OH and HO_2 during the OPALE campaign, the τ_{chem} for NO_x is estimated to be 3 h at 12:00 local time (LT) and 7 h at 00:00 LT at Dome C (Legrand et al., 2014). NO_x chemical lifetime in the FC experiments is therefore expected to be much longer than the residence time, making the observed NO_x concentrations directly proportional to the NO_x production.

3.2.3 Instrumentation

The twin instruments used for the NO_x were developed, tested and validated in the laboratory prior the campaign (Barbero et al., 2020). They are based on Incoherent Broad-Band Cavity Enhanced Absorption Spectroscopy (IBBCEAS) for the detection of NO_2 in the 400 – 475 nm wavelength region. The implementation on the inlet gas line of a compact ozone generator based on water electrolysis allows the measurement of NO_x after quantitative conversion of all ambient NO to NO_2 via NO + $O_3 \rightarrow NO_2 + O_2$. The 10-min measurement time used during the experiments permits the acquisition of both the reference and the absorption spectra with detection limits of 54 and 48 x 10^{-12} mol mol^{-1} (3σ) for NO_x and NO_2, respectively, according to an Allan-Werle statistical method (Werle et al., 1993). Additionally, the IBBCEAS instruments were calibrated prior field deployment against a calibrator (FlexStream™ Gas Standards Generator, KINTEK Analytical, Inc.) that produced a stable NO_2 source, covering a large range of concentrations, from the pmol mol^{-1} to nmol mol^{-1} range, with a slope of 1.015 ± 0.006 and a correlation factor of R^2 = 0.9996 (Barbero et al., 2020). Field calibrations were made using a NO_2 gas bottle (Air Liquide B10 - NO_2 1 x 10^{-6} mol mol^{-1} in N_2) calibrated prior field deployment against the same calibrator FlexStream™.

The O_3 inside the chamber was monitored using a UV Photometric O_3 analyzer (Thermo Scientific, Model 49i) that achieves 1.5 nmol mol^{-1} (3σ) detection limit within 60 seconds and was calibrated with an O_3 calibration source (2B Technologies Model 306 Ozone Calibration Source™). This instrument was not solely dedicated to the FC experiments but was connected to a snow tower experiment (Helmig et al., 2020), with one inlet dedicated to the FC experiments: samples were drawn sequentially at flows of typically ~ 1-2 slpm through a series of switching valves following a 2-hour duty cycle of 8 minutes measurements downstream the FC.

The meteorological data (Fig. **??**) and information were obtained from the IPEV/PNRA Project, "Routine Meteorological Observation at Station Concordia" (http://www.climantartide.it), using an automatic weather station (AWS – Vaisala Milos 520). The UV radiation was measured with a broadband UV radiometer (Kipp & Zonen – CUV 4, spectral range 305–385 nm) and the intensity of the UV radiation was similar within the experiments. SZA measurements were taken from ground-based SAOZ (Système d'Analyse par Observation Zénitale) as part of the Network for the Detection of Atmospheric Composition Change (NDACC) and the data are publicly available (see http://www.ndacc.org).

Flows were controlled using a piston membrane vacuum pump (Welch™ Standard Duty WOB-LTM Piston Vacuum Pump - Model 2534C-02) and two mass flow controllers (MKS – Mass Flow Controller 10 cm^3 min^{-1} and 10,000 cm^3 min^{-1} at standard conditions: 273.15 K / 1,015 hPa), also used for dilution of gas source NO_2 during multi-point calibration of the IBBCEAS on the field (0, 20, 30, 40, 80, 100, 125 and 150 nmol mol^{-1}). The NO_3^- concentration analysis was repeated twice on each snow samples using an Ion Chromatography (IC) system (Dionex™ ICS – 2000, Thermo Scientific) located in the station's laboratory, and snow density was calculated by gravimetry.

3.2.4 Sampling strategy

Concordia is a permanent research station on the Antarctic Plateau, and scientific activities occurring in summer regularly involve vehicles, implying possible pollution. For this reason, two types of snow were collected in order to study possible spatial variability: local snow, located in the station's clean area sector (Fig. 3.3) and snow qualified as pristine snow, located 25 km south of the station.

The same protocol was followed on each site: a pit (2 m long, 1 m wide, 1 m deep) was dug using clean shovels. The windward side was then cleaned over the entire depth of the pit. Using a small clean plastic shovel, isotherm boxes (scufa – 115 cm x 35 cm x 45 cm – cleaned prior sampling) were filled with snow and homogenized by mixing. Each site was sampled three times at different depths: 2-7 cm, 10-20 cm and 40-50 cm for the local snow and 2-7 cm, 10-20 cm and 30-40 cm for the pristine snow. Finally, a sample of drifted snow was collected in the clean area sector on the 2^{nd} of December 2019 during a windy episode, with wind speed of 8.07 ± 0.32 m s^{-1} (1σ) from 10:00 to 15:00 local time. Scufa boxes containing the homogenized samples were then stored in a snow cave in the dark at constant temperature (-55 °C). The estimated age of each snow sample, calculated following Picard et al. (2019) is reported in Table 3.1.

Table 3.1 – Ages of snow samples estimated from a mean snow accumulation in Dome C of ca. 8.7 cm per year, (Picard et al., 2019)

Type of Snow	Estimated age
Drifted Snow	-
2-7 cm Layer	≈ 3 months to 10 months
10-20 cm Layer	≈ 1 to 2.5 years
30-40 cm Layer	≈ 3.5 to 4.5 years
40-50 cm Layer	≈ 4.5 to 6 years

3.2.5 Typical experiment

Prior to the experiments, the empty chamber was cleaned by injecting O_3 (∼ 600 nmol mol^{-1}) for 12 hours followed by zero-air flushing for another 12 hours until reaching stable levels of NO_x, (0.068 ± 0.012) nmol mol^{-1}, corresponding to the chamber blank and close to the NO_2 sensitivity of the instrument (section 3.2.3). The snow samples contained in the scufa box was homogenized again and weighed once transferred in the chamber to obtain the density by gravimetry. 8.5 to 12.0 kg of snow were used to fill up the chamber. The densities calculated for each experiment ranging from 0.32 to 0.45 g cm^{-3} agreed well with previous observations (Gallet et al., 2011). A mechanical scale (TERAILLON Nautic) installed on a stable surface and leveled was used for the weighing of the snow before and after each experiment. A mean average loss of 1.1 % was measured representing about ∼ 100 g of snow sample. The losses observed are not significant in our case for the need of weight corrections. A total of eight snow samples (≈ 25 cm^3 each) were taken randomly in the chamber before the FC was sealed, for each experiment. The chamber was then buried in the snowpack, taking care to disturb the surrounding snow as little as possible, and connected to the zero-air flow. The production from the snow was then monitored continuously after the setup of the FC, for 2 to 4 days. To investigate the possibility of nitrate stratification and denitrification during the experiments, samples (≈ 25 cm^3 each) at 2 cm snow depth resolution were collected from the box after each experiment (4 samples for each 2 cm layer were taken resulting in 40 samples).

3.3 Data processing

The NO_x measurements from the IBBCEAS were corrected for the chamber blank (0.068 ± 0.012 nmol mol^{-1}) before being further processed for validation. A 2h-running mean was calculated and the standard deviation (σ_{mean}) was determined within the same window. The data falling beyond 2 x σ_{mean} were discarded, which resulted in less than 6 % rejection. Clouds passing by would impact NO_x and would not be detected as outliers. However, the radiative conditions were the same from one day to another during the FC experiments. The measurements were then averaged every 20 minutes, corresponding to the best performance of the instruments to achieve the ultimate NO_x detection limit of 30 pmol mol^{-1} (Barbero et al., 2020).

As mentioned in section 3.2.3, the O_3 inside the chamber was monitored using a UV Photometric O_3 analyzer (Thermo Scientific, Model 49i) connected by tubing to an automatic snow tower platform which housed the switching manifold and the analytical equipment. To eliminate the response time after the switching manifold, only the last three minutes of measurements, when concentrations reach steady-state, were used and averaged, giving one measurement of ozone concentration every 2 hours. The data were then interpolated linearly every 20 minutes to match the resolution of the NO_x measurements.

Snow nitrate concentrations were disregarded when the absolute value of the measurement $[NO_3^-]$ - $[NO_3^-]_{mean}$ was above two standard deviations (2σ). $[NO_3^-]_{mean}$ is the average of repeated measurements for the same sample. 11 % of the samples were rejected corresponding to 42 of 392 total samples.

3.4 Results and discussions

3.4.1 Snow nitrate content and NO_x gas phase mixing ratios

During the seven experiments, the O_3 excess with respect to the levels expected from the photochemical NO-NO_2-O_3 equilibrium through the Leighton relationship (Leighton, 1961), was not significant: from 0.7 to 10 nmol mol^{-1} (details of the calculations can be found in appendix A.3). Due to this insignificance, we concluded that the potential impact from ozone on our results was negligible, therefore, we decided that there was no need to discuss the ozone data.

Figure 3.5 shows the nitrate concentration in ng g^{-1} of snow measured in each snow sample before and after the experiments. Drifted snow was found to be up to 30 times more enriched in nitrate than the mean of all the rest of the snow samples, likely due to being blown and stirred by the strong wind (dark blue colors, Fig. 3.5). The pristine snow from the 25 km site shows a rapid decrease in nitrate concentrations with depth (red colors, Fig. 3.5), with less than 50 ng g^{-1} of nitrate remaining in the 30-40 cm layer, while local snow shows fairly uniform concentrations over the topmost 50 cm (green colors, Fig. 3.5).

The exponential decrease of nitrate concentration from the surface to depth is a common feature on the Antarctic plateau, determined by photolysis denitrification occurring in the photic zone. And indeed, the concentrations in the 25 km South snow samples are in agreement with previous observations taken at Dome C shortly after Concordia station construction (Erbland et al., 2013; France et al., 2011).

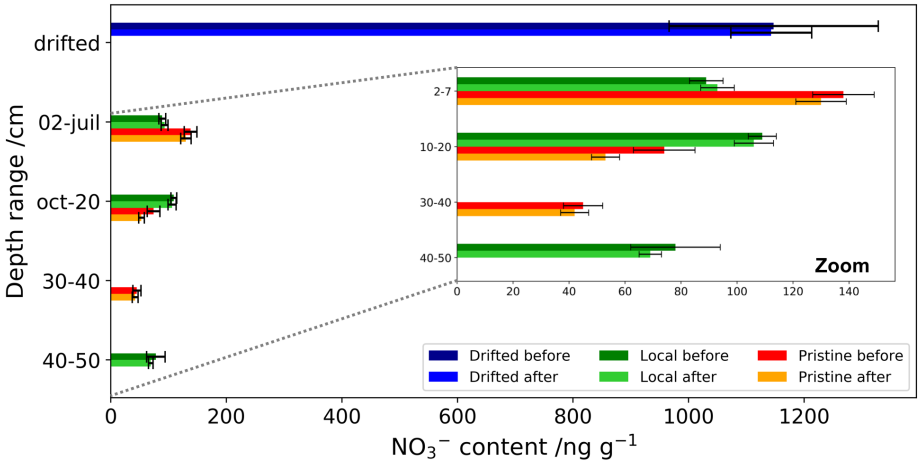

Figure 3.5 – Mixing ratio of NO_3^- contained in the snow [ng g^{-1} of snow] at the two sampling sites before and after the FC experiments. In blue colors, the drifted snow, in red colors, the pristine snow, i.e., 25 km South, and in green colors, the local snow. The error bars correspond to one standard deviation, $\pm 1\sigma$, over samples measurements: before experiment = average of 8 samples analyzed twice, and after experiment = average of 40 samples analyzed twice, both after data processing explained in section 3.3. The bottom layers at the two sampling sites do not match in depths due to a sampling error.

A part from the top layer sample, the local snow samples appeared enriched in nitrate compare to the pristine snow samples, phenomena probably due to site pollution as demonstrated by Helmig et al. (2020). Additionally, the local sampling area is known to have been very locally contaminated during the previous summer campaign of 2018-2019 by technical activity as shown on Figure **??** given in appendix A.5. Therefore, the results given by the local 2-7 cm layer sample, corresponding to a snow aged from the previous summer campaign, (Table 3.1), will be considered with caution.

As explained in section 3.2.5, four profiles were taken in the flux chamber after each experiment with a 2-cm resolution to observe a potential stratification that would have occurred during the experiments. Samples were analyzed twice with the IC system and the results are shown in Figure 3.6. The variability observed with depth for the four different profiles of each snow sample is lower than the standard deviation of the measurements. It is reasonable to state that no apparent stratification occurred during the experiments, thus sensible to conclude that our nitrate reservoir is constant.

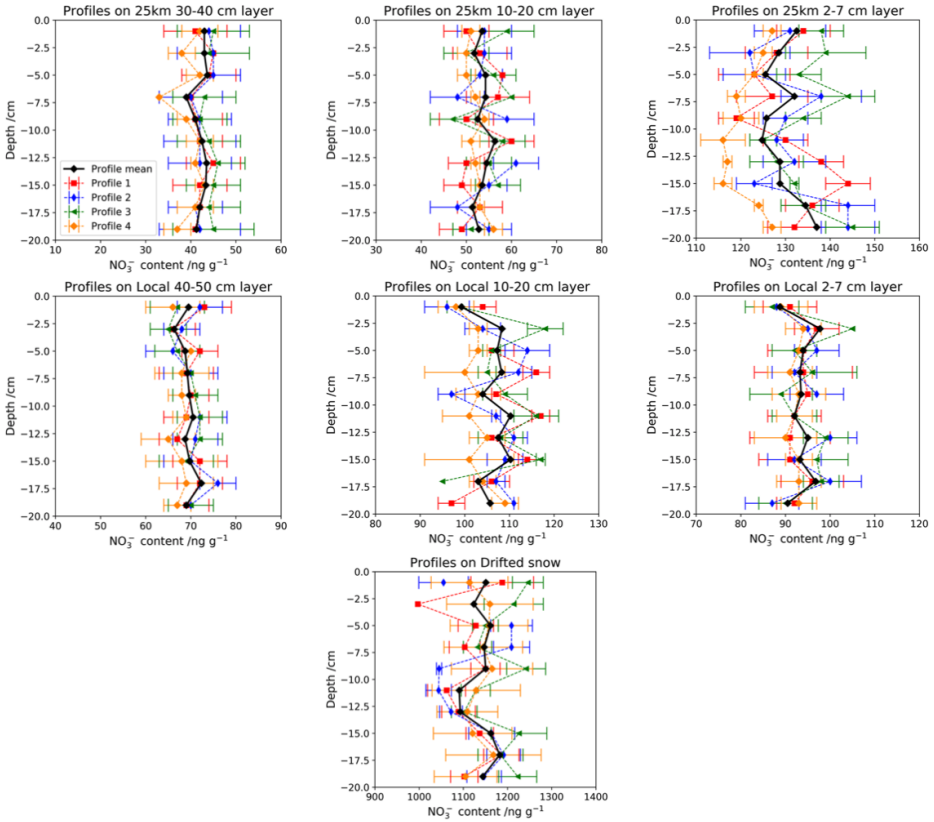

Figure 3.6 – NO_3^- profiles [ng g^{-1}] on the chamber depth for each experiment. Samples were collected with a 2-cm resolution and analyzed twice using the IC system. Blue, red, green and orange colors correspond to four different profiles collected at the end of each experiment, and black colors to the average profile. Error bars correspond to the standard deviation, 1σ, observed for each sample repetition analysis.

A strong diurnal variability in the NO_x production from the snow is observed for each experiment (Fig. 3.7), with a minimum around midnight and a maximum around local noon, following the daily UV radiation cycle. An apparent proportionality is observed between the nitrate concentrations contained in the snow samples and the amplitude of NO_x mixing ratios produced as a snow with 10 times the concentration of nitrate seems to produce 10 times more NO_x (Fig. 3.7). Secondly, an exponential decrease in NO_x mixing ratio during the experiments is also observed, potentially due the reservoir denitrification. Assuming one photolyzed molecule of NO_3^- produces one molecule of NO_x (reactions R3.1 to R3.5) the denitrification occurring during the experiments represents on average 0.12 ± 0.08 % of the initial amount of nitrate, therefore negligible with respect to the initial nitrate reservoir (more details are provided in the A.4).

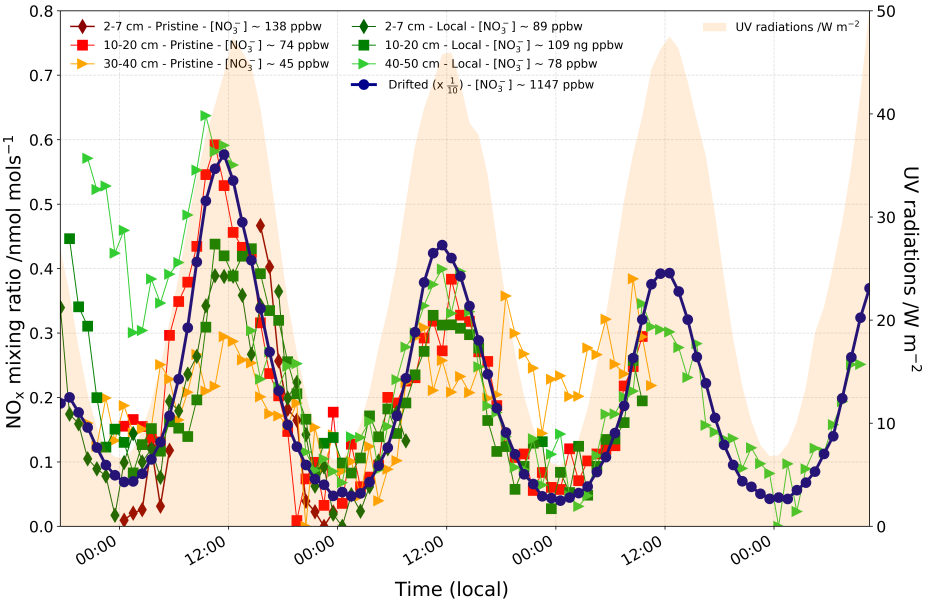

Figure 3.7 – NO_x gas phase mixing ratios measured downstream of the FC [nmol mol^{-1} of air], during FC experiments. Drifted snow mixing ratios (dotted blue curve) are divided by 10. Red colors represent the pristine snows, i.e., 25 km South, and green colors the local snows. The intensity of the UV radiation (305-385 nm) was similar within the experiments and the mean value is reported in the shaded orange area. The time is given as local time (UTC + 08:00) where local solar sun maximum is noon.

Two main patterns of temporal variations are observed for all experiments in Figure 3.7: an oscillation driven by the diurnal cycle of UV radiation, called steady-state regime in the following sections, to which is superimposed a slower exponentially decreasing trend with a maximum of NO_x mixing ratio on the first day, called the transitory regime. Below, both regimes are discussed separately. For the stationary regime, a comparison between the different experiments is made with the aim of better characterizing the nitrate photolysis. In a second part, the exponential decrease is studied within the same experiment in an attempt to explain the transitory regime.

3.4.2 Steady-state regime study

Flux chambers are a useful tool for directly measuring production rates of a defined sample. Combining their results with other observations could lead to the estimation of a flux area. On one hand, the instantaneous NO_x production, P_{NO_x} [molecules s^{-1}], can be calculated based on the measured NO_x mixing ratios, [NO_x] [mol mol^{-1}], and the air-flow passing through the chamber, F_{air} [cm^3 s^{-1}] corrected from the snow porosity n [unit-less], as described in Equation 3.3:

$$P_{NO_x} = [NO_x] \times F_{air} \times n \times \frac{PN_A}{RT} \tag{3.3}$$

with N_A Avogadro's Number (6.022 x 10^{23} molecules mol^{-1}); R, the ideal gas constant (82.06 cm^3 atm mol^{-1} K^{-1}); and P and T taken from the meteorological conditions at Dome C (section 3.2.1).

On the other hand, our experiment works as pseudo-first order kinetic where nitrate concentration, $[NO_3^-]$ [g g^{-1} of snow] is assumed to be constant and NO_x production, P_{NO_x}, is only driven by the photolysis rate constant $J_{NO_3^-}$ [s^{-1}], following Equation 3.4:

$$P_{NO_x} = J_{NO_3^-} \times [NO_3^-] \times m_{snow} \times \frac{N_A}{M_{NO_3^-}} \tag{3.4}$$

with $M_{NO_3^-}$ = 62.0049 g mol^{-1} the molar mass of NO_3^-; and m_{snow} [g] the mass of snow sample.

An estimation of the maximum instantaneous P_{NO_x} at local noon for each experiment is made using Equation 3.3, taking the last day of each experiment as the most representative of the steady-state regime. The results for the maximum NO_x production, $P_{NO_{x-max}}$ [molecules s^{-1}], as well as the results from measurements carried out at Neumayer II Atmospheric Observatory (70°38'S, 8°15'W, 40 m a.s.l) in summer 1997 Jones et al. (2000), are reported in Table 3.2.

Table 3.2 – Calculated $P_{NO_{x-max}}$ [x 10^{11} molecules s^{-1}] from Equation 3.3 at solar noon.

Pristine snow samples				Local snow samples				Neumayer* snow sample			
Sampling depth	NO_3^- [ng g^{-1}]	$P_{NO_{x-max}}$	Day	Sampling depth	NO_3^- [ng g^{-1}]	$P_{NO_{x-max}}$	Day	Sampling depth	NO_3^- [ng g^{-1}]	$P_{NO_{x-max}}$	Day
30-40 cm	45	1.44	16/12/2019	40-50 cm	78	2.71	13/12/2019	0-20 cm	50	0.31	22-23/02/1999
10-20 cm	74	3.38	06/01/2020	10-20 cm	109	3.34	03/01/2020				
2-7 cm	138	4.05	24-25/12/2019	2-7 cm	89	1.70	22/12/2019				
				drift	1,147	42.82	30/12/2019				

* From Jones et al. (2000) experiment on a 20 cm x 20 cm x 20 cm block

The NO_x production of the FC experiments is proportional to the nitrate concentration initially present in the snow samples as shown in Table 3.2, where linear regression for the pristine snow shows an R^2 = 0.691; and, excluding the local 2-7cm layer, the linear regression for the local snow shows an R^2 = 0.999 (0.659 without the drift sample), note that the linear regressions were calculated with their intercepts forced at zero. This is consistent with previous finding (e.g., Grannas et al. (2007)). The local snow sample at 2-7 cm depth exhibits a lower NO_x production, and we strongly suspect that this sample contained absorbing contaminants emitted by the station activities (more details can be found in appendix A.5). The NO_x production of snow with similar nitrate concentrations, calculated over one day, is very similar for different snow sources (Fig. 3.8).

It can be observed that for two different types of snow of the Antarctic Plateau, the NO_x production is very similar (green triangles and red squares, Fig. 3.8). However, such similarity in production does not exist when it is compared with the Neumayer experiment (Jones et al., 2000), which was located on the western coast of Antarctica but at similar latitude (70 °S) as Concordia station (75 °S) (solid blue circles, Fig. 3.8). Additionally, the conditions of the Neumayer experiment were different to what was done for this study with the FC experiments. At Neumayer, a snow block of 0.01 m^3 was placed 1 m above the snow surface and exposed to sun light but also to air ventilating all around the block (Jones et al., 2000). As shown in Figure 3.8, daily mean NO_x production rates from snowpack photolysis are a factor of 10 higher than the values from Jones et al. (2000), which is likely induced by differences in experimental set-up but also in the NO_x snow sources and photolytic mechanisms, i.e., differences in radiation fluxes, between East and West Antarctica.

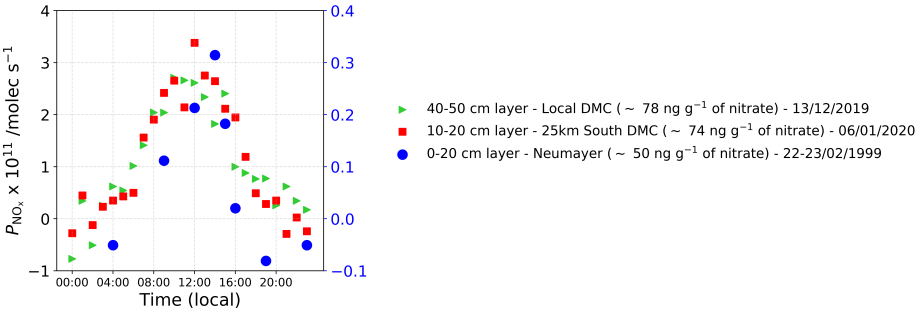

Figure 3.8 – Comparisons of the diurnal variability of snowpack NO_x production rates at different locations for similar nitrate concentrations snows on the Antarctic Plateau: local snow (40-50 cm deep – Concordia station clean area – green triangles, $[NO_3^-] \sim 78$ ng g^{-1}), pristine snow (10-20 cm deep – 25 km south from Concordia station – red squares, $[NO_3^-] \sim 74$ ng g^{-1}) on the left-hand scale; and measurements over the western coast of Antarctica (blue dots, $[NO_3^-] \sim 50$ ng g^{-1}), on the right hand-scale.

The maximum P_{NO_x} observed at Dome C was around 4.0 x 10^{11} molecules s^{-1} while Neumayer's maximum was ~ 0.3 x 10^{11} molecules s^{-1} for similar UV radiations and snow nitrate concentration. As mentioned previously, the major difficulty in performing the measurement of NO_x fluxes is related to the fact that the latter depends on both transport and photochemical production. Indeed, measurements above snow of NO_x fluxes represent a net flux, thus include contributions from transport and chemical sinks or sources. Our FC design experiments are insensitive to the transport component. Therefore, this ~ 10 times difference observed at noon could be due, not only to the location of the snow (Coast vs Plateau, West vs East) and to the different actinic flux due to different concentrations of snow impurities, but also to this transport component. In addition, Jones et al. (2000) did not observe any change in the nitrate concentration after 50 hours of experiment, which supports our conclusion that the nitrate reservoir in the snowpack cannot be photolytically depleted within few hours to few days. Additionally, the snow grain specific surface area (SSA) cannot explain the observed difference in NO_x production (Table 3.2) between the samples. Indeed, at a depth of 20 cm there was a maximum actinic flux difference of ~ 40 % between the most scattering snow (drifted snow) and the least scattering snow (40-50 cm local snow), Figure 3.10, which is lower than the observed production differences between the samples.

To estimate the photolysis rate coefficient, $J_{NO_3^-}$ [s^{-1}], Equations 3.3 and 3.4 are combined and derived to produce Equation 3.5.

$$J_{NO_3^-} = \frac{P_{NO_x} \times M_{NO_3^-}}{[NO_3^-] \times m_{snow} \times N_A} \tag{3.5}$$

with P_{NO_x} [molecules s^{-1}], the NO_x production calculated from Equation 3.3; $M_{NO_3^-}$ [g mol^{-1}], the molar mass of NO_3^-; $[NO_3^-]$ [g g^{-1} of snow], the amount of nitrate measured in the snow sample; m_{snow} [g], the mass of the snow sample; and N_A [molecules mol^{-1}], Avogadro's number. Results for the steady state regime, i.e., last day of each experiment, are presented in Figure 3.9.a. The propagated error from the individual measurement uncertainties are within two times the standard deviation of the calculated values (2σ) for each calculated diurnal $J_{NO_3^-}$.

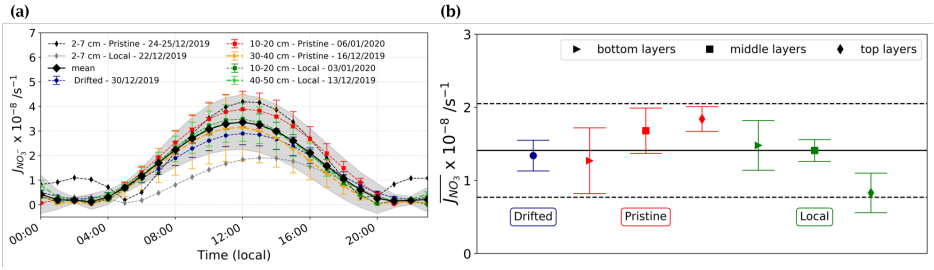

Figure 3.9 – **(a)** $J_{NO_3^-}$ calculated for each experiment. Dark blue dot represents the drifted snow, red color the pristine snow samples, i.e., 25 km South of Concordia station, and green color the local snow samples. Triangles represent the bottom layers (30-40 cm or 40-50 cm), squares the 10-20 cm layers and diamonds the 2-7 cm layers. The mean ± 2σ is represented by the black diamond and the shaded area and has been calculated from the experiments, excluding the top layers due to: 1) the local top layer is suspected to be locally contaminated; 2) the $J_{NO_3^-}$ of the pristine top layer was reconstructed due to missing data. **(b)** $\overline{J_{NO_3^-}}$ calculated for each experiment. Dark blue dot represents the drifted snow, red color the pristine snow samples, i.e., 25 km South of Concordia station, and green color the local snow samples. Triangles represent the bottom layers (30-40 cm or 40-50 cm), squares the 10-20 cm layers and diamonds the 2-7 cm layers. The mean ± 2σ calculated from all the experiments, is represented by the solid and dashed black lines.

On Figure 3.9.b are shown the daily average photolysis rate coefficients for each experiment, $\overline{J_{NO_3^-}}$ [s^{-1}]. With the exception of the local snow sample at 2-7 cm depth suspected to have been polluted by the station activities, the rest of the measurements lies within the estimated uncertainties, and a mean (± 1σ) $\overline{J_{NO_3^-}}$ of (1.50 ± 0.22) x 10^{-8} s^{-1} was found for the 0-20 cm snow layer from the 10/12/2019 to the 07/01/2020, to which further 58 % are added to include 3 *e*-folding depths, leading to a daily (± 1σ) $\overline{J_{NO_3^-}}$ of (2.37 ± 0.35) x 10^{-8} s^{-1} over the entire photic zone (0-50 cm) for the same period. Those results suggest the same photolysis rate constant for different types of snow and snow ages as their $\overline{J_{NO_3^-}}$ range from (1.27 ± 0.55) x 10^{-8} s^{-1} (16/12/2019) to (1.84 ± 0.17) x 10^{-8} s^{-1} (26/12/2019). Additionally, the lifetime of NO_3^- in the chamber against loss by photolysis can be calculated as $\tau_{NO_3^-_{photolysis}} = \frac{1}{\overline{J_{NO_3^-}}}$, (Winton et al., 2020; Zatko et al., 2016), and is ranging from 2 to 4 years for our FC experiments, much longer than our experiment's duration.

Using the TARTES (Two-streAm Radiative TransfEr in Snow model) optical radiative transfer model (Libois et al., 2013, 2014) coupled with the SBDART (Santa Barbara DISTORT Atmospheric Radiative Transfer) model (Ricchiazzi et al., 1998)) we calculated a theoretical $\sigma_{NO_3^-}(\lambda,T)\phi(T,pH)$ product. Assuming that the black carbon in the snow at Dome C varies between 1 and 5 ng g^{-1} (France et al., 2011) and that it represents all impurities in the model, a $\sigma_{NO_3^-}(\lambda,T)\phi(T,pH)$ product ranging from 1.36 x 10^{-23} to 1.84 x 10^{-23} cm^2 $photon^{-1}$ is necessary to estimate a $\overline{J_{NO_{3-modeled}}}$ ranging from 2.02 x 10^{-8} s^{-1} to 2.72 x 10^{-8} s^{-1}, i.e., within the 1σ of our observed $\overline{J_{NO_3^-}}$, for $300 < \lambda < 340$ nm. In gas phase photochemistry, the quantum yield ϕ corresponds to the ratio between the number of dissociations produced and the number of absorbed photons. Nitrate photolysis quantum yield from 0.0015-0.0052 molecules $photon^{-1}$, was measured by Chu and Anastasio (2003) on nitrate in ice, and used by Zatko et al. (2016) for the NO_x production, but values up to 0.6 molecules $photon^{-1}$ have been measured for HNO_3 adsorbed on ice films in laboratory experiment (Zhu et al., 2010).

These disparities are explained by the difficulty, in heterogeneous phase, to define the quantum yield as there is a great diversity of effective absorption cross-sections, which directly influences its calculation. Therefore, it is preferable, in our case (snow-air chemistry), to estimate experimentally the product $\sigma\phi$. In our approach, the use of FC to infer a $\sigma\phi$ product allows to check different snow types, depths and ages and permits to circumvent the uncertainty in both individual terms for NO_3^- on ice, which is needed for models.

Assuming a constant nitrate reservoir as discussed previously, the NO_x production would therefore be a process only driven by the amount of nitrate accessible to the photolysis. Because drifted snow (young) and snow collected in depth (old) possess the same photolysis rate under the same incident light flux despite showing radically different nitrate concentrations, it can reasonably be concluded that nitrate has the same accessibility to photolysis. This implies similar $\sigma_{NO_3^-}(\lambda,T)\phi(T,pH) = (1.60 \pm 0.34)$ x 10^{-23} cm^2 $photon^{-1}$ (1σ) (with $300 < \lambda < 340$ nm). Using Chu and Anastasio's (2003) nitrate ion cross-section of 1.20 x 10^{-20} cm^2 $molecules^{-1}$, we calculated $\phi(T,pH) \approx 0.0013 \pm 0.0003$ (with $300 < \lambda < 340$ nm) for the measurement period (10/12/2019 to 07/01/2020), which is three times lower than the value usually used in the models. This contradicts previous studies of Davis et al. (2008) and Meusinger et al. (2014) which proposed two nitrate domains: an easy photolabile nitrate fraction (i.e., adsorbed on the surface of ice) and a more difficult to successfully photolyze fraction (i.e., incorporated within the ice crystal lattice). However, our observations are consistent with Bock et al. (2016) and Chan et al. (2018) which proposed a single mechanism responsible for the incorporation of nitrate in the snow at cold sites such as Dome C.

3.4.3 Transitory regime study

The transitory regime represents the decreasing exponential trend observed over the few days of the FC experiments, with a maximum of NO_x gas phase mixing ratios the first day observed in Figure 3.7. NO_x productions decrease from one day to the next with no special pattern observed between the experiments: for the drifted snow, $(\frac{\Delta P_{NO_x}}{P_{NO_x}})$ represents ~ 22 % for day 1 to day 2 and ~ 12 % for day 2 to day 3 while it represents ~ 48 % and ~ 21 % for the local 40-50 cm layer, respectively, both with an exponential time constant of 22 hours. The total NO_x production ($P_{NO_{x-tot}}$) observed in Figure 3.7 can be expressed as the sum of the steady state regime production ($P_{NO_{x-steady}}$) and the transitory regime production ($P_{NO_{x-trans}}$), Equation 3.6. Although the hypothesis of two types of nitrate was disregarded in section 3.4.2 because it is not compatible with our findings, where and older snow presents similar photolysis rate coefficient as a younger snow, we still want to question if this transient regime could be produced by a minor family of nitrate that could be depleted more rapidly than the bulk nitrate. Therefore, the hypothesis of two nitrate populations is explored with $P_{NO_{x-steady}}$ already discussed in section 3.4.2.

$$P_{NO_{x-tot}} = P_{NO_{x-steady}} + P_{NO_{x-trans}} \tag{3.6}$$

$P_{NO_{x-trans}}$ is calculated as a function of $J_{NO_3^-{}_{trans}}$ and $N_{NO_{3^-_{trans}}}$, following Equation 3.1 and expressed here by Equation 3.7:

$$P_{NO_{x-trans}} = J_{NO_3^-{}_{trans}} N_{NO_{3^-_{trans}}} \tag{3.7}$$

We hypothesize that the nitrate photolysis rate at the transitory regime $J_{NO_3^-{}_{trans}}$ varies with time and depends on a variety of parameters represented in Equation 3.2. However, in this experiment, the $\sigma_{NO_3^-}(\lambda)\phi(\lambda,T,pH)$ product is considered constant as the experiments were carried out under

the full natural sunlight spectrum and similar temperature diurnal cycle from one day to the next during the experiments. The snow pH is considered to be around 5 and constant over those layers. Furthermore, $I_{act}(\theta, \psi, \lambda, z)$ is considered only θ and ψ dependent as the measurements are integrated over the chamber's depth and under the full spectrum. There is no indication that the actinic flux varies substantially from one day to the next within the chamber's depth; thus, the radiative conditions were the same from one day to another (good weather, homogeneous snow layer, slow metamorphism) and a $J_{NO_{3^-trans}}$ that varies from one day to another cannot explain the decrease in NO_x mixing ratios observed for each experiment. Therefore, there are no reasons for a varying $J_{NO_{3^-}}$ from one day to the next within the same experiment and $J_{NO_3^-}$ can be calculated as an integrated parameter over depth and wavelength, Equation 3.8:

$$J_{NO_3^-}(\lambda) = \sigma_{NO_3^-}\phi \int_{(\theta,\psi)} I_{act}(\theta,\psi) d\theta d\psi \tag{3.8}$$

It is possible that a thin surface layer is denitrified much faster due to a phenomenon of amplification of the photolysis in this layer, (Traversi et al., 2017), but that was not captured with a coarse sampling resolution of 2 cm. Simpson et al. (2002) modelled the ratio of the in-snow actinic flux to the incident down-welling actinic flux as a function of extinction optical depth (proportional to depth for homogeneous snow) within the snowpack. Snow increases the actinic flux within the topmost layers of the snowpack, due to the high albedo in the UV region. The actinic flux at the snow surface is equal to the atmospheric actinic flux above the snow, whereas in the first few mm, depending on SZA, the actinic flux is either increased or decreased. For SZA = 0°, the actinic flux is enhanced by the conversion of direct light to diffuse light (Chan et al., 2015). Madronich (1987) argued that the maximum enhancement factor is four times higher than the incident actinic flux.

Using the TARTES optical radiative transfer model, relative actinic fluxes for each snow samples at 305 nm were simulated (Fig. 3.10), using specific surface area (SSA) as a function of snow depth following Gallet et al. (2011). No significant differences between the up-welling and the down-welling irradiance are observed (solid orange curve and dotted dashed green curve, Fig. 3.10), making the travel of the light nearly isotropic within the snowpack (i.e., the same properties in every direction), even near the surface. The actinic flux is thus relatively smooth and ranges between 1.2 and 2.8 times the flux received by the snowpack at 305 nm for the 0-20 cm layer. This variation range is far too small to explain a localized layer with highly photolabile nitrate that would be depleted over the three days of the experiment given the initial abundance of nitrate in all the samples. Moreover, old snows of 6-year-old should not experience such a transitory regime as the $\tau_{NO_{3^-photolysis}}$ for those samples were calculated to be ≈ 2 to 4 years (section 3.4.2). This leaves the hypothesis of a strong denitrification.

In section 3.4.1, it has been demonstrated that the NO_x production scales with the nitrate concentration in the snow samples. Logically, a decrease in NO_x production will imply a decrease in nitrate concentrations of the same amplitude which was not observed (section 3.2.5). Expected NO_3^- losses were calculated for each experiment using Equation 2 from Meusinger et al. (2014), $J^* = -ln\left(\frac{[NO_3^-]_{after}}{[NO_3^-]_{before}}\right)\frac{1}{t_{photolysis}}$, with $t_{photolysis}$ [s] the experiments duration; [NO_3^-] [molecules cm^{-3} of snow] the concentrations before and after the experiments; and J^* [s^{-1}] the apparent photolysis rate constant, calculated in section 3.4.2. NO_3^- losses were expecting to be ranging from 0.11 to 4.94 ng g^{-1}, which was not detectable with our IC measurements as it falls below the instrumental precision (Fig. 3.5): the least concentrated snow was measured at 45 ± 7 ng g^{-1} and the most

concentrated snow at 1.15 ± 0.18 µg g^{-1}. As the whole thickness of a snow sample undergoes the same exponential I_{act} decrease, and the photolysis rate constant does not depend on the snow age nor location and that no change in nitrate concentration has been observed within the measurement uncertainty, it is difficult to explain this decrease from a variability of $[NO_3^-]_{trans}$ or $J_{NO_{3^-trans}}$. Thus, we conclude that this transitory regime is potentially due to an experimental interference or artefact.

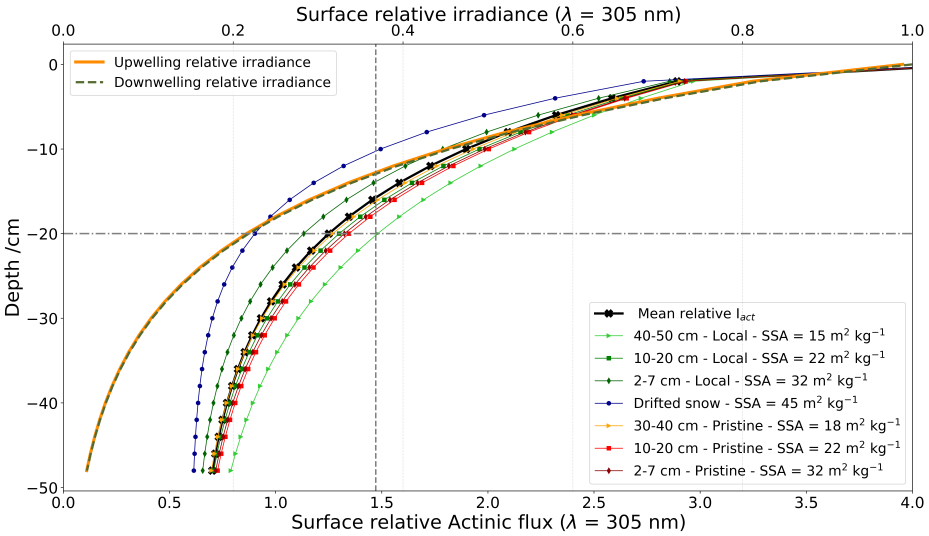

Figure 3.10 – Simulated surface relative actinic fluxes and irradiance for each experiment using TARTES model at 305 nm. The actinic flux describes the number of photons incident at a point, while the irradiance describes the radiant energy crossing a surface. Dotted horizontal line represent the depth of the chamber while the vertical dotted line represents the *e*-folding depth, 20 cm for the 40-50 cm local snow sample and ~ 12 cm for the drifted snow. Note that surface relative Actinic flux is referenced to the enhanced layer a few mm below the surface, explaining the factor 4.

The adsorption of nitric acid (HNO_3) on the walls of the chamber during the installation of the experiment could be an explanation. Zhu et al. (2008) determined the absorption cross-sections of surface-adsorbed HNO_3, noted $HNO_{3-adsorbed}$, in the 290-330 nm region using cavity ring-down spectroscopy. They found that the $HNO_{3-adsorbed}$ absorption cross-section at 305 nm was (1.09 ± 0.17) x 10^{-18} cm^2 $molecules^{-1}$. This makes the absorption cross-section of $HNO_{3-adsorbed}$ ~ 700 times higher than that in the gas phase (HNO_{3-gas}): (1.68 ± 0.19) x 10^{-21} (Zhu et al., 2008), 1.50 x 10^{-21} (Burkholder et al., 1993) and 1.45 x 10^{-21} cm^2 $molecules^{-1}$ at 305 nm (Rattigan et al., 1992). Chu and Anastasio (2003) measured the absorption cross-section of the nitrate ion around 1.2 x 10^{-20} cm^2 $molecules^{-1}$ at Dome C. Therefore, with a cross-section of $HNO_{3-adsorbed}$ about 10^2 times greater than the absorption cross-section of the nitrate ion, the observed exponential decay could indeed be caused by the $HNO_{3-adsorbed}$ on the chamber's walls during the experiments set-up. Additionally, Rajeswari et al. (2016) studied the removal of nitrate ion from aqueous solution and the results obtained in their study illustrate the high adsorption capacity of ion nitrate on polymeric materials. It seems therefore reasonable to estimate similar levels $HNO_{3-adsorbed}$ on PMMA

material. A simple calculation giving the number of molecules of $HNO_{3-adsorbed}$ on the chamber's walls needed to produce the amount of NO_x observed in the transitory regime, called $NO_{x-trans}$, support this hypothesis: 1.02 x 10^8 to 3.12 x 10^{10} molecules cm^{-2} of $HNO_{3-adsorbed}$, corresponding to 0.02 to 7.22 ppt, would be needed to produce this $NO_{x-trans}$ trend by its photolysis destruction. The lifetime of NO_3^- from $HNO_{3-adsorbed}$ in the chamber ranges from 5 to 13 minutes with a enhanced $J_{NO_3^-trans}$ and assuming that all molecules of $HNO_{3-adsorbed}$ are photolized. Furthermore, Crowley et al. (2010) defined the adsorption equilibrium of HNO_3 on ice, and, for Dome C conditions, an estimation of 14 x 10^{12} molecules cm^{-2} has been established. Therefore, the removal of $HNO_{3-adsorbed}$ would be 1,000 times higher, between approximately 2 to 27 days, making the hypothesis of atmospheric HNO_3 adsorbing on the PMMA walls of the chamber, plausible.

Another hypothesis can also be addressed: the storage of the snow samples before running the FC experiments could as well be involved. As mentioned in section 3.2.4, the snow samples were stored in a snow cave, in the dark and at constant temperature (-55 °C) for many days. Therefore, it would be possible that mobile species, surface-adsorbed on the walls of the isotherm boxes during sampling had diffused to the surface during storage. Thibert and Dominé (1998) give a parameterization to estimate the diffusion coefficient of HNO_3 in ice as a function of T: $D = 1.37 \times 10^{\frac{-2610}{T}}$ [$cm^2\ s^{-1}$]. D = 1.5 x 10^{-12} $cm^2\ s^{-1}$ in our conditions.

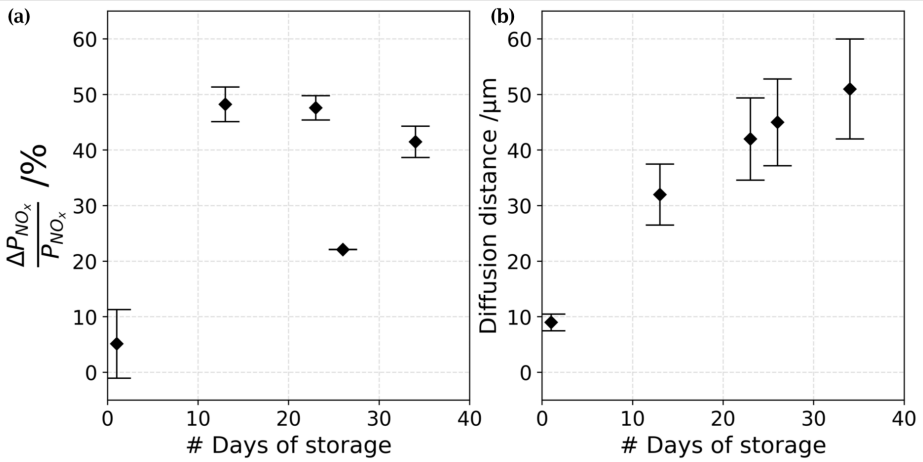

Figure 3.11 – **(a)** % of NO_x production decrease as a function of the number of days the sample stayed in storage and **(b)** Estimation of the distance (μm) that HNO_3, adsorbed on the walls, could have travelled in the isotherm box at -55 °C.

The snow samples in their isotherm boxes were stored from 1 to 34 days at most, and the ratio $\frac{\Delta P_{NO_x}}{P_{NO_x}}$ from day 1 to day 2 might seem related to the number of days it stayed in the storage cave, Figure 3.11.a. An estimation of the distance that HNO_3, adsorbed on the walls, could have travelled at -55 °C in the snow samples during the storage is calculated using Equation 3.9.

$$x = \sqrt{q_i D t} \tag{3.9}$$

with x [cm] the mean distance from the starting point that the molecule will have diffused in time t (diffusivity); q_i a numerical constant which depends on dimensionality (q_i = 2, 4, or 6, for 1, 2, or 3 dimensional diffusion), here q_i = 6 since the molecule is diffusing in every direction; D [$cm^2\ s^{-1}$] the diffusion coefficient previously mentioned and t [s] the storage time. A range of 5-50 μm was found at -55 °C (258 K) (Fig. 3.11.b).

With the available data, both theories proposed to explain the observed transitory regime, i.e., HNO_3 surface adsorption during the experiments set-up and/or HNO_3 desorption in the snowpack, could agree with the observations. More experiments with different storage times and longer NO_x gas phase mixing ratios monitoring may be helpful to support our hypothesis. Also, the flushing of the interstitial air contained in the snow samples could be a cause of this transitional regime, and to eliminate this unknown, the answer of monitoring instrument to NO_2 spike tests would help identify possible "dead-air" pockets that may form in the chamber and result in this transitory regime observation. Note that this does not question the previous conclusions of section 3.4.2 as the hypothesis explored tend to confirm an experimental artifact during the set-up of our FC experiments.

3.4.4 NO_x flux estimates and implications on the Antarctic Plateau

By using open circuit FC with clean air flow injection, instantaneous production can be measured and an estimated average daily production can be obtained. The next step is to estimate the flux per unit of surface area. NO_x flux is estimated at Dome C and an extrapolation to the entire Antarctic continent is proposed in order to obtain a continental N-budget.

3.4.4.1 Estimated NO_x flux at Dome C during the observation period

NO_x flux is defined as the NO_x production per surface unit area. From Equations 3.3 and 3.4, the production was estimated for each experiment and a relatively constant daily $\overline{J_{NO_3^-}}$ of (2.37 ± 0.35) x 10^{-8} s^{-1} (1σ) was found for a 50 cm snow thickness. In order to estimate the NO_x flux during the observation period at Dome C, Equation 3.10, a representative NO_3^- concentration in the snowpack is needed. Monthly snow pits at Dome C have been sampled for several years through the programs NITEDC and CAPOXI. A total of 33 measurements from snow pits taken at Dome C during the summer months from 2011 to 2019 were averaged to match the observation period of the FC. This provided a robust estimate of the average nitrate concentration in the first 50 cm of the snowpack for Dome C to 108 ± 8 ng g^{-1} (more information in appendix A.6).

$$F_{NO_x} = \int_z^0 \overline{J_{NO_3^-}}[NO_3^-]\frac{\rho_{snow} N_A}{M_{NO_3^-}} dz \tag{3.10}$$

with $\overline{J_{NO_3^-}}$ [s^{-1}] the daily photolysis rate constant; z = -50 cm; and [NO_3^-] [$g\ g^1$] the nitrate concentration of the photic zone. With a snow density of 0.344 ± 0.001 g cm^{-3} for a 0-50 cm layer (Gallet et al., 2011), a daily F_{NO_x} of (4.3 ± 1.2) x 10^8 molecules cm^{-2} s^{-1} was calculated for the entire photic zone at Dome C during the observation period.

Previous estimations of snowpack emissions at Dome C are ~ 1.5 to 7 times higher than what is estimated in this work (Table 3.3) with a daily photolysis rate constant 12 % to 19 % lower than the one used by Frey et al. (2015). Frey et al. (2015) scaled $J_{NO_3^-}$ computed with TUV to observations of $J_{NO_3^-}$ from a spectral radiometer.

Table 3.3 – Daily NO_x Flux estimates from observations at Dome C

References	F_{NO_x} [x 10^8 molecules cm^{-2} s^{-1}]	$\overline{J_{NO_3^-}}$ [x 10^{-8} s^{-1}]	Observations Period	Location
Frey et al. (2013)	6.6	-	23/12/2009 - 12/01/2010	Dome C
Frey et al. (2013)	8.2 ± 7.4	-	22/12/2009 - 28/01/2010	Dome C
Frey et al. (2015)	9.4	-	01-08/12/2011	Dome C
Frey et al. (2015)	31	2.93	09-22/12/2011	Dome C
Frey et al. (2015)	13	2.68	23/12/2011 - 12/01/2012	Dome C
This work (2021)	**4.3 ± 1.2**	**2.37 ± 0.35**	**10/12/2019 - 07/01/2020**	**Dome C**

Additionally, Frey et al. (2013, 2015) used observed profiles of $J_{NO_3^-}$ and $[NO_3^-]$ and not an average value over the photic zone. Table 3.4 hereafter highlights the disparity of the daily average $\overline{F_{NO_x}}$ estimated from field observations and models at both poles.

Because of lower likelihood of chemical loss during transport or of potential dilution, $\overline{F_{NO_x}}$ from FC experiment were expected to be larger than the above snow measurements. The *e*-folding depth of the snow samples may be different after the mechanical homogenising, and a smaller *e*-folding depth would lead to a lower NO_x production therefore lower flux estimation. Using a snow block with intact stratigraphy would allow to reduce the uncertainties on the conversion of P_{NO_x} to F_{NO_x}.

Additionally, FC air flow may be only through preferential pathways in the interconnected pore space of the snow matrix, which would result also in a smaller P_{NO_x}. A tracer spike test (e.g. NO_2) would allow to characterise the sample and constrain porosity. However, here we report for the first time the $\overline{F_{NO_x}}$ estimate using our FC approach at Dome C Table 3.3, and the results from our approach and the flux gradient method (Frey et al., 2013, 2015) fall within the same order of magnitude, confirming the usefulness of the FC approach.

A combined experiment of in-snow dynamic FC, as described in this work, with surface-snow dynamic FC, as described in Figure 1 of Ma et al. (2020b), would allow to better estimate NO_x production from the snow-pack and the resulted F_{NO_x} released at the surface. Indeed, P_{NO_x} could be used directly in snowpack-air models, which simulate realistic in-snow transport, allowing the community to overcome the difficulty of the quantum yield estimation by directly using the $\sigma\phi$ product from the FC.

Table 3.4 – Polar NO_x net fluxes measured above the snow surface in molecules cm^{-2} s^{-1}

	Direct measurement				Model-derived			
	$\overline{F_{NO_x}}$ [x 10^8 molecules cm^{-2} s^{-1}]	Period	Site	Ref	$\overline{F_{NO_x}}$ [x 10^8 molecules cm^{-2} s^{-1}]	Period	Site	Ref
Antarctica	1.3	Feb. 1999	Neumayer	Jones et al. (2001)	3.2 - 4.2	Dec. 2003	South Pole	Wang et al. (2007)
	3.9 ± 0.4	Nov. 2000	South Pole	Oncley et al. (2004)	3.2 - 17	Jan.	Dome C	Zatko et al. (2013)
	2.42 ± 50 %	Jan. 2005	Halley	Jones et al. (2011)	3.3 - 22	Jan.	South Pole	Zatko et al. (2013)
	1.7	Summer 2005	Halley	Bauguitte et al. (2012)	3.5	Summer 2005	Halley	Bauguitte et al. (2012)
	8.2 ± 7.4	Jan. 2010	Dome C	Frey et al. (2015)				
	25 ± 8	Dec. 2011	Dome C	Frey et al. (2013)				
	42.5	Dec. 2008	WAIS Divide	Masclin et al. (2013)				
	4.3 ± 1.2	**Dec. 2019**	**Dome C**	**This work (2021)**				
Arctic	2.5	Summer 2000	Summit	Honrath et al. (2002)	13 - 28	Jan.	Summit Pole	Zatko et al. (2013)
	≥ 6.7	Apr. 2004	Alert	Beine et al. (2002)				

3.4.4.2 Annual NO_x budget extrapolated to the continent

The chemical reactivity of the snowpack and its connection to the overlying oxidative atmosphere is key to understand how it influences the polar environment. A better estimation of the interactions between the snowpack and NO_x emissions offers the perspective of quantifying its importance on a continental scale. Several studies agree that nitrate concentrations in the Antarctic snowpack are generally constant from the coast into the plateau (Becagli et al., 2004; Shi et al., 2018b,a; Winton et al., 2020). Therefore, the average $[NO_3^-]$ measured at Dome C on the 0-50 cm layer, 108 ± 8 ng g^{-1}, can be taken as a fair approximation for the entire Antarctic continent.

To estimate an annual N-budget for the continent, the daily production of NO_x must be calculated for each day of the year. As shown by Equations 3.2 and 3.8, J is also a function of SZA, θ affecting the position of the sun over the year, and the sun declination, ψ controlling the length of the day of each day over the year. The term ψ, difficult to be analytically resolved (Finlayson-Pitts and Pitts, 2000b), can be approached by calculating it relatively to a reference day, in our case, the 30^{th} of December. here, we used the ratio $L_{day-i} : L_{day-ref}$ with L_{day-i} being the day duration of a day of interest and $L_{day-ref}$ the length of the reference day (more details on the calculation are found in appendix A.7).

In addition, the variability of the SZA, associated to the maximum amplitude of the NO_x production, should be considered in the extrapolation and it is represented here by a cosine ratio of the solar noon sun's position for the day of interest over the one of reference. This calculation is deduced by Equation 3.11 hereafter (Finlayson-Pitts and Pitts, 2000b; Forsythe et al., 1995).

$$P_{NO_{x-year}} = [NO_3^-]_{mean} V_{cont} \sum \overline{J_{NO_{3^-ref}}} \frac{L_{day-i}}{L_{day-ref}} \frac{\cos(\theta_i)}{\cos(\theta_{ref})} \tag{3.11}$$

θ_i is taken from NDACC and $\overline{J_{NO_{3^-ref}}}$ is (2.37 ± 0.35) x 10^{-8} s^{-1} (1σ).

The annual Antarctic continent NO_x budget from the nitrate snow-source calculated from Equation 3.11 is (0.073 ± 0.017) Tg(nitrate) y^{-1}, or (0.017 ± 0.003) Tg·N y^{-1}. This is a small source on a global scale compared to natural sources, such as biomass burning (7.1 Tg·N y^{-1}), soil (5.6 Tg·N y^{-1}) or lightning (5.0 Tg·N y^{-1}) (Ehhalt et al., 2018). Nevertheless, this comparison on a continental scale with a nitrogen source of the Antarctic atmosphere, such as the stratosphere denitrification, is more useful to understand its significance. Indeed, the evidence for denitrification in the Antarctic stratosphere is well established since the 90s (Deshler et al., 1991; Fahey et al., 1990; Mulvaney and Wolff, 1993; Salawitch et al., 1989; Santee et al., 1995; Van Allen et al., 1995). Savarino et al. (2007), estimated a N-budget of (0.035 ± 0.015) Tg(nitrate) y^{-1} or (0.008 ± 0.003) Tg·N y^{-1} coming from the stratosphere denitrification, only 2 times less the N-budget of the snowpack denitrification estimated here, making the snowpack source a rather substantial source.

However, McCabe et al. (2007), by studying the oxygen nitrate isotopic composition, suggested that nitrate was the result of a mixture of 25 % stratospheric and 75 % tropospheric origin, making the total nitrate source around 0.032 Tg·N y^{-1}. Therefore, the recycled nitrogen from the snowpack nitrate photolysis would represent approximately half of the nitrogen atmospheric input. Furthermore, Erbland et al. (2015) simulated that ~ 20 % of the total nitrate mass fluxes, i.e. stratospheric and tropospheric inputs as well as photolytic recycling, was exported. Two scenarios are conceivable: i) all the NO_x produced by the snowpack denitrification are re-oxidized, making the balance null and closing the nitrate budget in Antarctica; ii) photolysis destruction of snow nitrate is potentially an important denitrification factor of the Antarctic cryosphere.

That said, note that this extrapolation to the continent is a first order estimate as it does not consider the differences on the *e*-folding depth and the quantum yield variations with temperature and pH, especially at the coast; neither the latitude's differences modifying the ratios used in Equation 3.11. Indeed, Noro and Takenaka (2020) recently showed that at a coastal site called H128 (69°23'S, 41°34'E) that is located approximately 100 km away from the Japanese Syowa Station in East Antarctica, 50 % of the nitrate on surface snow is lost by photolysis. Additionally, they suggest that a photic zone of 45 cm depth is observed at a low impurity coastal site such as H128, making the photic zone at the coast close to the one observed at the higher plateau. Ideally, a 3-dimensional global chemical transport model of this snowpack source, supported by more FC experiments performed at strategic locations in Antarctica, to constrain the nitrate photolysis and the NO_x production, may be able to answer this question.

3.5 Conclusion

Flux chambers experiments carried out from December 10^{th} to January 7^{th} during the 2019-2020 campaign at Dome C, Antarctica, allowed to improve our understanding of the mechanisms of snow-contained nitrate photolysis.A common daily average photolysis rate coefficient of (1.50 ± 0.22) x 10^{-8} s–1 (1σ) was estimated for different types of snow samples (different ages and locations) on a 0-20 cm layer. This finding suggests that the photolyzable nitrate present in the snow acts as a uniform source with similar photochemical characteristics and a robust average daily photolysis rate coefficient $\overline{J_{NO_3^-}}$ of (2.37 ± 0.35) x 10^{-8} s–1 (1σ) was estimated for the Antarctic Plateau photic zone (0-50 cm layer).

Daily summer NO_x fluxes at Dome C were estimated to be (4.3 ± 1.2) x 10^8 molecules cm^{-2} s^{-1} over the observation period, if all NO_x produced were to be carried out of the snowpack, which is 1.5 to 7 times less than what has been estimated in previous studies at Dome C based on atmospheric gradient measurements, consistent with strong recycling and inter-annual variability of snow pack and atmospheric conditions at a single site. Observations here are in agreement with Bock et al. (2016) and Chan et al. (2018) theories suggesting that a single dominant incorporation mechanism is controlling the nitrate deposition onto snow (i.e., co-condensation) and that, at cold sites such as Dome C, a young snow will have a similar nitrate distribution in the snow's ice crystal as an older snow.

By extrapolating our FC observations, an annual snow-source NO_x budget of 0.017 ± 0.003 Tg·N y^{-1} was found for Antarctica. Because FC measurements were critical to our findings, we argue that they should be increasingly used across the cryosphere to improve calculations of NO_x budgets as it appears that the recycled nitrogen from the snowpack nitrate photolysis would represent at least half of the net nitrogen input from stratosphere and to the ocean. Knowledge gained in Antarctica may have broader impacts as well, as the re-emission of NO_x (re-noxification) of the atmosphere is a global phenomenon not limited to polar regions (McCalley and Sparks, 2009; Michoud et al., 2015; Su et al., 2011; Seok et al., 2009).

Additional experiments using the methodology and equipment detailed in this work can also better constrain the nitrate photolysis description and the NO_x production estimation, therefore refine parameters for NO_x flux estimation. Their results could help improve uncertainties in the parameterization of the models, in particular the $\sigma\phi$ product, found at Dome C to be $\sigma_{NO_3^-}(\lambda,T)\phi(T,pH)$ = (1.60 ± 0.34) x 10^{-23} cm^2 $photon^{-1}$ (1σ) (with $300 < \lambda < 340$ nm), and, using Chu and Anastasio's (2003) nitrate ion cross-section of 1.20 x 10^{-20} cm^2 $molecules^{-1}$, a $\phi(T,pH) \approx 0.0013 \pm 0.0003$ (with

$300 < \lambda < 340$ nm) molecules photon^{-1}. Using the $\sigma\phi$ product from the FC is an elegant way to circumvent the uncertainty in both individual terms for NO_3^- on ice. Therefore, with this technique, the NO_x snow-source could be better defined and differences in photolytic mechanics between East and West Antarctica, and between the coast and plateau regions, could be addressed.

This chapter is based on an article submitted to the Journal of Geophysical Research: Atmospheres. This work couldn't have been possible without the great help of the co-authors but also of others and institutions. Therefore, many thanks are adressed to the reviewers for their thoughtful comments and efforts towards improving the manuscript. The research leading to these results has received funding from: the LabEx OSUG@2020 ("Investissements d'avenir" – ANR10 LABX56); the French National program LEFE (Les Enveloppes Fluides et l'Environnement) via LEFE REACT; the Agence Nationale de la Recherche (ANR) via contract ANR-16-CE01-0011-01 EAIIST; the Foundation BNP-Paribas through its Climate & Biodiversity Initiative program and by the French Polar Institute (IPEV) through programs 1177 (CAPOXI 35–75) and 1169 (EAIIST). The meteorological data and information were obtained from IPEV/PNRA Project "Routine Meteorological Observation at Station Concordia" http://www.climantartide.it. The data used in this publication for the irradiations fluxes were obtained from LATMOS, with the help of Florence Goutail et Jean-Pierre Pommereau as part of the Network for the Detection of Atmospheric Composition Change (NDACC) and are publicly available (see http://www.ndacc.org). Great thanks to Maria Zatko, Becky Alexander, Shaddy Ahmed, Jennie Thomas and Charles Amory for their inputs on the global atmospheric chemistry and boundary layer modelling. Special thanks to Pete Akers for his help with reviewing the English of the manuscript. Finally,many thanks to the technical staff of IGE and IPEV for their technical and logistic support in Grenoble and during the field campaign.

Chapter 4

Summer variability of the atmospheric NO_2:NO ratio on the Antarctic Plateau

Contents

Abstract

Previous Antarctic summer campaigns have shown unexpectedly high levels of oxidants in the continental plateau as well as at coastal regions, with atmospheric hydroxyl radical (OH) concentrations up to 4×10^6 cm^{-3}. It is now well established that such high reactivity of the summer Antarctic boundary layer results in part from the emissions of nitrogen oxides ($NO_x \equiv NO + NO_2$) produced during the photo-denitrification of the snowpack.

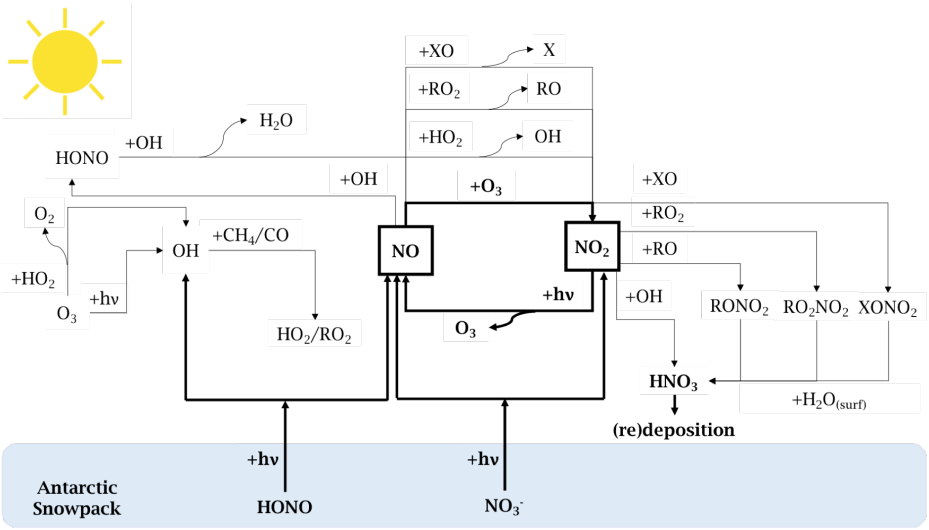

Figure 4.1 – Schematic of the gas phase chemistry of NO_x in the Antarctic Plateau. In bold the NO_x cycle and the NO_x direct snow-sources.

However, the mechanisms leading to such high oxidative capacity are yet to be completely understood. Indeed, some of the chemical species involved, especially NO_2, are still to be observed directly and in situ without interferences, or at least with controlled interferences. This leaves significant uncertainties on the snow-air-radiation interaction. To overcome this crucial lack of information, newly developed optical instruments based on the IBBCEAS technique were deployed for the first time at Dome C during the 2019–2020 summer campaign. These instruments allow direct measurement of NO_2 with a detection limit of 30 pptv (30×10^{-12} mol mol^{-1}) (3σ). Two sets of measurements were performed: in December 2019 during the early photolytic season, and in January 2020 during the late photolytic season.

Late in the season, the averaged NO_2:NO ratio observed (0.4 ± 0.4) is explainable by the extended Leighton's equilibrium involving RO_x (0.6 ± 0.3). In December, however, an averaged NO_2:NO ratio of 1.3 ± 1.1 is calculated from NO_2 and NO measurements, which is approximately twice the ratio of 0.7 ± 0.4 calculated from the extended Leighton's relationship. The preliminary exploratory results presented in this chapter suggest additional NO_2 sources in December, which could be explained by a stronger continuous NO_2 snow-source in the early photolytic season.

4.1 Introduction

For the last three decades, intense field campaigns took place in Arctic and Antarctic research stations to study the polar boundary layer composition and photochemistry (Bauguitte et al. (2012), and references therein). The growing interest in these regions lies in the importance of their atmospheric chemistry, being relatively free of local anthropogenic emissions, and in the interpretation of polar ice cores (Wolff, 1995). Antarctica is the most isolated continent on Earth, therefore providing the last continent scale laboratory for studying past and present natural atmospheric cycles (EPICA community members, 2004). Because of this presumed pristineness, the scientific community was puzzled by initial observations of high oxidative capacity in the polar boundary layer which resembled those seen in urbanized environments (Beine et al., 2002; Honrath et al., 1999; Jones et al., 2008; Kukui et al., 2014; Preunkert et al., 2012; Saiz-Lopez et al., 2008).

It is today well established that such high reactivity of the summer Antarctic boundary layer results from the presence of high reactive species such as nitrogen oxides ($NO_y \equiv NO$, NO_2, HONO, HO_2NO_2, HNO_3 etc.), hydroxyl and peroxyl radicals ($RO_x \equiv OH$, HO_2, RO_2) and halogen oxides ($XO \equiv BrO$, IO, ClO). Despite their very short lifetime and their low abundance in the atmosphere, because of their high reactivity they are controlling the oxidative capacity and the composition of the atmospheric chemistry of these regions. Today this phenomenon is not yet fully understood due to the combination of the difficulty of measuring NO_2 free of interferences and a complex oxidation/reduction scheme between NO_x, O_3, and radicals in the snow and atmosphere (Fig. 4.1).

NO_x ($\equiv NO_2 + NO$) is produced by the photolysis of nitrate ions (NO_3^-) in the snow (Grannas et al., 2007). Gas phase nitrogen dioxide (NO_2) may absorb a photon to produce nitrogen oxide (NO) and ozone (O_3), which then reacts together to reform NO_2 (bold cycle in Fig. 4.1). In this recycling reaction, no net production or loss of any species is involved. However, in the presence of other species such as peroxyl radicals (RO_x) or halogenated radicals (XO), NO can produce NO_2 without consuming ozone (Fig. 4.1). NO_2 can also be consumed by reacting with hydroxyl or halogenated radicals to form HNO_3, which will redeposit at the snowpack surface. NO can also react with OH to form HONO, which was measured on the Antarctic Plateau during the OPALE campaign and assumed to be present at around 8 to 12 pptv (parts per trillion by volume or 10×10^{-12} mol mol^{-1}) during the Austral summer (Legrand et al., 2014). However, Legrand et al. (2014) showed that the oxidation of NO by the OH radical is not sufficient to explain the levels of HONO observed, and the main source of HONO comes the snowpack emissions, as shown on Figure 4.1.

Despite the numerous observations of nitrogen-bearing species collected at various sites during previous campaigns such as ISCAT 1998, ISCAT 2000, ANTCI, NITEDC and OPALE, no direct NO_2 measurements free of interferences have been taken, and this absence hinders efforts to correctly evaluate the NO_x cycle on the Antarctic Plateau (Davis et al., 2008, 2004; Eisele et al., 2008; Frey et al., 2015; Oncley et al., 2004; Preunkert et al., 2012; Frey et al., 2013). This leaves significant uncertainties in the NO_x cycle and more broadly in the snow-air-radiation interaction. To overcome this lack of information, direct and accurate NO_2 measurements are needed. This motivated us to deploy in the field newly developed optical instruments based on the IBBCEAS technique that allow direct measurement of NO_2 and indirect measurement of NO with detection limits of 30 and 63 pptv (3σ), respectively (Barbero et al., 2020). Although indirect, the NO measurement is well constrained with potential external impacts identified and discussed in Chapter 2 Sections 2.5 and 2.6.

The main focus of the study is to present new results on the NO_2:NO summer variability over the Antarctic Plateau and explore the mechanisms involved in the atmospheric boundary layer of the Antarctic Plateau during the photolytic season in light of this new data sets. Section 4.2 provides details of the measurement studies undertaken and describes the data validation process applied. Section 4.3 presents the results, then, exploratory analysis to potentially explain the observations is provided in Section 4.4. Finally, conclusions and final thoughts are provided in Section 4.5.

4.2 Methods

4.2.1 Site description, sampling location and set-up

Atmospheric NO_x measurements were conducted for a total of 16 days, from December 4^{th} to 9^{th} and from January 16^{th} to 25^{th}, during the 2019-2020 summer campaign at the French-Italian Concordia Station, Dome C, Antarctica (75°06'S, 123°20'E, 3233m a.s.l). A description of the site, its location and its particular local weather was given in Chapter 3 Section 3.2.

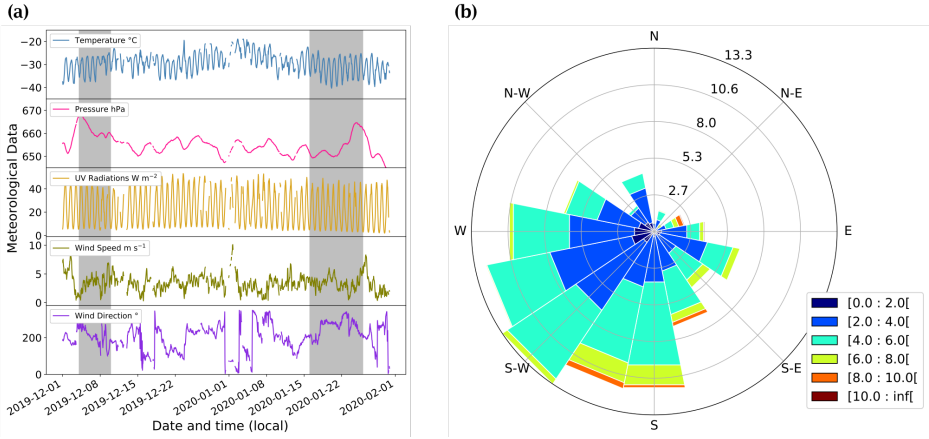

Figure 4.2 – **(a)** Local meteorological conditions (2-m observations) encountered during the campaign measured by the local automatic weather station (AWS– Vaisala Milos 520) completed with a broadband UV radiometer, spectral range 305–385 nm. The shaded area represents the periods when atmospheric measurements were conducted. **(b)** The corresponding wind rose in m s^{-1} at Dome C during the campaign.

The meteorological conditions encountered during the campaign are illustrated in Figure 4.2. The shaded aeras correspond to the periods when atmospheric measurements were conducted. Additionally, by using the HYSPLIT (Hybrid Single-Particle Lagrangian Integrated Trajectory) transport and dispersion model and READY website (https://www.ready.noaa.gov) from NOAA Air Resources Laboratory (ARL) (Stein et al., 2015; Rolph et al., 2017), five days back-trajectories were conducted, highlighting that the air masses were principally coming from the continent during the measurement periods (more information is provided in Appendix B.1). The meteorological conditions encountered for both atmospheric measurement periods can be found in Appendix B.2.

Atmospheric sampling was done in the station's clean area sector, where the FC experiments described in Chapter 3 were also conducted (Fig. **??**). Figure 4.3 shows a schematic of the set-up installed in the buried container.

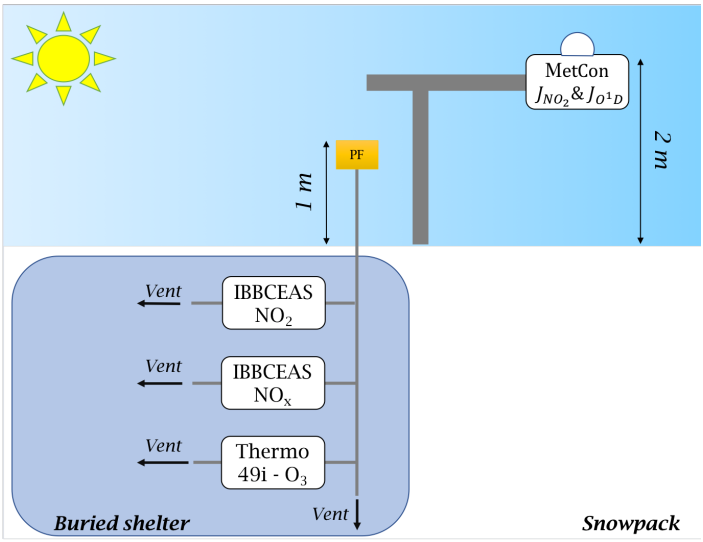

Figure 4.3 – Set-up schematic: the photolysis rate constant of NO_2 and O^1D are measured by a 2π spectral radiometer placed 2 meters above the snow surface and measuring the downwelling flux, i.e. facing the sky; the atmospheric sampling of NO_2, NO_x and O_3 were made 1 meter above the snow surface through $\frac{1}{4}$" PTFE tubing. Note that 5 μm particle filters (PF) were placed at the inlets to protect the optics of the measuring cells of the instruments.

4.2.2 Instrumentation and data processing

4.2.2.1 Measurement of atmospheric NO_x and O_3

The twin instruments described in Chapter 2 were used for NO_x detection in the 400–475 nm wavelength region. They are based on incoherent broadband cavity-enhanced absorption spectroscopy (IBBCEAS) relying on the injection of a high-power LED source in a high-finesse cavity (F ≈ 33,100), with the transmission signal being detected by a compact spectrometer equipped with a charge-coupled device (CCD) camera. Through this, we achieved direct detection of NO_2 with ultimate detection limit of 30 pptv within ≈ 20 min of measurement (3σ). To indirectly measure NO, we installed a compact ozone generator (water electolysis) converting all ambient NO into NO_2 via the reaction $NO + O_3 \rightarrow NO_2 + O_2$. Ultimate detection limits of 33 and 63 pptv (3σ), for NO_x and NO, respectively, are achieved (Barbero et al., 2020) within ≈ 20 min of measurement.

The instruments were calibrated prior to field deployment using a stable NO_2 source (FlexStream™ Gas Standards Generator, KINTEK Analytical, Inc.). In the field, we decided to use a shorter time average of 10 min measurement, which includes the acquisition of the reference (I_0) and absorption (I) spectra. It still provides low enough detection limits, 54 and 48 pptv (3σ) for NO_x and NO_2, respectively, according to an Allan-Werle statistical method (Werle et al., 1993), while allowing an

higher resolution dataset, which is then filtered as explained below. Field calibrations were made using a NO_2 gas bottle (Air Liquide - 1 ppm NO_2 in N_2) diluted with a zero-air flow for multi-points calibrations. The NO_2 gas bottle was calibrated against the KINTEK FlexStream™ Gas Standards Generator prior the field campaign.

The zero-air was produced by pumping outdoor air through two zero-air cartridges connected in series (TEKRAN, 90-25360-00 Analyzer Zero Air Filter) and pushed into the dilution line controlled by two mass flow controllers (MKS - Mass Flow Controller 0.01 and 10 slpm, i.e., standard liter per minute, for the NO_2 flow and the zero-air flow, respectively). The NO_x measurements from the IBBCEAS were synchronized in time for a more accurate estimate of the NO mixing ratio (NO = NO_x – NO_2).

To limit the impact of variable weather and atmospheric conditions on our NO_2 and NO observations, we restricted data acceptance to periods where the wind speed was less than 5 m s^{-1} and the wind coming from SE to NW were studied (i.e. between 135° and 338°, in order to exclude outlier data which may be affected by the contamination due to the station activities). This resulted in 17 % rejection for the first observation period and 11 % rejection for the second period. The measurements were then averaged every hour. During the first observation period, the weather conditions were favorable for atmospheric measurements leading to a low data rejection. During the second period, approximately 4 days of measurements were further rejected because the instruments were used for intercomparison and calibration tests.

Atmospheric ozone was monitored using a UV Photometric O_3 analyzer (Thermo Scientific™, Model 49i) that provides 1.5 ppbv (3σ) detection limits within 60 seconds. The instrument was calibrated with an O_3 calibration source (2B Technologies Model 306 Ozone Calibration Source™) and connected to a snow tower experiment (Helmig et al., 2020), (Appendix B.3). Here, samples were drawn sequentially at flows of typically ≈ 1-2 slpm through a series of switching valves connected to several inlet lines, following a 2-hour duty cycle of 8 minutes measurements on each inlet, including the one of interest placed at 1 meter above the snow surface. To account for the response time after the switching manifold (time for renewing the gas mixture in the line), only the last three minutes of measurements, when concentrations reached steady-state, were used and averaged, giving one measurement of ozone mixing ratio every 2 hours on the 1 m inlet. A linear data interpolation was applied to match the resolution of the NO_x measurements.

Particle filters (Whatman™ PTFE membrane filters – TE 38, 5 μm, 47 mm) were placed in the inlet lines (IBBCEAS and Thermo 49i) to prevent soiling of the optical mirrors of the instruments from aerosol particles.

4.2.2.2 Ancillary data

Standard meteorological data were collected from an automatic weather station (AWS) located one kilometer from the atmospheric measurements (Fig. **??**). The UV radiation spectrum was analyzed with a broadband UV radiometer (Kipp & Zonen – CUV 4, spectral range 305–385 nm) deployed near the clean sector.

4.2.2.3 The photolysis rate coefficients J_{NO_2} and J_{O^1D}

The photolysis rate coefficients, J_{NO_2} and J_{O^1D} were calculated from measurements made by a MetCon 2π spectral radiometer with a CCD detector offering a spectral range from 285 to 700 nm. The spectral radiometer was mounted on a mast of 2 m height from the snow surface (Fig. 4.3). The

mast was fastened in the snow by means of anchoring rods and turnbuckles in order to adjust the orientation of the measuring instrument. Downwelling radiance over a complete hemisphere was recorded over 285–700 nm. Later, the total 4π steradian radiance was calculated by multiplying the measurements by 1.9. This factor was evaluated from downwelling and upwelling radiance measurements during the OPALE campaign, by inverting the spectral radiometer (Kukui et al., 2014).

Unfortunately, the instrument operated very intermittently during the season, probably due to the instability of the power supply, and the continuous signal of the photolysis constant rate had to be extrapolated. Continuous data obtained from the broadband UV radiometer were used to scale the data from the 2π spectral radiometer. The estimated J_{NO_2} for both measurement periods is shown in Figure 4.4, and details on the fit analysis are provided in the Appendix B.4. Due to the intermittent measurement periods, especially at night, differences between the fit analysis and the J_{NO_2} measurements were found to be around 1 ± 7 % (1σ) in December and 4 ± 15 % (1σ) in January.

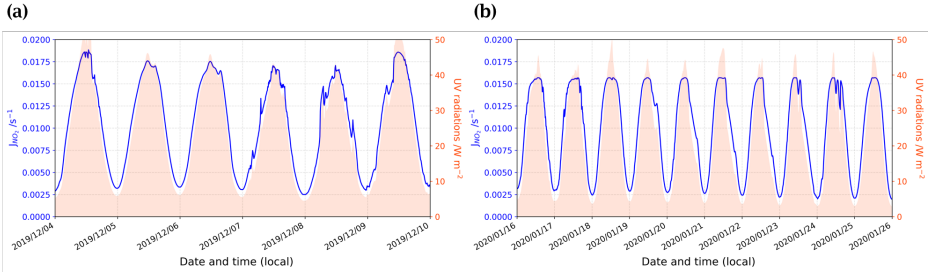

Figure 4.4 – J_{NO_2} (blue solid lines) reconstruction following the 2 degrees polynomial regression fit with UV radiations (shaded orange) measured by a broadband UV radiometer, spectral range 305-385 nm for both December **(a)** and January **(b)** observation periods.

Additionally, those results well agree with previous measurements done during the OPALE campaign using the same 2π spectral radiometer. Kukui et al. (2014) found a median value of J_{NO_2} = 1.3×10^{-2} s^{-1} (0.4 to 2.1) from the 19/12/2011 to the 10/01/2012 while here, for the same period, a median value of 1.2×10^{-2} s^{-1} (0.3 to 1.9) is estimated, very close to the 2011-2012 observations. The same approach was used for the calculation of J_{O^1D}.

4.3 Results

4.3.1 Atmospheric mixing ratios

Figure 4.5 summarizes all the measurements from both periods. On the top panel are reported the hourly mean mixing ratios of NO_2 (dashed blue), NO_x (dashed cyan) and NO (dashed black) measured at 1 m above the snow surface in pptv (blue left-hand scale) as well as the NO_2:NO ratio (red right-hand scale). On the bottom panel, the O_3 mixing ratios (dashed green left-hand scale) in ppbv are reported with the UV radiations (orange right-hand scale) in W m^{-2}. Solid lines represent the 6-hour running mean smoothed signals for each species. During the first observation period,

the weather conditions were favorable for atmospheric measurements leading to a low data rejection. During the second period, approximately 4 days of measurements were additionally discarded because of intercomparison and calibration tests.

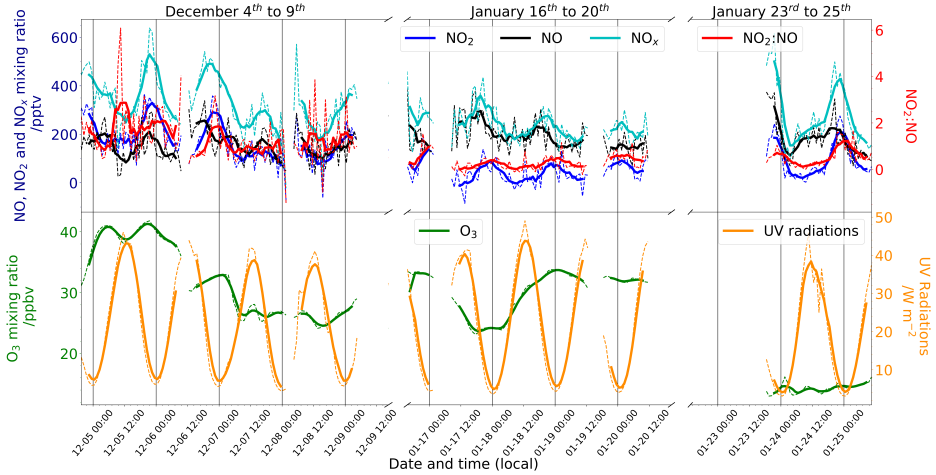

Figure 4.5 – **(top)** Darkblue left-hand scale: mixing ratios (pptv) of NO_2 (blue), NO (black) and NO_x (cyan) and red right-hand scale: NO_2:NO ratio. The signals are 6-hour running means (solid) on top of one hour means signals (dashed). **(bottom)** Green left-hand scale: mixing ratio of O_3 (ppbv) and orange right-hand scale: UV radiations (W m^{-2}) measured with broadband radiometer, spectral range 305-385 nm. The signals of O_3 are 6-hours running mean (solid) on top of one hour mean signal (dashed). Each day is marked with vertical black lines at 00:00 local time (LT).

4.3.2 NO_2:NO ratio analysis

Using the atmospheric measurements at 1 m above the snow surface, an average NO_2:NO ratio was estimated at 1.3 ± 1.1 (1σ) for December and 0.4 ± 0.4 (1σ) for January. The NO_2:NO ratio is generally driven by the steady state reaction between NO + O_3 and NO_2 photolysis, known as the simple Leighton's relationship (Leighton, 1961).

$$NO_2 : NO = \frac{k_{NO+O_3}[O_3]}{J_{NO_2}} \tag{4.1}$$

with $[O_3]$, the ozone concentration in molecules cm^{-3}; k_{NO+O_3}, the constant rate of the reaction NO + O_3: $k_{NO+O_3} = 1.4 \times 10^{-12} \exp(\frac{-1.89}{RT})$ (Atkinson et al., 2004) and expressed in cm^3 $molecules^{-1}$ s^{-1}; and J_{NO_2} the NO_2 photolysis rate constant in s^{-1}, measured with the Met-Con instrument and reconstructed as explain in Section 4.2.2.3. However, as illustrated in Figure 4.1, the simple Leighton's relationship can be perturbed by other species such as peroxy radicals and halogenated radicals. Therefore, the NO_2:NO ratio can also be calculated from an extended Leighton mechanism including only the peroxy radicals as described in Equation 4.2 (Ridley et al., 2000):

$$NO_2 : NO = \frac{k_{NO+O_3}[O_3] + \sum k_{NO+RO_x}[RO_x]}{J_{NO_2}} \tag{4.2}$$

Kukui et al. (2014) measured the RO_x at Dome C during the OPALE campaign at 1 m above the snow surface. They assumed that HO_2 and CH_3O_2 radicals represent the major part of all RO_2 radicals at Dome C, with a ratio of HO_2:RO_2 = 0.67 ± 0.05. Additionally, they found a linear correlation between the J_{NO_2}, measured with the same Met-Con instrument, and the concentrations of RO_2 (see Figure 3 of their study). Here, we used the same correlation and the ratio of 0.67 to estimate RO_2 and HO_2 atmospheric concentrations, respectively (more information can be found in the Appendix B.5). The reactions between those dominating peroxy radicals, RO_2 and HO_2, and nitrogen oxide are rapid with respect to NO + O_3, with mean rate coefficients of (1.10 ± 0.02) × 10^{-11} cm^3 $molecules^{-1}$ s^{-1} and (0.91 ± 0.02) × 10^{-11} cm^3 $molecules^{-1}$ s^{-1}, respectively, while k_{NO+O_3} = (6.35 ± 0.53) × 10^{-15} cm^3 $molecules^{-1}$ s^{-1}, in Dome C conditions. Therefore, Equation 4.3 is used to consider those reactions and calculate NO_2:NO ratios from O_3 in-situ measurements and RO_x observations taken from Kukui et al. (2014).

$$NO_2 : NO = \frac{k_{NO+O_3}[O_3] + k_{NO+HO_2}[HO_2] + k_{NO+CH_3O_2}[CH_3O_2]}{J_{NO_2}} \tag{4.3}$$

NO_2:NO ratios were calculated for both periods. Figure 4.6 shows time series plots of NO_2:NO observed and calculated using Equation 4.1 and 4.3 for both measurement periods. In December, the NO_2:NO is systematically higher than the one estimated using simple and extended Leighton's equilibrium (Fig. 4.6.a) while in January, it is systematically lower, except at the end of the measurement period, where it is, to some extent, following the extended equilibrium estimations (Fig. 4.6.b).

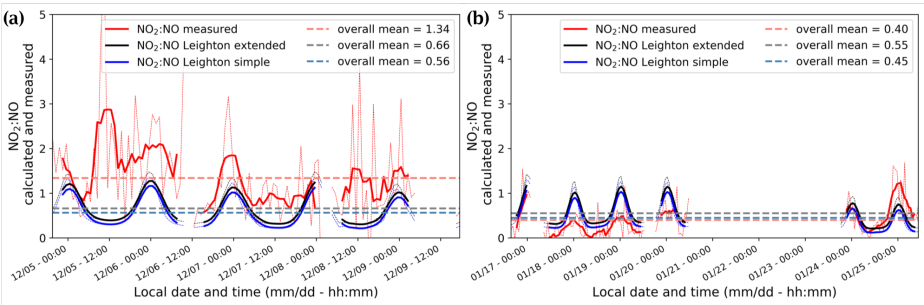

Figure 4.6 – NO_2:NO ratios measured (red) and estimated from Equation 4.1 (blue) and Equation 4.3 (black) for both observed periods: December **(a)** and January **(b)**. Solid lines represent the 6-hour running mean smoothed signals.

4.3.3 Atmospheric dynamic and polar boundary layer effect

One can observe on Figure 4.5 a drastic loss of O_3 at the end of the measurement period, from the 23^{rd} to the 25^{th} of January, with average mixing ratios of 14.3 ± 0.8 ppbv, which is half the average measured from the 16^{th} to the 20^{th} of January, 29.8 ± 3.6 ppbv. Legrand et al. (2016, 2009) characterized air masses arriving at Dome C with 5 days backward trajectories using the HYSPLIT model and concluded that O_3 mixing ratios below 20 ppbv were observed when the air masses spent at least one day above the ocean during the previous 5 days. Therefore it is possible that for those two days observations, the air mass was partially affected by marine influences. Indeed, the HYSPLIT 5 days backward trajectories ran at 4 different times of day on the 23^{rd} of January shows a

drastic change in the air mass origin between 14:00 and 20:00 local time (LT). For this time, the air mass originated from the east coast of Antarctica, and this can explain the sudden 10 ppbv drop of O_3 observed around 17:00 - 18:00 LT (Fig. 4.5). More informations are available in Appendix B.1.2. These two particular days are, for the moment, not included in the following discussion.

Additionally, the polar boundary layer (PBL) plays an important role in the mixing of the atmosphere at Dome C, as NO_2 records show a typical diurnal cycle defined by a minimum around noon and a maximum in the evening, corresponding to the development and collapse of the boundary layer, as previously described by Frey et al. (2013), Legrand et al. (2009), and others. In an attempt to decipher the mechanisms occuring at Dome C during our observations, we decided to account for the dilution effect due to the diurnal variation of the PBL. To do so, we observed the total number of molecules using Equation 4.4 hereafter:

$$N_i = [i]V \tag{4.4}$$

with N_i the total number of molecules of the specie i (i = NO_x, NO, NO_2, HO_2, RO_2 and O_3), $[i]$ its concentration expressed in molecule cm^{-3} and V an arbitrary volume expressed as 1 cm × 1cm × H_{PBL} with H_{PBL} the boundary layer height, retrieved using the MAR regional model and expressed in cm (see Appendix B.6 for details). This calculation assumes an homogeneous concentration of species within the PBL, an assumption supported by the flat concentration profiles observed by Legrand et al. (2016) and Frey et al. (2015) within the PBL during the OPALE campaign. Figure 4.8.a and 4.8.b shows in the top panels the daily averaged NO_x (cyan), NO (black) and NO_2 (blue) total number of molecules for both observation periods. The NO_2:NO ratios observed (red) in comparison with the theoretical NO_2:NO calculated from Equation 4.1 (NO_2:NO simple, grey) and Equation 4.3 (NO_2:NO extended, black) are reported in the lower panels of Figure 4.8.a and 4.8.b.

With the objective of testing the consistency of the observed NO_2:NO ratios with ozone production and destruction, we also reported the total number of O_3 molecules (green, left hand-scale), Figure 4.7.c and 4.7.d, with its variation over time, $\frac{dO_3}{dt}$, in molecules h^{-1} (blue-gray, right hand-scale). The production of ozone, P_{O_3}, calculated as the NO_2 production rate from the reaction $RO_2 + NO \rightarrow NO_2 + RO$ and $HO_2 + NO \rightarrow NO_2 + OH$, as reported by Kukui et al. (2014), is calculated following Equation 4.5 and reported in purple in Figure 4.7.c and 4.7.d.

$$P_{O_3} = (k_{RO_2+NO}[RO_2] + k_{HO_2+NO}[HO_2])[NO]V \tag{4.5}$$

with k_{RO_2+NO} and k_{HO_2+NO} the kinetic rate coefficients of the reactions $RO_2 + NO \rightarrow NO_2 + RO$ and $HO_2 + NO \rightarrow NO_2 + OH$, respectively, experessed in cm^3 $molecules^{-1}$ s^{-1}; $[RO_2]$ and $[HO_2]$, the species concentrations expressed in molecule cm^{-3} and derived from the correlation between J_{NO_2} and $[RO_2]$ and the $\frac{RO_2}{HO_2}$ ratio (Kukui et al., 2014); [NO] the concentration of NO expressed in molecule cm^{-3}; and V the arbitrary volume expressed as 1 cm × 1cm × H_{PBL} cm.

The overall daily mean $\frac{P_{O_3}}{V}$ calculated for this study ($\approx 4.3 \times 10^9$ molecules $cm^{-3}h^{-1}$ or 0.22 ppbv h^{-1}) is close to the 0.3 ppbv h^{-1} calculated by Kukui et al. (2014) , and the 0.2 ppbv h^{-1} derived from the study of the ozone diurnal concentration by Legrand et al. (2009). In the lower panels of Figure 4.7.c and 4.7.d are reported the deviations of the observed ratio (NO_2:NO_{obs}) from the simple and extended Leigthon's equilibria, ΔNO_2:NO sim = NO_2:NO_{obs} - NO_2:NO_{simple} and ΔNO_2:NO ext = NO_2:NO_{obs} - NO_2:$NO_{extended}$, for each period, respectively.

Looking at Figure 4.7.a and 4.7.b, the NO_x, NO and NO_2 peaks are now approximately in phase with the UV radiation. NO total number of molecules appears constant from December to January

with a maximum from 11:00 to 17:00 LT. NO_2 shows simular trend in December with a maximum from 10:00 to 18:00 LT, while in January, the total number of NO_2 molecules in the atmospheric boundary layer is somewhat constant during the day, with a slight increase from 09:00 to 12:00 LT.

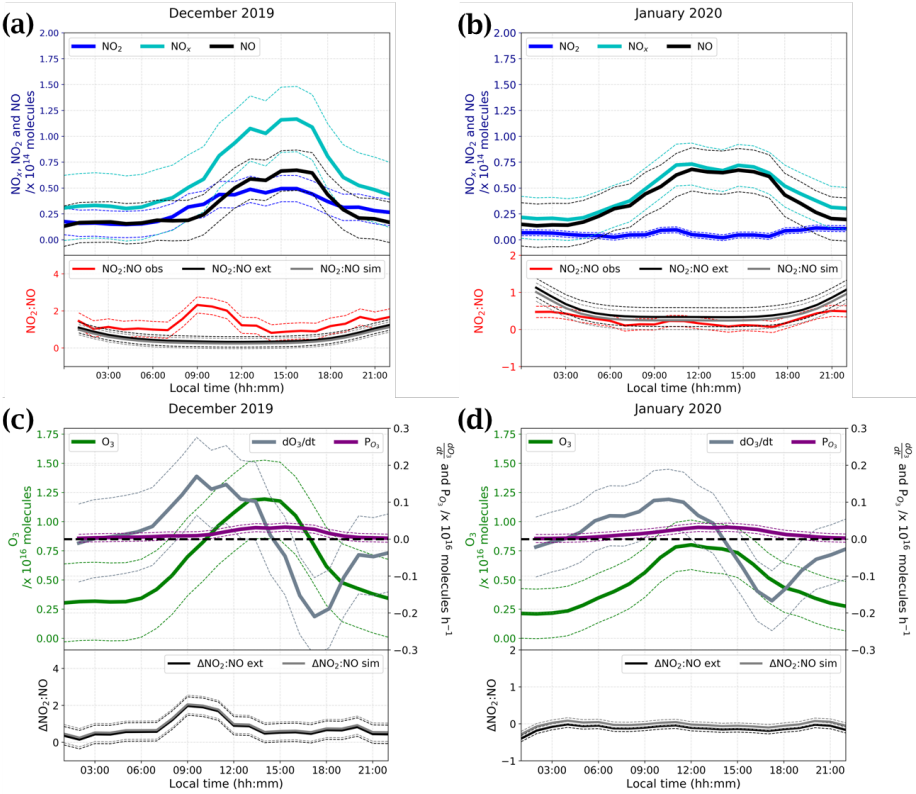

Figure 4.7 – **(a)** and **(b)** 3-hour running mean (solid lines) ± 1σ (thin dashed lines) of the diurnal cycles of NO (black), NO_x (cyan) and NO_2 (blue) total number of molecules in a column of 1 cm × 1 cm × 1 H_{PBL} [cm] (top panels) and NO_2:NO ratios (bottom panels) observed (red) and equilibrium's calculations (simple Leighton in grey /extended Leighton in black) for December and January, respectively. **(c)** and **(d)** top panels represent the 3-hour running mean (solid lines) ± 1σ (thin dashed lines) of the diurnal cycle of the total number of ozone molecules in a column of 1 cm × 1 cm × 1 H_{PBL} [cm] (green), the O_3 variations, $\frac{dO_3}{dt}$, in molecules h^{-1} (grey) and the ozone production, P_{O_3} (purple) in molecules h^{-1} calculated from the total number of RO_2 and NO molecules; the bottom panels represent the differences between NO_2:NO observed and NO_2:NO calculated, ΔNO_2:NO in grey for simple Leighton and ΔNO_2:NO in black for extended Leighton.

Additionally, a constant factor of 5 between NO_2 levels in December and January is observed. In December, the NO_2:NO is above the NO_2:NO predicted by Leighton's equilibria (simple and extended) with a peak in the morning, from 07:00 to 12:00 LT, but approaches equilibrium from noon

onwards, inversely following ozone signal. In January, it is following quite well the equilibirum except during nighttime, where it is approximately half the predicted value calculated at steady-state.

The O_3 variations measured in our study ($\frac{dO_3}{dt}$) show significant differences with the ozone production (P_{O_3}) calculated using RO_2, HO_2 and NO concentrations. P_{O_3} from Figure 4.7.c and 4.7.d, shows not only a factor 10 of difference with the O_3 daily variations, but a rather different behaviour as well. Indeed, using RO_2, HO_2 and NO concentrations, O_3 appears to be gradually produced, following the UV radiation, with a maximum production in the afternoon, from approximately 12:00 to 16:00 LT. However, this calculated production is largely insufficient to explain the observed variability of O_3. Observations show ozone production, (i.e., values above the dashed black line in Fig. 4.7), from around 02:00 to 14:00 LT, with the maximum reached at 11:00 (local solar noon) and destruction of ozone, (i.e., values under the dashed black line in Fig. 4.7), from 14:00 to midnight (LT), with the maximum consumption around 17:00 – 18:00 LT.

While Legrand et al. (2009) attributed this behaviour to the variability of the PBL, here, its impact is accounted for through the observation of a total number of molecules in a column whose height represents the boundary layer height. Therefore, the dynamic of the PBL is not the only explanation for the O_3 variability and local chemical reactions play an important role in the diurnal O_3 behaviour. Even though the deviation (ΔNO_2:NO) from Leighton's equilibria is always positive, at those levels of O_3, a deviation of ΔNO_2:NO = 0.5 from steady-state might not be enough to maintain an O_3 production (Fig. 4.7.c). Additionally, the ΔNO_2:NO peak in December is slightly shifted with respect to the $\frac{dO_3}{dt}$ (Fig. 4.8.c). This shift is explained by the chemical lifetime of the species. NO_2 lifetime, $\tau_{NO_2} = \frac{1}{J_{NO_2}}$ is varying from $\approx$ 6 min at 00:00 LT to $\approx$ 1 min at 11:00 LT, largely inferior to O_3 chemical lifetime. Legrand et al. (2016) show that the main sink of O_3 is the HO_2 radical, therefore, driving its lifetime: $\tau_{O_3} = \frac{1}{k_{HO_2+NO}[HO_2]}$ is varying from $\approx$ 2 years at 00:00 LT to $\approx$ 0.4 year at 11:00 LT. However, the O_3 dry deposition was not takent into account in the P_{O_3} calculation.

The NO_2:NO ratio seems to follow Leigthon's equilibrium in January and as NO does not evolve between the two periods of observation, it highlights the necessity of an additional primary source of NO_2 other than the conversion of NO to NO_2 by reactions with O_3 and radicals as shown in Figure 4.1. Additionally, in January, the seemingly extended Leigthon's equilibrium cannot explain the O_3 loss observed from the $\frac{dO_3}{dt}$ signal. The chemical lifetime of O_3 with respect to its photolysis, $\tau_{O_3} = \frac{1}{J_{O^1D}}$, J_{O^1D} reconstructed from the Met-Con instrument, is estimated to be ranging from 7 hours to several days. Another sink of O_3, with chemical lifetime closer to τ_{NO_2} is necessary to explain the O_3 loss observed for both periods. In an attempt to explain the large NO_2 excess observed at maximum sunlight in December, the NO_x snow-source is studied in light of the conclusions given in Chapter 3.

4.4 Discussion

4.4.1 Comparison with previous studies

Previous studies estimated the NO_2:NO ratio on the East Antarctic Plateau at Dome C. Frey et al. (2013) measured atmospheric NO_x during the 2009-2010 NITEDC campaign, from December 10 to January 28, for a total of 50 days. They used a 2-channel chemiluminescence detector, based on the

reaction of NO with excess O_3 to produced NO_2. One channel was dedicated to the measurement of NO, the other one to the measurement of NO_x, that is to say the sum of atmospheric NO plus the NO originating from quantitative photolytic conversion of NO_2. Atmospheric NO_2 concentrations were then calculated as the signal difference between those two channels (Bauguitte et al., 2012). Results of Frey et al. (2013) suggested that either an unknown process enhancing NO_2 was taking place at Dome C, or that peroxy and other radicals would be significantly higher than elsewhere in Antarctica. Table 4.1 summarizes results from previous campaigns at Dome C, i.e., NITEDC and OPALE in comparison with the results of this campaign using a different technique for the NO_x detection.

In this work, during the first period of observation (December 4^{th} to 9^{th}), an average mixing ratio of 158 ± 68 pptv (1σ) was measured for NO, similar to Frey et al. (2013, 2015) measurements during NITEDC and OPALE campaigns, with NO mixing ratios of 169 ± 115 pptv and 146 ± 63 pptv, respectively, for similar periods. However, higher concentration levels of NO_x and NO_2 where observed previously, ≈ 1.3 times more than what measured in this study (Table 4.1). The same observations are therefore reported on the NO_2:NO ratios.

Table 4.1 – NO, NO_2 and NO_x mixing ratios (pptv) and NO_2:NO ratios measured at Dome C during this campaign, in comparison with previous NITEDC and OPALE campaigns for similar periods (periods averages).

	December					January				
	NO (pptv)	NO_2 (pptv)	NO_x (pptv)	NO_2:NO	*Period*	NO (pptv)	NO_2 (pptv)	NO_x (pptv)	NO_2:NO	*Period*
NITEDC	169 ± 115	205 ± 107	383 ± 150	1.6 ± 1.1	10-15/12/2009[a]	80 ± 62	59 ± 41	139 ± 91	1.1 ± 1.1	15-25/01/2010[a]
OPALE	146 ± 63	259 ± 138	409 ± 194	1.8 ± 0.7	04-09/12/2011[b]	34 ± 33	64 ± 77	100 ± 108	1.7 ± 6.4	08-12/01/2012[b]
This work	158 ± 68	173 ± 85	331 ± 116	1.3 ± 1.1	04-09/12/2019	188 ± 63	43 ± 46	231 ± 62	0.3 ± 0.3	17-20/01/2020
						183 ± 82	97 ± 76	231 ± 134	0.6 ± 0.4	23-25/01/2020

[a] From Frey et al. (2013)
[b] From Frey (2021)

A period average mixing ratio of 188 ± 63 pptv (1σ) in January was measured for NO from the 17^{th} to 20^{th}, and this is almost 2.5 times what Frey et al. (2013) measured (80 ± 62 pptv) from the 15^{th} to the 25^{st} of January 2010. Moreover, during the OPALE campaign, Frey et al. (2015) measured ∼ 6 times less NO but similar NO_2 mixing ratios (looking at periods averages), leading to a high NO_2:NO of 1.7 ± 6.4 whereas we estimated a ratio of 0.3 ± 0.3 from our results.

While differences in atmospheric dynamics and snow cover during the different campaigns could explain the discrepancy observed in December and January, it may also be due to different detection techniques being used.

In our study, NO_2 is measured directly. However, the NO measurement is made indirectly through the detection of NO_x after quantitative conversion of all ambient NO to NO_2 via $NO + O_3 \rightarrow NO_2 + O_2$. In Chapter 2 Section 2.6, we discussed the possible interferences on NO_2 measurements in the presence of high levels of O_3 as several reactions could be triggered at those levels. However, the instrument configuration allows operation of the spectrometer at low temperature, making potential interferences from the thermal degradation of HO_2NO_2, for example, negligible and estimated at 1 pptv at 10 °C. Furthermore, very limited NO_2 (0.001 pptv) would be produced by the reaction of $HONO + OH \rightarrow NO_2 + H_2O$ and less than 8 to 16 ppqv for 200 pptv of NO_2 would be formed throught the heterogenous reaction of NO_2 and H_2O. Finally, the possible interferences due to NO_2, NO or NO_3 appeared to be limited. Because their rate constant is a few order of magnitude less than the one for the NO oxidation, a maximum threshold on the O_3 concentration is applied regarding the reaction time imposed by the volume of the inlet line and the flow rate. Additionally, spectral

interferences were studied as small imperfections on the fit could lead to large effects on the NO_2 retrieved mixing ratio, particularly at sub-ppb levels. Yet, no significant effects of potential artifacts were observed when O_3 concentrations up to 8 ppmv were used. Finally, during this field study, applied O_3 concentrations were kept under 6 ppmv (5.6 ± 1.5 and 4.3 ± 0.5 ppmv in December and January, respectively).

The discrepancies observed between the IBBCEAS measurements and the previous CLD measurements could be explained by positive and negative interferences on the CLD technique. Indeed, the quantification of NO_2 can be interfered by the presence of other gaseous species in the inlet lines which will be then photolytically converted, such as HONO and HO_2NO_2. Reed et al. (2016) suggested that measurements of NO_2 using CLD systems may be significantly biased in low-NO_x environments, especially in pristine environments, such as Dome C, where the NO_y to NO_x ratio may be high. The thermal decomposition of NO_y species within the NO_2 converter can produce unreasonably high measurements. Additionally, the photolytic conversion unit of the CLD instrument used in previous campaigns was at 30 °C, therefore the thermal decomposition of HO_2NO_2 could indeed be an important source of interferences. Frey et al. (2013, 2015) discussed those possible interferences due to the thermal decomposition of HO_2NO_2 and estimated them to 8-16 % of the average NO_2 measurement at 1 m from the snowpack. This interference might indeed explain the higher NO_2:NO ratio observed during previous campaigns in respect to our study.

4.4.2 Presence of halogenated radicals

During the OPALE campaign, bromine oxide (BrO) column amounts were measured using a ground-base UV-visible spectrometer (MAX-DOAS, Roscoe et al. (2014)). Based on a complex analysis of the spectra, Frey et al. (2015) estimated a BrO median daily value of 2-3 pptv near the surface at Dome C. Additionally, Schönhardt et al. (2012) observed via satellite the presence of BrO and IO over Antarctica. However, the monthly maps of IO vertical column amounts (Fig. 4 of the study) show the presence of IO in the Antarctic Plateau late in spring (September-October) around 1.0 to 1.5 $\times 10^{12}$ molecules cm^{-2}. In constrat, in summer, they found a vertical amount of IO close to zero (satellite observations averaged over six subsequent years 2004-2009). Vertical amount of BrO were found to be quite constant between December and January, and ranging from 6.0×10^{13} to 7.0×10^{13} molecules cm^{-2} (Fig. 5 of the study). To our knowledge, there are no reports of near-surface ClO measurement in Antarctica. The reactions NO + XO → NO_2 + X show very similar reactions rate coefficients for XO ≡ BrO, IO and ClO. Therefore, we consider here an average of all halogenated radicals XO to have a daily average rate coefficient of $(2.5 \pm 0.4) \times 10^{-11}$ cm^3 $molecules^{-1}$ s^{-1}. The necessary amount of XO to reach steady-state in December was calculated following Equation 4.6:

$$NO_2 : NO = \frac{k_{NO+O_3}[O_3] + k_{NO+HO_2}[HO_2] + k_{NO+CH_3O_2}[CH_3O_2] + k_{NO+XO}[XO]}{J_{NO_2}} \quad (4.6)$$

which is simplified in Equation 4.7:

$$[XO] = \Delta NO_2 : NO \frac{J_{NO_2}}{k_{XO+NO}} \quad (4.7)$$

Daily mean average of XO of 17 pptv were estimated, with a peak of 64 pptv at 11:00 LT. If such high levels of XO were present, they would have been detected by Frey et al. (2015) MAX-DOAS as XO is suspected to be mainly BrO at Dome C. Additionally, such high levels of XO would induced some fast destruction of O_3, which was not observed either, and finally, NO levels would be lower in December than January.

Therefore, the assumption of an additional conversion of NO to NO_2 through XO or RO_x seems unsufficient to explain the observations, and only the increased production of NO_2 from primary sources of NO_2 by a factor of 2 can justify the NO_2 excess observed in December and not in January. In the following sub-chapters, the NO_x snow-source is studied in the light of the conclusions of Chapter 3.

4.4.3 NO_x snow-source

In Chapter 3, we presented the results of flux chamber experiments deployed for the first time on the Antarctic Plateau at Dome C. We have estimated a nitrate daily average photolyse rate coefficient, $J_{NO_3^-} = (2.17 \pm 0.24) \times 10^{-8}$ s^{-1} for all different snow samples (depth and location) of the Antarctic Plateau (from the 10^{th} of December to the 07^{th} of January). In the light of this new estimate, the NO_x snow-source is studied here to evaluate the NO_x fluxes, F_{NO_x} and NO_x production rate, P_{NO_x} in December and January using Equation 4.8:

$$F_{NO_x} = \int_z J_{NO_3^-}[NO_3^-]dz \tag{4.8}$$

with $[NO_3^-]$ the concentration of nitrate in molecules cm^{-3} of snow available in the photic zone, define as z = 50 cm (see Chapter 3 Section 3.4.2).

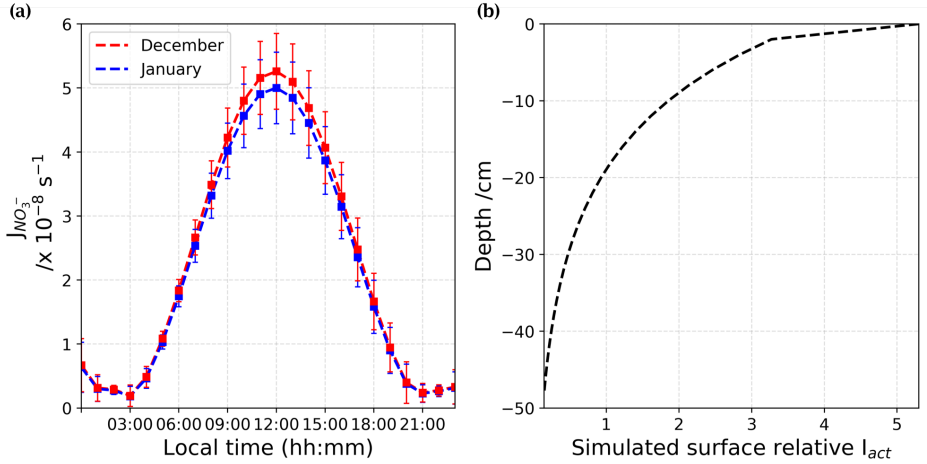

Figure 4.8 – **(a)** Adjusted $J_{NO_3^-}$ [s^{-1}] from December (red) and January (blue) estimated from Chapter 3 results. **(b)** Mean surface relative actinic flux, I_{act}, profile at 305 nm. The actinic flux describes the number of photons incident at a point.

The nitrate photolysis rate coefficients were adjusted for the solar zenith angle (SZA) variations, and corrective factors of 0.987 and 0.938 were found for December and January, respectively. $J_{NO_3^-}$ [s^{-1}] for both periods is presented in Figure 4.8.a. At maximum sunlight, the $J_{NO_3^-}$ is slightly lower in January than in December due to the increase of SZA lowering the maximum peak of UV radiation. Figure 4.8.b shows the mean surface relative I_{act} profile over the photic zone extracted from the

SBDART model, Libois et al. (2013, 2014), at 305 nm, the optimal wavelentgh of nitrate photolysis. The attenuation of $J_{NO_3^-}$ in the photic zone is driven by the attenuation of the $I_{act}(\theta, \lambda, z)$ as shown by Equation 4.9:

$$J_{NO_3^-}(\lambda) = \int_z \sigma_{NO_3^-}(\lambda, T)\phi(T, pH)I_{act}(\lambda, \theta, z)dz \tag{4.9}$$

where θ is the SZA; λ [nm] is the wavelength; and z [m] is the snowpack's depth; $\sigma_{NO_3^-}(\lambda, T)$ is the absorption cross-section of nitrate; $\phi(\lambda, T, pH)$ and $I_{act}(\theta, \lambda, z)$ are nitrate photolysis quantum yield and actinic flux, respectively.

4.4.3.1 Surface snow

From Figure 4.8.b, one can see that I_{act} attenuates quickly with depth in the snowpack following an exponential decrease. Thus, the first few millimeters of the snow column dominate the availability of photons for photochemical reactions in the UV. Surface snow has been sampled for nitrate at Dome C (≈ 1 every 3 days) for several years through the programs NITEDC and CAPOXI, and their results are useful to the analyses here. To reduce spatial and temporal variability, average surface concentration for periods corresponding to our atmospheric observations are used.

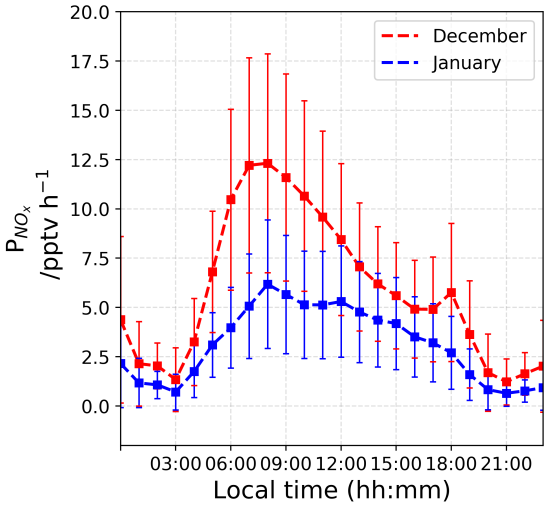

Figure 4.9 – Estimated P_{NO_x} [pptv h^{-1}] in a column of 1 cm × 1 cm × H_{PBL} cm from December (red) and January (blue).

The average nitrate concentration in surface snow (few mm) is 991 ± 341 ppbw (parts per billion by weight or ng g^{-1} of snow) (median 931 - 70 samples) in December and 588 ± 248 ppbw (median 558 - 65 samples) in January, respectively. The ∼ 40 % difference between December and January at the surface of the snowpack is quite large. Considering Equation 4.8 with a negligible dz for surface snow samples, we estimated the NO_x fluxes [molecules cm^{-2} s^{-1}] from the snow surface source and converted it into a production rate in molecules cm^{-3} h^{-1} using the PBL height (cm). This production was then converted into pptv h^{-1} using atmospheric pressure, P [hPa], and temperature,

T [K] measurements. Additionally, the mean surface relative I_{act} profile shows an enhancement of the actinic flux in the very first mm of snow (4.8.b), therefore, we multiplied the results by a factor of enhancement of 5. Figure 4.9 pictures the estimated P_{NO_x} [pptv h^{-1}] from the surface snow for both periods.

A mean factor of 2 between the maximum production of NO_x is observed in a column of 1 cm × 1cm × H_{PBL} cm. It is worth noticing that factor up to 6 in the surface snow NO_x production between December and January could be reached in the early morning.

4.4.3.2 Snowpack

The automatic snow tower experiment (Helmig et al., 2020), allows continuous year-round NO_x and O_3 measurements at different snow depths and heights above the snow surface, and this monitoring has been maintained since 2015 at the same location as our atmospheric observations. However, during our measurements, only the O_3 monitoring instrument was running. Figure 4.10 shows averaged 24 h NO_x mixing ratios in the interstitial air at -48 cm recorded in 2016-2017 for similar periods of time. One can see that the NO_x measured at -48 cm, the bottom of the photic zone is ≈ 1.5 times higher in December 2016 than in January 2017, strengthening the theory of a strong variability in the NO_x snow-source during the photolytic season.

Additionally, calculations based on the FC results are probably underestimating the actual NO_x snow-source, as mentioned in Chapter 3 Section 3.4.4.1. Indeed, as discussed in Frey et al. (2013) the observed night time increase in wind shear at Dome C (Fig. 4.2) likely causes enhanced upward ventilation of NO_x which had been temporarily accumulated in the upper snow pack during very stable conditions. This analysis is strengthening the hypothesis of an enhanced NO_2 snow-source in December.

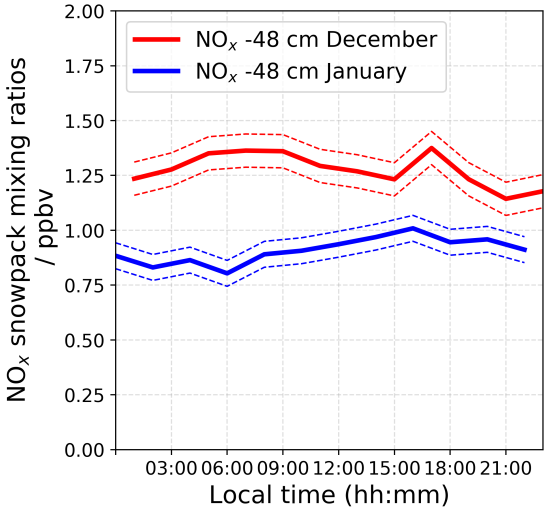

Figure 4.10 – Averaged NO_x snowpack mixing ratios measured by the snow-tower set-up for similar periods in December 2016 (red) and January 2017 (blue) at -48 cm.

However, if the NO_x snow-source might explain the differences between December and January in the NO_x cycle, this does not match the observed O_3 variations. Additional investigations on possible unidentified mechanisms or unidentified sink of O_3, probably emitted by the snow pack, are needed. It is worth noticing that the RO_x concentrations used in this study were retrieved from Kukui et al. (2014) who estimated aswell a possible interference due to HO_2NO_2. The characterization of HO_2NO_2 diurnal cycle and thermal equilibrium at Dome C is needed to overcome the uncertainties on the RO_x mixing ratios.

4.5 Conclusions

For the first time, direct and in-situ atmospheric measurements of NO_2 were carried out on the Antarctic Plateau at Dome C. The summer variability of the NO_2:NO ratio was study in light of this new set of observations. For the early photolysis season, a high NO_2:NO ratio of 1.3 ± 1.1 was observed, which is not explainable with the extended Leighton's relationship (0.7). However, the NO_2:NO ratio observed during the late photolytic season can be explained by an extended Leighton's relationship involving RO_x. Estimation of the NO_x snow-source in the light of the results of Chapter 3 suggests that the NO_x snow-source is the main driver of the atmospheric oxidative capacity in the austral summer at Dome C. However, this study must be reinforced with direct HO_2NO_2 measurements to be able to quantify its role and possible interferences on previous studies.

This research leading to this chapter will be strenghtened in the future and proposed for publication in the scientific journal Atmospheric Chemistry and Physics. This research has received funding from: the LabEx OSUG@2020 ("Investissements d'avenir" – ANR10 LABX56); the French National program LEFE (Les Enveloppes Fluides et l'Environnement) via LEFE REACT; the Agence Nationale de la Recherche (ANR) via contract ANR-16-CE01-0011-01 EAIIST; the Foundation BNP-Paribas through its Climate & Biodiversity Initiative program and by the French Polar Institute (IPEV) through programs 1177 (CAPOXI 35–75) and 1169 (EAIIST). The meteorological data and information were obtained from IPEV/PNRA Project "Routine Meteorological Observation at Station Concordia" http://www.climantartide.. The data used in this publication for the irradiations fluxes were obtained from LATMOS, with the help of Florence Goutail et Jean-Pierre Pommereau as part of the Network for the Detection of Atmospheric Composition Change (NDACC) and are publicly available (see http://www.ndacc.org). Gratefull aknowledgments are adressed to the NOAA Air Resources Laboratory (ARL) for the provision of the HYSPLIT transport and dispersion model and READY website (https://www.ready.noaa.gov) used in this reasearch work. Thanks to Charles Amory for running the MAR regional model and providing the PBL height. Finally, once again, many thanks to the technical staff of the IGE and IPEV for their technical and logistic support in Grenoble and during the field campaign.

Chapter 5

Conclusions and perspectives

"S'élancer à la conquête des terres vierges, c'est être poussé par le goût de l'aventure, par l'appétit scientifique ou encore par le mystérieux attrait de l'inconnu. Chacun de ces trois motifs eut sa part dans ma décision de repartir pour l'Antarctique."
Ernest Shackleton

Contents

5.1 General conclusions

The research work presented here aimed to improve our understanding of the atmosphere oxidizing capacity on the Antarctic Plateau. While the study of ice cores has provided unparalleled information on the atmospheric CO_2 and CH_4 contents and temperature fluctuations of the atmosphere for the past 800,000 years, we know comparatively very little about past changes in atmospheric oxidative capacity.

Nitrate, the product of NO_x oxidation, is transported and deposited on the Antarctic snowpack. However, the interpretation of its records in ice cores is not straightforward because nitrate undergoes photochemical processes strongly altering its concentration and isotopic composition in the first layers of the snowpack (Röthlisberger et al., 2000). Recent studies have detailed how snow-borne nitrate is frequently converted to NO_x which is re-emitted into the atmosphere and commonly re-oxidized into nitrate that again is deposited on the snow surface.

To date, the impacts of this reactive chemistry on the signal preservation in the ice is poorly known and unconstrained, limiting a coherent climatic interpretation of the records (Legrand et al., 1999). The NO_x emission mechanisms are not fully constrained mainly because of the challenge of measuring NO_x at very low concentration levels and controlling the numerous factors that can interfere with these measurements in the field. Additionally, no direct measurements of NO_2 at the snow-atmosphere interface on the Antarctic Plateau are available.

Therefore, the objectives of this research work were: i) to validate and deploy accurate instruments dedicated to the direct and in-situ measurement of NO_2; ii) to better characterize nitrate photolysis through the study of different snows from the Antarctic Plateau (different ages and locations) and iii) to measure NO_x concentrations in the Antarctic atmosphere with a better accuracy.

5.1.1 Can interferences with NO_2 measurements be eliminated or at least controlled?

Previous studies have measured the NO_x in the Antarctic atmosphere using different techniques. At Dome C, a chemiluminescent instrument was used that allows direct NO detection, and NO_x detection, through a quantitative photolytic converter, but unfortunately not direct NO_2 measurements. The NO_2 signal is retrieved as the NO_x minus de NO measurements (Bauguitte et al., 2012). The limits of detection in this technique were found to be around 5 pptv and the converter photolytic efficiency around 55-60 %. However, the photolytic converter can be subjected to interferences due to the presence of other nitrogen species. Especially, HO_2NO_2 can undergo thermal decomposition inside the converter which temperature can reach 30 °C, leading to an overestimation of NO_2 mixing ratios.

In an attempt to diminish or at least control the possible interferences on the NO_x detection, we choose an optical technique that would allow direct NO_2 detection. The choice of Incoherent Broad-Band Cavity Enhanced Absorption Spectroscopy (IBBCEAS) technique was driven by its numerous advantages such as: high sensitivity and selectivity, in-situ multi-species detection, ease of use, versatility, adaptability, and relatively low power consumption.

Chapter 2 presented the development of compact, affordable and robust twin instruments based on this technique in the 400-475 nm wavelength region. Indeed, working in this spectral region allows us to have access to other molecules of atmospheric interest such as IO and CHOCHO as well as

avoiding the issue of absorption lines saturation occurring in the mid-IR region, as explained by Richard et al. (2018) and explained in Chapter 1 Section 1.3.2.3 of this thesis.

We developed two instruments for simultaneous detections of NO_2, IO, CHOCO and O_3 with detection limits of 11, 0.3, 10 pptv and 47 ppbv (1σ), respectively, within 22 minutes of measurement. The implementation on the inlet gas line of a compact ozone generator based on water electrolysis allowed the measurement of NO_x after quantitative conversion of all ambient NO to NO_2 via NO + O_3 → NO_2 + O_2. An indirect detection of NO was then possible, with detection limits for NO_x and NO of 10 and 21 pptv (1σ), respectively. The device was designed to fit in a 19", 3U rack-mount case, weights 15 kg and has a total electrical power consumption < 300 W. Artifacts of the method have also been studied:

- the light emitting diode (LED) being sensitive to temperature fluctuations, a temperature stabilization (Pelletier) controls its temperature,
- because the alignment of the optical cavity was affected by thermal variations, we stabilized the entire instrument in temperature to ensure its long-term stability.

The technique, developed, tested and validated during the course of this thesis is robust, allows long acquisition times, and reaches detection limits adapted to the concentrations present in Antarctica in about 10-20 min. Additionally, the detection limits could be further improved by replacing the spectrometer with a spectrometer with an integrated cooled CCD. The cooling would allow an improvement on the signal to noise ratio of up to a factor of 10, by reducing the dark noise at the CCD, which would directly apply to the detection limits.

Additionally, we have studied possible chemical and spectral interferences using a kinetics model and experiments in the laboratory. No appreciable effects of possible artifacts were observed for the conditions of use that the instruments would have to face in the further course of this research.

Finally, this research work was the subject of a publication, in August 2020, in Atmospheric Measurement Techniques, (Barbero et al., 2020):

Barbero, A., Blouzon, C., Savarino, J., Caillon, N., Dommergue, A., and Grilli, R.: *A compact incoherent broadband cavity-enhanced absorption spectrometer for trace detection of nitrogen oxides, iodine oxide and glyoxal at levels below parts per billion for field applications*, Atmospheric Measurement Techniques, 13, 4317–4331, https://doi.org/10.5194/amt-13-4317-2020, 2020.

5.1.2 What is the chemical reactivity of the snowpack and how does it connect to the overlying oxidative atmosphere?

The high oxidative capacity of the central Antarctic atmosphere is driven by the snow emission of oxidized nitrogen gases (NO, NO_2, HONO) from photo-denitrification of nitrate in the snow. The difficulty in explaining the observed oxidative capacity of the atmosphere in Antarctica also lies in the fact that the deposition processes of reactive species in the snowpack are not yet fully understood. In fact, with today's knowledge, it is not possible to model this oxidizing capacity without a wide range of uncertainty. It is thus fundamental to understand the physical and chemical conditions that drive the NO_x emissions. Snow-tower experiments (Helmig et al., 2020) were designed to measure these phenomena in natural conditions. They are aiming at observing the seasonal and

long term variability of NO_x in the interstitial air (up to 1 m below the surface) and in the atmosphere (up to 10 m above the snow surface). However, information on the processes recorded by these experiments is difficult to extract because the atmospheric conditions, and, in particular the snowpack ventilation, are not yet fully constrained to use those sets of data. This context has led us to develop the flux chamber experiments presented in Chapter 3, in order to study the NO_x emissions processes in a controlled environment.

Therefore, new experiments were designed during my first two years of research and deployed in the Antarctic field during the 2019-2020 Dome C campaign with a focus on studying the snow nitrate photolysis. For the first time in the antarctic field, flux chamber experiments were performed with several snow samples of different ages ranging from newly formed drift snow to 6-year-old firn.

Surprisingly, a similar daily average nitrate photolysis rate constant, $J_{NO_3^-}$, of $(2.17 \pm 0.24) \times 10^{-8}$ s^{-1} (1σ) was obtained for the different types of snow samples, suggesting that the photolabile nitrate in snow behaves as a single-family source with common photochemical properties, supporting Chan et al. (2018) and Bock et al. (2016) modeling studies. Air-snow interactions of nitrate between the air and skin layer snow can be described as a combination of non-equilibrium surface adsorption and co-condensation on ice, coupled with solid-state diffusion inside the grain. Indeed, because drift snow (young) and snow collected in depth (old), despite showing radically different nitrate concentrations, possess the same photolysis rate under the same incident light flux, it can reasonably be concluded that nitrate is always accessible to photolysis in the same manner.

Daily average NO_x fluxes, F_{NO_x} were estimated to be $(3.9 \pm 0.7) \times 10^8$ molecules cm^{-2} s^{-1}, for the mid-December to early January period, which is lower, but in the same order of magnitude, than what has been estimated in previous studies. Using the SBDART and TARTES models and the results from the FC experiments, a critical parameter for the models, the product $\sigma_{NO_3^-}(\lambda, T)\phi(T, pH)$, was estimated at $(1.47 \pm 0.23) \times 10^{-27}$ m^2 $photon^{-1}$ (1σ) (with $300 < \lambda < 340$ nm). Assuming Chu and Anastasio (2003) nitrate ion cross-section of 1.20×10^{-20} cm^2 $molecules^{-1}$, a $\phi(T, pH) = 0.0012 \pm 0.0002$ photon molecule s^{-1} (with $300 < \lambda < 340$ nm) is estimated, significantly different than the value usually used in models: 0.003 photon molecule s^{-1}. The FC method allows to measure directly a NO_x production rate which is then extrapolated to a NO_x flux with some assumptions. Indeed, the underestimation of our NO_x fluxes could be due to: i) the *e*-folding depths that may have changed after the mechanical homogenizing, and a smaller *e*-folding depth that would lead to a lower NO_x production, therefore a lower NO_x flux estimation; ii) the air flow inside the chamber that may have undergone preferential pathways in the interconnected pore space of the snow matrix, also resulting in a smaller NO_x production, iii) as discussed in Frey et al. (2013), the observed night time increase in wind shear at Dome C likely that causes enhanced upward ventilation of NO_x which had been temporarily accumulated in the upper snow pack during very stable condition, leading to another underestimation of the NO_x fluxes during nighttime.

In summary, the flux chamber NO_x production measurements can be used directly in snowpack-air models, which simulate realistic in-snow transport. FC is an important tool to measure NO_x production and $\sigma_{NO_3^-}(\lambda, T)\phi(T, pH)$ product for defined snow samples under controlled natural conditions. However, to correctly estimate NO_x fluxes, it should be used in complementarity of the above-snow flux measurements using the gradient method.

Finally, this research has been submitted in April 2021, in the Journal of Geophysical Research: Atmospheres:

A. Barbero, J. Savarino, R. Grilli, C. Blouzon, G. Picard, M. M. Frey, Y. Huang and N. Caillon: *New estimation of the NO_x snow-source on the Antarctic Plateau*, Journal of Geophysical Research: Atmosphere, under review.

5.1.3 Does the high NO_2:NO ratio measured at Dome C represent a lack of our understanding of the NO_x chemistry?

Chapter 4 is reporting, for the first time, direct and in-situ atmospheric measurements of NO_2 that were carried out in the Antarctic Plateau, at Dome C. A comparison with past studies at Dome C, showed that the NO_2 mixing ratios have possibly been overestimated previously, especially during the late photolysis period (January).

Two sets of measurements were performed: in December 2019 during the early photolytic season, and in January 2020 during the late photolytic season. In the light of this new set of observations, the summer variability NO_2:NO was studied. While the NO_2:NO ratio observed late in the season (0.4 ± 0.4) is explainable by the extended Leighton's equilibrium involving RO_x (0.6 ± 0.3), we cannot yet explain the early season ratio through chemical mechanisms in the PBL. Indeed, in December, a NO_2:NO ratio of 1.3 ± 1.1 has been calculated from NO_2 and NO measurements, which is approximately twice the ratio of 0.7 ± 0.4 calculated from the extended Leighton's relationship, using in situ measurements of O_3 and J_{NO_2}, RO_2 and HO_2.

With constant NO levels throughout the season, the assumption of an additional conversion of NO to NO_2 through XO or RO_x is not sufficient and only the increased production of NO_2 from primary sources of NO_2 can explain the NO_2 excess observed in December and not in January. By using the characterization of the NO_x snow-source developed in Chapter 3 and long term snow surface sampling at Dome C, we found it could be indeed the explanation. However, unidentified mechanisms or unidentified sink of O_3, possibly emitted by the snow pack, is strongly suspected to be playing an important role in the O_3 diurnal variation.

5.2 Perspectives

The use of IBBCEAS technique for direct measurement of NO_2 and NO_x in remote low NO_x environment has been tested and validated during the course of my PhD as described in Chapter 2. However, in urban environment, the NO_x instrument is subject to substantial interferences, especially at night, due to the presence of N_2O_5 and the high O_3 levels in the O_3 generator. Further technical research to adapt the O_3 levels in the IBBCEAS-NO_x instrument in urban environment are needed. A new optical instrument for the measurement of NO was recently developed by our colleagues at LIPhy in Grenoble (Richard et al., 2018) and intercomparison experiments with our IBBCEAS in urban environment would help understand the artefact and therefore minimize or at least control and quantify it. Furthermore, in the future, this instrument based on the Optical-Feedback Cavity Enhanced technique (OF-CEAS) in the mid-IR region could be used for direct measurement of NO and coupled with direct measurements of NO_2 by the IBBCEAS system presented here in Chapter 2.

The findings of Chapters 3 and 4 will help improve the knowledge of the snow-pack reactivity and its connection to the overlying atmosphere, to decipher the mechanisms controlling the oxidative capacity of the Antarctic Plateau. Even though, the FC experiments were useful to confirm the mechanism of nitrate incorporation onto the snowpack, other experiments should be undertaken

with intact stratigraphy of a snow block. Additionally, tracer spike tests (e.g., with a sudden release of NO_2 in the FC) would allow to characterize the sample, constrain the porosity, and characterise the ventilation of the snowpack in controlled conditions. Longer FC experiments would also help understand the transitory regime. A confirmation that it is not linked to the steady state regime, as the results of our investigations seem to show, would allow to confirm the possible retrieval of nitrate $\sigma_{NO_3^-}(\lambda,T)\phi(T,pH)$ product through direct NO_x production rate for snows across the Antarctic continent and better estimate the atmospheric NO_x snow-sourced fluxes.

A more full understanding of the nitrate photolysis mechanism and how it is linked to the NO_x mixing ratios observed above the snowpack could also be acheived by using the isotopic signature of NO_2. Very recently, Albertin et al. (2020) developed an efficient method to collect atmospheric NO_2 for isotopic analysis. The authors argue for the high accuracy of the analytical field sampling method and confirm the sensitivity of the NO_2 isotope signature as a tracer of atmospheric chemical regimes and local emissions in polar urban environments. Unfortunatly, today, the technique is not adapted to remote polar environnement, therefore, laboratory research for adapting this multi-isotopic approach to such remote environment will allow the collection of $\delta^{15}N(NO_2)$, $\delta^{17}O(NO_2)$ and $\delta^{18}O(NO_2)$, in the snowpack and the overlying atmosphere. The results of such investigations would indeed allow to further deepen the study of the complete reactive nitrogen cycle.

Additionally, the suspected presence of halogen species in the snowpack and the emissions of halogenated radicals in the atmosphere could be further investigated. A follow up PhD project proposes to use an innovative technique, LP-DOAS (long-path differential optical absorption spectroscopy) which could be coupled with a drone for vertical profiles of atmospheric BrO (bromine monoxide) and IO (iodine monoxide). Those findings, coupled with open cavity measurements for IO with our IBBCEAS may help decipher the role of halogenated radicals in Antarctica.

Finally, this corpus of studies will allow to analyze currently available data sets across the Antarctic Plateau such as:

- Seven years of snow-tower experiment monitoring at Dome C: measurements of NO_x in the interstitial air (up to 1 m below the surface) and in the atmosphere (up to 10 m above the snow surface)
- Measurements of the snow chemical content (nitrate and halogens) and atmospheric NO_x during the East Antarctica International Ice Sheet Travers (EAIIST) from the Coast to the East Antarctic Plateau

Appendices

Appendix A

Supplementary material of Chapter 3

A.1 Meteorological conditions

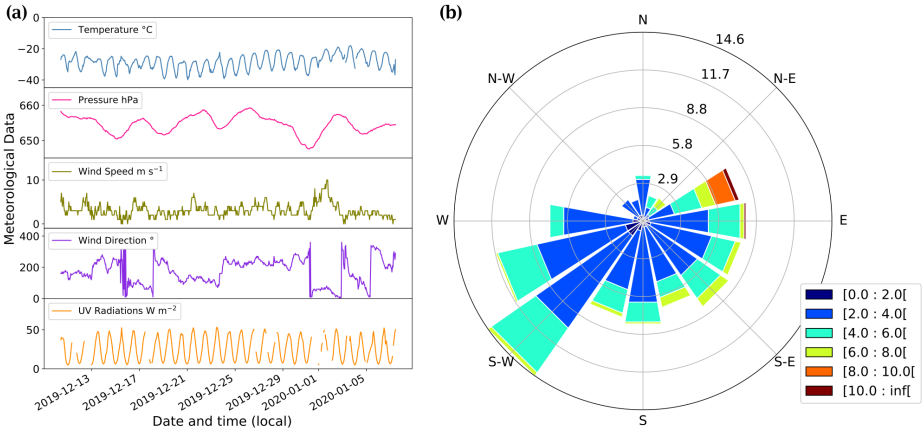

Figure A.1 – **(a)** Local meteorological conditions encountered during the experiments measured by the local AWS station (2-m observations) completed with a broadband UV radiometer, spectral range 305-385 nm and **(b)** the corresponding wind rose in m s^{-1} at Dome C during the FC experiments.

The meteorological conditions encountered during the 2019-2020 FC experiment (T_{mean} = -28 ± 4 °C; P_{mean} = 654 ± 3 hPa; $W_{speed-mean}$ = 3.4 ± 1.4 m s^{-1}; $W_{dir-mean}$ = 185 ± 79 °; and UV_{mean} = 25 ± 15 W m^{-2}) were typical of the summer climatology observed at Dome C. Two episodes of strong northeast wind (up to 10 m s^{-1}) occurred mid-December and early January (Fig. A.1). However, as the FC experiments are not subject to natural air flow, those episodes had no substantial impact on the results.

A.2 Transmission spectra of polymethyl methacrylate (PMMA)

The transparency and thickness of different types of PMMA were tested using a 6850 UV/Vis Spectrometer (JenWay Bibby Scientific) ranging from 200 to 1,100 nm. The results (Fig. A.2) show that the EBLA Brand is the most UV-transparent PMMA available.

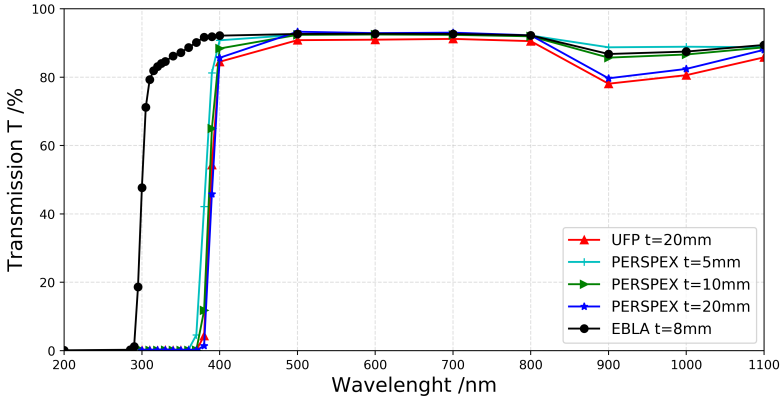

Figure A.2 – Transparency test of different brands (UFP, PERSPEX and EBLA) and thickness (5, 10, 8 and 20 mm) of PMMA.

A.3 Leighton equilibrium and ozone production

Estimations of ozone production in the flux chambers were calculated following Leighton's photostationary equilibrium (Leighton, 1961):

$$NO_2 + h\nu \quad (\lambda < 420 \quad \text{nm}) \rightarrow NO + O(^3P) \tag{RA.1}$$

$$O(^3P) + O_2 + M \rightarrow O_3 + M \tag{RA.2}$$

$$NO + O_3 \rightarrow NO_2 + O_2 \tag{RA.3}$$

If equilibrium is reached, then the concentrations of the species involved can be derived following Equation A.1:

$$[O_3] = \frac{J_{NO_2}[NO_2]}{k_{NO+O_3}[NO]} \tag{A.1}$$

where J_{NO_2} [s^{-1}] is the photolysis constant rate of reaction (R.A1) and k_{NO+O_3} [cm^3 $molecules^{-1}$ s^{-1}] is the reaction rate of reaction (R.A3). From Atkinson et al. (NIST Kinetics Database), the rate

expression of k_{NO+O_3} is given by $1.4 \times 10^{-12} \exp\left(\frac{-10.89[\pm 1.66]}{RT}\right)$ [cm^3 molecules^{-1} s^{-1}] and a J_{NO_2} = 0.016 s^{-1} is taken from Kukui et al. (2014). [O_3] estimations were calculated at the daily maximum and in the meteorological conditions of the experiments. The O_3 levels expected from the Leighton relationship were ranging from ~ 3 to 15 nmol mol^{-1} where 0.7 to 10 nmol mol^{-1} (Table A.1) where measured, confirming that equilibrium was not reached during the FC experiments.

Table A.1 – NO_2, NO and O_3 mixing ratios and meteorological parameters, P and T, at daily maximum observed during the FC experiments. The expected O_3 mixing ratio from Equation A.1 is reported at the bottom of the table.

Parameters	Values
NO_2 [nmol mol^{-1}]	0.21 to 3.46
NO [nmol mol^{-1}]	0.054 to 0.51
$O_{3\_measured}$ [nmol mol^{-1}]	0.7 to 10
P [atm]	648 to 655
T [°C]	-29 to -20
$O_{3\_expected}$ [nmol mol^{-1}]	2.9 to 15

A.4 Denitrification

Assuming one photolyzed molecule of NO_3^- produces one molecule of NO_x (Reactions R3.1 to R3.5 in the manuscript), the denitrification occurring during the experiments can be calculated following Equation A.2:

$$\%_{Den} = 100 \frac{N_{NO_{x_{total}}}}{N_{NO_{3\,total}^-}} \tag{A.2}$$

with $N_{NO_{x_{total}}}$ the total number of molecules of NO_x emitted during one experiment and $N_{NO_{3\,total}^-}$, the total number of NO_3^- molecules initially present in the chamber. $N_{NO_{3\,total}^-}$ and $N_{NO_{x_{total}}}$ are calculated for each experiment following Equations A.3 and A.4:

$$N_{NO_{x_{total}}} = \rho_{air} \frac{N_A}{M_{NO_x}} [NO_x] V_{FC} \tag{A.3}$$

$$N_{NO_{3\,total}^-} = \rho_{snow} \frac{N_A}{M_{NO_{3^-}}} [NO_3^-] V_{FC} \tag{A.4}$$

- N_A = Avogadro's number = 6.022×10^{23} molecules mol^{-1}
- M_{NO_x} = Molar mass of NO_x = 76.0155 g mol^{-1}
- $M_{NO_3^-}$ = Molar mass of NO_3^- = 62.0049 g mol^{-1}
- V_{FC} = Chamber volume ≈ 26,500 cm^3
- ρ_{snow} = snow density calculated by gravimetry g cm^{-3}
- ρ_{air} = air density in the snow ≈ 0.929×10^{-3} g cm^{-3} at Dome C

A.5 Local 2-7 cm layer contamination

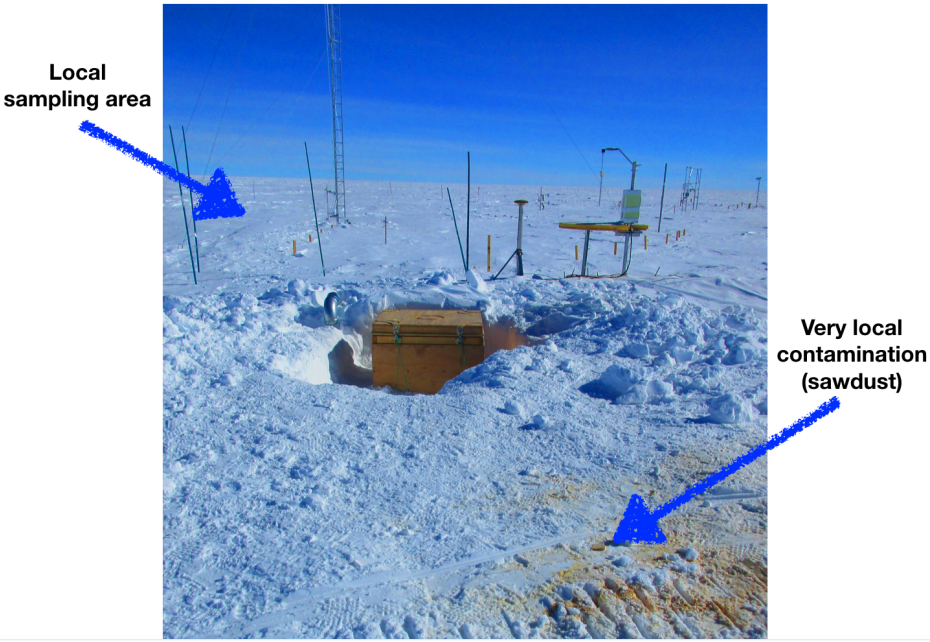

Figure A.3 – Picture taken in December 2018 showing the very local contamination, leading to the very different behaviour of the local 2-7 cm layer sample.

During the previous campaign of 2018-2019, a localized contamination occurred near the sampling area during a technical intervention necessary for the safety of the agents to access the snow-covered shelter containing the experiments as shown in Figure A.3.

A.6 Nitrate snow content profile

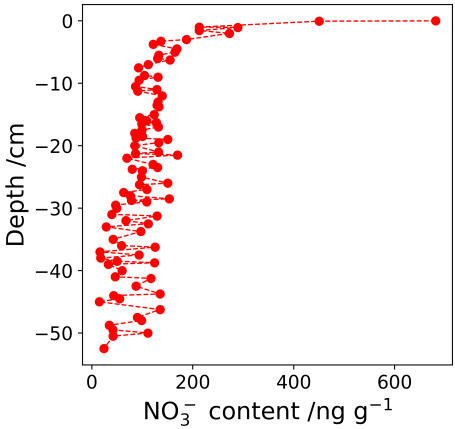

Figure A.4 – Profile of average NO_3^- concentration [ng g^{-1}] in the near surface snow column at Dome C.

As mentioned in the article, snow pits have been sampled at Dome C for several years through the programs NITEDC and CAPOXI. All the data corresponding to the observation period of the FC experiments were averaged giving the profile observed on Figure A.4. The average concentration of the photic zone is defined by the area under the averaged curve divided by the depth (Δz = 50cm), Equation A.5 hereafter, with z = -50 cm:

$$[NO_3^-]_{mean} = \frac{\int_z^0 [NO_3^-] dz}{\Delta z} \tag{A.5}$$

Using the trapezoidal rule, the average concentration found was [NO_3^-] = 108 ± 8 ng g^{-1}.

A.7 Length of days at Dome C

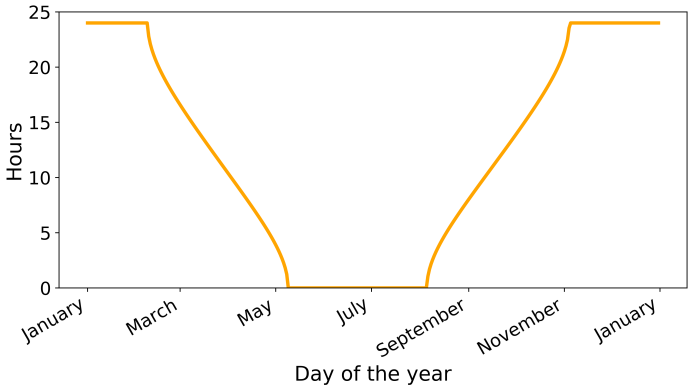

Figure A.5 – Hours of daylight over the year at Dome C.

Daylength calculation was made using a Center for Biosystems Modelling (CBM) model (Forsythe et al., 1995). The model estimates daylength with error less than one minute within 40 degrees of the equator and less than seven minutes within 60 degrees, described by Equations A.6, A.7 and A.8:

$$\theta = 0.2166108 + 2\arctan(0.9671396\tan(0.00860(J-186))) \tag{A.6}$$

$$\phi = \arcsin(0.39795\cos(\theta)) \tag{A.7}$$

$$D = 24 - \frac{24}{\pi}\arccos\left[\frac{\sin(\frac{p\pi}{180}) + \sin(\frac{L\pi}{180})\sin(\phi)}{\cos(\frac{L\pi}{180})\cos(\theta)}\right] \tag{A.8}$$

with θ the predicted revolution angle from the day of the year (J); ϕ the predicted sun's declination angle; D the predicted daylength from Latitude L, here L = -75.06. The daylength definition, defined by the position of the sun with respect to the horizon, chosen for this calculation is: sunrise/sunset is when the top of the sun is apparently even with horizon, giving p = 0.8333. Figure A.5 represents the length of day for one year at Dome C.

Appendix B

Supplementary material of Chapter 4

B.1 NOAA HYSPLIT backward trajectories

Using the HYSPLIT model, 5 days (120 hours) backward trajectories were conducted. For each, day of observation, 4 runs at different times (UTC): 00:00, 06:00, 12:00 and 18:00, therefore corresponding to 08:00, 14:00, 20:00 and 02:00 (day+1) local time (LT), at different altitudes: 3,200 a.m.s.l, 3,400 a.m.s.l and 3,800 a.m.s.l.

B.1.1 December

As mentionned in Chapter 4, the meteorological conditions and air masses origins in December were favorable for atmospheric measurements for the purpose of our study. Indeed, one can see on Figure B.1 that the air masses were originating from the Plateau during the observation period. The 9^{th} of December at 14:00 LT, i.e., 06:00 UTC, air masses at 3,800 a.m.s.l was simulated to be originating from the Antarctic Peninsula, but this had no impact on our observations as we stopped them around 10:00 LT.

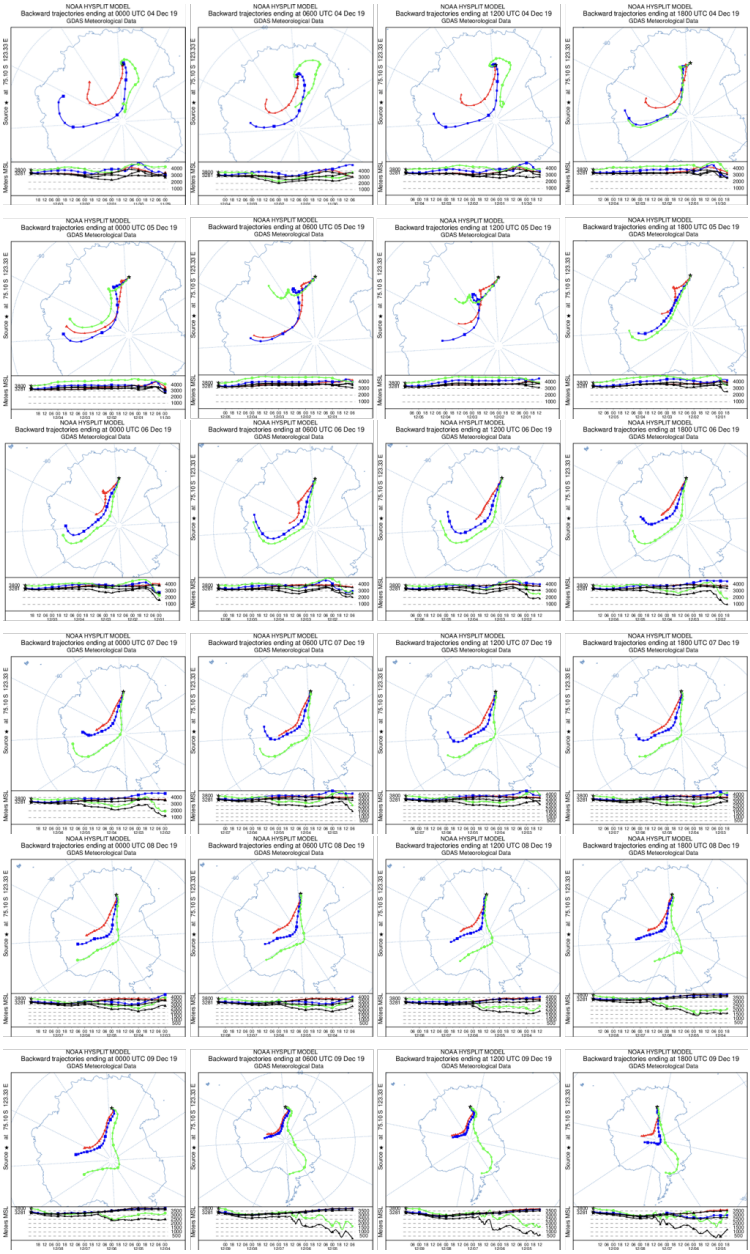

Figure B.1 – HYSPLIT 5 days backward trajectories from the 4^{th} to the 9^{th} of December 2019. The model was run every 6 hours for each day and at 3 different altitudes: 3,800 a.m.s.l (green), 3,400 a.m.s.l (blue) and 3,200 a.m.s.l (red).

B.1.2 January

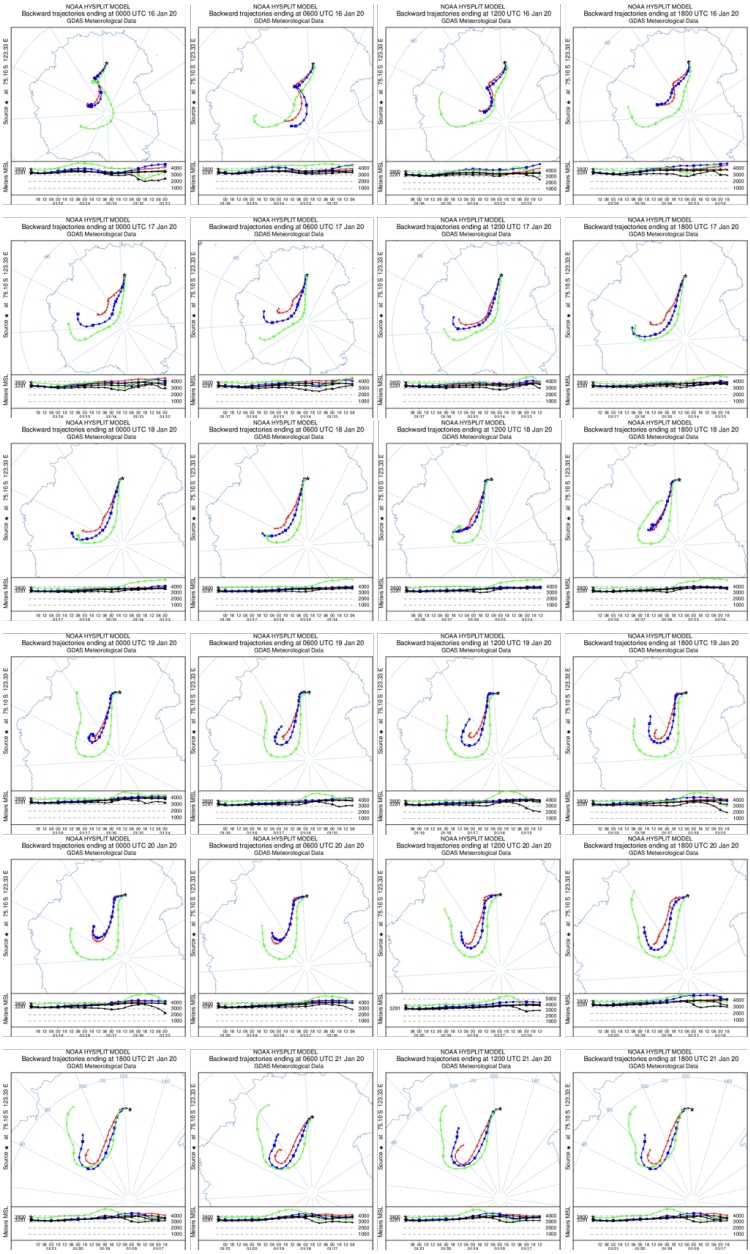

Figure B.2 – HYSPLIT 5 days backward trajectories from the 16^{th} to the 21^{st} of January 2020. The model was run every 6 hours for each day and at 3 different altitudes: 3,800 a.m.s.l (green), 3,400 a.m.s.l (blue) and 3,200 a.m.s.l (red).

As mentionned in Chapter 4, the meteorological conditions and air masses origins in January were favorable for atmospheric measurements from the 17^{th} to the 20^{th} of January (Fig. B.2).

However, the 10 ppbv drop of O_3 observed at the end of the observation period is suspected to be caused by oceanic inputs as suggested by Legrand et al. (2009). On Figure B.3, a drastic change in the origin of the ai masses is observed the 23^{rd} between 06:00 (UTC) and 12:00 (UTC), or 14:00 and 20:00 LT, corresponding to the sudden drop in O_3 mixing ratio around 17:00-18:00 LT.

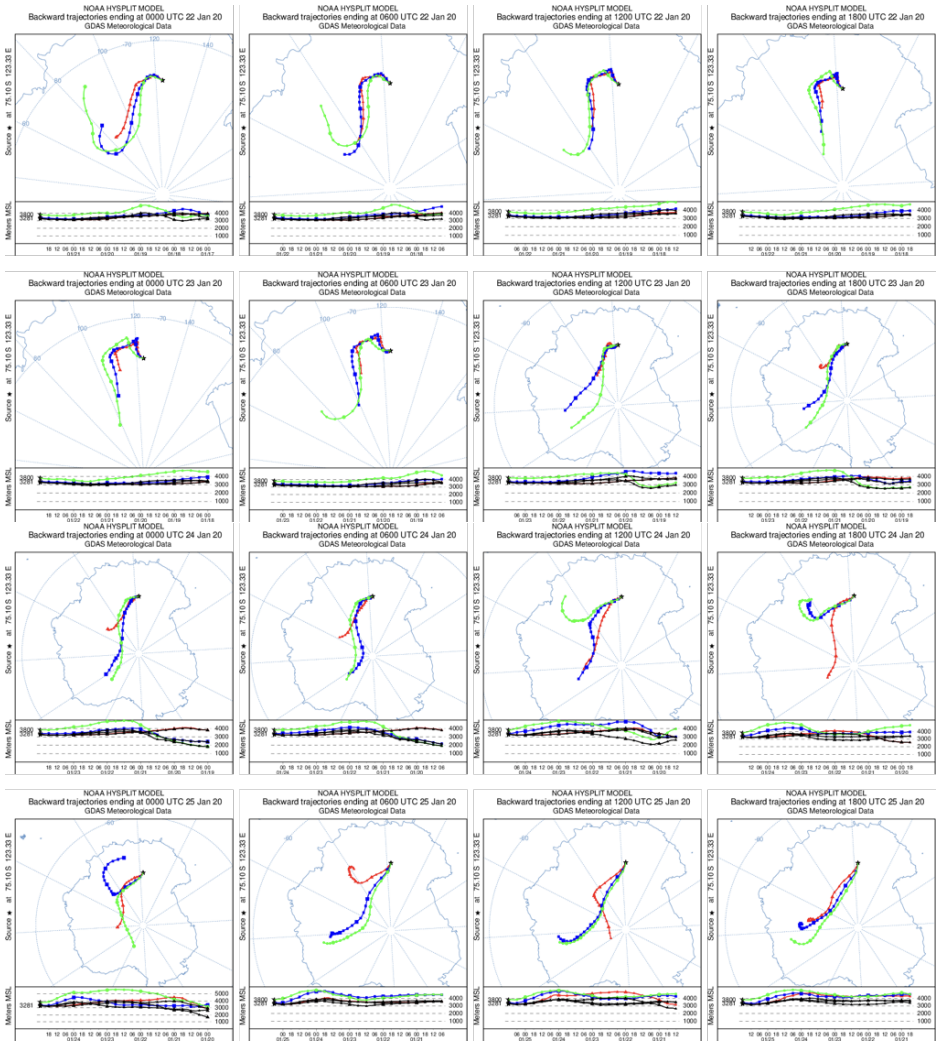

Figure B.3 – HYSPLIT 5 days backward trajectories from the 22^{nd} to the 25^{th} of January 2020. The model was run every 6 hours for each day and at 3 different altitudes: 3,800 a.m.s.l (green), 3,400 a.m.s.l (blue) and 3,200 a.m.s.l (red).

Figure B.4 shows the HYSPLIT 10 days backtrajectory estimation for the 23^{rd} of January ending at 20:00 LT at Dome C. One can see that for the 3,400 a.m.s.l, the model predicts air masses coming from the east coast of Antarctica, strengthening our conclusions of an air mass influenced by the ocean reaching the Antarctic Plateau, leading to the 10 ppbv O_3 drop observed in the early evening of the 23^{rd} of January 2020.

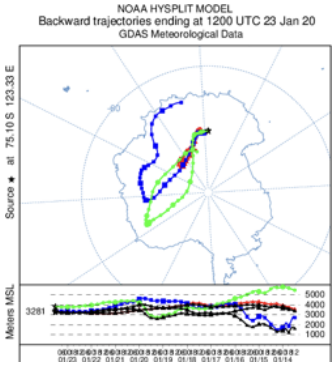

Figure B.4 – HYSPLIT 10 days backward trajectories of the 23^{rd} ending at 12:00 UTC (20:00 LT) at 3 different altitudes: 3,800 a.m.s.l (green), 3,400 a.m.s.l (blue) and 3,200 a.m.s.l (red).

B.2 Meteorological conditions

The wind rose of the January period (Fig. B.5.d) shows strong wind from the West/North-West direction. Looking at Figure B.5.c, this event occurred in late January, around the 23^{rd}, strengthening our hypothesis of ocean air masses that might have reached Dome C at the end of January.

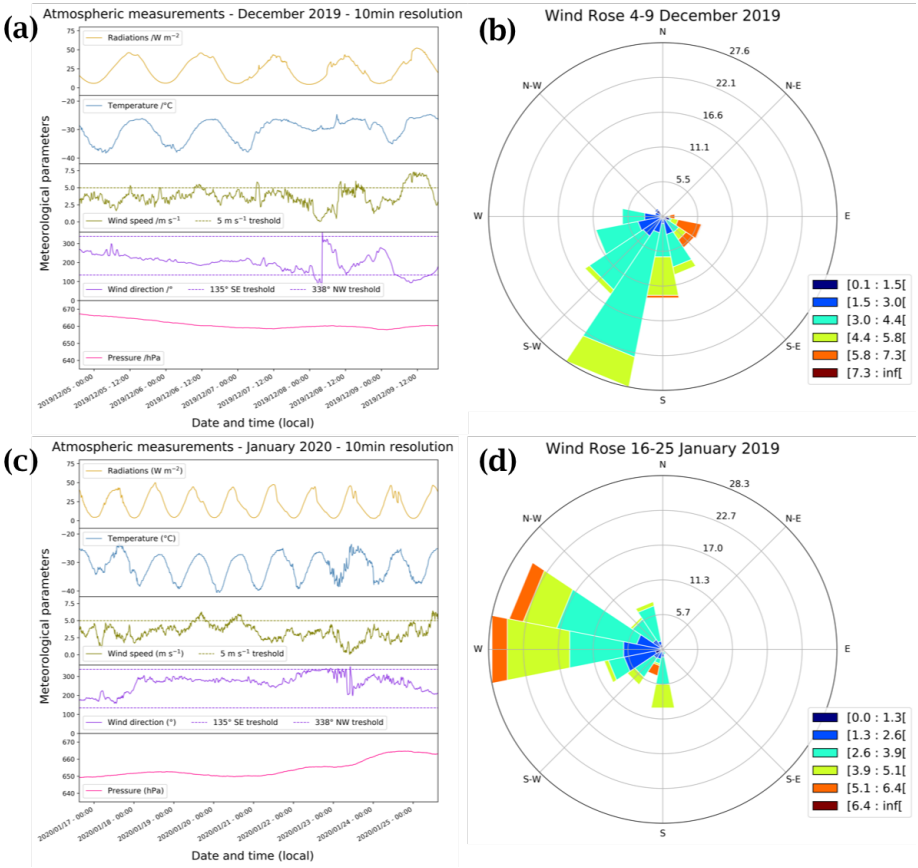

Figure B.5 – **(a)** and **(c)** Local meteorological conditions (2-m observations) encountered during the periods of atmospheric observations measured by the local automatic weather station (AWS– Vaisala Milos 520) completed with a broadband UV radiometer, spectral range 305–385 nm. **(b)** and **(d)** The corresponding wind rose in m s^{-1} at Dome C.

B.3 Snow-tower experiment

Figure B.6 shows the schematic of the snow-tower device, along with a photograph of one of the snow towers. We can see the two partially buried snow towers at the ends of the diagram, as well as the fully exposed atmospheric mast in the middle.

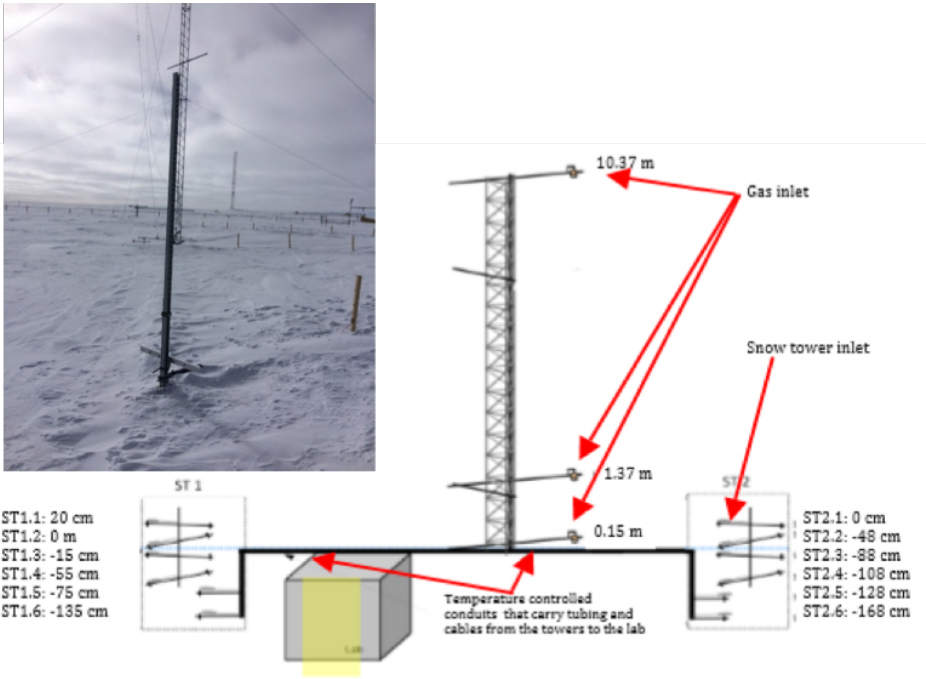

Figure B.6 – Snow-Tower installation at Dome C.

B.4 NO_2 photolysis rate coefficient reconstruction: $J_{NO_{2-recons}}$

The $J_{NO_{2-recons}}$ [s^{-1}] is reconstructed using a correlation fit analysis between the UV radiations signal and the sparse J_{NO_2} measurements obtained with the Met-Con 2π spectral radiometer (Fig. B.7). A two degrees polynomial function , Equation B.1, was found to be the best correlation fit (dashed black line in Fig. B.7).

$$J_{NO_{2-recons}} = a + bUV + cUV^2 \tag{B.1}$$

with $J_{NO_{2-recons}}$ the reconstructed photolysis rate coefficient; a, b and c the regression fits parameters; and UV the measured UV radiations.

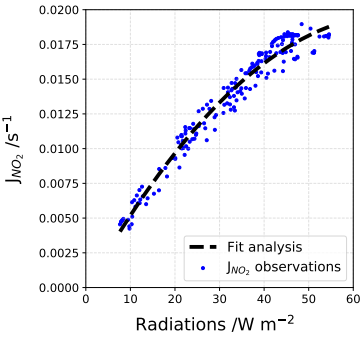

Figure B.7 – Fit analysis for the reconstruction of the $J_{NO_{2-recons}}$ signal.

Table B.1 gives the values of a, b and c parameters for the photolysis rate constant at both periods.

Table B.1 – Polynomial regresion fit parameters from Equation B.1 applied to reconstruct the photolysis rate coefficient signal.

	$J_{NO_{2-recons}} = a + bUV + cUV^2$		
	a	b	c
December 4^{th} to 9^{th}	0.0	5.722×10^{-04}	-4.141×10^{-06}
January 16^{th} to 25^{th}	0.0	7.029×10^{-04}	-7.868×10^{-06}

Figure B.8 represents the comparison between the reconstructed signal and the actual observations, on the bottom panel, the residual $\Delta J_{NO_{2-recons}}$ is represented showing a good agreement between the reconstructed signal and the original observations.

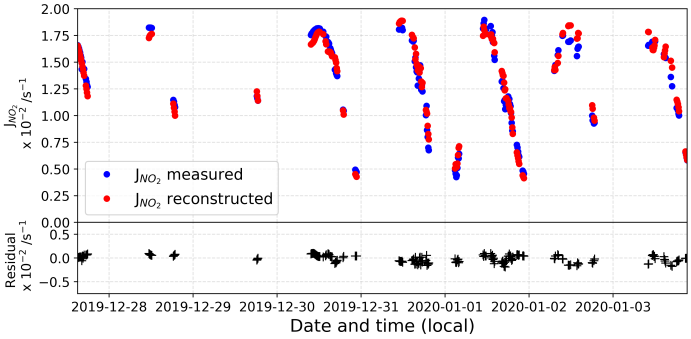

Figure B.8 – **(top)** Comparison between reconstructed and measured signal and **(bottom)** residual.

B.5 RO_x estimation from J_{NO_2}

Using the linear correlation between RO_2 and J_{NO_2} given by Kukui et al. (2014) (Fig. B.9.a); the RO_2 data from OPALE campaign (Kukui et al., 2014); and the reconstructed J_{NO_2} signal, we were able to estimate the RO_2 and HO_2 total number of molecules in the atmospheric boundary layer at Dome C during our periods of observation (Fig. B.9.b and B.9.c).

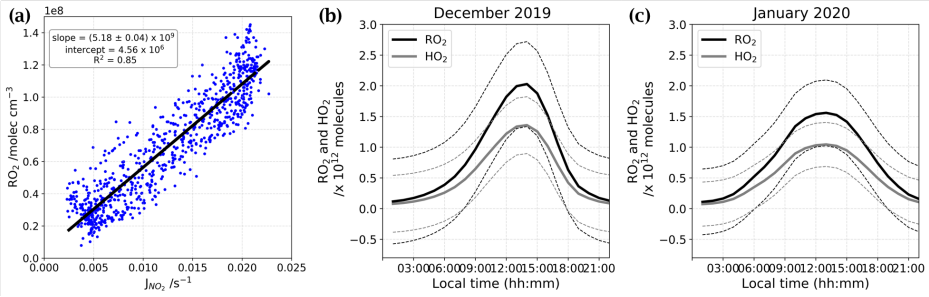

Figure B.9 – **(a)** linear correlation between RO_2 and J_{NO_2} taken from Kukui et al. (2014). **(b)** and **(c)** total number of molecules of RO_2 (black) and HO_2 (grey) estimated for both periods of observations.

B.6 Polar boundary layer height (H_{PBL})

The regional climate model MAR, which has been applied extensively for studying the polar regions, e.g., Agosta et al. (2019); Gallée et al. (2015b); Gallée and Gorodetskaya (2010), was used in its latest Antarctic configuration: version 3.11 (Kittel et al., 2020), including drifting-snow physics (Amory et al., 2020) at 35 km resolution and forced by ERA5 reanalysis (https://www.ecmwf.int/en/forecasts) to generate the Boundary Layer height extracted every hour to match the timestamp of our observations. Boundary layer height at Dome C during both periods of observations extracted from the regional model MAR are presented in Figure B.10.

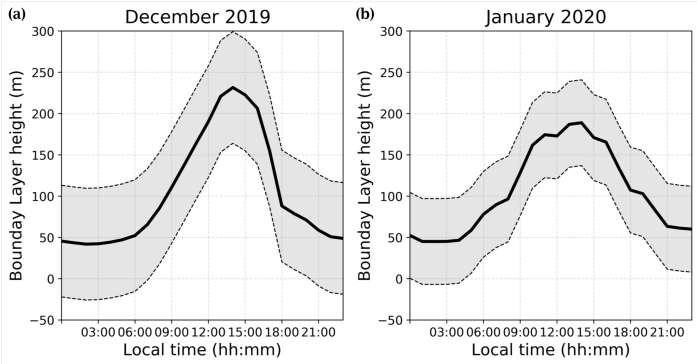

Figure B.10 – Atmospheric Boundary Layer height (PBL) (solid lines) ± 1σ (dashed lines) estimated for both periods by the MAR regional model.

B.7 Reactions and their chemical rates

The list of reactions at stakes in Dome C troposphere with the associated daily average chemical rates based on their expression given by Atkinson (1998, 2003); Atkinson et al. (2004, 2007), J_{NO_2} measurements and $J_{NO_3^-}$ estimation from Chapter 3, for Dome C conditions.

O_x reaction

$$O_3 + h\nu \rightarrow \text{products} \qquad (J_{O^1D} \approx 3.76 \times 10^{-5} s^{-1}) \qquad \text{(RB.1)}$$

HO_x reaction

$$HO_2 + O_3 \rightarrow OH + 2O_2 \qquad (k_{HO_2+O_3} \approx 1.2 \times 10^{-15} cm^3 molecules^{-1} s^{-1}) \qquad \text{(RB.2)}$$

NO_x reaction

$$OH + NO + M \rightarrow HONO + M \qquad (k_{OH+NO} \approx 1.0 \times 10^{-11} cm^3 molecules^{-1} s^{-1}) \qquad \text{(RB.3)}$$

$$OH + NO_2 + M \rightarrow HONO_2 + M \qquad (k_{OH+NO_2} \approx 1.8 \times 10^{-11} cm^3 molecules^{-1} s^{-1}) \qquad \text{(RB.4)}$$

$$HO_2 + NO \rightarrow OH + NO_2 \qquad (k_{HO_2+NO} \approx 1.1 \times 10^{-11} cm^3 molecules^{-1} s^{-1}) \qquad \text{(RB.5)}$$

$$NO + O_3 \rightarrow NO_2 + O_2 \qquad (k_{NO+O_3} \approx 6.3 \times 10^{-15} cm^3 molecules^{-1} s^{-1}) \qquad \text{(RB.6)}$$

$$HONO + h\nu \rightarrow \text{products} \qquad (J_{HONO} \approx 1.2 \times 10^{-3} s^{-1}) \qquad \text{(RB.7)}$$

$$NO_2 + h\nu \rightarrow \text{products} \qquad (J_{NO_2} \approx 1.3 \times 10^{-2} s^{-1}) \qquad \text{(RB.8)}$$

ClO_x reaction

$$ClO + NO \rightarrow Cl + NO_2 \qquad (k_{ClO+NO} \approx 2.1 \times 10^{-11} cm^3 molecules^{-1} s^{-1}) \qquad \text{(RB.9)}$$

$$ClO + NO_2 + M \rightarrow ClONO_2 + M \qquad (k_{ClO+NO_2} \approx 2.0 \times 10^{-11} cm^3 molecules^{-1} s^{-1}) \qquad \text{(RB.10)}$$

BrO_x reaction

$$BrO + NO \rightarrow Br + NO_2 \qquad (k_{BrO+NO} \approx 2.5 \times 10^{-11} cm^3 molecules^{-1} s^{-1}) \qquad \text{(RB.11)}$$

$$BrO + NO_2 + M \rightarrow BrONO_2 + M \qquad (k_{BrO+NO_2} \approx 1.9 \times 10^{-11} cm^3 molecules^{-1} s^{-1}) \qquad \text{(RB.12)}$$

IO_x reaction

$$IO + NO \rightarrow I + NO_2 \qquad (k_{IO+NO} \approx 2.8 \times 10^{-11} cm^3 molecules^{-1} s^{-1}) \qquad \text{(RB.13)}$$

$$IO + NO_2 + M \rightarrow IONO_2 + M \qquad (k_{IO+NO_2} \approx 1.2 \times 10^{-11} cm^3 molecules^{-1} s^{-1}) \qquad \text{(RB.14)}$$

From the list above, one can see that the chemical sources of NO_2 and sinks from RO_x and XO have similar rates.

List of Tables

List of Figures

Bibliography

Agosta, C., Amory, C., Kittel, C., Orsi, A., Favier, V., Gallée, H., van den Broeke, M. R., Lenaerts, J. T. M., van Wessem, J. M., van de Berg, W. J., and Fettweis, X.: Estimation of the Antarctic surface mass balance using the regional climate model MAR (1979–2015) and identification of dominant processes, The Cryosphere, 13, 281–296, doi:10.5194/tc-13-281-2019, 2019.

Albertin, S., Savarino, J., Bekki, S., Barbero, A., and Caillon, N.: Measurement report: Nitrogen isotopes (δ^{15}N) and first quantification of oxygen isotope anomalies (Δ^{17}O, δ^{18}O) in atmospheric nitrogen dioxide, preprint, doi:10.5194/acp-2020-1143, 2020.

Amory, C., Kittel, C., Le Toumelin, L., Agosta, C., Delhasse, A., Favier, V., and Fettweis, X.: Performance of MAR (v3.11) in simulating the drifting-snow climate and surface mass balance of Adelie Land, East Antarctica, preprint, Cryosphere, doi:10.5194/gmd-2020-368, 2020.

Anderson, J. G., Toohey, D. W., and Brune, W. H.: Free radicals within the Antarctic vortex: the role of CFCs in Antarctic ozone loss, Science, 251, 39–46, doi:10.1126/science.251.4989.39, 1991.

Anderson, P. S. and Bauguitte, S. J.-B.: Behaviour of tracer diffusion in simple atmospheric boundary layer models, Atmospheric Chemistry and Physics, 7, 5147–5158, doi:10.5194/acp-7-5147-2007, 2007.

Arenillas, A., García, R., Sun, C., Snape, C. E., Moreno, A. H., Rubiera, F., and Pis, J. J.: Use of nitrogen stable isotope analysis to understand char nitrogen evolution during the fluidized-bed co-combustion of coal and sewage sludge, Energy & Fuels, 19, 485–488, doi:10.1021/ef049857y, 2005.

Atkinson, D. B.: Solving chemical problems of environmental importance using Cavity Ring-Down Spectroscopy, The Analyst, 128, 117–125, doi:10.1039/b206699h, 2003.

Atkinson, R.: Atmospheric chemistry of VOCs and NOV, Atmospheric Environment, 34, 2063–2101, doi:10.1016/S1352-2310(99)00460-4, 1998.

Atkinson, R., Baulch, D. L., Cox, R. A., Crowley, J. N., Hampson, R. F., Hynes, R. G., Jenkin, M. E., Rossi, M. J., and Troe, J.: Evaluated kinetic and photochemical data for atmospheric chemistry: Volume I - gas phase reactions of O_x, HO_x, NO_x and SO_x species, Atmospheric Chemistry and Physics, 4, 1461–1738, doi:10.5194/acp-4-1461-2004, 2004.

Atkinson, R., Baulch, D. L., Cox, R. A., Crowley, J. N., Hampson, R. F., Hynes, R. G., Jenkin, M. E., Rossi, M. J., and Troe, J.: Evaluated kinetic and photochemical data for atmospheric chemistry: Volume III – gas phase reactions of inorganic halogens, Atmospheric Chemistry and Physics, 7, 981–1191, doi:10.5194/acp-7-981-2007, 2007.

Baccarini, A., Karlsson, L., Dommen, J., Duplessis, P., Vüllers, J., Brooks, I. M., Saiz-Lopez, A., Salter, M., Tjernström, M., Baltensperger, U., Zieger, P., and Schmale, J.: Frequent new particle formation over the high Arctic pack ice by enhanced iodine emissions, Nature Communications, 11, 4924, doi:10.1038/s41467-020-18551-0, 2020.

Baergen, A. M. and Donaldson, D. J.: Photochemical renoxification of nitric acid on real urban grime, Environmental Science & Technology, 47, 815–820, doi:10.1021/es3037862, 2013.

Barbero, A., Blouzon, C., Savarino, J., Caillon, N., Dommergue, A., and Grilli, R.: A compact incoherent broadband cavity-enhanced absorption spectrometer for trace detection of nitrogen oxides, iodine oxide and glyoxal at levels below parts per billion for field applications, Atmospheric Measurement Techniques, 13, 4317–4331, doi:10.5194/amt-13-4317-2020, 2020.

Bartels-Rausch, T. and Donaldson, D. J.: HONO and NO_2 evolution from irradiated nitrate-doped ice and frozen nitrate solutions, preprint, doi:10.5194/acpd-6-10713-2006, 2006.

Bauguitte, S. J.-B., Bloss, W. J., Evans, M. J., Salmon, R. A., Anderson, P. S., Jones, A. E., Lee, J. D., Saiz-Lopez, A., Roscoe, H. K., Wolff, E. W., and Plane, J. M. C.: Summertime NO_x measurements during the CHABLIS campaign: can source and sink estimates unravel observed diurnal cycles?, Atmospheric Chemistry and Physics, 12, 989–1002, doi:10.5194/acp-12-989-2012, 2012.

Becagli, S., Proposito, M., Benassai, S., Flora, O., Genoni, L., Gragnani, R., Largiuni, O., Pili, S. L., Severi, M., Stenni, B., Traversi, R., Udisti, R., and Frezzotti, M.: Chemical and isotopic snow variability in East Antarctica along the 2001/02 ITASE traverse, Annals of Glaciology, 39, 473–482, doi:10.3189/172756404781814636, 2004.

Beine, H. J., Honrath, R. E., Dominé, F., Simpson, W. R., and Fuentes, J. D.: NO_x during background and ozone depletion periods at Alert: Fluxes above the snow surface, Journal of Geophysical Research, 107, 12, doi:10.1029/2002JD002082, 2002.

Berhanu, T. A., Savarino, J., Erbland, J., Vicars, W. C., Preunkert, S., Martins, J. F., and Johnson, M. S.: Isotopic effects of nitrate photochemistry in snow: a field study at Dome C, Antarctica, Atmospheric Chemistry and Physics, 15, 11 243–11 256, doi:10.5194/acp-15-11243-2015, 2015.

Berresheim, H. and Eisele, F. L.: Sulfur Chemistry in the Antarctic Troposphere Experiment: An overview of project SCATE, Journal of Geophysical Research: Atmospheres, 103, 1619–1627, doi:10.1029/97JD00103, 1998.

Besnard, K. and Pokryszka, Z.: Gases emission monitoring in a post-mining context, Symposium Post Mining 2005, Nancy, France, ineris-00972521, 12, 2005.

Blaszczak-Boxe, C. S. and Saiz-Lopez, A.: Nitrate photolysis in ice and snow: A critical review of its multiphase chemistry, Atmospheric Environment, 193, 224–241, doi:10.1016/j.atmosenv.2018.09.002, 2018.

Bloss, W. J., Evans, M. J., Lee, J. D., Sommariva, R., Heard, D. E., and Pilling, M. J.: The oxidative capacity of the troposphere: Coupling of field measurements of OH and a global chemistry transport model, Faraday Discussions, 130, 425, doi:10.1039/b419090d, 2005.

Bloss, W. J., Lee, J. D., Heard, D. E., and Salmon, R. A.: Observations of OH and HO_2 radicals in coastal Antarctica, Atmospheric Chemistry and Physics, 7, 4171–4185, doi:10.5194/acp-7-4171-2007, 2007.

Bloss, W. J., Camredon, M., Lee, J. D., Heard, D. E., Plane, J. M. C., Saiz-Lopez, A., Bauguitte, S. J.-B., Salmon, R. A., and Jones, A. E.: Coupling of HO_x, NO_x and halogen chemistry in the Antarctic boundary layer, Atmospheric Chemistry and Physics, 10, 10 187–10 209, doi:10.5194/acp-10-10187-2010, 2010.

Bock, J., Savarino, J., and Picard, G.: Air–snow exchange of nitrate: a modelling approach to investigate physicochemical processes in surface snow at Dome C, Antarctica, Atmospheric Chemistry and Physics, 16, 12 531–12 550, doi:10.5194/acp-16-12531-2016, 2016.

Brandt, R. E. and Warren, S. G.: Solar-heating rates and temperature profiles in Antarctic snow and ice, Journal of Glaciology, 39, 12, doi:10.3189/s0022143000015756, 1993.

Briday, R.: Une histoire de la chimie atmosphérique globale: enjeux disciplinaires et d'expertise de la couche d'ozone et du changement climatique, Ph.D. thesis, École des hautes études en sciences sociales (EHESS), 2014.

Brown, S. S., Stark, H., Ciciora, S. J., McLaughlin, R. J., and Ravishankara, A. R.: Simultaneous in situ detection of atmospheric NO_3 and N_2O_5 via Cavity Ring-Down Spectroscopy, Review of Scientific Instruments, 73, 3291–3301, doi:10.1063/1.1499214, 2002.

Browne, E. C., Wooldridge, P. J., Min, K.-E., and Cohen, R. C.: On the role of monoterpene chemistry in the remote continental boundary layer, Atmospheric Chemistry and Physics, 14, 1225–1238, doi:10.5194/acp-14-1225-2014, 2014.

Brune, W. H., Anderson, J. G., and Chan, K. R.: In situ observations of BrO over Antarctica: ER-2 aircraft results from 54°S to 72°S latitude, Journal of Geophysical Research, 94, 16 639, doi:10.1029/JD094iD14p16639, 1989.

Burkholder, J., Talukdar, A., Ravishankar, A. R., and Susansolomon, A.: Temperature Dependence of the HNO_3 UV Absorption Cross, Journal of Geophysical Research, 98, 22,937–22,948, doi:10.1029/93JD02178, 1993.

Burkholder, J. B., Curtius, J., Ravishankara, A. R., and Lovejoy, E. R.: Laboratory studies of the homogeneous nucleation of iodine oxides, Atmospheric Chemistry and Physics, 4, 19–34, doi:10.5194/acp-4-19-2004, 2004.

Carpenter, L., Wevill, D., Palmer, C., and Michels, J.: Depth profiles of volatile iodine and bromine-containing halocarbons in coastal Antarctic waters, Marine Chemistry, 103, 227–236, doi:10.1016/j.marchem.2006.08.003, 2007.

Carroll, M. A., Sanders, R. W., Solomon, S., and Schmeltekopf, A. L.: Visible and near-ultraviolet spectroscopy at McMurdo Station, Antarctica: 6. Observations of BrO, Journal of Geophysical Research, 94, 16 633, doi:10.1029/JD094iD14p16633, 1989.

Chan, H. G., King, M. D., and Frey, M. M.: The impact of parameterising light penetration into snow on the photochemical production of NO_x and OH radicals in snow, Atmospheric Chemistry and Physics, 15, 7913–7927, doi:10.5194/acp-15-7913-2015, 2015.

Chan, H. G., Frey, M. M., and King, M. D.: Modelling the physical multiphase interactions of HNO_3 between snow and air on the Antarctic Plateau (Dome C) and coast (Halley), Atmospheric Chemistry and Physics, 18, 1507–1534, doi:10.5194/acp-18-1507-2018, 2018.

Chan, K. L., Pöhler, D., Kuhlmann, G., Hartl, A., Platt, U., and Wenig, M. O.: NO_2 measurements in Hong Kong using LED based Long Path Differential Optical Absorption Spectroscopy, Atmospheric Measurement Techniques, 5, 901–912, doi:10.5194/amt-5-901-2012, 2012.

Chapman, S.: A Theory of Upper-Atmospheric Ozone, Memoirs of the Royal Meteorological Society, 111, 103–125, 1930.

Chu, L. and Anastasio, C.: Quantum Yields of hydroxyl radical and nitrogen dioxide from the photolysis of nitrate on ice, The Journal of Physical Chemistry A, 107, 9594–9602, doi:10.1021/jp0349132, 2003.

Clemitshaw, K.: A review of instrumentation and measurement techniques for ground-based and airborne field studies of gas-phase tropospheric chemistry, Critical Reviews in Environmental Science and Technology, 34, 1–108, doi:10.1080/10643380490265117, 2004.

Cooper, R. N., Houghton, J. T., McCarthy, J. J., and Metz, B.: Climate Change 2001: The Scientific Basis, Foreign Affairs, 81, 208, doi:10.2307/20033020, 2002.

Cotel, S., Schäfer, G., Traverse, S., Marzougui-Jaafar, S., Gay, G., and Razakarisoa, O.: Evaluation of VOC fluxes at the soil-air interface using different flux chambers and a quasi-analytical approach, Water, Air, & Soil Pollution, 226, 356, doi:10.1007/s11270-015-2596-y, 2015.

Cotter, E. S. N., Jones, A. E., and Wolff, E. W.: What controls photochemical NO and NO_2 production from Antarctic snow? Laboratory investigation assessing the wavelength and temperature dependence, Journal of Geophysical Research, 108, 10, doi:10.1029/2002JD002602, 2003.

Couach, O., Balin, J., Jimenez, R., Rjstorj, P., Simeonov, V., Quaglia, P., and Clappier, A.: Etude d'un épisode photochimique à l'alde d'un modèle méso-échelle et de mesures intensives sur la région de Grenoble - Study of a photochemical episode over the Grenoble area using a mesoscale model and intensive measurements, Pollution Atmosphérique, 174, 19, 2002.

Crowley, J. N., Ammann, M., Cox, R. A., Hynes, R. G., Jenkin, M. E., Mellouki, A., Rossi, M. J., Troe, J., and Wallington, T. J.: Evaluated kinetic and photochemical data for atmospheric chemistry: Volume V – heterogeneous reactions on solid substrates, Atmospheric Chemistry and Physics, 10, 9059–9223, doi:10.5194/acp-10-9059-2010, 2010.

Crutzen, P. J.: The influence of nitrogen oxides on the atmospheric ozone content, Quarterly Journal of the Royal Meteorological Society, 96, 320–325, doi:10.1002/qj.49709640815, 1970.

Crutzen, P. J.: My Life with O_3, NO_x, and Other YZO_x Compounds (Nobel Lecture), Angewandte Chemie International Edition in English, 35, 1758–1777, doi:10.1002/anie.199617581, 1996.

Davidson, E. A. and Kingerlee, W.: A global inventory of nitric oxide emissions from soils, Nutrient Cycling in Agroecosystems, 48, 37–50, doi:10.1023/A:1009738715891, 1997.

Davis, D., Eisele, F., Chen, G., Crawford, J., Huey, G., Tanner, D., Slusher, D., Mauldin, L., Oncley, S., Lenschow, D., Semmer, S., Shetter, R., Lefer, B., Arimoto, R., Hogan, A., Grube, P., Lazzara, M., Bandy, A., Thornton, D., Berresheim, H., Bingemer, H., Hutterli, M., McConnell, J., Bales, R., Dibb, J., Buhr, M., Park, J., McMurry, P., Swanson, A., Meinardi, S., and Blake, D.: An overview

of ISCAT 2000, Atmospheric Environment, 38, 5363–5373, doi:10.1016/j.atmosenv.2004.05.037, 2004.

Davis, D., Seelig, J., Huey, G., Crawford, J., Chen, G., Wang, Y., Buhr, M., Helmig, D., Neff, W., and Blake, D.: A reassessment of Antarctic plateau reactive nitrogen based on ANTCI 2003 airborne and ground based measurements, Atmospheric Environment, 42, 2831–2848, doi:10.1016/j.atmosenv.2007.07.039, 2008.

DeConto, R. M. and Pollard, D.: Contribution of Antarctica to past and future sea-level rise, Nature, 531, 591–597, doi:10.1038/nature17145, 2016.

Delon, C., Reeves, C. E., Stewart, D. J., Serça, D., Dupont, R., Mari, C., Chaboureau, J.-P., and Tulet, P.: Biogenic nitrogen oxide emissions from soils – impact on NO_x and ozone over West Africa during AMMA (African Monsoon Multidisciplinary Experiment): modelling study, Atmospheric Chemistry and Physics, 8, 2351–2363, doi:10.5194/acp-8-2351-2008, 2008.

Demtröder, W.: Laser Spectroscopy 1, Springer Berlin Heidelberg, Berlin, Heidelberg, doi:10.1007/978-3-642-53859-9, 2014.

Dennison, P., Charoensiri, K., Roberts, D., Peterson, S., and Green, R.: Wildfire temperature and land cover modeling using hyperspectral data, Remote Sensing of Environment, 100, 212–222, doi:10.1016/j.rse.2005.10.007, 2006.

Deshler, T., Adriani, A., Hofmann, D. J., and Gobbi, G. P.: Evidence for denitrification in the 1990 Antarctic spring stratosphere: II. Lidar and aerosol measurements, Geophysical Research Letters, 18, 1999–2002, doi:10.1029/91GL02311, 1991.

Domine, F. and Shepson, P. B.: Air-Snow Interactions and Atmospheric Chemistry, Science, 297, 1506–1510, doi:10.1126/science.1074610, 2002.

Domine, F., Albert, M., Huthwelker, T., and Simpson, W. R.: Snow physics as relevant to snow photochemistry, Atmospheric Chemistry and Physics, 8, 171–208, doi:10.5194/acp-8-171-2008, 2008.

Dooly, G., Fitzpatrick, C., and Lewis, E.: Deep UV based DOAS system for the monitoring of nitric oxide using ratiometric separation techniques, Sensors and Actuators B: Chemical, 134, 317–323, doi:10.1016/j.snb.2008.05.011, 2008.

Duan, J., Qin, M., Ouyang, B., Fang, W., Li, X., Lu, K., Tang, K., Liang, S., Meng, F., Hu, Z., Xie, P., Liu, W., and Häsler, R.: Development of an incoherent broadband cavity-enhanced absorption spectrometer for in situ measurements of HONO and NO_2, Atmospheric Measurement Techniques, 11, 4531–4543, doi:10.5194/amt-11-4531-2018, 2018.

Ehhalt, D., Prather, M., Dentener, F., Derwent, R., Dlugokencky, E., Holland, E., Isaksen, I., Katima, J., Kirchhoff, V., Matson, P., Midgley, P., Wang, M., Berntsen, T., Bey, I., Brasseur, G., Buja, L., Collins, W. J., Daniel, J., DeMore, W. B., Derek, N., Dickerson, R., Etheridge, D., Feichter, J., Fraser, P., Friedl, R., Fuglestvedt, J., Gauss, M., Grenfell, L., Grübler, A., Harris, N., Hauglustaine, D., Horowitz, L., Jackman, C., Jacob, D., Jaeglé, L., Jain, A., Kanakidou, M., Karlsdottir, S., Ko, M., Kurylo, M., Lawrence, M., Logan, J. A., Manning, M., Mauzerall, D., McConnell, J., Mickley, L., Montzka, S., Müller, J. F., Olivier, J., Pickering, K., Pitari, G., Roelofs, G. J., Rogers, H., Rognerud, B., Smith, S., Solomon, S., Staehelin, J., Steele, P., Stevenson, D., Sundet, J., Thompson, A., van Weele, M., Joos, F., and McFarland, M.: Atmospheric Chemistry and Greenhouse Gases, IPCC, pp. 240–287, 2018.

Eisele, F., Davis, D., Helmig, D., Oltmans, S., Neff, W., Huey, G., Tanner, D., Chen, G., Crawford, J., and Arimoto, R.: Antarctic Tropospheric Chemistry Investigation (ANTCI) 2003 overview, Atmospheric Environment, 42, 2749–2761, doi:10.1016/j.atmosenv.2007.04.013, 2008.

Eklund, B.: Practical guidance for flux chamber measurements of fugitive volatile organic emission rates, Journal of the Air & Waste Management Association, 42, 1583–1591, doi:10.1080/10473289.1992.10467102, 1992.

EPICA community members: Eight glacial cycles from an Antarctic ice core, Nature, 429, 623–628, doi:10.1038/nature02599, 2004.

Erbland, J., Vicars, W. C., Savarino, J., Morin, S., Frey, M. M., Frosini, D., Vince, E., and Martins, J. M. F.: Air–snow transfer of nitrate on the East Antarctic Plateau – Part 1: Isotopic evidence for a photolytically driven dynamic equilibrium in summer, Atmospheric Chemistry and Physics, 13, 6403–6419, doi:10.5194/acp-13-6403-2013, 2013.

Erbland, J., Savarino, J., Morin, S., France, J. L., Frey, M. M., and King, M. D.: Air–snow transfer of nitrate on the East Antarctic Plateau – Part 2: An isotopic model for the interpretation of deep ice-core records, Atmospheric Chemistry and Physics, 15, 12 079–12 113, doi:10.5194/acp-15-12079-2015, 2015.

Ervens, B., Turpin, B. J., and Weber, R. J.: Secondary organic aerosol formation in cloud droplets and aqueous particles (aqSOA): a review of laboratory, field and model studies, Atmospheric Chemistry and Physics, 11, 11 069–11 102, doi:10.5194/acp-11-11069-2011, 2011.

Fahey, D. W., Kelly, K. K., Kawa, S. R., Tuck, A. F., Loewenstein, M., Chan, K. R., and Heidt, L. E.: Observations of denitrification and dehydration in the winter polar stratospheres, Nature, 344, 321–324, doi:10.1038/344321a0, 1990.

Farman, J. C., Gardiner, B. G., and Shanklin, J. D.: Large losses of total ozone in Antarctica reveal seasonal ClO_x/NO_x interaction, Nature, 315, 207–210, doi:10.1038/315207a0, 1985.

Fiedler, S. E., Hese, A., and Ruth, A. A.: Incoherent broad-band cavity-enhanced absorption spectroscopy, Chemical Physics Letters, 371, 284–294, doi:10.1016/S0009-2614(03)00263-X, 2003.

Finlayson-Pitts, B. J. and Pitts, J. N.: Analytical methods and typical atmospheric concentrations for gases and particles, in: Chemistry of the Upper and Lower Atmosphere, pp. 547–656, Elsevier, doi:10.1016/B978-012257060-5/50013-7, 2000a.

Finlayson-Pitts, B. J. and Pitts, J. N.: Chapter 7 - Chemistry of Inorganic Nitrogen Compounds, in: Chemistry of the Upper and Lower Atmosphere, pp. 264 – 293, Academic Press, doi:10.1016/B978-012257060-5/50009-5, 2000b.

Finlayson-Pitts, B. J., Wingen, L. M., Sumner, A. L., Syomin, D., and Ramazan, K. A.: The heterogeneous hydrolysis of NO_2 in laboratory systems and in outdoor and indoor atmospheres: an integrated mechanism, Physical Chemistry Chemical Physics, 5, 223–242, doi:10.1039/b208564j, 2003.

Forsythe, W. C., Rykiel, E. J., Stahl, R. S., Wu, H.-i., and Schoolfield, R. M.: A model comparison for daylength as a function of latitude and day of year, Ecological Modelling, 80, 87–95, doi:10.1016/0304-3800(94)00034-F, 1995.

France, J. L., King, M. D., Frey, M. M., Erbland, J., Picard, G., Preunkert, S., MacArthur, A., and Savarino, J.: Snow optical properties at Dome C (Concordia), Antarctica; implications for snow emissions and snow chemistry of reactive nitrogen, Atmospheric Chemistry and Physics, 11, 9787–9801, doi:10.5194/acp-11-9787-2011, 2011.

Frey, M. M.: Frey, M.M., Atmospheric NO_x mixing ratios at Dome C (East Antarctica) during the OPALE campaign in austral summer 2011/12', Polar Data Centre, Natural Environment Research Council, UK Research & Innovation„ doi:submitted 2021, 2021.

Frey, M. M., Savarino, J., Morin, S., Erbland, J., and Martins, J. M. F.: Photolysis imprint in the nitrate stable isotope signal in snow and atmosphere of East Antarctica and implications for reactive nitrogen cycling, Atmospheric Chemistry and Physics, 9, 8681–8696, doi:10.5194/acp-9-8681-2009, 2009.

Frey, M. M., Brough, N., France, J. L., Anderson, P. S., Traulle, O., King, M. D., Jones, A. E., Wolff, E. W., and Savarino, J.: The diurnal variability of atmospheric nitrogen oxides (NO and NO_2) above the antarctic plateau driven by atmospheric stability and snow emissions, Atmospheric Chemistry and Physics, 13, 3045–3062, doi:10.5194/acp-13-3045-2013, 2013.

Frey, M. M., Roscoe, H. K., Kukui, A., Savarino, J., France, J. L., King, M. D., Legrand, M., and Preunkert, S.: Atmospheric nitrogen oxides (NO and NO_2) at Dome C, East Antarctica, during the OPALE campaign, Atmospheric Chemistry and Physics, 15, 7859–7875, doi:10.5194/acp-15-7859-2015, 2015.

Frey, M. M., Norris, S. J., Brooks, I. M., Anderson, P. S., Nishimura, K., Yang, X., Jones, A. E., Nerentorp Mastromonaco, M. G., Jones, D. H., and Wolff, E. W.: First direct observation of sea salt aerosol production from blowing snow above sea ice, Atmospheric Chemistry and Physics, 20, 2549–2578, doi:10.5194/acp-20-2549-2020, 2020.

Frieß, U., Wagner, T., Pundt, I., Pfeilsticker, K., and Platt, U.: Spectroscopic measurements of tropospheric iodine oxide at Neumayer Station, Antarctica, Geophysical Research Letters, 28, 1941–1944, doi:10.1029/2000GL012784, 2001.

Frieß, U., Hollwedel, J., König-Langlo, G., Wagner, T., and Platt, U.: Dynamics and chemistry of tropospheric bromine explosion events in the Antarctic coastal region: BrO in the Antarctic coastal region, Journal of Geophysical Research: Atmospheres, 109, D06 305, doi:10.1029/2003JD004133, 2004.

Frieß, U., Deutschmann, T., Gilfedder, B. S., Weller, R., and Platt, U.: Iodine monoxide in the Antarctic snowpack, Atmospheric Chemistry and Physics, 10, 2439–2456, doi:10.5194/acp-10-2439-2010, 2010.

Fu, T.-M., Jacob, D. J., Wittrock, F., Burrows, J. P., Vrekoussis, M., and Henze, D. K.: Global budgets of atmospheric glyoxal and methylglyoxal, and implications for formation of secondary organic aerosols, Journal of Geophysical Research, 113, D15 303, doi:10.1029/2007JD009505, 2008.

Fuchs, H., Dubé, W. P., Lerner, B. M., Wagner, N. L., Williams, E. J., and Brown, S. S.: A sensitive and versatile detector for atmospheric NO_2 and NO_x based on Blue Diode Laser Cavity Ring-Down Spectroscopy, Environmental Science & Technology, 43, 7831–7836, doi:10.1021/es902067h, 2009.

Fuchs, H., Ball, S. M., Bohn, B., Brauers, T., Cohen, R. C., Heitmann, U., Jones, R. L., Kleffmann, J., Mentel, T. F., Kiendler-Scharr, A., Schlosser, E., Shillings, A. J. L., Tillmann, R., Varma, R. M.,

Venables, D. S., Tapia, G. V., Wahner, A., Wegener, R., Wooldridge, P. J., and Brown, S. S.: Intercomparison of measurements of NO_2 concentrations in the atmosphere simulation chamber SAPHIR during the NO_3Comp campaign, Atmospheric Measurement Techniques, 3, 21–37, doi:10.5194/amt-3-21-2010, 2010.

Gagliardi, G. and Loock, H.-P., eds.: Cavity-enhanced spectroscopy and sensing, no. 179 in Springer series in optical sciences, 2014.

Gallet, J.-C., Domine, F., Arnaud, L., Picard, G., and Savarino, J.: Vertical profile of the specific surface area and density of the snow at Dome C and on a transect to Dumont D'Urville, Antarctica – albedo calculations and comparison to remote sensing products, The Cryosphere, 5, 631–649, doi:10.5194/tc-5-631-2011, 2011.

Gallée, H. and Gorodetskaya, I. V.: Validation of a limited area model over Dome C, Antarctic Plateau, during winter, Climate Dynamics, 34, 61–72, doi:10.1007/s00382-008-0499-y, 2010.

Gallée, H., Barral, H., Vignon, E., and Genthon, C.: A case study of a low-level jet during OPALE, Atmospheric Chemistry and Physics, 15, 6237–6246, doi:10.5194/acp-15-6237-2015, 2015a.

Gallée, H., Preunkert, S., Argentini, S., Frey, M. M., Genthon, C., Jourdain, B., Pietroni, I., Casasanta, G., Barral, H., Vignon, E., Amory, C., and Legrand, M.: Characterization of the boundary layer at Dome C (East Antarctica) during the OPALE summer campaign, Atmospheric Chemistry and Physics, 15, 6225–6236, doi:10.5194/acp-15-6225-2015, 2015b.

Garcia, R.: Transport of thermospheric NO_x to the stratosphere and mesosphere, Advances in Space Research, 12, 57–66, doi:10.1016/0273-1177(92)90444-3, 1992.

Gherman, T. and Romanini, D.: Mode–locked cavity–enhanced absorption spectroscopy, Optics Express, 10, 1033–1042, doi:10.1364/OE.10.001033, 2002.

Gherman, T., Venables, D. S., Vaughan, S., Orphal, J., and Ruth, A. A.: Incoherent Broadband Cavity-Enhanced Absorption Spectroscopy in the near-Ultraviolet: application to HONO and NO_2, Environmental Science & Technology, 42, 890–895, doi:10.1021/es0716913, 2008.

Grannas, A. M., Jones, A. E., Dibb, J., Ammann, M., Anastasio, C., Beine, H. J., Bergin, M., Bottenheim, J., Boxe, C. S., Carver, G., Chen, G., Crawford, J. H., Domine, F., Frey, M. M., Guzman, M. I., Heard, D. E., Helmig, D., Hoffmann, M. R., Honrath, R. E., Huey, L. G., Hutterli, M., Jacobi, H. W., Klan, P., Lefer, B., McConnell, J., Plane, J., Sander, R., Savarino, J., Shepson, P. B., Simpson, W. R., Sodeau, J. R., Weller, R., Wolff, E. W., and Zhu, T.: An overview of snow photochemistry: evidence, mechanisms and impacts, Atmospheric Chemistry and Physics, 7, 4329–4373, doi:10.5194/acp-7-4329-2007, 2007.

Grilli, R., Méjean, G., Kassi, S., Ventrillard, I., Abd-Alrahman, C., Fasci, E., and Romanini, D.: Trace measurement of BrO at the ppt level by a transportable Mode-Locked Frequency-Doubled Cavity-Enhanced Spectrometer, Applied Physics B, 107, 205–212, doi:10.1007/s00340-011-4812-9, 2012a.

Grilli, R., Méjean, G., Kassi, S., Ventrillard, I., Abd-Alrahman, C., and Romanini, D.: Frequency Comb Based Spectrometer for in situ and real time measurements of IO, BrO, NO_2, and H_2CO at pptv and ppqv levels, Environmental Science & Technology, 46, 10 704–10 710, doi:10.1021/es301785h, 2012b.

Grilli, R., Legrand, M., Kukui, A., Méjean, G., Preunkert, S., and Romanini, D.: First investigations of IO, BrO, and NO_2 summer atmospheric levels at a coastal East Antarctic site using mode-locked cavity enhanced absorption spectroscopy, Geophysical Research Letters, 40, 791–796, doi:10.1002/grl.50154, 2013.

Grosjean, D. and Harrison, J.: Response of chemiluminescence NO_x analyzers and ultraviolet ozone analyzers to organic air pollutants, Environmental Science & Technology, 19, 862–865, doi:10.1021/es00139a016, 1985.

Haagen-Smit, A. J.: Chemistry and physiology of Los Angeles Smog, Industrial and Engineering Chemistry, 44, 1342–1346, doi:10.1021/ie50510a045, 1952.

Heard, D. E., Carpenter, L., Creasey, D., Hopkins, J., Lee, J., Lewis, A. C., Pilling, M., and Seakins, P.: High levels of the hydroxyl radical in the winter urban troposphere, Geophysical Research Letters, 31, L18 112, doi:10.1029/2004GL020544, 2004.

Helmig, D., Johnson, B., Warshawsky, M., Morse, T., Neff, W., Eisele, F., and Davis, D.: Nitric oxide in the boundary-layer at South Pole during the Antarctic Tropospheric Chemistry Investigation (ANTCI), Atmospheric Environment, 42, 2817–2830, doi:10.1016/j.atmosenv.2007.03.061, 2008.

Helmig, D., Liptzin, D., Hueber, J., and Savarino, J.: Impact of exhaust emissions on chemical snowpack composition at Concordia Station, Antarctica, The Cryosphere, 14, 199–209, doi:10.5194/tc-14-199-2020, 2020.

Hodgson, N. and Weber, H.: Optical Resonators, Springer London, London, doi:10.1007/978-1-4471-3595-1, 1997.

Honrath, R. E., Peterson, M. C., Guo, S., Dibb, J. E., Shepson, P. B., and Campbell, B.: Evidence of NO_x production within or upon ice particles in the Greenland snowpack, Geophysical Research Letters, 26, 695–698, doi:10.1029/1999GL900077, 1999.

Honrath, R. E., Guo, S., Peterson, M. C., Dziobak, M. P., Dibb, J. E., and Arsenault, M. A.: Photochemical production of gas phase NO_x from ice crystal NO_3^-, Journal of Geophysical Research: Atmospheres, 105, 24 183–24 190, doi:10.1029/2000JD900361, 2000.

Honrath, R. E., Lu, Y., Peterson, M. C., Dibb, J. E., Arsenault, M. A., Cullen, N. J., and Steffen, K.: Vertical fluxes of NO_x, HONO, and HNO_3 above the snowpack at Summit, Greenland, Atmospheric Environment, 36, 2629–2640, doi:10.1016/S1352-2310(02)00132-2, 2002.

Hönninger, G. and Platt, U.: Observations of BrO and its vertical distribution during surface ozone depletion at Alert, Atmospheric Environment, 36, 2481–2489, doi:10.1016/S1352-2310(02)00104-8, 2002.

Hönninger, G., Leser, H., Sebastian, O., and Platt, U.: Ground-based measurements of halogen oxides at the Hudson Bay by active longpath DOAS and passive MAX-DOAS, Geophysical Research Letters, 31, L04 111, doi:10.1029/2003GL018982, 2004.

Jacobi, H.-W., Kleffmann, J., Villena, G., Wiesen, P., King, M., France, J., Anastasio, C., and Staebler, R.: Role of nitrite in the photochemical formation of radicals in the snow, Environmental Science & Technology, 48, 165–172, doi:10.1021/es404002c, 2014.

Jaworski, N. A., Howarth, R. W., and Hetling, L. J.: Atmospheric deposition of nitrogen oxides onto

the landscape contributes to coastal eutrophication in the northeast United States, Environmental Science & Technology, 31, 1995–2004, doi:10.1021/es960803f, 1997.

Jefferson, A., Tanner, D. J., Eisele, F. L., Davis, D. D., Chen, G., Crawford, J., Huey, J. W., Torres, A. L., and Berresheim, H.: OH photochemistry and methane sulfonic acid formation in the coastal Antarctic boundary layer, Journal of Geophysical Research, 103, 1647–1656, doi:10.1029/97JD02376, 1998.

Jin, J., Ma, J., Lin, W., Zhao, H., Shaiganfar, R., Beirle, S., and Wagner, T.: MAX-DOAS measurements and satellite validation of tropospheric NO_2 and SO_2 vertical column densities at a rural site of North China, Atmospheric Environment, 133, 12–25, doi:10.1016/j.atmosenv.2016.03.031, 2016.

Johnston, H.: Reduction of stratospheric ozone by nitrogen oxide catalysts from supersonic transport exhaust, Science, 173, 517–522, doi:10.1126/science.173.3996.517, 1971.

Jones, A. E., Weller, R., Wolff, E. W., and Jacobi, H. W.: Speciation and rate of photochemical NO and NO_2 production in Antarctic snow, Geophysical Research Letters, 27, 345–348, doi:10.1029/1999GL010885, 2000.

Jones, A. E., Weller, R., Anderson, P. S., Jacobi, H.-W., Wolff, E. W., Schrems, O., and Miller, H.: Measurements of NO_x emissions from the Antarctic snowpack, Geophysical Research Letters, 28, 1499–1502, doi:10.1029/2000GL011956, 2001.

Jones, A. E., Wolff, E. W., Salmon, R. A., Clemitshaw, K. C., Fleming, Z. L., Bloss, W. J., Heard, D. E., Lee, J. D., Read, K. A., Hamer, P., Shallcross, D. E., Jackson, A. V., Walker, S. L., Lewis, A. C., Mills, G. P., Plane, J. M. C., Saiz-Lopez, A., Sturges, W. T., and Worton, D. R.: Chemistry of the Antarctic Boundary Layer and the Interface with Snow: an overview of the CHABLIS campaign, Atmospheric Chemistry and Physics, 8, 3789–3803, doi:10.5194/acp-8-3789-2008, 2008.

Jones, A. E., Wolff, E. W., Ames, D., Bauguitte, S. J.-B., Clemitshaw, K. C., Fleming, Z., Mills, G. P., Saiz-Lopez, A., Salmon, R. A., Sturges, W. T., and Worton, D. R.: The multi-seasonal NO_y budget in coastal Antarctica and its link with surface snow and ice core nitrate: results from the CHABLIS campaign, Atmospheric Chemistry and Physics, 11, 9271–9285, doi:10.5194/acp-11-9271-2011, 2011.

Joos, F. and Spahni, R.: Rates of change in natural and anthropogenic radiative forcing over the past 20,000 years, PNAS, 105, 1425–1430, doi:10.1073/pnas.0707386105, 2008.

Jordan, N., Ye, C. Z., Ghosh, S., Washenfelder, R. A., Brown, S. S., and Osthoff, H. D.: A broadband cavity-enhanced spectrometer for atmospheric trace gas measurements and Rayleigh scattering cross sections in the cyan region (470–540nm), Atmospheric Measurement Techniques, 12, 1277–1293, doi:10.5194/amt-12-1277-2019, 2019.

Jouzel, J., Masson-Delmotte, V., Cattani, O., Dreyfus, G., Falourd, S., Hoffmann, G., Minster, B., Nouet, J., Barnola, J. M., Chappellaz, J., Fischer, H., Gallet, J. C., Johnsen, S., Leuenberger, M., Loulergue, L., Luethi, D., Oerter, H., Parrenin, F., Raisbeck, G., Raynaud, D., Schilt, A., Schwander, J., Selmo, E., Souchez, R., Spahni, R., Stauffer, B., Steffensen, J. P., Stenni, B., Stocker, T. F., Tison, J. L., Werner, M., and Wolff, E. W.: Orbital and millennial antarctic climate variability over the past 800,000 years, Science, 317, 793–796, doi:10.1126/science.1141038, 2007.

Jágerská, J., Jouy, P., Tuzson, B., Looser, H., Mangold, M., Soltic, P., Hugi, A., Brönnimann, R., Faist, J., and Emmenegger, L.: Simultaneous measurement of NO and NO_2 by dual-wavelength quantum cascade laser spectroscopy, Optics Express, 23, 1512, doi:10.1364/OE.23.001512, 2015.

Kenagy, H. S., Sparks, T. L., Ebben, C. J., Wooldrige, P. J., Lopez-Hilfiker, F. D., Lee, B. H., Thornton, J. A., McDuffie, E. E., Fibiger, D. L., Brown, S. S., Montzka, D. D., Weinheimer, A. J., Schroder, J. C., Campuzano-Jost, P., Day, D. A., Jimenez, J. L., Dibb, J. E., Campos, T., Shah, V., Jaeglé, L., and Cohen, R. C.: NO_x lifetime and NO_y partitioning during winter, Journal of Geophysical Research: Atmospheres, 123, 9813–9827, doi:10.1029/2018JD028736, 2018.

King, M. D., Howat, I. M., Candela, S. G., Noh, M. J., Jeong, S., Noël, B. P. Y., van den Broeke, M. R., Wouters, B., and Negrete, A.: Dynamic ice loss from the Greenland Ice Sheet driven by sustained glacier retreat, Communications Earth & Environment, 1, 7, doi:10.1038/s43247-020-0001-2, 2020.

Kittel, C., Amory, C., Agosta, C., Jourdain, N. C., Hofer, S., Delhasse, A., Doutreloup, S., Huot, P.-V., Lang, C., Fichefet, T., and Fettweis, X.: Diverging future surface mass balance between the Antarctic ice shelves and grounded ice sheet, preprint, doi:10.5194/tc-2020-291, 2020.

Kovalev, V. A. and Eichinger, W. E.: Elastic Lidar: Theory, Practice, and Analysis Methods, John Wiley & Sons, Inc., doi:10.1002/0471643173, 2004.

Kreher, K., Johnston, P. V., Wood, S. W., Nardi, B., and Platt, U.: Ground-based measurements of tropospheric and stratospheric BrO at Arrival Heights, Antarctica, Geophysical Research Letters, 24, 3021–3024, doi:10.1029/97GL02997, 1997.

Kukui, A., Legrand, M., Preunkert, S., Frey, M. M., Loisil, R., Gil Roca, J., Jourdain, B., King, M. D., France, J. L., and Ancellet, G.: Measurements of OH and RO_2 radicals at Dome C, East Antarctica, Atmospheric Chemistry and Physics, 14, 12 373–12 392, doi:10.5194/acp-14-12373-2014, 2014.

Langridge, J. M., Ball, S. M., and Jones, R. L.: A compact broadband cavity enhanced absorption spectrometer for detection of atmospheric NO_2 using light emitting diodes, The Analyst, 131, 916, doi:10.1039/b605636a, 2006.

Lee, J. S., Kim, Y. J., Kuk, B., Geyer, A., and Platt, U.: Simultaneous measurements of atmospheric pollutants and visibility with a Long-Path DOAS System in urban areas, Environmental Monitoring and Assessment, 104, 281–293, doi:10.1007/s10661-005-1616-6, 2005.

Lee, J. S., Kim, K.-H., Kim, Y. J., and Lee, J.: Application of a Long-Path Differential Optical Absorption Spectrometer (LP-DOAS) on the measurements of NO_2, SO_2, O_3, and HNO_2 in Gwangju, Korea, Journal of Environmental Management, 86, 750–759, doi:10.1016/j.jenvman.2006.12.044, 2008a.

Lee, S.-H., Young, L.-H., Benson, D. R., Suni, T., Kulmala, M., Junninen, H., Campos, T. L., Rogers, D. C., and Jensen, J.: Observations of nighttime new particle formation in the troposphere, Journal of Geophysical Research, 113, D10 210, doi:10.1029/2007JD009351, 2008b.

Legrand, M., Feniet-Saigne, C., Saltzman, E. S., and Germain, C.: Spatial and temporal variations of methanesulfonic acid and non sea-salt sulfate in Antarctic ice, Journal of Atmospheric Chemistry, 14, 245–260, doi:10.1007/BF00115237, 1992.

Legrand, M., Wolff, E., and Wagenbach, D.: Antarctic aerosol and snowfall chemistry: implications for deep Antarctic ice-core chemistry, Annals of Glaciology, pp. 66–72, 1999.

Legrand, M., Preunkert, S., Jourdain, B., Gallée, H., Goutail, F., Weller, R., and Savarino, J.: Year-round record of surface ozone at coastal (Dumont d'Urville) and inland (Concordia) sites in East Antarctica, Journal of Geophysical Research, 114, D20 306, doi:10.1029/2008JD011667, 2009.

Legrand, M., Preunkert, S., Frey, M., Bartels-Rausch, T., Kukui, A., King, M. D., Savarino, J., Kerbrat, M., and Jourdain, B.: Large mixing ratios of atmospheric nitrous acid (HONO) at Concordia (East Antarctic Plateau) in summer: a strong source from surface snow?, Atmospheric Chemistry and Physics, 14, 9963–9976, doi:10.5194/acp-14-9963-2014, 2014.

Legrand, M., Preunkert, S., Savarino, J., Frey, M. M., Kukui, A., Helmig, D., Jourdain, B., Jones, A. E., Weller, R., Brough, N., and Gallée, H.: Inter-annual variability of surface ozone at coastal (Dumont 'Urville, 2004–2014) and inland (Concordia, 2007–2014) sites in East Antarctica, Atmospheric Chemistry and Physics, 16, 8053–8069, doi:10.5194/acp-16-8053-2016, 2016.

Leighton, P. A.: Photochemistry of Air Pollution, Academic Press, New York, 1961.

Lenschow, D.: Micrometeorological techniques for measuring biosphere-atmosphere trace gas exchange, vol. Oxford: Blackwell Science, p. a. matson & r. c. hariss edn., 1995.

Leser, H., Hönninger, G., and Platt, U.: MAX-DOAS measurements of BrO and NO_2 in the marine boundary layer, Geophysical Research Letters, 30, 441–444, doi:10.1029/2002GL015811, 2003.

Liang, S., Qin, M., Xie, P., Duan, J., Fang, W., He, Y., Xu, J., Liu, J., Li, X., Tang, K., Meng, F., Ye, K., Liu, J., and Liu, W.: Development of an Incoherent Broadband Cavity-Enhanced Absorption Spectrometer for measurements of ambient glyoxal and NO_2 in a polluted urban environment, Atmospheric Measurement Techniques, 12, 2499–2512, doi:10.5194/amt-12-2499-2019, 2019.

Libois, Q., Picard, G., France, J. L., Arnaud, L., Dumont, M., Carmagnola, C. M., and King, M. D.: Influence of grain shape on light penetration in snow, The Cryosphere, 7, 1803–1818, doi:10.5194/tc-7-1803-2013, 2013.

Libois, Q., Picard, G., Dumont, M., Arnaud, L., Sergent, C., Pougatch, E., Sudul, M., and Vial, D.: Experimental determination of the absorption enhancement parameter of snow, Journal of Glaciology, 60, 714–724, doi:10.3189/2014JoG14J015, 2014.

Liu, J., Li, X., Yang, Y., Wang, H., Wu, Y., Lu, X., Chen, M., Hu, J., Fan, X., Zeng, L., and Zhang, Y.: An IBBCEAS system for atmospheric measurements of glyoxal and methylglyoxal in the presence of high NO_2 concentrations, Atmospheric Measurement Techniques, 12, 4439–4453, doi:10.5194/amt-12-4439-2019, 2019.

Ma, J., Dörner, S., Donner, S., Jin, J., Cheng, S., Guo, J., Zhang, Z., Wang, J., Liu, P., Zhang, G., Pukite, J., Lampel, J., and Wagner, T.: MAX-DOAS measurements of NO_2, SO_2, HCHO, and BrO at the Mt. Waliguan WMO GAW global baseline station in the Tibetan Plateau, Atmospheric Chemistry and Physics, 20, 6973–6990, doi:10.5194/acp-20-6973-2020, 2020a.

Ma, J., McHugh, T., and Eklund, B.: Flux chamber measurements should play a more important role in contaminated site management, Environmental Science & Technology, 54, 11 645–11 647, doi:10.1021/acs.est.0c04078, 2020b.

Ma, Q. and Tipping, R. H.: The distribution of density matrices over potential-energy surfaces: Application to the calculation of the far-wing line shapes for CO_2, The Journal of Chemical Physics, 108, 3386–3399, doi:10.1063/1.475774, 1998.

Madronich, S.: Photodissociation in the Atmosphere 1. Actinic Flux and the Effects of Ground Reflections and Clouds, Journal of Geophysical Research, 92, 9740–975 214, doi:10.1029/JD092iD08p09740, 1987.

Maeda, Y., Aoki, K., and Munemori, M.: Chemiluminescence method for the determination of nitrogen dioxide, Analytical Chemistry, 52, 307–311, doi:10.1021/ac50052a022, 1980.

Masclin, S., Frey, M. M., Rogge, W. F., and Bales, R. C.: Atmospheric nitric oxide and ozone at the WAIS Divide deep coring site: a discussion of local sources and transport in West Antarctica, Atmospheric Chemistry and Physics, 13, 8857–8877, doi:10.5194/acp-13-8857-2013, 2013.

Mauldin, R., Kosciuch, E., Henry, B., Eisele, F., Shetter, R., Lefer, B., Chen, G., Davis, D., Huey, G., and Tanner, D.: Measurements of OH, HO_2+RO_2, H_2SO_4, and MSA at the South Pole during ISCAT 2000, Atmospheric Environment, 38, 5423–5437, doi:10.1016/j.atmosenv.2004.06.031, 2004.

Mauldin, R., Kosciuch, E., Eisele, F., Huey, G., Tanner, D., Sjostedt, S., Blake, D., Chen, G., Crawford, J., and Davis, D.: South Pole Antarctica observations and modeling results: new insights on HO_x radical and sulfur chemistry, Atmospheric Environment, 44, 572–581, doi:10.1016/j.atmosenv.2009.07.058, 2010.

Mauldin, R. L., Eisele, F. L., Tanner, D. J., Kosciuch, E., Shetter, R., Lefer, B., Hall, S. R., Nowak, J. B., Buhr, M., Chen, G., Wang, P., and Davis, D.: Measurements of OH, H_2SO_4 and MSA at the South Pole during ISCAT, Geophysical Research Letters, 28, 3629–3632, doi:10.1029/2000GL012711, 2001.

McCabe, J. R., Thiemens, M. H., and Savarino, J.: A record of ozone variability in South Pole Antarctic snow: Role of nitrate oxygen isotopes, Journal of Geophysical Research, 112, D12 303, doi:10.1029/2006JD007822, 2007.

McCalley, C. K. and Sparks, J. P.: Abiotic gas formation drives nitrogen loss from a desert ecosystem, Science, 326, 837–840, doi:10.1126/science.1178984, 2009.

Meusinger, C., Berhanu, T. A., Erbland, J., Savarino, J., and Johnson, M. S.: Laboratory study of nitrate photolysis in Antarctic snow. I. Observed quantum yield, domain of photolysis, and secondary chemistry, The Journal of Chemical Physics, 140, 244 305, doi:10.1063/1.4882898, 2014.

Michoud, V., Doussin, J.-F., Colomb, A., Afif, C., Borbon, A., Camredon, M., Aumont, B., Legrand, M., and Beekmann, M.: Strong HONO formation in a suburban site during snowy days, Atmospheric Environment, 116, 155–158, doi:10.1016/j.atmosenv.2015.06.040, 2015.

Mills, G. P., Sturges, W. T., Salmon, R. A., Bauguitte, S. J.-B., Read, K. A., and Bandy, B. J.: Seasonal variation of peroxyacetylnitrate (PAN) in coastal Antarctica measured with a new instrument for the detection of sub-part per trillion mixing ratios of PAN, Atmospheric Chemistry and Physics, 7, 4589–4599, doi:10.5194/acp-7-4589-2007, 2007.

Min, K.-E., Washenfelder, R. A., Dubé, W. P., Langford, A. O., Edwards, P. M., Zarzana, K. J., Stutz, J., Lu, K., Rohrer, F., Zhang, Y., and Brown, S. S.: A Broadband Cavity Enhanced Absorption Spectrometer for aircraft measurements of glyoxal, methylglyoxal, nitrous acid, nitrogen dioxide, and water vapor, Atmospheric Measurement Techniques, 9, 423–440, doi:10.5194/amt-9-423-2016, 2016.

Molina, M. J. and Rowland, F. S.: Stratospheric sink for chlorofluoromethanes: chlorine atom-catalysed destruction of ozone, Nature, 249, 810–812, doi:10.1038/249810a0, 1974.

Monks, P., Granier, C., Fuzzi, S., Stohl, A., Williams, M., Akimoto, H., Amann, M., Baklanov, A., Baltensperger, U., Bey, I., Blake, N., Blake, R., Carslaw, K., Cooper, O., Dentener, F., Fowler, D.,

Fragkou, E., Frost, G., Generoso, S., Ginoux, P., Grewe, V., Guenther, A., Hansson, H., Henne, S., Hjorth, J., Hofzumahaus, A., Huntrieser, H., Isaksen, I., Jenkin, M., Kaiser, J., Kanakidou, M., Klimont, Z., Kulmala, M., Laj, P., Lawrence, M., Lee, J., Liousse, C., Maione, M., McFiggans, G., Metzger, A., Mieville, A., Moussiopoulos, N., Orlando, J., O'Dowd, C., Palmer, P., Parrish, D., Petzold, A., Platt, U., Pöschl, U., Prévôt, A., Reeves, C., Reimann, S., Rudich, Y., Sellegri, K., Steinbrecher, R., Simpson, D., ten Brink, H., Theloke, J., van der Werf, G., Vautard, R., Vestreng, V., Vlachokostas, C., and von Glasow, R.: Atmospheric composition change – global and regional air quality, Atmospheric Environment, 43, 5268–5350, doi:10.1016/j.atmosenv.2009.08.021, 2009.

Monks, P. S.: Gas-phase radical chemistry in the troposphere, Chemical Society Reviews, 34, 376, doi:10.1039/b307982c, 2005.

Monks, P. S., Ravishankara, A. R., von Schneidemesser, E., and Sommariva, R.: Opinion: papers that shaped tropospheric chemistry, preprint, doi:10.5194/acp-2020-1266, 2021.

Mulvaney, R. and Wolff, E. W.: Evidence for winter/spring denitrification of the stratosphere in the nitrate record of Antarctic firn cores, Journal of Geophysical Research: Atmospheres, 98, 5213–5220, doi:10.1029/92JD02966, 1993.

Muto, A., Scambos, T. A., Steffen, K., Slater, A. G., and Clow, G. D.: Recent surface temperature trends in the interior of East Antarctica from borehole firn temperature measurements and geophysical inverse methods, Geophysical Research Letters, 38, doi:10.1029/2011GL048086, 2011.

Nasse, J.-M., Eger, P. G., Pöhler, D., Schmitt, S., Frieß, U., and Platt, U.: Recent improvements of Long-Path DOAS measurements: impact on accuracy and stability of short-term and automated long-term observations, Atmospheric Measurement Techniques, 12, 4149–4169, doi:10.5194/amt-12-4149-2019, 2019.

Noro, K. and Takenaka, N.: Post-depositional loss of nitrate and chloride in Antarctic snow by photolysis and sublimation: a field investigation, Polar Research, 39, 5146–5155, doi:10.33265/polar.v39.5146, 2020.

Oncley, S., Buhr, M., Lenschow, D., Davis, D., and Semmer, S.: Observations of summertime NO fluxes and boundary-layer height at the South Pole during ISCAT 2000 using scalar similarity, Atmospheric Environment, 38, 5389–5398, doi:10.1016/j.atmosenv.2004.05.053, 2004.

O'Keefe, A. and Deacon, D. A. G.: Cavity Ring-Down Optical Spectrometer for absorption measurements using pulsed laser sources, Review of Scientific Instruments, 59, 2544–2551, doi:10.1063/1.1139895, 1988.

O'Keefe, A., Scherer, J. J., Paul, J. B., and Saykally, R. J.: Cavity Ringdown Laser Spectroscopy (CRDS): history, development, and applications, p. 21, 2002.

Palchetti, L., Bianchini, G., Di Natale, G., and Del Guasta, M.: Far-Infrared radiative properties of water vapor and clouds in antarctica, Bulletin of the American Meteorological Society, 96, 1505–1518, doi:10.1175/BAMS-D-13-00286.1, 2015.

Penner, J. E., Atherton, C. S., Dignon, J., Ghan, S. J., Walton, J. J., and Hameed, S.: Tropospheric nitrogen: a three-dimensional study of sources, distributions, and deposition, Journal of Geophysical Research, 96, 959–990, doi:10.1029/90JD02228, 1991.

Petit, J. R., Jouzel, J., Raynaud, D., Barkov, N. I., Barnola, J.-M., Basile, I., Bender, M., Chappellaz, J., Davis, M., Delaygue, G., Delmotte, M., Kotlyakov, V. M., Legrand, M., Lipenkov, V. Y., Lorius, C.,

PÉpin, L., Ritz, C., Saltzman, E., and Stievenard, M.: Climate and atmospheric history of the past 420,000 years from the Vostok ice core, Antarctica, Nature, 399, 429–436, doi:10.1038/20859, 1999.

Picard, G., Arnaud, L., Caneill, R., Lefebvre, E., and Lamare, M.: Observation of the process of snow accumulation on the Antarctic Plateau by time lapse laser scanning, The Cryosphere, p. 17, 2019.

Pikelnaya, O., Hurlock, S. C., Trick, S., and Stutz, J.: Intercomparison of MultiAXis and Long-Path Differential Optical Absorption Spectroscopy measurements in the marine boundary layer: intercomparison of MAX- and LP-DOAS, Journal of Geophysical Research: Atmospheres, 112, doi:10.1029/2006JD007727, 2007.

Platt, U. and Perner, D.: Direct measurements of atmospheric CH_2O, HNO_2, O_3, NO_2, and SO_2 by Differential Optical Absorption in the near UV, Journal of Geophysical Research: Oceans, 85, 7453–7458, doi:10.1029/JC085iC12p07453, 1980.

Platt, U. and Stutz, J.: Differential optical absorption spectroscopy: principles and applications, Physics of Earth and space environments, Springer, Berlin, 2008.

Pokryszka, Z. and Tauziède, C.: Method of measuring surface emissions of methane, International Conference on Latest Achievements in the Field of Mine Ventilation Fire and Methane Hazrad Fighting, pp. 277–283, 1999.

Prados-Roman, C., Gómez-Martín, L., Puentedura, O., Navarro-Comas, M., Iglesias, J., de Mingo, J. R., Pérez, M., Ochoa, H., Barlasina, M. E., Carbajal, G., and Yela, M.: Reactive bromine in the low troposphere of Antarctica: estimations at two research sites, Atmospheric Chemistry and Physics, 18, 8549–8570, doi:10.5194/acp-18-8549-2018, 2018.

Preunkert, S., Ancellet, G., Legrand, M., Kukui, A., Kerbrat, M., Sarda-Estève, R., Gros, V., and Jourdain, B.: Oxidant Production over Antarctic Land and its Export (OPALE) project: an overview of the 2010-2011 summer campaign, Journal of Geophysical Research: Atmospheres, 117, 307–319, doi:10.1029/2011JD017145, 2012.

Preunkert, S., Legrand, M., Frey, M. M., Kukui, A., Savarino, J., Gallée, H., King, M., Jourdain, B., Vicars, W., and Helmig, D.: Formaldehyde (HCHO) in air, snow, and interstitial air at Concordia (East Antarctic Plateau) in summer, Atmospheric Chemistry and Physics, 15, 6689–6705, doi:10.5194/acp-15-6689-2015, 2015.

Prinn, R. G.: The cleansing capacity of the atmosphere, Annual Review of Environment and Resources, 28, 29–57, doi:10.1146/annurev.energy.28.011503.163425, 2003.

Pöhler, D., Vogel, L., Friess, U., and Platt, U.: Observation of halogen species in the Amundsen Gulf, Arctic, by active Long-Path Differential Optical Absorption Spectroscopy, Proceedings of the National Academy of Sciences, 107, 6582–6587, doi:10.1073/pnas.0912231107, 2010.

Rajeswari, A., Amalraj, A., and Pius, A.: Adsorption studies for the removal of nitrate using chitosan/PEG and chitosan/PVA polymer composites, Journal of Water Process Engineering, 9, 123–134, doi:10.1016/j.jwpe.2015.12.002, 2016.

Rattigan, O., Lutman, E., Jones, R. L., and Coxt, R. A.: Temperature-dependent absorption cross-sections of gaseous nitric acid and methyl nitrate, Journal of Photochemistry and Photobiology A: Chemistry, 66, 313–326, doi:10.1002/bbpc.19920960331, 1992.

Read, K. A., Lewis, A. C., Bauguitte, S., Rankin, A. M., Salmon, R. A., Wolff, E. W., Saiz-Lopez, A., Bloss, W. J., Heard, D. E., Lee, J. D., and Plane, J. M. C.: DMS and MSA measurements in the Antarctic Boundary Layer: impact of BrO on MSA production, Atmospheric Chemistry and Physics, 8, 2985–2997, doi:10.5194/acp-8-2985-2008, 2008.

Reed, C., Evans, M. J., Di Carlo, P., Lee, J. D., and Carpenter, L. J.: Interferences in photolytic NO_2 measurements: explanation for an apparent missing oxidant?, Atmospheric Chemistry and Physics, 16, 4707–4724, doi:10.5194/acp-16-4707-2016, 2016.

Ricchiazzi, P., Yang, S., Gautier, C., and Sowle, D.: SBDART: a research and teaching software tool for plane-parallel radiative transfer in the Earth's atmosphere, Bulletin of the American Meteorological Society, 79, 14, doi:10.1175/1520-0477(1998)079<2101:SARATS>2.0.CO;2, 1998.

Richard, L., Romanini, D., and Ventrillard, I.: Nitric oxide analysis down to ppt levels by Optical-Feedback Cavity-Enhanced Absorption Spectroscopy, Sensors, 18, 1997, doi:10.3390/s18071997, 2018.

Ridley, B., Walega, J., Montzka, D., Grahek, F., Atlas, E., Flocke, F., Stroud, V., Deary, J., Gallant, A., Boudries, H., Bottenheim, J., Anlauf, K., Worthy, D., Sumner, A. L., Splawn, B., and Shepson, P.: Is the Arctic surface layer a source and sink of NO_x in Winter/Spring?, Journal of Atmospheric Chemistry, 36, 1–22, doi:10.1023/A:1006301029874, 2000.

Rolph, G., Stein, A., and Stunder, B.: Real-time Environmental Applications and Display sYstem: READY, Environmental Modelling & Software, 95, 210–228, doi:10.1016/j.envsoft.2017.06.025, 2017.

Romanini, D., Ventrillard, I., Méjean, G., Morville, J., and Kerstel, E.: Introduction to Cavity Enhanced Absorption Spectroscopy, in: Cavity-Enhanced Spectroscopy and Sensing, edited by Gagliardi, G. and Loock, H.-P., vol. 179, pp. 1–60, Springer Berlin Heidelberg, Berlin, Heidelberg, doi:10.1007/978-3-642-40003-2_1, series Title: Springer Series in Optical Sciences, 2014.

Roscoe, H., Brough, N., Jones, A., Wittrock, F., Richter, A., Van Roozendael, M., and Hendrick, F.: Characterisation of vertical BrO distribution during events of enhanced tropospheric BrO in Antarctica, from combined remote and in-situ measurements, Journal of Quantitative Spectroscopy and Radiative Transfer, 138, 70–81, doi:10.1016/j.jqsrt.2014.01.026, 2014.

Rozanov, V. V. and Rozanov, A. V.: Differential Optical Absorption Spectroscopy (DOAS) and air mass factor concept for a multiply scattering vertically inhomogeneous medium: theoretical consideration, Atmospheric Measurement Techniques, 3, 751–780, doi:10.5194/amt-3-751-2010, 2010.

Ruth, A. A., Dixneuf, S., and Raghunandan, R.: Broadband Cavity-Enhanced Absorption Spectroscopy with Incoherent Light, in: Cavity-Enhanced Spectroscopy and Sensing, edited by Gagliardi, G. and Loock, H.-P., vol. 179, pp. 485–517, Springer Berlin Heidelberg, doi:10.1007/978-3-642-40003-2_14, 2014.

Ryerson, T. B., Williams, E. J., and Fehsenfeld, F. C.: An efficient photolysis system for fast-response NO_2 measurements, Journal of Geophysical Research: Atmospheres, 105, 26 447–26 461, doi:10.1029/2000JD900389, 2000.

Röthlisberger, R., Hutterli, M. A., Sommer, S., Wolff, E. W., and Mulvaney, R.: Factors controlling nitrate in ice cores: Evidence from the Dome C deep ice core, Journal of Geophysical Research: Atmospheres, 105, 20 565–20 572, doi:10.1029/2000JD900264, 2000.

Saigne, C. and Legrand, M.: Measurements of methanesulfonic acid in Antarctic ice, Nature, 330, doi:10.1038/330240a0, 1987.

Saiz-Lopez, A., Chance, K., Liu, X., Kurosu, T. P., and Sander, S. P.: First observations of iodine oxide from space, Geophysical Research Letters, 34, L12 812, doi:10.1029/2007GL030111, 2007a.

Saiz-Lopez, A., Mahajan, A. S., Salmon, R. A., Bauguitte, S. J.-B., Jones, A. E., Roscoe, H. K., and Plane, J. M. C.: Boundary Layer Halogens in Coastal Antarctica, Science, 317, 348–351, doi:10.1126/science.1141408, 2007b.

Saiz-Lopez, A., Plane, J. M. C., Mahajan, A. S., Anderson, P. S., Bauguitte, S. J.-B., Jones, A. E., Roscoe, H. K., Salmon, R. A., Bloss, W. J., Lee, J. D., and Heard, D. E.: On the vertical distribution of boundary layer halogens over coastal Antarctica: implications for O_3, HO_x, NO_x and the Hg lifetime, Atmospheric Chemistry and Physics, 8, 887–900, doi:10.5194/acp-8-887-2008, 2008.

Salawitch, R. J., Gobbi, G. P., Wofsy, S. C., and McElroy, M. B.: Denitrification in the Antarctic stratosphere, Nature, 339, 525–527, doi:10.1038/339525a0, 1989.

Salmon, R. A., Bauguitte, S. J.-B., Bloss, W., Hutterli, M. A., Jones, A. E., Read, K., and Wolff, E. W.: Measurement and interpretation of gas phase formaldehyde concentrations obtained during the CHABLIS campaign in coastal Antarctica, Atmospheric Chemistry and Physics, 8, 4085–4093, doi:10.5194/acp-8-4085-2008, 2008.

Santee, M. L., Read, W. G., Waters, J. W., Froidevaux, L., Manney, G. L., Flower, D. A., Jarnot, R. F., Harwood, R. S., and Peckham, G. E.: Interhemispheric differences in polar stratospheric HNO_3, H_2O, ClO, and O_3, Science, 267, 849–852, doi:10.1126/science.267.5199.849, 1995.

Savarino, J., Kaiser, J., Morin, S., Sigman, D. M., and Thiemens, M. H.: Nitrogen and oxygen isotopic constraints on the origin of atmospheric nitrate in coastal Antarctica, Atmospheric Chemistry and Physics, 7, 1925–1945, doi:10.5194/acp-7-1925-2007, 2007.

Savarino, J., Vicars, W. C., Legrand, M., Preunkert, S., Jourdain, B., Frey, M. M., Kukui, A., Caillon, N., and Roca, J. G.: Oxygen isotope mass balance of atmospheric nitrate at Dome C, East Antarctica, during the OPALE campaign, Atmospheric Chemistry and Physics, 16, 2659–2673, doi:10.5194/acp-16-2659-2016, 2016.

Savitskiy, G. B. and Lessing, V. M.: Tropospheric jet streams in the Antarctic, Polar Geography, 3, 157–160, doi:10.1080/10889377909377113, 1979.

Scheutz, C., Bogner, J., Chanton, J. P., Blake, D., Morcet, M., Aran, C., and Kjeldsen, P.: Atmospheric emissions and attenuation of non-methane organic compounds in cover soils at a French landfill, Waste Management, p. 17, doi:10.1016/j.wasman.2007.09.010, 2008.

Schumann, U. and Huntrieser, H.: The global lightning-induced nitrogen oxides source, Atmospheric Chemistry and Physics, 7, 3823–3907, doi:10.5194/acp-7-3823-2007, 2007.

Schönhardt, A., Begoin, M., Richter, A., Wittrock, F., Kaleschke, L., Gómez Martín, J. C., and Burrows, J. P.: Simultaneous satellite observations of IO and BrO over Antarctica, Atmospheric Chemistry and Physics, 12, 6565–6580, doi:10.5194/acp-12-6565-2012, 2012.

Seok, B., Helmig, D., Williams, M. W., Liptzin, D., Chowanski, K., and Hueber, J.: An automated system for continuous measurements of trace gas fluxes through snow: an evaluation of the gas

diffusion method at a subalpine forest site, Niwot Ridge, Colorado, Biogeochemistry, 95, 95–113, doi:10.1007/s10533-009-9302-3, 2009.

Sheppard, M. G. and Walker, R. B.: Wigner method studies of ozone photodissociation, The Journal of Chemical Physics, 78, 7191–7199, doi:10.1063/1.444760, 1983.

Shi, G., Buffen, A., Ma, H., Hu, Z., Sun, B., Li, C., Yu, J., Ma, T., An, C., Jiang, S., Li, Y., and Hastings, M.: Distinguishing summertime atmospheric production of nitrate across the East Antarctic Ice Sheet, Geochimica et Cosmochimica Acta, 231, 1–14, doi:10.1016/j.gca.2018.03.025, 2018a.

Shi, G., Hastings, M. G., Yu, J., Ma, T., Hu, Z., An, C., Li, C., Ma, H., Jiang, S., and Li, Y.: Nitrate deposition and preservation in the snowpack along a traverse from coast to the ice sheet summit (Dome A) in East Antarctica, The Cryosphere, 12, 1177–1194, doi:10.5194/tc-12-1177-2018, 2018b.

Sihota, N. J., Singurindy, O., and Mayer, K. U.: CO_2-Efflux Measurements for evaluating source zone natural attenuation rates in a petroleum hydrocarbon contaminated aquifer, Environmental Science & Technology, 45, 482–488, doi:10.1021/es1032585, 2010.

Simpson, W. R., King, M. D., Beine, H. J., Honrath, R. E., and Zhou, X.: Radiation-transfer modeling of snow-pack photochemical processes during ALERT 2000, Atmospheric Environment, 36, 2663–2670, doi:10.1016/S1352-2310(02)00124-3, 2002.

Sinreich, R., Volkamer, R., Filsinger, F., Friess, U., Kern, C., Platt, U., Sebastian, O., and Wagner, T.: MAX-DOAS detection of glyoxal during ICARTT 2004, Atmospheric Chemistry and Physics, 7, 1293–1303, doi:10.5194/acp-7-1293-2007, 2007.

Skiba, U. and Fowler, D.: Emissions of NO and N_2O from soils, Environmental Monitoring and Assessment, 31, 153–158, doi:10.1007/BF00547191, 1993.

Solomon, S.: Stratospheric ozone depletion: a review of concepts and history, Reviews of Geophysics, 37, 275–316, doi:10.1029/1999RG900008, 1999.

Stein, A. F., Draxler, R. R., Rolph, G. D., Stunder, B. J. B., Cohen, M. D., and Ngan, F.: NOAA's HYSPLIT Atmospheric Transport and Dispersion Modeling System, Bulletin of the American Meteorological Society, 96, 2059–2077, doi:10.1175/BAMS-D-14-00110.1, 2015.

Stone, D., Evans, M. J., Walker, H., Ingham, T., Vaughan, S., Ouyang, B., Kennedy, O. J., McLeod, M. W., Jones, R. L., Hopkins, J., Punjabi, S., Lidster, R., Hamilton, J. F., Lee, J. D., Lewis, A. C., Carpenter, L. J., Forster, G., Oram, D. E., Reeves, C. E., Bauguitte, S., Morgan, W., Coe, H., Aruffo, E., Dari-Salisburgo, C., Giammaria, F., Carlo, P. D., and Heard, D. E.: Radical chemistry at night: comparisons between observed and modelled HO_x, NO_3 and N_2O_5 during the RONOCO project, Atmospheric Chemistry and Physics, 14, 1299–1321, doi:10.5194/acp-14-1299-2014, 2014.

Stutz, J., Kim, E. S., Platt, U., Bruno, P., Perrino, C., and Febo, A.: UV-visible absorption cross sections of nitrous acid, Journal of Geophysical Research: Atmospheres, 105, 14 585–14 592, doi:10.1029/2000JD900003, 2000.

Stutz, J., Thomas, J. L., Hurlock, S. C., Schneider, M., Glasow, R. V., Piot, M., Gorham, K., Burkhart, J. F., Ziemba, L., Dibb, J. E., and Lefer, B. L.: LongPath DOAS observations of surface BrO at Summit, Greenland, Atmospheric Chemistry and Physics, 11, 9899–9910, doi:10.5194/acp-11-9899-2011, 2011.

Su, H., Cheng, Y., Oswald, R., Behrendt, T., Trebs, I., Meixner, F. X., Andreae, M. O., Cheng, P., Zhang, Y., and Pöschl, U.: Soil nitrite as a source of atmospheric HONO and OH radicals, Science, 333, 1616–1618, doi:10.1126/science.1207687, 2011.

Thalman, R. and Volkamer, R.: Inherent calibration of a blue LED-CE-DOAS instrument to measure iodine oxide, glyoxal, methyl glyoxal, nitrogen dioxide, water vapour and aerosol extinction in open cavity mode, Atmospheric Measurement Techniques, 3, 1797–1814, doi:10.5194/amt-3-1797-2010, 2010.

Theys, N., Roozendael, M. V., Hendrick, F., Fayt, C., Hermans, C., Baray, J.-L., and Goutail, F.: Retrieval of stratospheric and tropospheric BrO columns from multi-axis DOAS measurements at Reunion Island (21° S, 56° E), Atmos. Chem. Phys., 7, 4733–4749, doi:10.5194/acp-7-4733-2007, 2007.

Theys, N., Van Roozendael, M., Hendrick, F., Yang, X., De Smedt, I., Richter, A., Begoin, M., Errera, Q., Johnston, P. V., Kreher, K., and De Mazière, M.: Global observations of tropospheric BrO columns using GOME-2 satellite data, Atmospheric Chemistry and Physics, 11, 1791–1811, doi:10.5194/acp-11-1791-2011, 2011.

Thibert, E. and Dominé, F.: Thermodynamics and Kinetics of the Solid Solution of HNO_3 in Ice, The Journal of Physical Chemistry B, 102, 4432–4439, doi:10.1021/jp980569a, 1998.

Thomas, J. L., Stutz, J., Lefer, B., Huey, L. G., Toyota, K., Dibb, J. E., and Glasow, R. V.: Modeling chemistry in and above snow at Summit, Greenland - Part 1: model description and results, Atmospheric Chemistry and Physics, 11, 4899–4914, doi:10.5194/acp-11-4899-2011, 2011.

Thomas, J. L., Dibb, J. E., Huey, L. G., Liao, J., Tanner, D., Lefer, B., von Glasow, R., and Stutz, J.: Modeling chemistry in and above snow at Summit, Greenland – Part 2: Impact of snowpack chemistry on the oxidation capacity of the boundary layer, Atmospheric Chemistry and Physics, 12, 6537–6554, doi:10.5194/acp-12-6537-2012, 2012.

Thomason, L. and Peter, T.: SPARC Assessment of Stratospheric Aerosol Properties (ASAP), World Climate Research Programme, p. 322, 2006.

Tillman, F. D., Choi, J.-W., and Smith, J. A.: A comparison of direct measurement and model simulation of total flux of volatile organic compounds from the subsurface to the atmosphere under natural field conditions: measurement and simulation of VOC flux, Water Resources Research, 39, doi:10.1029/2003WR002098, 2003.

Traversi, R., Becagli, S., Brogioni, M., Caiazzo, L., Ciardini, V., Giardi, F., Legrand, M., Macelloni, G., Petkov, B., Preunkert, S., Scarchilli, C., Severi, M., Vitale, V., and Udisti, R.: Multi-year record of atmospheric and snow surface nitrate in the central Antarctic plateau, Chemosphere, 172, 341–354, doi:10.1016/j.chemosphere.2016.12.143, 2017.

Triki, M., Cermak, P., Méjean, G., and Romanini, D.: Cavity-Enhanced Absorption Spectroscopy with a red LED source for NO_x trace analysis, Applied Physics B, 91, 195–201, doi:10.1007/s00340-008-2958-x, 2008.

Tuzson, B., Zeyer, K., Steinbacher, M., McManus, J. B., Nelson, D. D., Zahniser, M. S., and Emmenegger, L.: Selective measurements of NO, NO_2 and NO_y in the free troposphere using quantum cascade laser spectroscopy, Atmospheric Measurement Techniques, 6, 927–936, doi:10.5194/amt-6-927-2013, 2013.

Valin, L. C., Russell, A. R., and Cohen, R. C.: Variations of OH radical in an urban plume inferred from NO_2 column measurements: NO_2 column and variations of OH radical, Geophysical Research Letters, 40, 1856–1860, doi:10.1002/grl.50267, 2013.

Van Allen, R., Liu, X., and Murcray, F. J.: Seasonal variation of atmospheric nitric acid over the South Pole in 1992, Geophysical Research Letters, 22, 49–52, doi:10.1029/94GL02794, 1995.

Van der A, R. J., Eskes, H. J., Boersma, K. F., van Noije, T. P. C., Van Roozendael, M., De Smedt, I., Peters, D. H. M. U., and Meijer, E. W.: Trends, seasonal variability and dominant NO_x source derived from a ten-year record of NO_2 measured from space, Journal of Geophysical Research, 113, D04 302, doi:10.1029/2007JD009021, 2008.

Vandaele, A., Hermans, C., Simon, P., Carleer, M., Colin, R., Fally, S., Mérienne, M., Jenouvrier, A., and Coquart, B.: Measurements of the NO_2 absorption cross-section from 42 000 cm^{-1} to 10 000 cm^{-1} (238–1000 nm) at 220 K and 294 K, Journal of Quantitative Spectroscopy and Radiative Transfer, 59, 171–184, doi:10.1016/S0022-4073(97)00168-4, 1998.

Venables, D. S., Gherman, T., Orphal, J., Wenger, J. C., and Ruth, A. A.: High sensitivity in situ monitoring of NO_3 in an atmospheric simulation chamber using Incoherent Broadband Cavity-Enhanced Absorption Spectroscopy, Environmental Science & Technology, 40, 6758–6763, doi:10.1021/es061076j, 2006.

Ventrillard, I.: Optical Feedback - Cavity Enhanced Absorption Spectroscopy : Applications d'intérêt atmosphérique et à l'analyse de l'air expiré, in: Laboratoire Interdisciplinaire de Physique, p. 88, Communauté Université Grenoble Alpes, 2018.

Ventrillard, I., Gorrotxategi-Carbajo, P., and Romanini, D.: Part per trillion nitric oxide measurement by optical feedback cavity-enhanced absorption spectroscopy in the mid-infrared, Applied Physics B, pp. 180–188, doi:10.1007/s00340-017-6750-7, 2017.

Ventrillard-Courtillot, I., Sciamma O'Brien, E., Kassi, S., Méjean, G., and Romanini, D.: Incoherent Broad-Band Cavity-Enhanced Absorption Spectroscopy for simultaneous trace measurements of NO_2 and NO_3 with a LED source, Applied Physics B, 101, 661–669, doi:10.1007/s00340-010-4253-x, 2010.

Verginelli, I., Pecoraro, R., and Baciocchi, R.: Using dynamic flux chambers to estimate the natural attenuation rates in the subsurface at petroleum contaminated sites, Science of The Total Environment, 619-620, 470–479, doi:10.1016/j.scitotenv.2017.11.100, 2018.

Vicars, W. C. and Savarino, J.: Quantitative constraints on the ^{17}O-excess ($\Delta^{17}O$) signature of surface ozone: Ambient measurements from 50°N to 50°S using the nitrite-coated filter technique, Geochimica et Cosmochimica Acta, 135, 270–287, doi:10.1016/j.gca.2014.03.023, 2014.

Villena, G., Bejan, I., Kurtenbach, R., Wiesen, P., and Kleffmann, J.: Interferences of commercial NO_2 instruments in the urban atmosphere and in a smog chamber, Atmospheric Measurement Techniques, 5, 149–159, doi:10.5194/amt-5-149-2012, 2012.

Vitousek, P. M., Aber, J. D., Howarth, R. W., Likens, G. E., Matson, P. A., Schindler, D. W., Schlesinger, W. H., and Tilman, D. G.: Human alteration of the global nitrogen cycle: sources and consequences, Ecological Applications, 7, 737–750, doi:10.1890/1051-0761(1997)007[0737:HAOTGN]2.0.CO;2, 1997.

Volkamer, R., Spietz, P., Burrows, J., and Platt, U.: High-resolution absorption cross-section of glyoxal in the UV–vis and IR spectral ranges, Journal of Photochemistry and Photobiology A: Chemistry, 172, 35–46, doi:10.1016/j.jphotochem.2004.11.011, 2005.

Volkamer, R., San Martini, F., Molina, L. T., Salcedo, D., Jimenez, J. L., and Molina, M. J.: A missing sink for gas-phase glyoxal in Mexico City: formation of secondary organic aerosol, Geophysical Research Letters, 34, L19 807, doi:10.1029/2007GL030752, 2007.

Wachsstock, D.: Tenua: the kinetics simulator for Java, 2007.

Wagner, T., Ibrahim, O., Shaiganfar, R., and Platt, U.: Mobile MAX-DOAS observations of tropospheric trace gases, Atmospheric Measurement Techniques, 3, 129–140, doi:10.5194/amt-3-129-2010, 2010.

Wang, H., Chen, J., and Lu, K.: Development of a portable cavity-enhanced absorption spectrometer for the measurement of ambient NO_3 and N_2O_5: experimental setup, lab characterizations, and field applications in a polluted urban environment, Atmospheric Measurement Techniques, 10, 1465–1479, doi:10.5194/amt-10-1465-2017, 2017.

Wang, Y., Choi, Y., Zeng, T., Davis, D., Buhr, M., Gregory Huey, L., and Neff, W.: Assessing the photochemical impact of snow NO_x emissions over Antarctica during ANTCI 2003, Atmospheric Environment, 41, 3944–3958, doi:10.1016/j.atmosenv.2007.01.056, 2007.

Washenfelder, R. A., Langford, A. O., Fuchs, H., and Brown, S. S.: Measurement of glyoxal using an Incoherent BroadBand Cavity Enhanced Absorption Spectrometer, Atmospheric Chemistry and Physics, 8, 7779–7793, doi:10.5194/acp-8-7779-2008, 2008.

Weller, R., Minikin, A., König-Langlo, G., Schrems, O., Jones, A. E., Wolff, E. W., and Anderson, P. S.: Investigating possible causes of the observed diurnal variability in Antarctic NO_y, Geophysical Research Letters, 26, 2853–2856, doi:10.1029/1999GL900608, 1999.

Werle, P., Mücke, R., and Slemr, F.: The limits of signal averaging in atmospheric trace-gas monitoring by Tunable Diode-Laser Absorption Spectroscopy (TDLAS), Applied Physics B: Photophysics and Laser Chemistry, 57, 131–139, doi:10.1007/BF00425997, 1993.

Williams, E. J., Baumann, K., Roberts, J. M., Bertman, S. B., Norton, R. B., Fehsenfeld, F. C., Springston, S. R., Nunnermacker, L. J., Newman, L., Olszyna, K., Meagher, J., Hartsell, B., Edgerton, E., Pearson, J. R., and Rodgers, M. O.: Intercomparison of ground-based NO_y measurement techniques, Journal of Geophysical Research: Atmospheres, 103, 22 261–22 280, doi:10.1029/98JD00074, 1998.

Wilmouth, D. M., Salawitch, R. J., and Canty, T. P.: Stratospheric Ozone Depletion and Recovery, Green Chemistry, pp. 177–209, doi:10.1016/B978-0-12-809270-5.00008-X, 2018.

Wine, P. H. and Nicovich, J. M.: Atmospheric Radical Chemistry, in: Encyclopedia of Radicals in Chemistry, Biology and Materials, edited by Chatgilialoglu, C. and Studer, A., p. rad015, John Wiley & Sons, Ltd, Chichester, UK, doi:10.1002/9781119953678.rad015, 2012.

Winton, V. H. L., Ming, A., Caillon, N., Hauge, L., Jones, A. E., Savarino, J., Yang, X., and Frey, M. M.: Deposition, recycling, and archival of nitrate stable isotopes between the air–snow interface: comparison between Dronning Maud Land and Dome C, Antarctica, Atmospheric Chemistry and Physics, 20, 5861–5885, doi:10.5194/acp-20-5861-2020, 2020.

Wittrock, F., Oetjen, H., Richter, A., Fietkau, S., Medeke, T., Rozanov, A., and Burrows, J. P.: MAX-DOAS measurements of atmospheric trace gases in Ny-Ålesund - radiative transfer studies and their application, Atmospheric Chemistry and Physics, 4, 955–966, doi:10.5194/acp-4-955-2004, 2004.

Wolff, E. W.: Nitrate in Polar Ice, Ice Core Studies of Global Biogeochemical Cycles, pp. 195–224, doi:10.1007/978-3-642-51172-1_10, 1995.

Wolff, E. W., Rankin, A. M., and Röthlisberger, R.: An ice core indicator of Antarctic sea ice production?, Geophysical Research Letters, 30, doi:10.1029/2003GL018454, 2003.

Wolff, E. W., Jones, A. E., Bauguitte, S. J.-B., and Salmon, R. A.: The interpretation of spikes and trends in concentration of nitrate in polar ice cores, based on evidence from snow and atmospheric measurements, Atmospheric Chemistry and Physics, 8, 5627–5634, doi:10.5194/acp-8-5627-2008, 2008.

Ye, C., Zhou, X., Pu, D., Stutz, J., Festa, J., Spolaor, M., Tsai, C., Cantrell, C., Mauldin, R. L., Campos, T., Weinheimer, A., Hornbrook, R. S., Apel, E. C., Guenther, A., Kaser, L., Yuan, B., Karl, T., Haggerty, J., Hall, S., Ullmann, K., Smith, J. N., Ortega, J., and Knote, C.: Rapid cycling of reactive nitrogen in the marine boundary layer, Nature, 532, 489–491, doi:10.1038/nature17195, 2016.

Young, G. L.: NO_x formation in rotary kilns producing cement, clinker applicable NO_x control techniques and cost effectiveness of these control techniques, Conference record - IEEE Cement Industry Technical Conference, 2002.

Zatko, M., Geng, L., Alexander, B., Sofen, E., and Klein, K.: The impact of snow nitrate photolysis on boundary layer chemistry and the recycling and redistribution of reactive nitrogen across Antarctica and Greenland in a global chemical transport model, Atmospheric Chemistry and Physics, 16, 2819–2842, doi:10.5194/acp-16-2819-2016, 2016.

Zatko, M. C., Grenfell, T. C., Alexander, B., Doherty, S. J., Thomas, J. L., and Yang, X.: The influence of snow grain size and impurities on the vertical profiles of actinic flux and associated NO_x emissions on the Antarctic and Greenland ice sheets, Atmospheric Chemistry and Physics, 13, 3547–3567, doi:10.5194/acp-13-3547-2013, 2013.

Zheng, K., Zheng, C., Zhang, Y., Wang, Y., and Tittel, F. K.: Review of Incoherent Broadband Cavity-Enhanced Absorption Spectroscopy (IBBCEAS) for Gas Sensing, Sensors, 18, 3646–3671, doi:10.3390/s18113646, 2018.

Zhou, X., Zhang, N., TerAvest, M., Tang, D., Hou, J., Bertman, S., Alaghmand, M., Shepson, P. B., Carroll, M. A., Griffith, S., Dusanter, S., and Stevens, P. S.: Nitric acid photolysis on forest canopy surface as a source for tropospheric nitrous acid, Nature Geoscience, 4, 440–443, doi:10.1038/ngeo1164, 2011.

Zhu, C., Xiang, B., Zhu, L., and Cole, R.: Determination of absorption cross sections of surface-adsorbed HNO_3 in the 290–330nm region by Brewster angle cavity ring-down spectroscopy, Chemical Physics Letters, 458, 373–377, doi:10.1016/j.cplett.2008.04.125, 2008.

Zhu, C., Xiang, B., Chu, L. T., and Zhu, L.: 308 nm photolysis of nitric acid in the gas phase, on aluminum surfaces, and on ice films, The Journal of Physical Chemistry A, 114, 2561–2568, doi:10.1021/jp909867a, 2010.